# Investigation of Silicon-Based and Multicomponent Electrodes for High Energy Density Li-ion Batteries

James Sturman

Thesis submitted in partial fulfillment of the requirements for the
degree of Doctor of Philosophy in Chemical Engineering

Department of Chemical and Biological Engineering
Faculty of Engineering
University of Ottawa

# Abstract

Li-ion batteries have enabled the widespread adoption of portable electronics and are becoming the technology of choice for electric vehicles and grid storage. One of the most promising ways to accommodate this demand is to increase the energy density and cycle life of battery electrode materials. Key strategies promoted in the literature include the use of nickel-rich cathodes as well as high-capacity anodes like silicon and lithium metal. While these materials enable a high energy density, this advantage is often counterbalanced with deficits such as poor stability and high cost. Multicomponent electrodes refer to strategies that try to leverage the relative advantages of different materials to offer an attractive compromise of energy density, cost, and cycle life. This thesis has investigated various aspects of multicomponent electrodes with a special emphasis on silicon-based anodes and high-entropy materials.

Silicon (Si) is the second-most abundant element on earth and has one of the highest gravimetric capacities. However, silicon anodes are notorious for their poor cycle stability. Herein, improvements in the stability of silicon-based electrodes are achieved with multicomponent composite strategies involving the use of nanostructured spherical silicon. The nanosilicon is studied in high-fraction (80 wt% Si) and low-fraction (≤20 wt% Si) formulations to investigate both failure mechanisms and practical capacity retention, respectively. Composite strategies in which nanosilicon is encapsulated within a $Li_4Ti_5O_{12}$ ceramic or MOF-derived carbon matrix are shown to deliver superior capacity retention compared to simple composites of silicon and graphite. Considerable attention is given to the selection of a water-soluble binder and its role in electrochemical stability and electrode cohesion in high-loading silicon electrodes. It is found that unmodified high-molecular-weight sodium carboxymethyl cellulose offers better capacity retention compared to xanthan gum or low-molecular-weight binders.

The high-entropy design strategy has created a diverse and largely unexplored set of multicomponent oxides and alloys with great potential as electrode materials. This strategy is applied to the family of layered cathodes, where the synthesis and electrochemical properties of the best-performing $Li(NiCoMnTiFe)_1O_2$ are reported. Despite the low Ni content, the cathode delivers a high initial capacity with unique overlithiation stability despite being charged to 4.4 V.

Throughout the thesis, Operando XRD is used to reveal important insight into the lithiation mechanisms of the multicomponent electrodes including intercalation-based graphite, alloying-based silicon, and a novel organic azaacene.

# Statement of Contribution

I hereby declare that I am the lead-author of all chapters in this thesis. Artificial Intelligence was not used to generate any text in this thesis.

Chapter 2 and 3 were written solely by James Sturman while considering minor editorial comments by Yaser-Abu Lebdeh and Elena A. Baranova.

Chapter 4 is derived from a research paper published in the Journal of the Electrochemical Society (JES). This chapter was written solely by James Sturman. Chae-Ho Yim was responsible for the machine-learning (including Figure 4.1). James Sturman was responsible for all material synthesis, XRD, and electrochemical testing. Additional credit has been given in the acknowledgement section.

Chapter 5 is derived from a research paper published in ACS Energy & Fuels. This work was part of a collaboration with the University of Toronto. The chapter was written primarily by James Sturman. James Sturman was responsible for all electrochemical tests. Eloi Grignon was responsible for SmAz synthesis and Figure 5.1. Eloi Grignon contributed to part of the introduction and organic molecule characterization. Supplementary Information related to this paper is found in the Appendix.

Chapter 6 is derived from a research paper published in JES. The chapter was written primarily by James Sturman while considering minor editorial comments by the co-authors of the publication. Mathieu Toupin expanded on a few paragraphs in the discussion. James Sturman was responsible for all sample preparation and electrochemical testing. Additional credit has been given in the acknowledgement section. Supplementary Information related to this paper is found in the Appendix.

Chapter 7 is derived from a research paper published in JES. This chapter was written solely by James Sturman while considering minor editorial comments by the co-authors of the publication. Supplementary Information related to this paper is found in the Appendix.

Chapter 8 is derived from a research paper accepted in ACS Applied Energy Materials. This work was part of a collaboration with the University of Ottawa. The chapter was written primarily by James Sturman. Mohamed Houache contributed to part of the introduction and prepared the figures related to XPS. Walace Doti do Pim was responsible for the MOF synthesis.

Chapter 9 was written solely by James Sturman.

# Acknowledgements

I would like to thank my supervisors Dr. Yaser Abu-Lebdeh at the National Research Council (NRC) and Dr. Elena A. Baranova at the University of Ottawa for their support and guidance. Additional thanks to Dr. Mathieu Toupin from NRC in Boucherville for his support regarding the work with Tekna silicon. I would also like to thank Dr. Yong Zhang from the Hefei University of Technology for his support and hospitality during my time as a visiting student in China.

I would like to thank the members of the battery materials innovation team at NRC: Chae-Ho Yim, Svetlana Niketic, Dr. Mohamed Houache, Dr. Zouina Karkar, as well as other graduate students Dr. Hilal Al-Salih, Shuo Yan, and Eloi Grignon.

Finally, I would like to thank the members of the thesis evaluation committee including Dr. Arnaud Weck, Dr. Benoit Lessard, and Dr. Ghassan Jabbour from the University of Ottawa, as well as Dr. Xia Li from Concordia University.

# Table of Contents

# List of Figures and Tables

Chapter 4: Exploring the Design Space of High-Entropy Layered Cathodes ............................ 73

Chapter 5: Small Molecule Azaacene as an Anode Material for Lithium-ion Batteries ............. 82

## List of Abbreviations and Acronyms

| | |
|---|---|
| @ | Refers to coating designs (e.g., core@shell) |
| 11111 | Refers to equimolar HE cathodes ($LiNi_{0.2}Mn_{0.2}Co_{0.2}Fe_{0.2}Ti_{0.2}O_2$ in particular) |
| CE | Coulombic Efficiency |
| CMC (also NaCMC) | Sodium Carboxymethyl Cellulose |
| CPE | Constant Phase Element |
| CV | Cyclic Voltammetry |
| DEC | Diethyl Carbonate |
| dQ/dV | Differential Capacity |
| EC | Ethylene Carbonate |
| EDX | Energy-Dispersive X-ray Spectroscopy |
| EELS | Electron Energy Loss Spectroscopy |
| EIS | Electrochemical Impedance Spectroscopy |
| EMC | Ethyl Methyl Carbonate |
| FEC | Fluoro Ethylene Carbonate |
| FTIR | Fourier Transform Infrared Spectroscopy |
| G | Graphite |
| HE (also HEO and HEA) | High-Entropy (Oxide and Alloy) |
| ICP-OES | Inductively Coupled Plasma-Optical Emission Spectrometry |
| JES | Journal of the Electrochemical Society |
| LTO | Lithium Titanium Oxide |
| MOF | Metal Organic Framework |
| NMC | Refers to $LiNi_xMn_yCo_zO_2$ cathode family |
| OCV | Open Circuit Voltage |
| PVDF | Polyvinylidene Fluoride |

| | |
|---|---|
| SEI | Solid Electrolyte Interphase (sometimes Interface) |
| SEM | Scanning Electron Microscopy |
| Si | Silicon |
| SmAz | Small Molecule Azaacene |
| SP | Super P |
| TEM | Transmission Electron Microscopy |
| TRL | Technology Readiness Level |
| V | Voltage (vs. $Li/Li^+$ unless otherwise specified) |
| XG | Xanthan Gum |
| XPS | X-ray Photoelectron Spectroscopy |
| XRD | X-ray Diffraction |

# Chapter 1: Introduction

## Background and Motivation

In many ways, Lithium (Li) is unrivaled in its ability to supply the world with abundant, safe, and renewable energy. Li has the lowest atomic weight (6.94) and density (0.534 g/cm$^3$) of any metal on the periodic table.[1] Li's low reduction potential (-3.04 V vs standard hydrogen electrode) and high gravimetric capacity (3860 mAh/g) ranks it among the most reactive and energy dense of all elements.[1] Li is also relatively abundant and has low toxicity compared to other energy dense materials like beryllium or radioactive elements. Moreover, unlike non-renewable hydrocarbons, Li-based material's reversible redox-based mechanism enables their use as a rechargeable power and energy source. These properties make Li (and to a lesser extent other alkali metals like Na) especially well-suited for portable energy storage applications for the foreseeable future.

Since their successful commercialization by Sony in the 1990s, Li-ion batteries have enabled the widespread adoption of portable devices like smartphones and laptops, and they are becoming the technology of choice for electric vehicles and grid storage.[2] The great success of this technology has recently been commemorated by the 2019 Nobel Prize in Chemistry, which was awarded to John B. Goodenough, M. Stanley Whittingham, and Akira Yoshino "for the development of lithium-ion batteries".[3] Li-ion batteries owe their success to key individuals as well as many research groups around the world over a period of several decades. Their evolution has been largely incremental, but is also marked by several milestones from fields specializing at vastly different length-scales. At the molecular level, the use of ethylene carbonate-based electrolytes (rather than propylene carbonate) was an important development that facilitated a stable SEI and enabled the graphite anode.[1] At the cell form factor level, Tesla's decision to build their Model S battery pack from over 7000 of the commonly available 18650 cylindrical cells (initially designed for a Sony camcorder) also stands out.[1]

In theory, a Li-ion battery consists of an anode, a cathode, a separator, and an electrolyte. However, each of these components represents a separate field of research. Moreover, the complex interplay between these components is often the greatest bottleneck to the development of better batteries. This challenge is best summarized by the humorous aphorism: "Given the best anode, cathode, separator and electrolyte, one could produce the worst battery by simply putting them together".[1]

Despite these challenges, Li-ion batteries have improved significantly over the past few decades (though notably *not* to the extend predicted by Moore's Law).[1] The cell level energy density of Li-ion batteries has increased from around 90 Wh/kg in the 1990s to over 270 Wh/kg in 2021.[4, 5] Moreover, mass production has helped to reduce cell prices from around 5000 $/kWh in 1991 to around 100 $/kWh in 2021.[5] The demand for Li-ion batteries has grown from 30 GWh in 2011 to over 490 GWh in 2021 and is forecasted to reach 2-3.5 TWh by 2030.[5] However, there is still a need to reduce cost and increase energy density if Li-ion batteries are to see the scale of adoption required for global electrification. Tesla recently released a report which claims a "fully electrified and sustainable economy" requires 240 TWh of energy storage.[6] Considering the 2030 demand is nearly two orders-of-magnitude lower than 240 TWh, there is still considerable work to be done.

In recent years, a rough consensus has crystalized within the battery community regarding the future direction of Li-ion battery development. This consensus affects a range of subdisciplines and can be summarized as follows: (1) the use of low-Co, Ni-rich cathodes, (2) the use of high-energy-density anodes like silicon or lithium metal.[5, 7, 8] This thesis has sought to address these points with a special focus on silicon-based and multicomponent electrodes.

The first point is related to cost reduction but is also relevant to increasing energy density. The use of cobalt has continued to dominate the cathode chemistry of Li-ion batteries in portable electronics and is still present to a lesser extent in the cathodes for Electric Vehicles (EV).[7] Cobalt has experienced a significant price increase in recent years to around 50 USD/kg, compared to around 22 USD/kg for nickel (2022 prices).[7] Moreover, the global production of cobalt is significantly lower than nickel (~170000 vs 2700000 tons in 2021).[7] There are also social problems associated with cobalt's supply chain; Co is sourced primarily from the Democratic Republic of the Congo, which is known to employ child labour.[7] As a result, researchers have endeavored to reduce or eliminate Co from the cathode. One solution, recently promoted by Tesla, is the use of the inexpensive iron-based $LiFePO_4$ (LFP) cathode.[6] Though it is worth noting that other geopolitical factors influence the adoption of certain technologies, such as Chinese Li-ion battery manufacturers' preference for the LFP cathode.[5] While LFP is suitable for economical standard-range vehicles, its relatively low energy density makes it unsuitable for long-range vehicles.[6] For these applications, cathodes using nickel are more suitable (the so-called high-energy density "Ni-rich" cathodes).[6] Another approach which can reduce or eliminate Co, and more generally reduce the reliance on any one element, is the high-entropy (HE) design strategy. This strategy uses multiple elements in equiatomic proportion to design new cathode and anode families. The HE strategy has been reviewed in great detail in Chapter 2 of this thesis. In addition, Chapter 4 reports some experimental work on low-Co HE layered cathodes.

The second point is related to the energy density of the anode. Li metal and silicon are promising materials that can increase a battery's energy density relative to pure graphite. [9] The use of silicon-based anodes together with Ni-rich layered cathodes is one of the most promising ways to achieve a cell level >300 Wh/kg energy density needed for next-generation batteries.[10] However, these anodes are not as stable as graphite and require careful interfacial and compositional engineering.[11] Silicon has a high gravimetric energy density that makes it suitable to replace or be used in conjunction with graphite. However, there is a need to reduce electrode pulverization and improve long-term performance. Silicon-based composites refer to the broad family of multicomponent electrodes that employ various strategies to enable the silicon anode; these materials are the subject of Chapters 6, 7, and 8. Moreover, some interesting results on high-capacity organic anodes are discussed in Chapter 5.

Finally, there is an increasing awareness of the importance of scalability with respect to the adoption of new Li-ion battery technologies.[8] Key issues include the tendency of battery researchers to use expensive materials, complex synthesis methods, or unrealistic conditions that improve the performance of reported battery data.[8] Moreover, there is a lack of standardization in the field of battery research owing to the myriad of different (and ever-growing) electrode formulations and electrolytes.[5, 12] This can make it difficult to compare results between other researchers and commercial baseline materials. Although these challenges are not unique to Li-ion battery research, the battery field has garnered a reputation for "hype, false promises and unrealistic goals", as has been discussed in a recent perspective in *Nature Communications* (noting also that there is "too much research that confuses rather than adds to progress").[5] What is implicit in this commentary is an appeal to the practical and a more transparent exchange of ideas across disciplines. Although the materials studied in this thesis are at a Technology Readiness Level (TRL) 1-4 (owing primarily to half-cell testing) and are therefore not practical in any commercial sense, many chapters in this thesis address certain facets of the problem. The work in Chapter 6 tries to move away from conditions in the literature which can inflate the cycling performance of silicon (i.e., exceedingly low total silicon loadings and high binder & Super P mass fractions). The silicon nanopowder used in Chapters 6 and 8 were supplied by Tekna, which uses an industrial-scale synthesis method. Moreover, the chapters on silicon anodes always used nature-derived and water-soluble biopolymer binders. Chapter 8 critically investigates the extent to which Metal-Organic Frameworks improve the performance of silicon anodes. A tendency towards the practical also has some overlap with the desire to reduce or eliminate Co, which is the subject of Chapter 4.

## Objectives

The main objectives of this thesis are to increase the energy density and lifetime of Li-ion battery electrodes while using relatively inexpensive materials and simple preparation methods. Technically, this involves the preparation, characterization, and electrochemical testing of these materials in Li-ion battery half-cells. The thesis objectives can be summarized with the five points below.

1. Design multicomponent electrodes to improve the electrochemical performance of high-capacity nanostructured silicon-based anodes. Compare the performance of these composites to simple baselines such as silicon-rich or silicon-graphite electrodes.
2. Investigate the preparation and electrochemical properties of aqueous binders integrated into silicon-based composite anodes. Study these binders in silicon-rich and low-silicon formulations to understand causes of failure and practical electrochemical performance, respectively.
3. Employ the high-entropy design strategy to the synthesis of new nickel-based layered cathodes with the goal of improving electrochemical performance.
4. Study capacity and capacity retention as the primary metrics of electrochemical performance in the electrode materials. Understand the fundamental electrochemical properties of these electrode materials with dQ/dV analysis, voltage curves, cyclic voltammetry, and impedance spectroscopy. Understand material-property relationships with physicochemical characterization techniques such as powder X-Ray Diffraction (XRD), Scanning Electron Microscopy (SEM), and Energy Dispersive X-Ray Spectroscopy (EDX).
5. Develop Operando XRD capabilities for the characterization of electrode materials to understand lithiation mechanisms and causes of failure during battery cycling.

## Thesis Structure

Chapter 2 presents an overview of Li-ion battery fundamentals. The basic working principle of the technology is discussed along with the chemistry of different cathode and anode materials. Considerable attention has been given to the silicon anode as it is a highlight of the thesis. Sub-chapter 2.4 is derived from a review paper in Frontiers in Energy Research. The chapter summarizes the use of high-entropy materials in Li-ion battery electrodes. The review primarily discusses the progress and challenges of high-entropy oxide-based anodes and cathodes. Some emerging results on high-entropy alloy anodes and solid electrolytes are also discussed.

Chapter 3 provides an overview of the main experimental techniques used throughout the thesis. It reviews basic theory and covers details that were not discussed in the experimental section of the research paper chapters. In particular, the chapter discusses various developments related to the design of Operando XRD capabilities.

Chapter 4 is derived from a research paper in the Journal of the Electrochemical Society (JES). It applies a multicomponent strategy to the development of new cathodes. After screening and synthesizing dozens of cathodes, the chapter reports the results of the best-performing high-entropy layered cathode. This cathode was however not competitive with current commercial baselines, and the majority of subsequent work focused primarily on multicomponent composites for the silicon anode.

Chapter 5 is derived from a research paper in ACS Energy & Fuels. It reports the electrochemical properties of a novel high-capacity organic anode and offers some insight into its lithiation mechanism with Operando XRD. Supplementary Information related to this paper is found in the Appendix.

Chapter 6 is derived from a research paper in JES. The binder plays an important role in the integrity of the silicon anode. The chapter investigates the causes of failure in high-loading silicon anodes prepared with different aqueous binders. Silicon-rich electrodes are used to differentiate causes of failure with each binder, and the multicomponent silicon-graphite composites are used to study the two binders under practical conditions. Supplementary Information related to this paper is found in the Appendix.

Chapter 7 is derived from a research paper in JES. The chapter reports the electrochemical performance of different surface-modified silicon anodes that employ either a carbon coating or a

$Li_4Ti_5O_{12}$ coating with graphite. The combination of the surface protective contribution of the LTO and the buffering contribution from the graphite are discussed. Supplementary Information related to this paper is found in the Appendix.

Chapter 8 is derived from a research paper accepted in ACS Applied Energy Materials. The chapter reports the results of different design strategies involving Metal-Organic-Frameworks (MOF) and silicon. The chapter builds off of the work of Chapter 7 but employs a MOF-derived carbon matrix with Co rather than a brittle ceramic coating. Supplementary Information related to this paper is found in the Appendix.

Chapter 9 discusses some key conclusions and future recommendations.

References continue into Chapter 2.

# Chapter 2: Review of the Literature

## 2.1 Fundamentals of Li-ion Battery Technology

Figure 2.1.1 illustrates a typical lithium-ion battery. It consists of two electrodes (a positive and negative electrode), a membrane that separates both electrodes, and a Li-salt containing carbonate-based liquid electrolyte to facilitate Li ion transport.[2, 13] During the charge of a full-cell, Li ions migrate from the positive electrode to the negative electrode and the electrons travel outside an external circuit (i.e., current). The charging of a Li-ion battery is a thermodynamically unfavorable reaction and requires the supply of a current. During the discharge of a full cell, the process is reversed, and the Li ions migrate from the negative electrode to the positive electrode. The discharge of a Li-ion battery is a thermodynamically favorable reaction and results in the generation of a current.

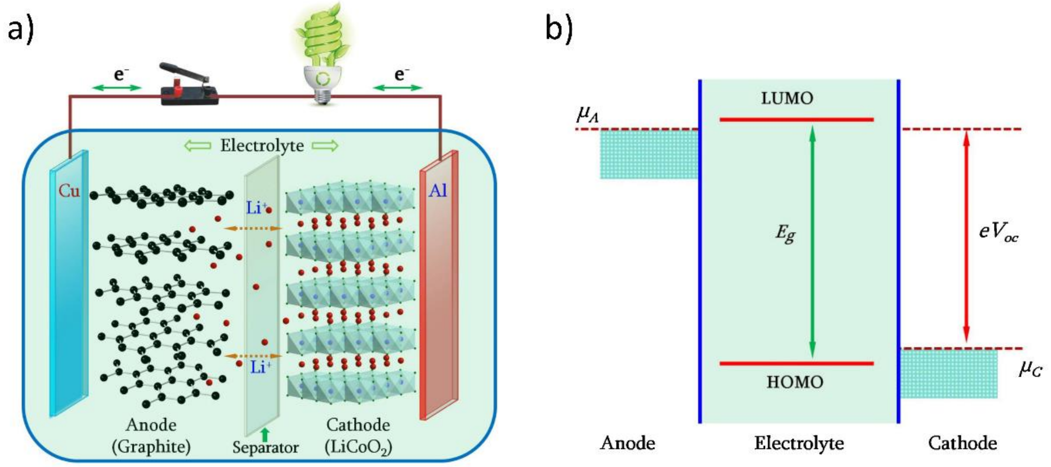

Figure 2.1.1 a) Lithium-ion battery schematic with b) associated energy diagram [13]

Capacity and voltage are the primary metrics related to the energy density and power density of a battery, respectively.[14] Capacity is a fundamental property of an electrode material and can be calculated theoretically with Equation 2.1.[15] Capacity quantifies the ability of an electrode material to store electrochemical energy and is measured in milliamp-hours per gram (mAh/g). Voltage is measured in volts (V) and depends on the difference between the chemical potential of the anode ($\mu_a$) and cathode ($\mu_c$), seen with Equation 2.2.[15] This difference is illustrated with the energy diagram of Figure 2.1.1b.

$$Capacity\left(\frac{mAh}{g}\right) = \frac{nF}{3.6MM} \qquad \text{Equation 2.1}$$

$n$ is the number of electrons
$F$ is Faraday’s constant, 96485 C/mol
$MM$ is the molar mass of the active material
in g/mol

$$Volt\left(\frac{J}{C}\right) = \frac{\mu_a - \mu_c}{zF} \qquad \text{Equation 2.2}$$

z is the charge transferred

$$Power\ (W) = V \times I \qquad \text{Equation 2.3}$$

W is watt

It is common to use the terms “anode” and “cathode” for the negative and positive electrodes, respectively. As such, this terminology will be used throughout the thesis. However, it should be noted that while this terminology is ubiquitous, it is academically incorrect when referring to the charging process.[5] The cathode is the original source of Li ions in a full-cell battery and is typically a lithiated metal oxide ceramic, whereas the anode is typically made of graphite.[13, 16] The anode is the electrode that stores Li ions when they migrate from the cathode to the anode during battery charging. In half-cell testing, the negative electrode is a Li metal foil (voltage vs Li/Li$^+$), where Li is present in great excess and serves as the counter/reference electrode. This allows for the electrochemical investigation of the anode and cathode materials separately versus a stable reference. However, it should be noted that the “anode” electrode material will technically serve as the positive electrode in half-cells with Li metal. The term “Li-ion” will be used as a generic term to refer to any technology where solvated Li$^+$ migrates through the electrolyte, or where Li exists in a pseudometallic state found in certain anode materials.[17]

## 2.2 Fundamentals of Cathode and Anode Chemistry

While the history of Li-ion batteries was complex and involved many incremental contributions, the developments listed below were central to the modern iteration of the technology.

1. In the early 1970s, Michel Armand proposed the "rocking chair" battery concept in which Li ions shuttle between two different electrode materials during charging and discharging.[18]
2. In 1976, pioneering work on the reversible cathode material $LiTiS_2$ (LTS) was published by Stanley Whittingham while working at Exxon.[1, 19]
3. In the early 1980s, the John Goodenough research group at the University of Oxford published work on $LiCoO_2$ (LCO), which would later become a dominant commercial cathode material.[1, 15]
4. In the mid-1980s, a research group at the Asahi Kasei Corporation designed a Li-ion battery with an LCO cathode and a carbonaceous anode derived from petroleum coke.[1]
5. In 1990, the Jeff Dahn group reported the first electrochemical synthesis of $LiC_6$ in a non-aqueous electrolyte.[1]
6. In 1991, Sony commercialized the first Li-ion battery which consisted of an LCO cathode and a carbon anode.[1, 2]

Since the early 1990s, research on Li-ion batteries has focused primarily on the development of high-capacity electrode materials. However, it should be understood that considerable work has been directed towards the understanding of the SEI, material compatibility, electrolyte solvents, additives, salts, separators, current collectors, etc. The cathode has been the subject of much research because the energy density of the entire battery is ultimately governed by the gravimetric capacity of the cathode material. In addition, the cathode accounts for 40-50% of the total cell cost.[7]

### Cathode Materials

Cathode materials are classified according to their structure. Figure 2.2.1 illustrates the most common structure families, which include layered (e.g., $LiCoO_2$ or LCO), spinel (e.g.,

$LiMn_2O_4$ or LMO), and olivine (e.g., $LiFePO_4$ or LFP).[13, 16] The most commercially successful cathodes have been the layered oxides (LCO being the first) due primarily to their high operating voltage, high capacity, and stability in air.[16] LCO was also the first cathode used by Tesla in their early Roadster.[5] Layered cathodes have a α-$NaFeO_2$ type layered structure with the generalized stoichiometry $LiMO_2$ (where M is a 3d transition metal) and belong to the *R-3m* space group.[20] The Li and M occupy octahedral sites of alternating layers.[16, 20] Layered cathodes have among the highest theoretical capacities (274 mAh/g for LCO).[16] However, the experimentally observed capacity is always much lower (135-200 mAh/g). The extractable lithium is limited to about half of the total available lithium.[15] Efforts to extract more lithium by deep cycling above 4.2 V will cause lattice distortion and significant capacity fade.[16]

Despite the commercial success of LCO, it has several disadvantages. First, cobalt is expensive and not sustainably sourced.[7] Moreover, LCO displays poor thermal stability which can cause an exothermic release of oxygen and precipitate a thermal runaway.[16] Efforts to replace the cobalt with different 3d transition metals (typically Ni and Mn) have given rise to several cathode materials with lower cost and better electrochemical properties than LCO. In theory, $LiNiO_2$ (LNO) is attractive owing to its higher capacity and lower cost than LCO.[16] However, it is difficult to prepare pure LNO because the $Ni^{2+}$ (0.69 Å) ion has a tendency to occupy the $Li^+$ (0.76 Å) sites owing to their similar atomic radii.[16, 21, 22] This causes cation mixing in the structure and is responsible for severe capacity fade owing to blocked $Li^+$ diffusion pathways.[16] Finally, $LiMnO_2$ is an unstable compound because it converts to spinel upon cycling, resulting in a large irreversible capacity.[16, 23] The combination of Co, Ni, and Mn or Al transition metals in the layered oxide cathode has been shown to improve both capacity and capacity retention.[7, 16] There exist a variety of stoichiometries, but common commercialized compositions include $LiNi_{0.5}Mn_{0.3}Co_{0.2}O_2$ (NMC532), $LiNi_{0.33}Mn_{0.33}Co_{0.33}O_2$ (NMC333 also NMC111), and $LiNi_{0.8}Mn_{0.1}Co_{0.1}O_2$ (NMC811).[16, 20, 23] In Ni-rich NMC, the $Mn^{3+}$ ion is oxidized to $Mn^{4+}$, as it donates electrons to the lower energy $Ni^{2+}/Ni^{3+}$ redox couple.[23] The $Mn^{4+}$ ion therefore remains electrochemically inactive and stabilizes the structure.[23] A greater nickel content is usually reported to increase the experimental capacity (>200 mAh/g for NMC811 vs 160 mAh/g for NMC111).[16, 23] Nickel-rich cathodes are also economical; for example, $LiNi_{0.92}Co_{0.06}Al_{0.02}O_2$ is 50% less expensive than LCO (per kg basis).[5] Research is currently focused on increasing the electrochemical capacity and nickel content while also preventing capacity decay. Moreover, recycling of the lithium, cobalt, nickel, and manganese from spent Li-ion batteries (yielding "black mass") is becoming a pressing research topic to address the long-term sustainability of these materials.[8]

Spinels like $LiMn_2O_4$ (LMO) are cost effective and desirable owing to the abundance of manganese.[16] Spinels have a 3D structure, where Li occupies the tetrahedral 8a sites, and Mn occupies the octahedral 16d sites.[16, 23] The 3D structure afford spinels certain desirable electrochemical properties like high-rate capability and high operating voltage. In contrast, their lower intrinsic Li content gives spinels a lower capacity and capacity retention than layered structures.[16] The dissolution of manganese into the electrolyte is believed to be one of the primary reasons for the electrochemical capacity fade.[16] The $Mn^{3+}$ ion can undergo a disproportionation reaction ($2Mn^{3+} \rightarrow Mn^{2+} + Mn^{4+}$) due to Jahn-Teller distortion, which results in the irreversible dissolution of the $Mn^{2+}$ ion into the electrolyte.[16, 23]

$LiFePO_4$ (LFP) is the most studied of the olivine cathode materials. It is a polyanionic compound, where the $Li^+$ and $Fe^{2+}$ occupy the octahedral sites and the P occupies the tetrahedral sites within a disordered hexagonal close-packed oxygen array.[16] LFP is inexpensive (owing to the abundance of iron), thermally stable, and has a reasonably high capacity (170 mAh/g).[16] While the disadvantages of LFP include a lower operating voltage than most layered cathodes and a low electronic and ionic conductivity.[16, 23] Commercial LFP is typically carbon coated to increase electrical conductivity.[18]

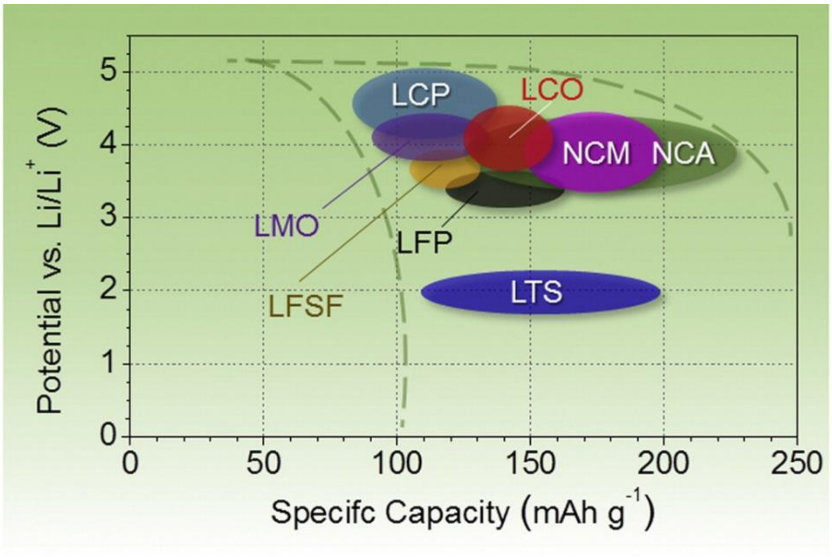

Figure 2.2.1 Theoretical capacities of various cathode families[16]

### Anode Materials

Anode materials differ based on their intrinsic capacity and electrochemical lithiation mechanism. There are three main categories of lithiation mechanism: intercalation, plating/stripping, and alloying. However, it is worth acknowledging other lithiation mechanisms, such as the conversion mechanism seen in certain metal oxides.[16] Figure 2.2.2 illustrates the different types of anode materials and their capacities. Intercalation is most often associated with traditional graphite. Graphite exists as layers of graphene bound together by weak van der Waals forces.[1] Lithium can intercalate into the space between these sheets, resulting in the final lithiated phase $LiC_6$ (with a theoretical capacity of 372 mAh/g).[2] The solid-electrolyte-interphase (SEI) is an important passivating film that forms when the carbonate-based electrolyte reacts with the pristine surface of the graphite.[16] This SEI serves to protect the anode from further reactions and is very relevant to the stability and safety of the battery. Graphite was initially an undesirable anode material because when used with older propylene carbonate (PC) based electrolytes, the graphite experienced solvent cointercalation, exfoliation, and unmitigated side reactions.[1] As a result, early Li-ion batteries used disordered carbons to circumvent exfoliation. Examples of these disordered carbons include petroleum-derived soft carbons or polyfurfuryl alcohol resin-derived hard carbons.[1] Hard carbons typically deliver gravimetric capacities similar to or greater than graphite.[24] However, their disadvantages include low volumetric capacity, a high cost due to high-temperature synthesis, and a low first cycle Coulombic Efficiency (CE).[2] Moreover, their lithiation mechanism is complex but is believed to involve a combination of Li adsorption and intercalation.[24] The use of ethylene carbonate (EC) based electrolytes were found to facilitate a stable SEI in the presence of a graphite anode, and thus eliminated the problems of graphite exfoliation and unmitigated side reactions.[1] Since the mid-1990s, graphite has been the dominant anode material in Li-ion batteries. There exist two main categories of graphite: natural and synthetic. Natural graphite has the advantage of being obtained from the mining and refining of natural reserves; it is therefore economical, abundant and has desirable electrochemical properties (capacity ~350 mAh/g and high CE).[5] However, its flaky morphology and high anisotropy causes a low rate capability.[2] As a result, natural graphite is typically mechanically processed into spherical particles to improve battery performance. In contrast, synthetic graphite offers additional benefits such as high purity and a tunable structure.[2] However, its high-temperature synthesis (being derived from soft carbon) is expensive and its intrinsic capacity is slightly lower than natural graphite.[2] Canada is especially well positioned to supply the world with graphite for composite anodes.[9] Canadian-based carbon and graphite companies include Nouveau Monde Graphite and Nanoxplore. Graphite is still the dominant anode material as of 2023.[5]

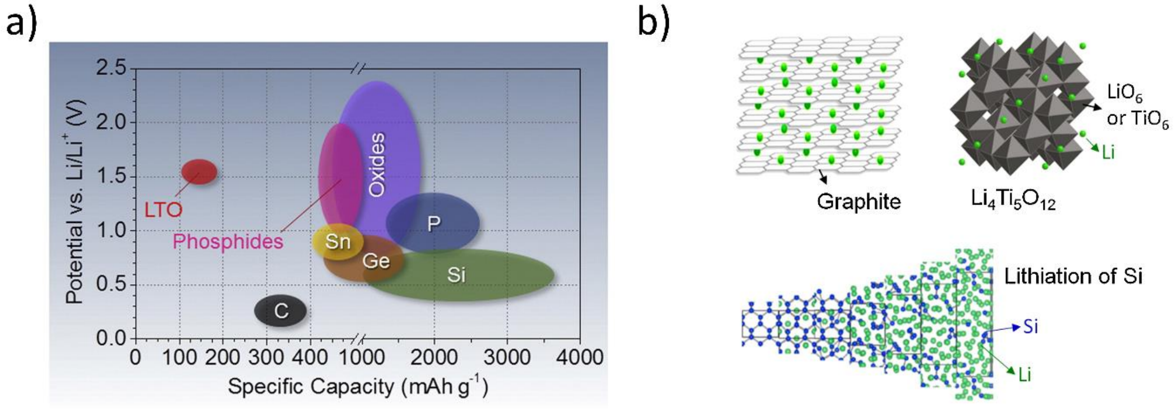

Figure 2.2.2 a) Theoretical capacities of various anode materials and b) schematic diagram illustrating the different anode lithiation mechanisms [16]

The second type of lithiation mechanism is plating/stripping, most notably seen with the lithium metal anode. Lithium metal is widely regarded as a promising anode material owing to its high theoretical capacity (3860 mAh/g) and low redox potential (-3.04 V vs SHE).[25, 26] This capacity is about ten times greater than traditional graphite (372 mAh/g) and is considered the highest anode capacity practically attainable in a material at room temperature. If successfully implemented, it would increase the energy density of a battery by about 30% (not ten-fold, since the anode and cathode capacity must be balanced).[27] The low redox potential of Li also allows it to offer the highest full-cell power density of any other Li-based negative electrode. While it is common to use lithium metal as an anode in primary batteries, their use in secondary (i.e. rechargeable) batteries is a challenge due to the plating/stripping mechanism.[28] Historically, rechargeable Li metal batteries have been commercialized with limited success. For example, in the late 1980s the Molicel (using $MoS_2$ cathode and a Li metal anode) was recalled due to a number of safety incidents involving fires.[1] The plating/stripping mechanism is unstable because it promotes the formation and propagation of metallic dendrites, which can cause an electrical short circuit.[29, 30] Figure 2.2.3 illustrates the lithium anode plating/stripping process. During discharge, Li is stripped from the bulk lithium metal and the subsequent solvated $Li^+$ intercalates into the cathode.[31] During charge, Li is de-intercalated from the cathode and lithium is plated back onto the anode surface.[31] Unlike host-based anodes like graphite that occupy a fixed volume in the battery, lithium metal is a hostless lithium source when used as an anode. [29] As a result, there is a large, continuous contraction and expansion of the space occupied by the lithium metal with every charge and discharge cycle. This expansion places stress on the lithium-electrolyte interface and can lead to void space formation and eventual delamination of the electrolyte from the lithium electrode.[32] The re-plating of the lithium is often loosely packed and of low density, leading to an inhomogeneous deposition layer.[26, 32] The resulting voids at the lithium-electrolyte interface reduces the surface area in contact with the metal.[32] This causes a concentration of the current density at the interface sites that have retained contact. There is a critical current density above which lithium dendrites will form.[31] The current density at the remaining contact sites can quickly exceed this critical current density, leading to dendrite propagation.[31] This can happen even if the applied current density through the cell is below the critical value.[31] Sometimes dendrites can detach from the bulk phase and deposit on the lithium surface as inactive or *dead* lithium.[29] This inactive phase and the unstable SEI increase the interfacial resistance.[26] In instances where the dendrite growth is unobstructed, an electrical short-circuit becomes a serious safety risk. Solid-state electrolytes (such as polymer, ceramic, or polymer-ceramic hybrids) greatly reduce this safety risk and have revived interest in the lithium metal anode for rechargeable batteries.[33] Companies like SolidPower and QuantumScape have received a large amount of funding to develop their own solid-state technology.[5] The BlueBus by Bolloré is an example of a commercialization of the solid-polymer electrolyte.[34] However, the use of the Li metal anode still presents safety concerns, as highlighted by recent incidents. Their lithium-metal-polymer technology also requires high-temperature operation (50-80 °C), which has limited their widespread adoption.[5] Moreover, many solid-state battery technologies suffer from material supply-chain bottlenecks. For example, lanthanum (a component in most ceramic oxide electrolytes) has a current production rate which could only support around 200 GWh of all-solid-state batteries.[5] The manufacturability of lithium metal, especially ultra-thin (10-20 µm), is also quite challenging and is the subject of much research.[8] As of 2023, there are no manufacturing plants able to accommodate the lithium metal foil throughput required for large-scale cell production.[5]

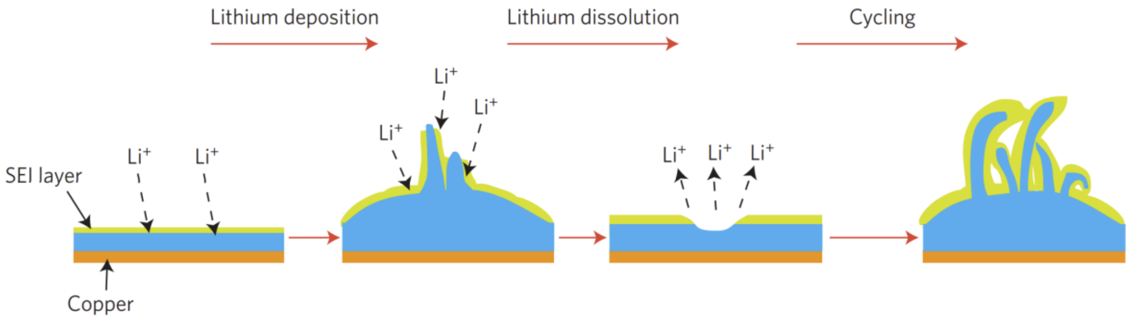

Figure 2.2.3 Stripping and plating mechanism seen with a lithium metal anode [35]

The third type of lithiation mechanism is the alloying mechanism. This occurs with elements that form alloys with lithium at low potential and near room temperature.[16] Many of these alloying elements are undesirable anodes due to considerations such as toxicity (Pb, Hg), low gravimetric capacity (Bi, Zn), high cost (Ag, Pd), and an undesirable high average voltage (Sb, Bi).[11] Silicon (Si) is the most notable alloying anode because it is an abundant element with a very high theoretical capacity around 3579 mAh/g and a relatively low average voltage around 0.4 V.[11] However, silicon experiences significant volume expansion during alloying, which causes electrode damage and rapid capacity fade.[11, 16] For over a decade, there has been considerable research on the design of different silicon morphologies to alleviate the problem associated with silicon expansion. These strategies are discussed in greater detail in the following section.

## 2.3 The Silicon Anode

Graphite is a very stable intercalation-based anode, but its low capacity has driven many researchers to identify alternatives. Although lithium metal has a high capacity, its plating-stripping mechanism causes many problems that have prevented its commercialization in rechargeable batteries. Alternative anodes like silicon have among the highest gravimetric energy densities known when alloyed with lithium. Unlike graphite which is limited to 1 lithium ion per 6 carbon atoms ($LiC_6$), the lithium-silicon alloy $Li_{15}Si_4$ has nearly 4 lithium ions per silicon atom.[11] This alloy has a theoretical capacity of 3579 mAh/g, compared to the 372 mAh/g for graphite. Although it is common to observe an initial discharge capacity greater than this theoretical value, the excess capacity is generally attributed to the formation of the SEI in the first cycle. [11] Because lithium is stored in silicon alloys in ionic form, not atomic form, there is an alloy packing density that enables capacities similar to Li metal.[36] The challenge with silicon lies with its poor stability, since the alloying of lithium and silicon is accompanied by a ~300% volume expansion.[11, 37] On a microscopic scale, this causes material swelling and pulverization, which in turn causes severe capacity fade over time. This continuous expansion and contraction with every lithiation and delithiation also continuously exposes new Si surface area to the electrolyte, which results in excessive SEI formation.[38, 39] In more stable materials like graphite, the SEI is desirable because it coats the electrode and prevents further unmitigated electrode-electrolyte side reactions.[1] However, with silicon expansion and contraction, the continuous SEI formation results in an unmitigated and irreversible consumption of the electrolyte. This also causes much of the silicon's high capacity to become inaccessible over time. These problems have made it difficult to commercialize silicon in full cells since the capacity loss can render a battery useless after only a few cycles.[40] Research on silicon has aimed to reduce the problems associated with silicon pulverization and improve cycle life in an otherwise high-capacity anode.

While there are many factors involved in the successful implementation of the silicon anode (the binder, the electrolyte, composite formulations, SEI), it is the structure of silicon (i.e., size and morphology), in particular nano structuring, which has been the subject of most research.[41] The history of nanosilicon for Li-ion battery applications is often described in terms of structure dimension.[41, 42] The late 1990s and early 2000s was the nascent phase of 0D nanosilicon and Si-based alloy research.[41, 43, 44] Work on 1D silicon nanowires & nanotubes, 2D silicon thin films, and 3D Si-C matrix composites began to grow in the mid-2000s.[41] Since the 2010s, research on all types of silicon-based anodes has accelerated significantly.

Today, silicon is often implemented in the form of pure silicon (micron-sized or nanoparticles), silicon oxides, or Si-C composites.[8] There has recently been a renewed interest in micron-sized silicon owing to its lower cost than nanosilicon.[43] Silicon-based anodes for Li-ion batteries have been developed or commercialized by companies like Hitachi, Shin-Etsu, Umicore, BTR New Material Group, ShanShan, Amprius, OneD Battery Sciences, Group 14, Sila Nanotechnologies, Nexeon, Enovix, Ionblox, and Tekna.[5, 45] Tesla is known to use a certain quantity of silicon oxide in their anodes.[5, 45] Silicon-based alloy anodes have also been a focus of research by companies like 3M and SKI.[45]

## Early work with Silicon

Work on silicon alloys with Li can be found as early as the 1970s. Highly lithiated Li-Si phases were reported at elevated temperatures (400-500 °C) in 1976.[43] When silicon is cited as having a theoretical capacity of 4200 mAh/g, it is referring to the phase $Li_{22}Si_5$.[11] However, this phase is not believed to form at room temperature.[11, 43] In contrast, the phase $Li_{15}Si_4$ has been confirmed to form electrochemically at room temperature in Li-ion batteries and has an associated capacity of 3579 mAh/g, which is a value that is often observed experimentally.[11] Some of the first work involving silicon-carbon composites for Li-ion batteries is the work of Dahn's group during the mid-1990s.[46, 47] In particular, they studied the deposition of silicon particles in the void sites of pregraphitic carbon using chemical vapour deposition with silane as a silicon source.[47] Later studies by Wilson *et al* focused on the pyrolysis of various siloxane-based polymers as a silicon source.[48–50] Siloxanes are a class of molecules with Si-O-Si bonds and are abundant in commercial silicones and industrial greases, polydimethylsiloxane (PDMS) being a common example. As siloxanes contain oxygen, the pyrolysis of these polymers produced glassy Si-O-C composites with electrochemical properties.[49] To optimize the electrochemical properties of these materials, studies by Xing and Wilson synthesized and pyrolyzed over 60 different polysilanes, polysiloxanes, and pitch-polysilane blends.[48, 51] These siloxanes were synthesized to have specific Si/O/C ratios or possess unique functional groups. In some instances, pitch was added to the composite to increase the free carbon content of the pyrolyzed product. Early electrochemical performance of these composites showed greater capacities (500-900 mAh/g) than traditional graphite but suffered from large voltage hysteresis upon cycling and high irreversible capacity. [48, 51] It was discovered that SiC and $SiO_2$ rich phases were responsible for much of the poor capacity retention.[48] Later work on silicon composites focused primarily on the most electrochemically active species: notably silicon and carbon.[41] Polysiloxane-derived nanosilicon continues to be a subject of research. The method is often described as an economical and environmentally friendly synthesis; such as the recent study by Lee et al, who decomposed inexpensive polysiloxanes in air, and then reduced the $SiO_2$ to Si via magnesiothermic reduction.[52]

### 0D Spherical Nanosilicon

Silicon nanoparticles are a zero-dimensional (0D) form of silicon.[41] The electrochemical superiority of nanosilicon over micron silicon in Li-ion batteries has been reported since the late 1990s.[44] The volumetric expansion of nanosilicon is not associated with the same particle fracture as micron silicon.[41] Silicon nanoparticles also have improved diffusion kinetics.[45] There appears to be a critical particle size of ~150 nm, below which particle fracture during lithiation is suppressed.[11, 45] This also improves the stability of the SEI during cycling; however, the intrinsically high surface area of nanosilicon may also promote excessive SEI formation. Silicon nanoparticles are primarily produced via Chemical Vapour Deposition (CVD) techniques involving the decomposition of silanes, ball/mechanical milling (including high-energy milling) of micron Si, and Radio-Frequency Thermal Plasma (RFTP).[45, 53] Ball-milling techniques are often used to produce amorphous silicon.[54] Tekna, a Quebec-based company, uses inductively coupled plasma technology for the synthesis of commercial nanosilicon powder.[55] The silane precursors (including derivatives like trichlorosilane) are very common in the preparation of nanostructured silicon and in the semiconductor industry. However, silanes are highly explosive and toxic gases that many industries have sought to phase out. It is nevertheless still used in the synthesis of nanostructured silicon-based anodes. As of 2022, Group 14 in collaboration with REC is building the world's largest silane-based facility in Washington state for the commercial production of Si-C anodes.[45]

### 1D Nanowires and Nanotubes

Silicon in the form of nanowires and nanotubes are 1D structures.[41] They have a high aspect ratio that facilitates 1D electron transport, a short Li diffusion length, good strain-relaxation properties, and the void space between the nanowires can accommodate the silicon expansion during lithiation.[41, 45] In 2008, Cui's research group prepared silicon nanowires of average diameter 89 nm which sustained a high capacity of ~3500 mAh/g after 20 cycles at C/5; moreover, the nanowire morphology was preserved after cycling, as observed with SEM.[56] 1D silicon nanotubes are also reported to deliver a sustained high capacity.[57] However, their synthesis is more complex and expensive than that of silicon nanoparticles, and the high void fraction reduces their volumetric capacity.[45] Common preparation methods for nanowire synthesis include CVD techniques along with vapour-liquid-solid growth employing a Au-Si alloy, molten salt electrolysis, and top-down chemical etching.[41, 45] Silicon nanotubes are typically prepared with a template assisted method along with CVD.[45] The ability to grow 1D silicon directly onto a current collector can eliminate the need for binders. Companies like Amprius and OneD Battery Sciences have integrated silicon nanowires into their high-capacity anodes.[5] Amprius recently claimed it has developed a 500 Wh/kg lithium battery.[5]

### 2D Nano Films and Sheets

2D silicon thin films have been studied because of their shortened Li diffusion path and suppressed volume expansion.[45, 58, 59] Takamura et al reported vacuum deposited silicon thin films (50 nm) with a capacity exceeding 2000 mAh/g for over 1000 cycles.[60] Their tunable thickness and uniform surface makes thin films especially well-suited for solid state batteries. In addition, Si thin films may be prepared without any conductive additive or binder. However, 2D silicon films are often prepared via expensive methods such as CVD and PVD techniques like magnetron sputtering; moreover, powdered materials are typically more conducive to industrial production.[41, 45] A related structure is 2D silicon nanosheets, which may be prepared with a relatively simple process. Ryu et al reported an inexpensive synthesis of silicon nanosheets by molten salt exfoliation and chemical reduction of natural clay.[58] They reported a capacity around 865 mAh/g with a current of 1 A/g and a capacity retention of 92% after 500 cycles.

### 3D Silicon-based Porous & Matrix Composites

3D silicon composites are a broad category of highly tunable structures that typically include a carbon matrix and/or high porosity. A silicon composite with a uniform carbon matrix can improve the intrinsically low electrical conductivity of silicon and reduce electrolyte-exposed Si, thus reducing SEI formation.[45] The carbon (or an inactive matrix) may buffer electrode expansion during silicon lithiation, whereas porosity clearly allocates room for silicon expansion and may also buffer whole electrode expansion.[61] Sila Nanotechnologies is among the most well-known companies to have developed these Si-C composites.[45] It should be noted that the carbon in 3D composites is typically more uniformly dispersed throughout the silicon than what occurs with Si-graphite composites. As the 3D composite category is more broad than lower dimensional structures, their synthesis methods are quite diverse. Common methods include pyrolysis of Si-organic precursors to yield Si-C composites, ball-milling to combine various structures, and chemical etching.[41] Magnesium thermal reduction or HF etching is often used to prepare porous Si composites from silica-containing precursors.[41] Porous Si-based multicomponent alloys may also be considered 3D structures and are typically prepared with ball-milling and then de-alloying or selective leaching of a component.[41]

### Core-Shell Design

Core-shell architecture (denoted core@shell) is known to buffer some of the volumetric expansion of silicon electrodes and improve cyclability, though it may not completely suppress silicon expansion.[62, 63] Historically, carbon has been employed as a shell to coat silicon nanoparticles.[41] However, the carbon can also fracture with the expansion of the silicon.[64] Inclusion of a void space (Si@void@C, sometimes "yolk-shell") may effectively mitigate the fracture of the carbon shell, as seen in Figure 2.3.1.[64–66] In a typical process, silicon nanoparticles are dispersed in solution and the surface is oxidized to form a Si@$SiO_2$ structure.[64] This is then coated with carbon via CVD & pyrolysis of a carbon source. Finally, a void is created via hydrofluoric acid etching of the $SiO_2$ interlayer. The void space between the silicon and the coating can serve as a buffer space for silicon expansion. Liu et al were one of the first to synthesize a Si@void@C material.[67] Their electrode delivered a capacity of 2800 mAh/g at 0.1C, with a 74% capacity retention after 1000 cycles. Later, the research group prepared a "pomegranate" inspired composite in which nanosilicon was encapsulated by a carbon layer, and clusters of the particles were then embedded within a thicker carbon layer.[63] While core-shell structures typically require complex synthesis methods, more simple derivatives like carbon-coated silicon composites using pyrolysis can be an economical and scalable way to improve the cyclability of the silicon electrode.

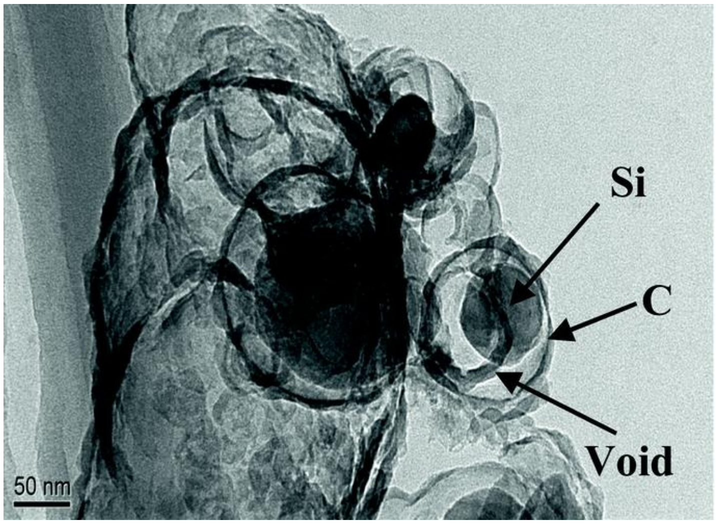

Figure 2.3.1 TEM image of Si@void@C core-shell design [64]

### Silicon-LTO Composite Electrodes

$Li_4Ti_5O_{12}$ (LTO) has historically been used as an anode material because of its high rate capability and negligible volumetric expansion upon lithiation.[16] However, its low energy density (capacity of 175 mAh/g) has prevented its use in high-energy-density applications. When LTO is combined with silicon, the resulting composite can benefit from the high-capacity associated with silicon and the stability of LTO.[68–72] Promising results have been reported when Si and LTO are prepared in a core-shell design. The LTO may be formed at the silicon surface by a sol-gel synthesis, spray-pyrolysis, or the silicon and LTO can be combined with simple ball-milling.[68, 70, 71] Lee et al produced a Si@LTO core-shell composite via a simple sol-gel technique.[71] The material was able to deliver around 1000 mAh/g, with a capacity retention of 65% after 1000 cycles at 1C.

## Silicon-Graphite Composites

Composites of silicon and graphite (G) are an established way to increase a battery's energy density, while also buffering the volumetric expansion to improve the capacity retention.[73] The performance of these composites depends on many factors including silicon and graphite morphology & size, homogeneity, the type of binder used (if any), or processing conditions (i.e., the solvent used to process the slurry, or the use of dry processing).[8, 54] However, the Si:G ratio is most relevant as it determines the gravimetric capacity of the composite. If the silicon content is too high, the capacity will fade rapidly as seen with a pure silicon electrode. The objective is to create a composite with a high practical capacity that is greater than pure graphite but lower than pure silicon. The capacity retention should be higher than pure silicon but will always be less than pure graphite. For example, an electrode with 60 wt% nanosilicon has an initial capacity of around 2000 mAh/g, although this capacity will still fade to below 1500 mAh/g after 100 cycles.[37] In the academic literature, the silicon content in composites is usually around 5-20 wt% to minimize capacity fade but it can be as high as 60-80 wt%. In industry, composites of silicon oxide (2-10 wt%) and graphite are becoming more common.[5] These composites are a scalable alternative to the complex morphological changes seen with nanotubes or thin films. Especially with high-Si electrodes, prelithiation strategies are often employed to increase first cycle coulombic efficiency and compensate for Li inventory loss.[8]

## Binders for Silicon-based Electrodes

The binder is known to play an important role in the electrode adhesion to the current collector, particle cohesion, and cycle stability of silicon-based anodes.[61] However, silicon-binder compatibility is multifaceted and involves the consideration of factors such as bonding mechanism, chemical compatibility (e.g., Si-binder and carbon-binder), ionic & electronic conductivity, and mechanical properties. Polyvinylidene fluoride (PVDF) has traditionally been the binder used in the preparation of both graphite anodes and lithium metal oxide cathodes.[61, 74] It is electrochemically stable since it is not reduced at the low potential of the anode (~5 mV vs Li) and is not oxidized at the high potential of the cathode (~5 V vs Li).[75] However, PVDF is known to be incompatible with the silicon anode. This incompatibility is primarily attributed to weak van der Waals interactions between PVDF and the Si surface.[61, 76] Because PVDF is a linear binder, it also has a reduced number of interactions with silicon relative to binders with many branched side chains. PVDF also cannot accommodate the large volumetric expansion of silicon lithiation.[61] As a result, silicon electrodes with PVDF as a binder will experience a very rapid drop in capacity.[77] Moreover, fluorine is known to be corrosive towards silicon.[78] There are also environmental and economical disadvantages with PVDF. It is not water soluble and requires the use of toxic organic solvents like N-Methyl-2-pyrrolidone (NMP) during electrode preparation.[20] Finally, the cost of PVDF is approximately 20 USD/kg, which is several times greater than competing binders like sodium carboxymethylcellulose (NaCMC) at 6 USD/kg.[75]

Next-generation binders must provide good silicon-binder interactions that accommodate the expansion of silicon, use environmentally friendly processing, and be inexpensive and scalable. Several natural binders are promising alternatives to standard PVDF. Common biopolymer binders include NaCMC, xanthan gum (XG), sodium alginate, gum arabic, and guar gum.[76] Synthetic polymeric binders such as polyacrylic acid (PAA) are also used with silicon. NaCMC is one of the most common binders used with silicon.[78] However, it is known to be especially brittle (in its low molecular weight formulations) and styrene-butadine rubber (SBR) is often used along with NaCMC to improve the flexibility and adhesion of electrodes.[78] Although this does not always improve performance.[61]

Polymeric binders typically possess side chains with many functional groups to aid in the binding with silicon.[61] Silicon possesses a passivating surface oxide layer (composed of $SiO_2$, $SiO_x$, and SiOH species) which is known to facilitate good silicon-binder interactions and improve capacity retention.[78, 79] Although it should be said that this oxide layer will also contribute to minor irreversible capacity due to the formation of lithium silicates. The oxide layer may be removed with HF etching, however this is typically reported to reduce silicon-binder interactions and hinder battery cycling.[79] Silicon particles can be treated with piranha solution to increase the number of hydroxyl groups.[78]

The binder can interact with the silicon surface via several types of bonding mechanisms such as van der Waals forces, covalent bonding, hydrogen bonding, and ionic bonding.[61, 76, 78] Covalent bonds (e.g., between PAA and PVA) are stronger than hydrogen bonds or van der Waals interactions; however, covalent bonds are irreversible and may no longer help with electrode cohesion if they are broken during silicon expansion.[76] Covalent bonds may occur in silicon electrodes with NaCMC under acidic slurry conditions (pH=3 buffer).[61] Hydrogen bonds are typically weaker than covalent bonds, but they are reversible.[76] This offers the silicon electrode a self-healing property since the bonds can re-form after silicon expansion.[11, 61] Ion-dipole interactions exist between oppositely charged ions (e.g. Na+ and $O^-$) and may also offer a self-healing property to the electrode.[76] This is especially relevant in binders with a counter ion (Na-alginate). The molecular weight of the binder is another relevant factor which is known to affect both the rheological properties of the slurry and the cycling performance of the electrode.[76] There appears to be a consensus that a high molecular weight improves capacity retention.[80] However, if the molecular weight is too high, the slurry viscosity may become too high, which will result in poor mixing and gumming. In contrast, if the molecular weight is too low, the resulting low-viscosity slurry may produce films that segregate upon drying and have poor homogeneity.

The mechanical strength and cohesion within silicon-based electrodes can be improved through various binder modification strategies. Grafting refers to the addition of side chains to a polymer while preserving the original main chain.[76] Block co-polymerization refers to the combination of two or more binder segments that are covalently linked.[76] Crosslinking more generally refers to the formation of a single binder network via the polymerization of monomers, or the bonding of different polymer chains. Depending on the binder formulation, crosslinking can occur with or without a crosslinking agent. For example, a 3D polymeric network can be obtained from the crosslinking of NaCMC and PAA at elevated temperatures.[81] Silicon anodes prepared with these binders have been reported to deliver better capacity retention than either binder alone. Other binder chemistries may require crosslinking agents such as small organic molecules (e.g., glycerin), metal ions (e.g., $Ca^{2+}$ with alginate), or inorganics (e.g., sodium borate).[76]

**The Electrolyte & SEI in Silicon-based Electrodes**

The SEI is formed from the reductive decomposition of the electrolyte species onto the silicon surface, and a small quantity of additive in the electrolyte is known to improve the stability of the SEI. A common additive for silicon-based electrodes is fluoroethylene carbonate (FEC). FEC is believed to undergo a reductive decomposition reaction, followed by radical polymerization, which contributes to the formation of a stable SEI.[82] When FEC is present, the SEI of Si-based electrodes is known to be composed of LiF, $Li_xPO_yF_z$, and $CHFCH_2$ species, among others.[82] The resulting elastomeric SEI is able to accommodate, to some degree, the expansion of silicon. Alternatively, work on glyme-based electrolytes (GlyEls) suggest this alternative to FEC can provide the silicon SEI with elastic polyether species and reduce electrode fracture after cycling.[83]

## 2.4 Review of High-Entropy Materials for Lithium-Ion Battery Electrodes

This chapter has been adapted from a review paper in Frontiers in Energy Research (DOI 10.3389/fenrg.2022.862551)

### Introduction and Working Principles

Multicomponent or high-entropy alloys (HEA) differ from traditional alloys in that they consist of multiple principal elements. HEAs were introduced in 2004 independently by authors Cantor and Yeh.[84, 85] Since then, high-entropy alloys have primarily been studied in the context of metallurgy, where they are known to provide desirable properties such as high strength and corrosion resistance.[86, 87] The role entropy plays in the phase stability of these compounds can be understood in terms of the Gibbs free energy of mixing ($\Delta G_{mix}$): [88–94]

$$\Delta G_{mix} = \Delta H_{mix} - T\Delta S_{mix} \tag{2.4.1}$$

where $\Delta H_{mix}$ is the mixing enthalpy, $\Delta S_{mix}$ is the mixing entropy, and T is the absolute temperature. If the $T\Delta S_{mix}$ term dominates the enthalpy term ($\Delta H_{mix}$), the overall $\Delta G_{mix}$ becomes negative and entropy stabilization has been established. The mixing entropy ($\Delta S_{mix}$) includes many entropic terms, however the configurational entropy ($\Delta S_{conf}$) is usually the dominant contribution.[88] Configurational entropy for an ideal solid solution is proportional to the number of components n: [88, 89]

$$\Delta S_{conf} = -R\sum_{i=1}^{n} x_i ln x_i \tag{2.4.2}$$

where R is the ideal gas constant and $x_i$ is the component mole fraction. When all components are present in equimolar proportion, the configurational entropy reaches its maximum and Eq. (2.4.2) simplifies to the equation below: [88, 89]

$$\Delta S_{conf} = Rln(n) \tag{2.4.3}$$

There are two formal definitions of high-entropy alloys. First, the compositional based definition states that the alloy must contain at least five elements, with each having an atomic percentage between 5% and 35%.[87, 89] This definition has often been used in physical metallurgy where it is common to dope alloys with small quantities of elements. Second, the entropy-based definition states that an alloy is high-entropy when $\Delta S_{conf}$ is greater than 1.5R.[87, 89] This criterion is satisfied for a solid solution with five equimolar components, where the $\Delta S_{conf}$ of Eq. (2.4.3) simplifies to 1.61R.

Four "core effects" are believed to be responsible for the unique properties of high-entropy materials: the aforementioned entropy stabilizing effect, lattice distortion, sluggish diffusion, and the so-called cocktail effect.[86, 95] Lattice distortion results from the different atomic sizes of the constituent elements. This can provide benefits like increased alloy strength or allow for the storage of hydrogen into interstitial sites.[86, 89] Sluggish diffusion refers to the low diffusion and phase transformation rates from the fluctuations of lattice potential energy.[95] Finally, the "cocktail effect" is the synergistic effect believed to result from the interplay between composition, structure, and microstructure.[86, 95] However, these "core effects" are not necessarily unique to high-entropy materials (HEM), and some authors have disputed their contribution to material properties.[86] HEMs have an additional economic benefit since they are often composed of inexpensive metals, which reduces reliance on any single element (e.g., Co.).

High-entropy oxides (HEO) are a newer class of HE material with numerous applications in energy storage. Like HEAs, entropy-based definitions have been proposed for HEOs, where the configurational entropy from both cations and anions is considered.[96, 97] Typically, the $O^{2-}$ anion entropy contribution is zero, but the presence of oxygen vacancies or other anions (e.g., $F^{-}$) can contribute to the system's entropy.[97] In practice, it is difficult to determine whether a multicomponent oxide is truly entropy stabilized. The term "entropy-stabilized oxides" should be reserved for materials with a proven entropy- driven reversible phase transformation.[97] As a result, the term "high-entropy" is more often employed to describe an oxide system containing five or more equimolar cations.

In 2015, Rost et al. showed that the (NiCuZnMgCo)O HEO could be stabilized into a single-phase rock-salt structure.[90] This was of interest to battery researchers as it allowed for the possibility of high-entropy electrodes, which are often oxide ceramics. The authors were able to show a reversible transformation from multi-phase to single-phase by varying calcination temperature. The transition was an endothermic process ($\Delta H>0$); hence the system was entropy stabilized because the $T\Delta S$ term must be large enough to overcome the positive enthalpy and render the Gibbs free energy negative. The removal of any one of the five components destabilized the solid solution, as seen in the X-ray diffraction (XRD) data of Figure 2.4.1a. This highlights the importance of five cations in entropy stabilized oxides. In addition, phase diagrams in Figure 2.4.1b confirm that the minimum transition temperature required for the formation of a single-phase occurs at maximum configurational entropy.[90]

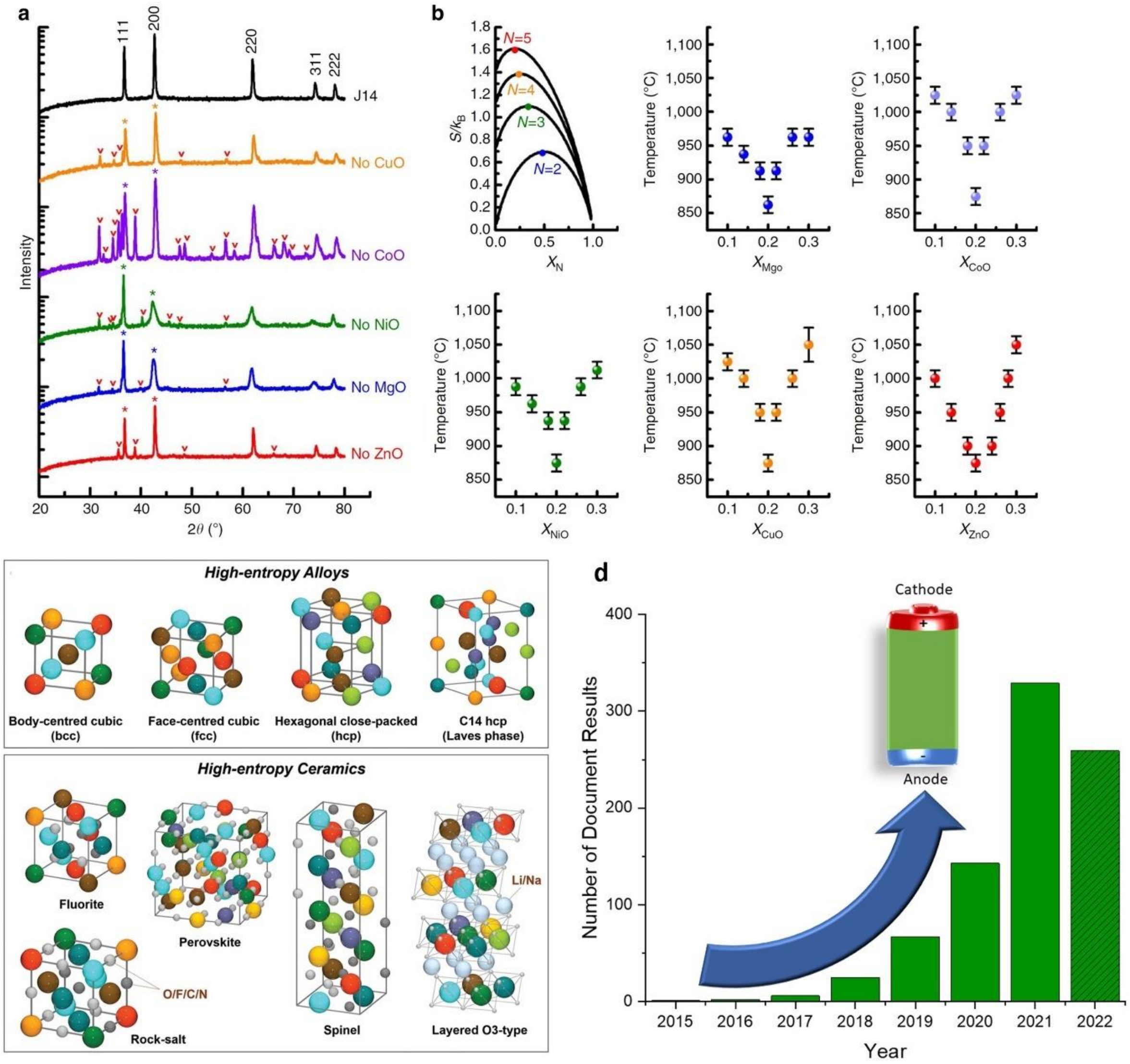

Figure 2.4.1. (a) XRD of multicomponent oxides (b) configurational entropy and phase diagrams of HEO elements (Rost et al., 2015). (c) common crystal structures for HEAs and HEOs (Ma et al., 2021). Reproduced under the terms of the CC BY license. (d) Rapid growth in publications on high-entropy materials for energy storage. Data was gathered from Scopus by searching for high-entropy oxides, anodes, or cathodes, and limiting the search to material science and/or energy. Please note data from 2022 includes only Jan-Apr.

Today, the high-entropy concept has been applied to alloys, oxides, carbides, nitrides, borides, hydrides, sulfides, among others.[92] Over 50 high-entropy oxides are known and take on a variety of crystal structures including rock-salt, perovskite, fluorite, spinel, and layered (Figure

2.4.1c).[94, 97] As seen in Figure 2.4.1d, publications on the topic have accelerated over the past few years, including a number of reviews.[88, 89, 91, 92, 94, 97–101] For energy storage, HEOs have shown promising results in the fields of batteries, supercapacitors, electrochemical catalysis, hydrogen storage, hydrogen evolution reaction, oxygen evolution reaction, carbon dioxide conversion, and oxidation reactions involving methanol, ethanol, or formic acid.[89, 92, 96, 102–106] In battery research, HEMs are often used as electrode materials for Li-ion batteries, but they have also been used in solid electrolytes, Li-Sulfur and Na-ion batteries, as well as MXenes.[92, 94, 107–112] Consult Table S2.4.1 for a list of recent publications on high-entropy materials for battery applications. In this review, we have summarized the recent research on HEMs with an emphasis on their use as anodes and cathodes for Li-ion batteries. In addition, we discuss common synthesis methods, characterization techniques, electrochemical performance, and proposed lithiation and failure mechanisms.

## Material Preparation and Characterization

### Synthesis and Material Discovery

The most common methods of HEA synthesis include arc melting and mechanical alloying.[87, 98] Mechanical alloying is widely used in the production of nanocrystalline HEAs. Preparation involves ball-milling of stoichiometric amounts of the metal powders followed by sintering.[98] The cooling rate is important to the formation of a single-phase, and quenching can be used to cool the material after heating. Moreover, de-alloying (where one element is selectively leached) can be used to create nano-porous HEAs with high catalytic activity.[92]

In contrast, the synthesis of HEOs often requires high temperature methods like solid-state sintering or spray pyrolysis.[92, 94, 97] Other methods include sol-gel combustion, coprecipitation, sonochemical, carbothermal shock, or sputtering deposition for the synthesis of thin films.[92] With solid state methods, metal oxides are ball-milled, pelletized, and sintered for multiple hours. In contrast, spray pyrolysis is desirable as it has a shorter residence time at elevated temperatures. It can produce nanocrystalline powders by passing an aerosol of metal precursors through a flame or reactor to induce rapid decomposition and structural transformation.[97] Sarkar et al. showed that nanocrystalline HEOs can be prepared by nebulized spray pyrolysis (NSP), flame spray pyrolysis (FSP), and reverse co-precipitation.[104] NSP was preferred as it was able to directly synthesize nanocrystalline single-phase rock-salt structures, whereas the other techniques required additional thermal treatments. The authors also confirmed the importance of a high configurational entropy when preparing these samples. A 4-cation (medium entropy) sample required a higher temperature to achieve single-phase. Other studies have also reported difficulty in preparing single-phase medium entropy oxides. [96]

Green synthesis methods for HEOs are increasingly the focus of publications. Kheradmandfard et al. used a microwave-assisted method to produce (MgCuNiCoZn)O nanoparticles (ave. size 44 nm) from nitrate metal precursors.[113] The solution was microwaved for only 3 min and did not require any additional high-temperature sintering. Alternatively, high-entropy oxide microparticles of uniform size distribution can be prepared by Joule heating within ~15s.[114] Surface modifications to rock-salt HEOs have been shown to enhance electrochemical performance. Guo et al. studied graphene modifications to the rock-salt $(Mg_{0.2}Co_{0.2}Ni_{0.2}Cu_{0.2}Zn_{0.2})O$.[115] The material was covered with graphene (denoted HEO@G) and increased electrical conductivity and Li-ion diffusion. In addition, they quantified the pseudocapacitive contribution to the capacity.

The importance of composition and temperature has been described for high-entropy perovskites. Sarkar et al. studied several perovskites, including the 10-cation $((Gd_{0.2}La_{0.2}Nd_{0.2}Sm_{0.2}Y_{0.2})(Co_{0.2}Cr_{0.2}Fe_{0.2}Mn_{0.2}Ni_{0.2})O_3)$.[116] They observed single-phase perovskites for 6 out of 11 different samples. The 10-cation sample was phase pure, but other heptanary samples were multiphase. Thus, for certain compositions, the net enthalpic contribution may overcome the high configurational entropy, preventing entropy stabilization. For example, the transition of ZnO (wurtzite) to ZnO (rock-salt) is known to incur a large enthalpic penalty.[90] Sometimes a higher temperature is sufficient to favour an entropy-driven transformation. This was shown to be true for $(Gd_{0.2}La_{0.2}Nd_{0.2}Sm_{0.2}Y_{0.2})MnO_3$, where a multiphase to single-phase transition occurred upon further heating.[116]

In addition to the synthesis procedure, researchers must consider the role individual elements and oxygen vacancies play in the properties of HEOs. Djenadic et al. synthesized HEOs with rare earth elements (CeLaPrSmY)O, among others.[117] They reported that a single-phase compound was not possible without Ce. This highlights the importance of a single element even in the presence of a high configurational entropy. Ce and Zr cations are also necessary to the formation of certain fluorite HEOs.[97] Sarkar et al. also synthesized and characterized various HEOs with rare earth elements. The materials were shown to have a high level of oxygen vacancies and a narrow band gap.[118] The concentration of oxygen vacancies is also known to play a role in the ionic conductivity of high-entropy solid electrolytes.[107]

As researchers identify the complex material-property- performance relationship of HEMs, the true scale of possible material candidates will become apparent. Material discovery has traditionally been guided by a combination of trial and error and systematic exploration (e.g., optimizing calcination temperature of a high-entropy oxide).[99] These approaches are suitable while a field is in its infancy, and they are sure to continue to advance our understanding through the mode of incremental improvement. This is seen, for example, in the growing body of research on high-entropy oxide spinels. Nevertheless, there is still much work to be done before high- entropy materials can replace traditional Li-ion battery electrodes. It is still unclear to what extent the electrochemical properties of HEMs are governed by element selection, the “cocktail effect”, entropy-stabilization, particle size and morphology, etc. In order to accelerate the Technology Readiness Level (TRL) of HEMs, researchers have increasingly relied on computation-driven approaches for material discovery.[99] In particular, Density Functional Theory (DFT) and machine learning can help narrow the vast design space of candidates with desirable properties, as will be seen in the work by Lun et al. In addition, high-throughput methods provide the experimental feedback needed to validate these computational methods and complete the material design cycle.

## Characterization

Physical characterization methods are necessary to confirm the material’s morphology, crystal structure, and composition.[89, 90] It is often desired to form a single- phase compound with a defined space group (such as Fd-3m for spinel). X-ray Diffraction (XRD) and Rietveld refinement can be used to determine the crystal structure and space group of the material, as well as reveal the presence of undesired impurity phases. Operando XRD may be used to observe changes in the crystal structure during battery cycling. This can provide information regarding the stability and lithiation mechanism of the material. X-ray Photoelectron Spectroscopy (XPS) is often used to determine the oxidation state of the metal cations or identify oxygen vacancies. This can provide insight into the mechanisms at play before and after lithiation. Scanning Electron Microscopy (SEM) and Transmission Electron Microscopy (TEM) are used to observe morphology. High-Resolution TEM (HR-TEM) is more appropriate in the case of nanoparticles or to verify the d-spacing associated with a particular lattice plane of the structure. Energy-Dispersive X-ray

Spectroscopy (EDX) is often used in conjunction with microscopy to quantify the homogeneous distribution of the elements in the sample. More precise quantification of elemental composition can be done with Inductively Coupled Plasma-Optical Emission Spectrometry (ICP-OES). This is particularly important in the synthesis of cathode materials, as there is concern of lithium evaporation at elevated temperatures (>800°C). As a result, many authors include 5–10% excess lithium in their samples prior to calcination.

Electrochemical characterization involves the testing of materials in batteries. Initial testing is usually done in half-cell (vs Li metal) coin-type batteries (such as CR 2032). It is increasingly common to study the material in full cells, which can also be prepared as large-scale pouch cells. A battery electrode is made by first applying a thin film of active material to a current collector. This is usually done by tape casting where the active material powder is combined with a conductive additive (usually carbon), a suitable binder, and mixed with a solvent (usually N-methyl pyrrolidone) to form a slurry. Typically, the binder is polyvinylidene fluoride (PVDF) because of its well-known electrochemical stability. However, polytetrafluoroethylene (PTFE) has been used for certain disordered rock-salts.[119] The slurry is applied as a thin film to a metal current collector that is subsequently dried and cut into electrodes. Initial electrochemical testing can involve Cyclic Voltammetry (CV) in a defined potential range to identify redox processes. Electrochemical Impedance Spectroscopy (EIS) may also be used to study the resistance of the material before and after cycling. Battery cycling is used to study capacity (related to energy density) and capacity retention (related to lifetime), which are the most relevant metrics of performance for practical applications.

## High-Entropy Anodes

### Oxide Ceramics

Graphite has traditionally been used as an anode material in Li-ion batteries. Its intercalation mechanism makes it very stable, but it suffers from a low inherent capacity of 372 mAh/g.[16] HEOs for batteries have been used as anode materials owing to their ability to host lithium ions via a conversion-type reaction. These materials typically have a capacity much greater than graphite, but they have poor cycle stability. The first cycle coulombic efficiency (CE) is typically less than 90% and is as low as 50% in some cases. [120] Many HEOs have the property of increasing capacity with extended cycling. The behaviour is also known to occur with older conversion-type materials such as CoO and $ZnMn_2O_4$. It is generally attributed to reversible lithium storage within a polymeric layer that forms at the electrode surface.[121] Other explanations include the gradual penetration of the electrolyte into inner oxide pores and structural changes during cycling.[96, 122, 123]

One of the most widely studied HEOs for battery applications is the $(Co_{0.2}Cu_{0.2}Mg_{0.2}Ni_{0.2}Zn_{0.2})O$ rock-salt. In 2018, Sarkar et al. synthesized this compound with NSP and used it as an anode that was shown to have a capacity around 500 mAh/g at a current of 0.1 A/g, as seen in Figures 2.4.2a and b. [96] They also tested medium-entropy derivatives of the high-entropy parent structure, but all had a more rapid capacity decay compared to the HEO (Figure 2.4.2b). Later, the same group successfully used the $(Co_{0.2}Cu_{0.2}Mg_{0.2}Ni_{0.2}Zn_{0.2})O$ HEO as an anode material in a full cell with NMC ($LiNi_{1/3}Mn_{1/3}Co_{1/3}O_2$) as a cathode.[120] Despite a low first cycle CE, the anode maintained a capacity of 300 mAh/g after 50 cycles. In addition, the material was used in pouch cells and delivered a capacity of 2.5 mAh. This anode suffered from a large first-cycle irreversible capacity as the initial coulombic efficiency was around 50%. An improvement in the cycling of their full cell was achieved with the pre-lithiation of the anode.

Nanosized $Mg_{0.2}Co_{0.2}Ni_{0.2}Cu_{0.2}Zn_{0.2}O$ rock-salt was synthesized by Qiu et al.[122] It was used as an anode and was compared with the baseline $Co_3O_4$. The HEO had a first cycle discharge capacity of 1585 mAh/g, compared to 1160 mAh/g for $Co_3O_4$. In addition, it retained a stable capacity of 920 mAh/g after 300 cycles. The HEO was shown to have a Li diffusion coefficient 1-2 orders of magnitude higher than $Co_3O_4$. The authors attribute the stability of the HEO to the homogeneously distributed inactive MgO. MgO is formed after the initial discharge and is believed to prevent transition metal oxide nanograins from agglomerating during cycling. In addition, sluggish diffusion in the structure reduces agglomeration of secondary particles. They also showed the dependence of electrochemical performance on elemental composition. Other element combinations (such as MgFeTiCuZn-HEO and GaFeCrMnNi-HEO) were shown to have a lower capacity or a more rapid capacity fade.

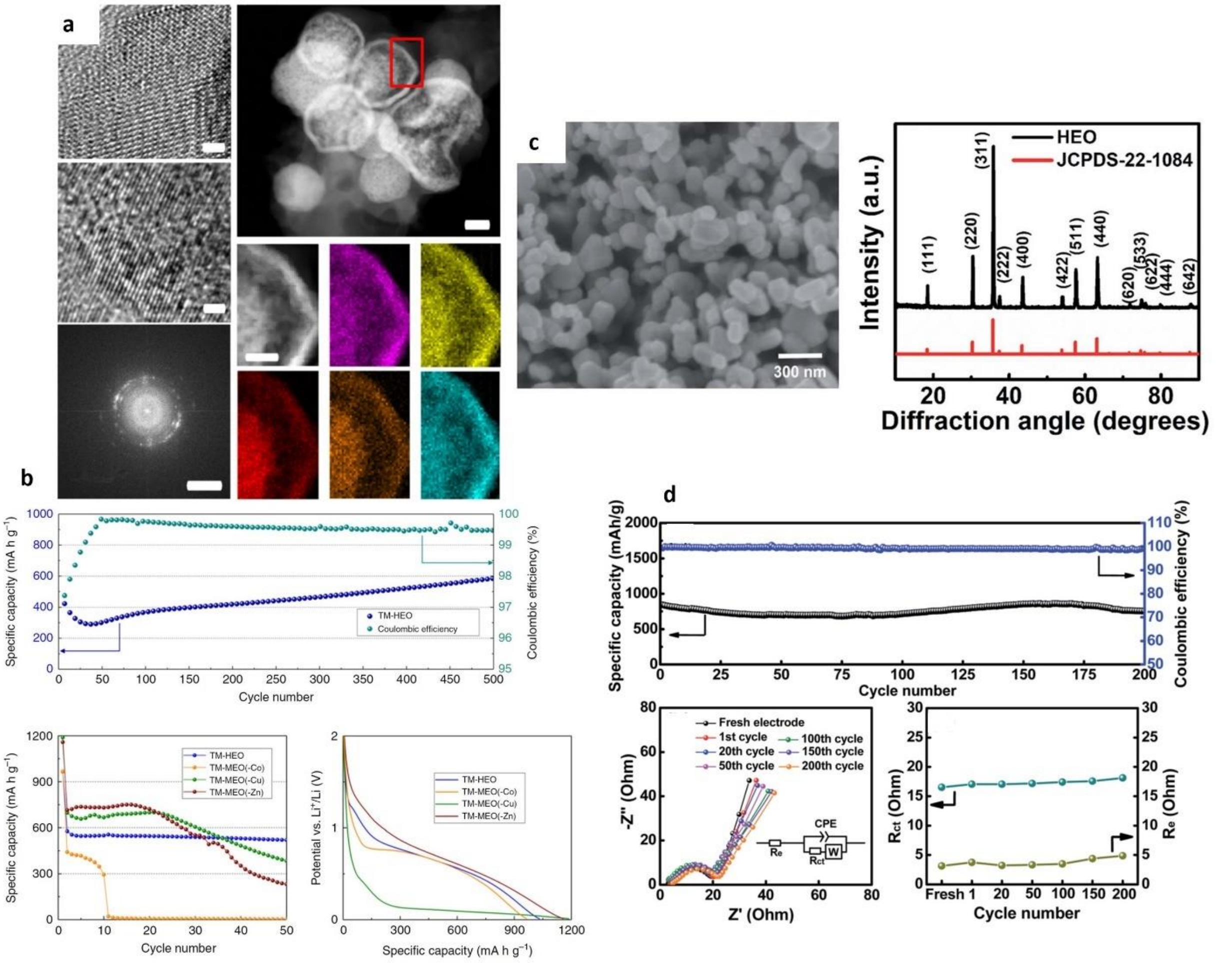

Figure 2.4.2. (a) HR-TEM and EDX characterization of rock-salt HEO and (b) cycling performance and voltage profiles of high-entropy and medium-entropy oxide anodes (Sarkar, et al., 2018a). (c) SEM and XRD characterization and (d) cycling performance and impedance of spinel HEO anode (Nguyen et al., 2020). Reproduced under the terms of the CCBY license. Note: For Figure a, the scalebars in the HR images correspond to 1 nm. For the EDX colourmap, the scale bar corresponds to 60nm and the colours correspond to: purple-Co, yellow-Cu, red-Ni, orange-Mg, blue-Zn.

Lökçü et al. studied the variation of Li content in rock-salt $(MgCoNiZn)_{1-x}Li_xO$ (x = 0.05, 0.15, 0.25, and 0.35).[124] XPS revealed that an increase in Li content was associated with the oxidation of $Co^{2+}$ to $Co^{3+}$, and an increase in the concentration of oxygen vacancies to preserve charge neutrality. This had the effect of increasing the discharge capacity, with the best material being $(MgCoNiZn)_{0.65}Li_{0.35}O$ with an initial capacity of 1930 mAh/g. Similar materials have been used as solid electrolytes and are discussed later.

Spinel HEOs have also been shown to provide high capacities when used as anodes. Chen et al. studied spinel $(Mg_{0.2}Ti_{0.2}Zn_{0.2}Cu_{0.2}Fe_{0.2})_3O_4$ as an anode and reported a reversible capacity of 504 mAh/g at a current density of 100 mA/g after 300 cycles.[125] In addition, the material was able to maintain a capacity around 280 mAh/g for 800 cycles at a high current of 2 A/g. With CV, a large pseudocapacitive contribution of 93% was found at a high scan rate of 1 mV/s. This surface redox process enables a high rate capability. They also observed a reduction in resistance after cycling as evidenced by EIS. Wang et al. studied spinel $(FeCoNiCrMn)_3O_4$ as an anode and optimized the synthesis temperature.[126] They attribute the electrochemical performance to mixed valence state metals that induce lattice distortion. The large lattice parameters afforded the material fast diffusion kinetics. Similar to rock-salts, diffraction peaks associated with the spinel structure disappeared during the first lithiation down to 0.01 V, indicating amorphization. Spinel peaks did not reappear after being charged to 3 V. Zhao et al. prepared the $(Co_{0.2}Cr_{0.2}Fe_{0.2}Mn_{0.2}Ni_{0.2})_3O_4$ spinel with a capacity of 428 mAh/g at a high current of 10 A/g. [127] The material had a greater discharge capacity and initial CE relative to low and medium entropy derivatives $Co_3O_4$ and $(Co_{0.25}Cr_{0.25}Fe_{0.25}Mn_{0.25})_3O_4$, respectively. The high- entropy material had the greatest number of oxygen vacancies (as shown by XPS and Electron Paramagnetic Resonance). They attributed the superior performance to these oxygen vacancies, which are believed to accommodate a greater number of Li ions and affect ion migration and electrical conductivity. In addition, thermal stability of the material showed good capacity retention between 0 and 50 °C.

Xiang et al. studied spinel $(Al_{0.2}CoCrFeMnNi)_{0.58}O_{4-\delta}$ nanocrystalline powder with a high concentration of oxygen vacancies. [128] The material had a porous structure from gas liberation during the combustion synthesis. The inclusion of aluminum in the structure doubled the capacity compared to a $(CoCrFeMnNi)_{0.6}O_{4-\delta}$ baseline. This use of inactive Al was inspired by Qiu et al., who showed how the addition of inactive MgO can improve structural stabilization. The authors suggest that small ionic radii Al enhances lattice distortion and allows for the accommodation of more Li. Nanoparticle spinel HEOs have also been prepared with the hydrothermal method (see Figure 2.4.2c). Nguyen et al. reported a high capacity of 1235 mAh/g and a high number of oxygen vacancies by removing the inactive MgO from the spinel (see Figure 2.4.2d).[129] Recently, the same group was able to synthesize the Co-free $(CrMnFeNiCu)_3O_4$ spinel anode.[130] The crystallinity and particle size were varied with post-annealing temperature, and the reported capacities ranged from 600 to 900 mAh/g. Operando XRD also revealed a gradual reduction in peak intensity during the first lithiation, indicative of a collapse in the long-range lattice ordering.

Duan et al. optimized the synthesis of different seven- element $(FeCoNiCrMnXLi)_3O_4$ (X

= Cu, Mg, Zn) spinels and used them as anodes.[131] The Zn-containing spinel had the best performance with a capacity of 522 mAh/g after 100 cycles. They also observed the trend in which the capacity increased gradually during cycling. The beneficial contribution of a single constituent element in spinels has also been studied by Xiao et al. They compared the electrochemical performance of Mg and Zn containing HEOs $(FeNiCrMnZn)_3O_4$ and $(FeNiCrMnMg)_3O_4$.[132] Zn was shown to increase the lithium storage capability, provide a higher amount of trivalent Mn, and improve the crystallinity of the material. In addition, it had a relatively stable capacity of 386 mAh/g at 0.5 A/g after 185 cycles. The same group later prepared the $(FeCoNiCrMn)_3O_4$ spinel anode with a capacity of 596 mAh/g at 2 A/g and 967 mAh/ g at 100 mA/g.[133] A ball-mill prepared sample of the material had a lower capacity than one prepared via the oxidation of commercial 50 µm HEA powder.

More recent publications on spinels include Tian et al., who prepared the $(CoNiZnXMnLi)_3O_4$ (X = Fe, Cr) anode. The material was tested in full cells and had a specific capacity of 260 mAh/g after 100 cycles at 500 mA/g.[134] Sun et al. studied the $(Cr_{0.2}Mn_{0.2}Fe_{0.2}Co_{0.2}Ni_{0.2})_3O_4$ spinel, which had a capacity of 560 mAh/g at 100 mA/g.[106] The pseudocapacitive contribution increased at higher scan rates, as has been reported in other studies.[126, 133, 135, 136]

## Metallic Alloys

High-entropy alloys are a relatively unexplored research area for the Li-ion battery anode, yet they may mitigate unresolved problems with conventional silicon-based (Si) electrodes. The problem with silicon (and most alloy anodes) is its poor cycle stability. The alloying of lithium and silicon is accompanied with a 300% volume expansion. On a microscopic scale, this causes material swelling, pulverization, and loss of electrical contact with the current collector.[11] In addition, the continuous formation of solid-electrolyte-interface (SEI) consumes the electrolyte. These problems are responsible for the rapid capacity decay of silicon and alloying materials in batteries.

There has been considerable research on two or three multicomponent alloys with Li for the negative electrode.[11, 137] Other than Si, common elements that alloy with lithium include Al, Zn, Ga, Ge, Ag, Sn, Sb, and Bi.[11, 137] For certain systems, varying the compositional ratio can create morphological changes that improve volumetric capacity, as seen with the eutectic Zn-Sn alloy.[138] It is known that a multicomponent alloy can improve battery performance relative to a simple binary alloy. For instance, binary alloys with the addition of inactive copper have been shown to improve rate capability and capacity retention.[139] Ternary alloys with silicon are known to reduce volume expansion and improve performance. [140] Obrovac et al. reported the preparation and electrochemical performance of 4-component alloys.[141] They prepared several alloys with silicon, including $Si_{49}Cu_{42}Ag_7Sn_2$, which showed a stable capacity around 1000 mA h/g.[141] Although not a high-entropy alloy, the material provides insight into the feasibility of multicomponent alloy electrodes. Recently, Ehrenberg's group prepared several high-entropy alloys of the $Gd_{1-x}La_xSn_{2-y}Sb_yM_z$ (M = Li, Na, Mg) system.[142] The large atomic size of Gd and La are believed to form voids that may accommodate Li atoms. Their work was mostly fundamental; however, preliminary electrochemical data showed stable cycling. High-entropy alloys have also been used as anode materials in nickel-metal hydride batteries. Edalati et al. studied the $Ti_xZr_{2-x}CrMnFeNi$ alloy with various Ti/Zr ratios.[143] The discharge capacity was observed to be dependent on the Ti/Zr ratio, suggesting a wide range of possible electrochemical performances by tuning composition. Moreover, the material displayed a low- capacity fade. High-entropy alloys have also been used to accelerate kinetics and increase cycle stability in Li-Sulfur batteries.[108, 144] It should be noted that Breitung's group recently prepared and characterized high-entropy sulfides for Li-ion batteries, but the materials had redox activity predominantly around 2 V.[145]

### High-Entropy Cathodes

The inclusion of fluorine into high-entropy rock-salts has been shown to increase their working potential to 3.4 V.[103] This should be contrasted with a HEO baseline without fluorine, which has a working potential around 1.0 V. In addition, their preparation is simple and can be done by ball-milling a HEO precursor with LiF. XRD and Nuclear Magnetic Resonance (NMR) confirmed the successful incorporation of Li and F into the structure. These high-entropy rock-salt oxyfluorides have been used as cathode materials for lithium-ion batteries. Wang et al. reported an initial charge capacity of 161 mAh/g at C/ 10 for $(Li_x(Co_{0.2}Cu_{0.2}Mg_{0.2}Ni_{0.2}Zn_{0.2})OF_x$.[103] This capacity was higher than a non-entropy stabilized $LiNiOF_x$ baseline, despite containing a greater fraction of redox active nickel. However, the material suffered from a large first cycle irreversible capacity and an overall low CE.[103] The authors attribute this capacity loss to electrolyte degradation, SEI formation, and side reactions. The oxyfluoride had an insertion-type lithiation mechanism, in contrast to the conversion-type mechanism seen in simple HEOs. Mg and Zn were redox inactive and remain divalent as shown with XPS. This cathode also exhibited a capacity increase during cycling.

The same group later studied various layered HEOs including $LiNa(NiCoMnAlFe)_1O_2$.[146] Figure 2.4.3a shows the material had an oxidation peak at 4.0 V, which is higher than the 3.8 V typically seen for standard $Li(NiCoMn)_1O_2$. However, the electrodes were reported to have a low capacity and a rapid capacity fade (<70 mAh/g after 20 cycles). The incorporation of a small amount of Na ions (Figure 2.4.3b) was done to improve the battery cycling by widening the diffusion channels. Inclusion of as little as 1 mol% Na (but not K or Rb) has also been reported to marginally improve capacity retention in conventional layered cathodes.[21] Recently, Sturman et al. reported similar electrochemical performance for the $Li(NiCoMnTiFe)_1O_2$ layered HEO and observed overlithiation properties that were shown to reduce capacity decay.[105] Interestingly, a cathode with the same stoichiometry has also been reported for Na-ion batteries. The cathode was investigated both computationally and experimentally, where it was reported to have a stable capacity of 180 mA h/g.[147] Another recent HE layered cathode is described in the work of Wang et al. They used pulsed laser deposition to prepare epitaxial thin films of the layered $LiCr_{1/6}Mn_{1/6}Fe_{1/6}Co_{1/6}Ni_{1/6}Cu_{1/6}O_2$.[148] The material was used as a cathode but had low capacity (<60 mAh/g) and high interfacial resistance. Zhen-Yi Gu et al. made a high-entropy derivative of the NASICON-type fluorophosphate cathode that was shown to increase operating voltage and electrochemical capacity in Na-ion batteries.[149]

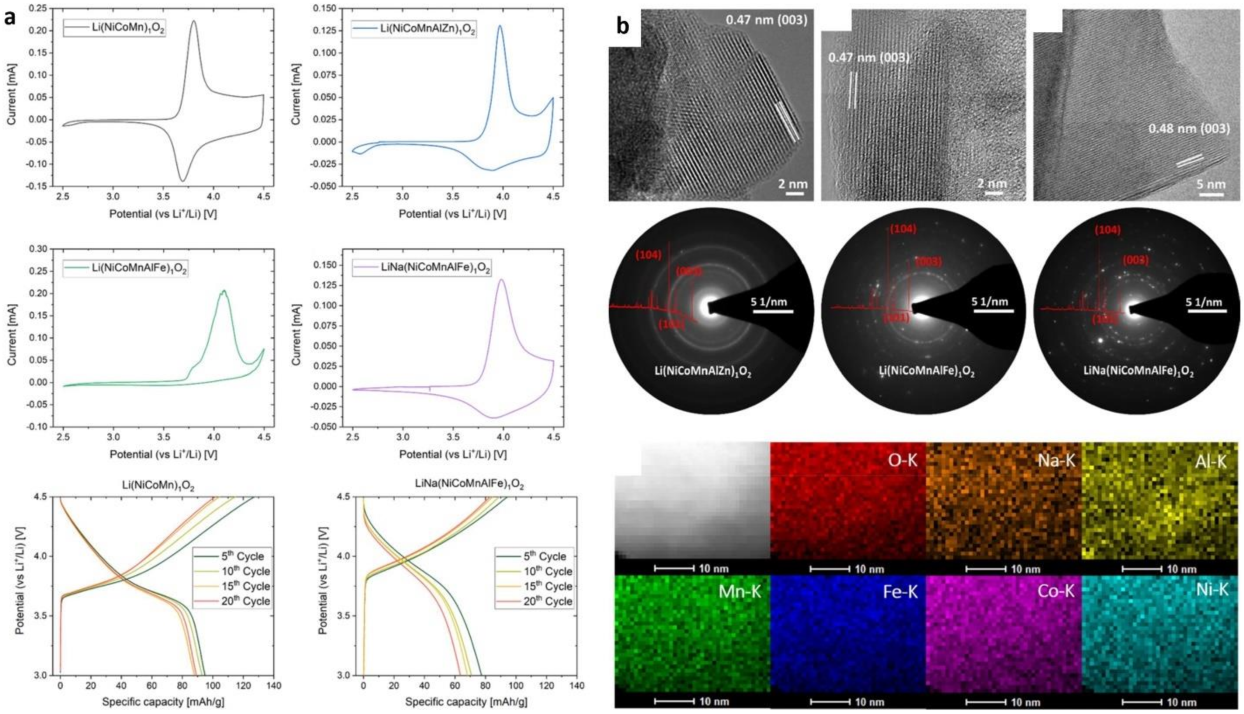

Figure 2.4.3. (a) CV and voltage profiles and (b) HR-TEM, SAED, and EDX mapping characterization of layered HEO cathode (J. Wang, et al., 2020b). Reproduced under the terms of the CC BY license.

Ceder's group used Density Functional Theory (DFT) to estimate the mixing temperature of different transition metal combinations in cation-disordered rock-salts (DRX).[119] As a design strategy, they suggest the incorporation of 30% excess Li and the inclusion of fluorine to increase the redox reservoir. In addition, short-range order (SRO) was suppressed as the number of cations in the DRX increased. SRO was also reported to decrease with increasing synthesis temperature. Their TM6 cathode had a high initial capacity of 307 mAh/g; however, cycling data was only reported for 20 cycles.

## Solid-State Electrolytes

Lithium containing HEO rock-salts have displayed properties that are promising for solid electrolyte applications. Some have been reported to have a Li-ion conductivity several orders of magnitude greater than LiPON.[107] Bérardan et al. studied the room-temperature ionic conductivity of rock-salt $(MgCoNiCuZn)_{1-x-y}Ga_yA_xO$ (with A = Li, Na, K) and reported a value exceeding $10^{-3}$

S cm$^{-1}$.[107] Later, the team studied $(MgCoNiCuZn)_{1-x}Li_xO$ with varying concentrations of Li. They identified a charge compensation mechanism that begins with the oxidation of $Co^{2+}$ to $Co^{3+}$, followed by the formation of oxygen vacancies when the Li fraction exceeds x = 0.21.[150] High-entropy electrolytes have also been applied to Na-ion batteries, such as HE NASICON phosphate electrolytes.[151]

Recent work on solid electrolytes includes HE garnets, argyrodites, and perovskites. Stockham et al. reported the successful synthesis of Ga-containing lithium garnet electrolytes composed of 9 and 11 elements (e.g., $Ga_{0.2}Li_{5.75}La_{2.5}Nd_{0.5}Nb_{0.65}Ce_{0.1}Zr_1Ti_{0.25}O_{12}$).[152] The electrolytes were simple to prepare and had both good room temperature conductivity (0.2 mS cm$^{-1}$) and stability. As we have seen, most current research targets a high configurational entropy for the cations. However, recent work by Strauss et al. reports HE-polyanionic argyrodite-type solid electrolytes.[153] Unlike most publications, the authors reported a nonuniform distribution of elements. The high entropy was reported to lower activation energy for conduction but did not significantly affect ionic conductivity. Equimolar high-entropy perovskite electrolytes with varying Al content were reported but had a conductivity on the order of $10^{-7}$ S cm$^{-1}$.[154] The authors also investigated the material as an anode, however the use of heavy elements (i.e. La and Ba) resulted in a low capacity of 58 mAh/g. Other studies have also used perovskites as electrode materials. Yan et al. reported results for the less-studied high-entropy perovskite titanate.[123] It had an initial capacity of 125 mAh/g followed by a large irreversible capacity, but a stable capacity of 80 mAh/g. The perovskite also had a gradual increase in capacity over 300 cycles, which the authors attribute to the gradual penetration of the electrolyte into the electrode and the formation of a gel-like film.

## Advanced Characterization and Storage Mechanism

Confirmation of the homogeneous elemental distribution in HEOs has been an important part of their characterization since Rost et al. It has traditionally been supported with EDX or XRD analysis on the bulk powder. However, this may not be sufficient to detect traces of secondary phases or localized heterogeneities, which can affect the material's property and electrochemical performance. Chellali et al. used Atomic Probe Tomography (APT) to study the atomic scale homogeneity of various transition metal, rare-earth metal, and perovskite-based HEOs prepared by a high-pressure compact method.[155] Their results confirm the random and homogeneous distribution of cations at the atomic level.

Moździerz et al. studied lattice distortion effects in $(CoCuMgNiZn)_{1-x}Li_xO$ by increasing lithium levels during synthesis ($x = 0–0.3$).[156] The internal strain increased up to a Li composition of 0.2, after which the introduction of more Li released the internal strain through the formation of oxygen vacancies. The compound displayed mixed ionic-electronic conductivity upon the insertion of Li. Different mechanisms were proposed: intercalation-based insertion at high voltage and conversion or alloying at low voltage. Cheng et al. studied the effects of pressure on lattice distortion in $(Ce_{0.2}La_{0.2}Pr_{0.2}Sm_{0.2}Y_{0.2})O_{2-\delta}$ HEO.[157] They observed pressure-induced transformations from the crystal state to the amorphous state below the melting point or glass-transition temperature. This property may allow for the development of ceramic-glass composites with applications in solid-state electrolytes.

Since 2018, authors have reported details regarding the partial conversion reaction in rock-salt HEOs. Sarkar suggested that certain cations ($Co^{2+}$ and $Cu^{2+}$) are involved in the conversion, whereas other cations ($Mg^{2+}$) stabilize the structure.[96] Operando XRD in Figure 2.4.4a shows the typical behaviour of a HE-rock-salt upon lithiation. Reflections from the rock-salt structure disappeared during the first lithiation due to the “formation of small crystallites” (which is often seen in conversion materials).[96] However, Selected Area Electron Diffraction (SAED) was still able to detect trace reflections from the rock-salt structure, providing evidence of a partially preserved structure that enables reversible lithium storage.[96] Similar observations have been made in subsequent studies. Tavani et al. studied the lithiation mechanism of HEO $(Mg_{0.2}Co_{0.2}Ni_{0.2}Cu_{0.2}Zn_{0.2})O$ with operando X-ray Absorption Spectroscopy (XAS) to quantify the reduction of transition metal species.[158] For this material, upon lithiation, $Cu^{2+}$ is first reduced to a mixture of 62% metallic Cu and 32% $Cu_2O$. Then, 75% of the $Ni^{2+}$ is reduced to metallic Ni. Finally, around 62% of the $Co^{2+}$ is reduced to metallic Co. The order of this sequence was noted to follow the redox potential of each element. These observations are also consistent with the work of Ghigna et al., where a lithiation/delithiation mechanism for $(Mg_{0.2}Co_{0.2}Ni_{0.2}Cu_{0.2}Zn_{0.2})O$ is proposed.[159] The mechanism is illustrated in Figure 2.4.5.

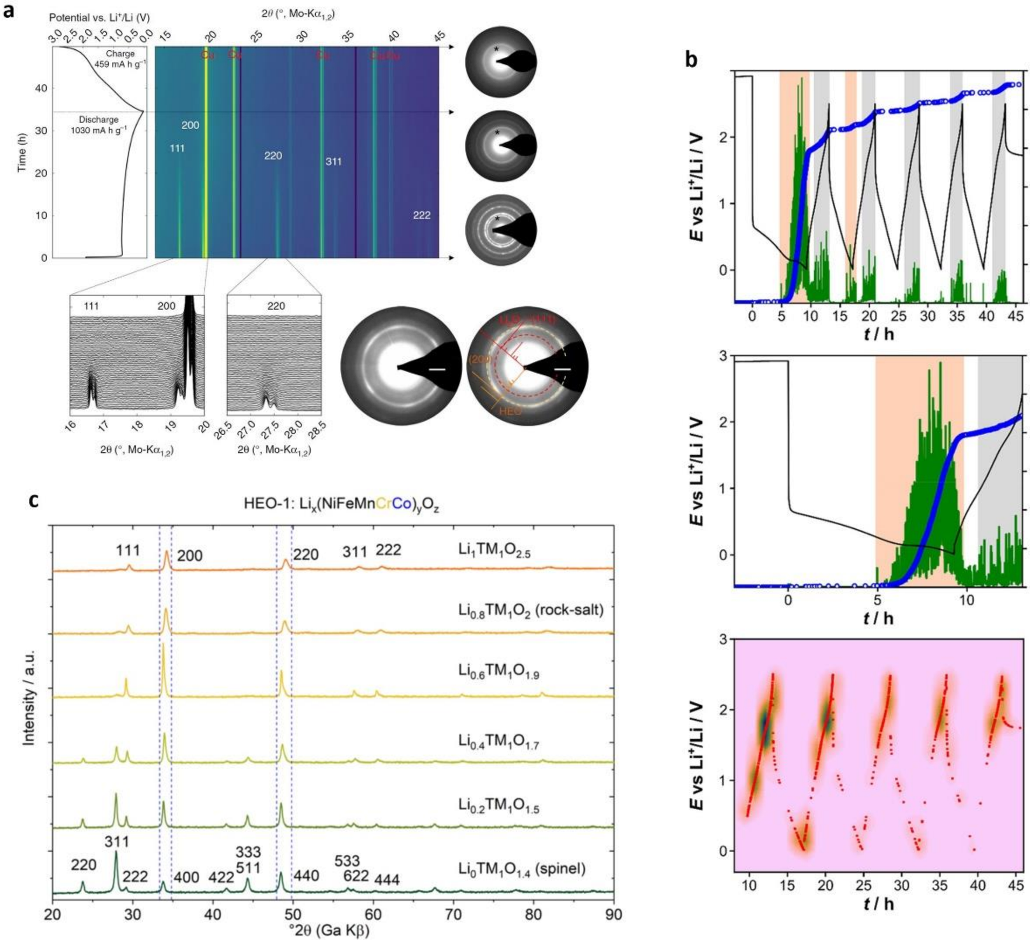

Figure 2.4.4. (a) Operando XRD of $(Co_{0.2}Cu_{0.2}Mg_{0.2}Ni_{0.2}Zn_{0.2})O$ anode (Sarkar, et al., 2018a). (b) Operando AE investigation of HEO anode (Schweidler et al., 2021). (c) XRD of the spinel to rock-salt transformation seen with high lithium concentrations (J. Wang, et al., 2020c). Reproduced under the terms of the CC BY license.

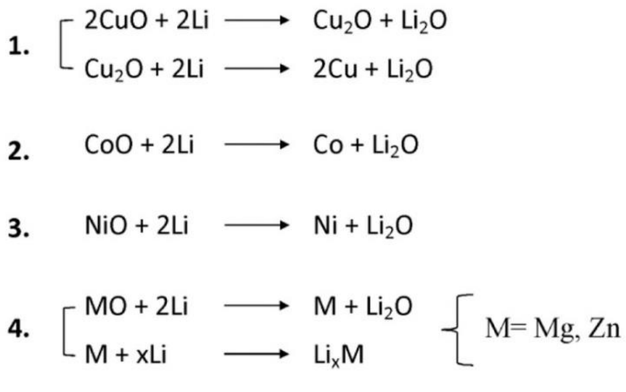

1. $2CuO + 2Li \longrightarrow Cu_2O + Li_2O$; $Cu_2O + 2Li \longrightarrow 2Cu + Li_2O$

2. $CoO + 2Li \longrightarrow Co + Li_2O$

3. $NiO + 2Li \longrightarrow Ni + Li_2O$

4. $MO + 2Li \longrightarrow M + Li_2O$; $M + xLi \longrightarrow Li_xM$ M= Mg, Zn

Figure 2.4.5. Proposed mechanism for TM-based HEO anode lithiation (Ghigna et al., 2020). Reproduced under the terms of the CC BY license.

They suggest a two-stage process beginning with the conversion of cations ($Cu^{2+}$, $Co^{2+}$, $Ni^{2+}$), followed by the conversion and eventual alloying/de-alloying of $Mg^{2+}$ and $Zn^{2+}$. Surprisingly, it was found that ZnO is also involved in the conversion mechanism, as shown by the presence of metallic Zn. The reaction is incomplete and irreversible and ultimately leads to a collapse of the rock-salt structure, although 60% of the capacity remains. Wang et al. studied different quantities of Mg in the structure of $(Mg_{0.2}Co_{0.2}Ni_{0.2}Cu_{0.2}Zn_{0.2})O$ and found homogeneous single-phase compounds for only the Mg-containing oxides.[160] However, the Mg-free sample still had good electrochemical performance. Operando X-Ray Microscope Spectroscopy revealed greater amounts of Mg were associated with a reduced pulverization.

More detailed characterization regarding HEO degradation is found in the work of Schweidler and Breitung. Schweidler et al. studied the lithiation of the $(Co_{0.2}Cu_{0.2}Mg_{0.2}Ni_{0.2}Zn_{0.2})O$ anode with Acoustic Emission (AE) monitoring (Figure 2.4.4b).[161] The first cycle showed strong AE activity at low voltage, which was attributed to SEI formation. Later, they observed AEs mostly during the delithiation cycles, which is often where there are mechanical stresses associated with alloying/dealloying. Schweidler et al. also studied high-entropy oxyfluorides with AE.[162] Acoustic activity was most prominent during the first cycle above 4.6 V and was attributed to mechanical degradation (crack propagation) and gas evolution. Further insight into the lithiation behaviour and side reactions that occur during the first cycle can be revealed by the gases released during cycling. For instance, oxygen release during cycling can be due to a phase transition in cathode materials. Breitung et al. investigated the gassing behaviour of the $Li(Co_{0.2}Cu_{0.2}Mg_{0.2}Ni_{0.2}Zn_{0.2})OF$ cathode and the $(Co_{0.2}Cu_{0.2}Mg_{0.2}Ni_{0.2}Zn_{0.2})O$ anode with the help of pressure measurements and Differential Electrochemical Mass Spectrometry (DEMS).[163] The anode evolved $C_2H_4$ gas mostly during the first cycle, which was attributed to the formation of a stable SEI. This was observed without the need for additives in the electrolyte, which are typically used in other high-capacity anodes like silicon. For the cathode, gassing behaviour was dependent on cut-off voltage. Onset of gas evolution was seen as early as 4.55 V for $CO_2$, however the 5 V cutoff was associated with the greatest gas evolution involving $CO_2$, CO, $H_2$, $O_2$, and $POF_3$. $CO_2$ and CO were attributed to oxidation of the electrolyte, which yields decomposition products that later form $H_2$. The $LiPF_6$ salt decomposition produced $POF_3$, and $O_2$ evolution was associated with surface lattice oxygen release. These observations are consistent with a mechanism similar to Li-rich disordered rock-salts.[163]

Spinels are known to convert to rock-salt during synthesis upon the addition of lithium, as seen in Figure 2.4.4c. Wang et al. investigated the spinel to rock-salt transformation that occurs upon the incorporation of Li into HEOs during synthesis.[164] The addition of lithium was accompanied with the oxidation of transition metals until oxidation was no longer possible, resulting in the transformation to rock-salt. The phase conversion in spinel $(CrMnFeCoNi)_3O_4$ during electrochemical cycling has also been studied at the atomic scale.[165] During lithiation, the authors observed the formation of $Cr_xFe_{3-x}O_4$ and $LiNi_xCo_{1-x}O_2$ phases along with metallic Mn nanocrystals at 0.5 V. Further lithiation to 0.01 V led to the emergence of metallic Fe, Cr, Co, and Ni. Upon delithiation, the remaining spinel grains grew by incorporating nearby metal nanoparticles.

Several publications have studied the magnetic properties of HEOs. Witte et al. studied the magnetic properties of perovskite-type HEOs with rare-earth metals and observed mostly antiferromagnetic behaviour.[166, 167] More recently, Sarkar et al. reviewed the magnetic properties of HEOs.[168] Sarkar also studied the electronic band structure of rare-earth metal based fluorite HEOs.[169] They highlighted the importance of synthesis temperature and atmosphere (reducing/oxidizing gas) on the band structure and number of oxygen vacancies.

## Summary and Outlook

The field of electrochemical energy storage has seen a recent growth in high-entropy materials. HEOs have the potential to be used as anode materials in Li-ion batteries as they offer very high capacity compared to the conventional graphite anode limited to 372 mAh/g. However, it must be stressed that these oxides typically have a large first cycle irreversible capacity and an electrochemical stability that is inferior to traditional anodes. In addition, they tend to operate at a higher potential (1 V—2 V) than graphite (0.2 V—0.3 V). For most applications, this is too high as it significantly drops the output voltage of the battery when coupled with conventional NMC layered cathodes (at around 4 V). Also, non-faradaic and surface pseudocapacitive contributions to the total capacity are still not fully understood. The presence of multiple cations, many of which have good catalytic activity, may react with the organic solvents and salts of the electrolytes. Alternatively, these novel electrode-electrolyte interactions may prove beneficial, as they may enable the formation of a highly stable SEI.

Disorder in cathode materials is known in the battery field to be a largely detrimental property. A classic example is $LiNiO_2$, where significant Li-Ni cation mixing causes degradation and eventual phase transition. The addition of other metal cations (i.e., Mn and Co.) has proven successful, as in the case of commercial NMC111. Here, stability was improved by these metal cations, and more careful cation selection may improve structural stability even further. However, it is not yet clear whether entropy stabilized cathodes are any less susceptible to degradation. In addition, certain promising high-capacity cathodes like DRXs require processing under argon which may limit their commercial viability. Nevertheless, HEO cathodes have the potential to stabilize the structure and allow metal cations to have greater stability and site energies that accommodate lithium. The use of five metal cations, without or with fluorination (such as in the case of DRX), or layered structures along with vacancies could lead to stable fully de-lithiated cathodes and hence higher capacities. Compared to HE-anodes, there is little work on HE- cathodes. Further work is needed to explore the full potential of these novel electrodes.

Finally, HEAs offer new opportunities to solve the challenges associated with conventional high-capacity anodes like silicon or lithium metal. Compared to HE-oxides, there is little research regarding HE-alloys for anode materials. Although it is unlikely that entropy stabilization would eliminate the swelling associated with Li alloying, HEAs may reduce capacity fade in otherwise high-capacity anodes. Researchers should consider strategies such as the combination of alloying (e.g., Si, Al) and inert/non-alloying elements (e.g., Cu), and the use of elements with a large atomic radius (e.g., La). The practical and economic feasibility of the latter option is increased if the composition is not limited to strict equiatomic proportions.

In recent years, high-entropy materials have been employed in numerous fields of energy research, but more work needs to be done. Given the complexity of these materials, it is expected that computational techniques and high-throughput experimentation will play a key role in the future of the material design cycle. However, this outlook should be approached critically. Computational design strategies arise out of pre-existing paradigms and may overlook truly novel materials. For instance, high-throughput studies on HE-*rocksalts* may direct resources away from the discovery of entirely new families of HE structures. Additional challenges are related to the collection of high-quality data (a prerequisite for the successful implementation of machine learning). Ideally, high-throughput experimentation will be used in conjunction with computational designs and the more traditional experimental exploration.

## Author Contributions

JS: research and writing. YA-L and EB: editing and revisions.

## Acknowledgements

We would like to thank the Office of Energy Research and Development (OERD) at Natural Resources Canada for financial support.

## References

[1] M. Winter, B. Barnett, and K. Xu, “Before Li Ion Batteries,” *Chem Rev*, vol. 118, no. 23, pp. 11433–11456, Dec. 2018, doi: 10.1021/acs.chemrev.8b00422.

[2] M. Yoshio, R. J. Brodd, and A. Kozawa, “Lithium-Ion Batteries,” New York: Springer US, 2009, p. 50.

[3] Nobel Prize, “The Nobel Prize in Chemistry 2019,” Oct. 09, 2019.

[4] Y. Tian *et al.*, “Promises and Challenges of Next-Generation ‘Beyond Li-ion’ Batteries for Electric Vehicles and Grid Decarbonization,” *Chem Rev*, vol. 121, no. 3, pp. 1623–1669, Feb. 2021, doi: 10.1021/acs.chemrev.0c00767.

[5] J. T. Frith, M. J. Lacey, and U. Ulissi, “A non-academic perspective on the future of lithium-based batteries,” *Nat Commun*, vol. 14, no. 1, p. 420, Jan. 2023, doi: 10.1038/s41467-023-35933-2.

[6] Tesla, “ Master Plan 3,” Apr. 2023.

[7] S. Lee and A. Manthiram, “Can Cobalt Be Eliminated from Lithium-Ion Batteries?,” *ACS Energy Lett*, vol. 7, no. 9, pp. 3058–3063, Sep. 2022, doi: 10.1021/acsenergylett.2c01553.

[8] J. Xiao, F. Shi, T. Glossmann, C. Burnett, and Z. Liu, “From laboratory innovations to materials manufacturing for lithium-based batteries,” *Nat Energy*, vol. 8, no. 4, pp. 329–339, Mar. 2023, doi: 10.1038/s41560-023-01221-y.

[9] M. S. E. Houache, C. H. Yim, Z. Karkar, and Y. Abu-Lebdeh, “On the Current and Future Outlook of Battery Chemistries for Electric Vehicles—Mini Review,” *Batteries*, vol. 8, no. 7, Jul. 2022, doi: 10.3390/batteries8070070.

[10] S. T. Myung *et al.*, “Nickel-Rich Layered Cathode Materials for Automotive Lithium-Ion Batteries: Achievements and Perspectives,” *ACS Energy Lett*, vol. 2, no. 1, pp. 196–223, 2017, doi: 10.1021/acsenergylett.6b00594.

[11] M. N. Obrovac and V. L. Chevrier, “Alloy negative electrodes for Li-ion batteries,” *Chem Rev*, vol. 114, no. 23, pp. 11444–11502, 2014, doi: 10.1021/cr500207g.

[12] G. Smith and E. J. F. Dickinson, “Error, reproducibility and uncertainty in experiments for electrochemical energy technologies,” *Nat Commun*, vol. 13, no. 1, p. 6832, Nov. 2022, doi: 10.1038/s41467-022-34594-x.

[13] C. Liu, Z. G. Neale, and G. Cao, “Understanding electrochemical potentials of cathode materials in rechargeable batteries,” *Materials Today*, vol. 19, no. 2. Elsevier B.V., pp. 109–123, Mar. 01, 2016. doi: 10.1016/j.mattod.2015.10.009.

[14] A. Manthiram, “An Outlook on Lithium Ion Battery Technology,” *ACS Cent Sci*, vol. 3, no. 10, pp. 1063–1069, 2017, doi: 10.1021/acscentsci.7b00288.

[15] R. A. Huggins, “Advanced Batteries: Materials Science Aspects,” in *Advanced Batteries: Materials Science Aspects*, New York: Springer US, 2009, p. 10. doi: 10.1007/978-0-387-76424-5.

[16] N. Nitta, F. Wu, J. T. Lee, and G. Yushin, “Li-ion battery materials: Present and future,” *Materials Today*, vol. 18, no. 5, pp. 252–264, 2015, doi: 10.1016/j.mattod.2014.10.040.

[17] M. Letellier *et al.*, “The first *in situ* Li7 nuclear magnetic resonance study of lithium insertion in hard-carbon anode materials for Li-ion batteries,” *J Chem Phys*, vol. 118, no. 13, pp. 6038–6045, Apr. 2003, doi: 10.1063/1.1556092.

[18] A. Mauger, C. M. Julien, J. B. Goodenough, and K. Zaghib, “Tribute to Michel Armand: from Rocking Chair – Li-ion to Solid-State Lithium Batteries,” *J Electrochem Soc*, vol. 167, no. 7, p. 070507, Jan. 2020, doi: 10.1149/2.0072007JES.

[19] M. S. Whittingham, “Electrical Energy Storage and Intercalation Chemistry,” *Science (1979)*, vol. 192, no. 4244, pp. 1126–1127, 1976.

[20] J. Niu, S. Kang, S.-T. Myung, C.-H. Jo, A. Konarov, and E. Kendrick, *Future Lithium-ion Batteries*. London: The Royal Society of Chemistry, 2019.

[21] T. He *et al.*, “The effects of alkali metal ions with different ionic radii substituting in Li sites on the electrochemical properties of Ni-Rich cathode materials,” *J Power Sources*, vol. 441, no. August, p. 227195, 2019, doi: 10.1016/j.jpowsour.2019.227195.

[22] P. Kalyani and N. Kalaiselvi, “Various aspects of LiNiO2 chemistry: A review,” *Sci Technol Adv Mater*, vol. 6, no. 6, pp. 689–703, 2005, doi: 10.1016/j.stam.2005.06.001.

[23] M. B. Sahana and R. Gopalan, “Recent Developments in Electrode Materials for Lithium-Ion Batteries for Energy Storage Application,” in *Handbook of Advanced Ceramics and Composites*, Cham: Springer International Publishing, 2020, pp. 1297–1333. doi: 10.1007/978-3-030-16347-1_44.

[24] L. Xie *et al.*, “Hard Carbon Anodes for Next-Generation Li-Ion Batteries: Review and Perspective,” *Adv Energy Mater*, vol. 11, no. 38, Oct. 2021, doi: 10.1002/aenm.202101650.

[25] W. Xu *et al.*, “Lithium metal anodes for rechargeable batteries,” *Energy Environ Sci*, vol. 7, no. 2, pp. 513–537, 2014, doi: 10.1039/c3ee40795k.

[26] S. Xia, X. Wu, Z. Zhang, Y. Cui, and W. Liu, “Practical Challenges and Future Perspectives of All-Solid-State Lithium-Metal Batteries,” *Chem*, vol. 5, no. 4, pp. 753–785, 2019, doi: 10.1016/j.chempr.2018.11.013.

[27] C. M. Maclaughlin, “Innovations in Lithium Ion Battery Technologies: A Conversation with Will West, Nancy Dudney, and Andrew Westover,” *ACS Energy Lett*, vol. 4, no. 3, pp. 786–788, 2019, doi: 10.1021/acsenergylett.9b00358.

[28] H. Yang *et al.*, “Recent progress and perspective on lithium metal anode protection,” *Energy Storage Mater*, vol. 14, no. January, pp. 199–221, 2018, doi: 10.1016/j.ensm.2018.03.001.

[29] X. B. Cheng, R. Zhang, C. Z. Zhao, and Q. Zhang, “Toward Safe Lithium Metal Anode in Rechargeable Batteries: A Review,” *Chem Rev*, vol. 117, no. 15, pp. 10403–10473, 2017, doi: 10.1021/acs.chemrev.7b00115.

[30] N. J. Dudney, “Approaches toward lithium metal stabilization,” *MRS Bull*, vol. 43, no. 10, pp. 759–767, 2018, doi: 10.1557/mrs.2018.233.

[31] J. Kasemchainan *et al.*, “Critical stripping current leads to dendrite formation on plating in lithium anode solid electrolyte cells,” *Nat Mater*, vol. 18, no. 10, pp. 1105–1111, 2019, doi: 10.1038/s41563-019-0438-9.

[32] P. Wang, W. Qu, W. L. Song, H. Chen, R. Chen, and D. Fang, “Electro–Chemo–Mechanical Issues at the Interfaces in Solid-State Lithium Metal Batteries,” *Adv Funct Mater*, vol. 29, no. 27, pp. 1–29, 2019, doi: 10.1002/adfm.201900950.

[33] D. Lin, Y. Liu, and Y. Cui, “Reviving the lithium metal anode for high-energy batteries,” *Nat Nanotechnol*, vol. 12, no. 3, pp. 194–206, 2017, doi: 10.1038/nnano.2017.16.

[34] Bollore, “Blue Solutions.” https://www.blue-solutions.com/en/battery-technology/ (accessed Apr. 08, 2023).

[35] G. Zheng *et al.*, “Interconnected hollow carbon nanospheres for stable lithium metal anodes,” *Nat Nanotechnol*, vol. 9, no. 8, pp. 618–623, 2014, doi: 10.1038/nnano.2014.152.

[36] M. Winter and J. O. Besenhard, “Electrochemical lithiation of tin and tin-based intermetallics and composites,” *Electrochim Acta*, vol. 45, no. 1–2, pp. 31–50, Sep. 1999, doi: 10.1016/S0013-4686(99)00191-7.

[37] M. Wetjen, D. Pritzl, R. Jung, S. Solchenbach, R. Ghadimi, and H. A. Gasteiger, “Differentiating the degradation phenomena in silicon-graphite electrodes for lithium-ion batteries,” *J Electrochem Soc*, vol. 164, no. 12, pp. A2840–A2852, 2017, doi: 10.1149/2.1921712jes.

[38] F. Zhang *et al.*, “Boosting the initial coulombic efficiency in silicon anodes through interfacial incorporation of metal nanocrystals,” *J Mater Chem A Mater*, vol. 7, no. 29, pp. 17426–17434, 2019, doi: 10.1039/c9ta05340a.

[39] T. Yoon, C. C. Nguyen, D. M. Seo, and B. L. Lucht, “Capacity Fading Mechanisms of Silicon Nanoparticle Negative Electrodes for Lithium Ion Batteries,” *J Electrochem Soc*, vol. 162, no. 12, pp. A2325–A2330, 2015, doi: 10.1149/2.0731512jes.

[40] S. Chae, M. Ko, K. Kim, K. Ahn, and J. Cho, “Confronting Issues of the Practical Implementation of Si Anode in High-Energy Lithium-Ion Batteries,” *Joule*, vol. 1, no. 1, pp. 47–60, 2017, doi: 10.1016/j.joule.2017.07.006.

[41] X. Zuo, J. Zhu, P. Müller-Buschbaum, and Y. J. Cheng, “Silicon based lithium-ion battery anodes: A chronicle perspective review,” *Nano Energy*, vol. 31, no. October 2016, pp. 113–143, 2017, doi: 10.1016/j.nanoen.2016.11.013.

[42] L. Sun, Y. Liu, R. Shao, J. Wu, R. Jiang, and Z. Jin, “Recent progress and future perspective on practical silicon anode-based lithium ion batteries,” *Energy Storage Mater*, vol. 46, pp. 482–502, Apr. 2022, doi: 10.1016/j.ensm.2022.01.042.

[43] Y. Cui, “Silicon anodes,” *Nat Energy*, vol. 6, no. 10, pp. 995–996, Oct. 2021, doi: 10.1038/s41560-021-00918-2.

[44] H. Li, “A High Capacity Nano-Si Composite Anode Material for Lithium Rechargeable Batteries,” *Electrochemical and Solid-State Letters*, vol. 2, no. 11, p. 547, 1999, doi: 10.1149/1.1390899.

[45] H. Li *et al.*, “Revisiting the Preparation Progress of Nano-Structured Si Anodes toward Industrial Application from the Perspective of Cost and Scalability,” *Adv Energy Mater*, vol. 12, no. 7, p. 2102181, Feb. 2022, doi: 10.1002/aenm.202102181.

[46] A. M. Wilson, J. N. Reimers, E. W. Fuller, and J. R. Dahn, “Lithium insertion in pyrolyzed siloxane polymers,” *Solid State Ion*, vol. 74, no. 3–4, pp. 249–254, 1994, doi: 10.1016/0167-2738(94)90217-8.

[47] A. M. Wilson, B. M. Way, J. R. Dahn, and T. Van Buuren, “Nanodispersed silicon in pregraphitic carbons,” *J Appl Phys*, vol. 77, no. 6, pp. 2363–2369, 1995, doi: 10.1063/1.358759.

[48] A. M. Wilson, G. Zank, K. Eguchi, W. Xing, and J. R. Dahn, “Pyrolysed silicon-containing polymers as high capacity anodes for lithium-ion batteries,” *J Power Sources*, vol. 68, no. 2, pp. 195–200, 1997, doi: 10.1016/S0378-7753(96)02551-7.

[49] A. M. Wilson, G. Zank, K. Eguchi, W. Xing, B. Yates, and J. R. Dahn, “Polysiloxane Pyrolysis,” *Chemistry of Materials*, vol. 9, no. 7, pp. 1601–1606, 1997, doi: 10.1021/cm970002r.

[50] W. Xing, A. M. Wilson, G. Zank, and J. R. Dahn, “Pyrolysed pitch-polysilane blends for use as anode materials in lithium ion batteries,” *Solid State Ion*, vol. 93, no. 3–4, pp. 239–244, 1997.

[51] W. Xing, A. M. Wilson, K. Eguchi, G. Zank, and J. R. Dahn, “Pyrolyzed Polysiloxanes for Use as Anode Materials in Lithium-Ion Batteries,” *J Electrochem Soc*, vol. 144, no. 7, p. 2410, 1997, doi: 10.1149/1.1837828.

[52] J. H. Lee, W. S. Choi, H. Y. Woo, H. H. Nersisyan, E. M. Jin, and S. M. Jeong, “Polysiloxane-derived silicon nanoparticles for Li-ion battery,” *J Energy Storage*, vol. 27, no. September 2019, p. 101141, 2020, doi: 10.1016/j.est.2019.101141.

[53] J. Knipping, H. Wiggers, B. Rellinghaus, P. Roth, D. Konjhodzic, and C. Meier, "Synthesis of high purity silicon nanoparticles in a low pressure microwave reactor," *J Nanosci Nanotechnol*, vol. 4, no. 8, pp. 1039–1044, 2004, doi: 10.1166/jnn.2004.149.

[54] C.-H. Yim, F. M. Courtel, and Y. Abu-Lebdeh, "A high capacity silicon–graphite composite as anode for lithium-ion batteries using low content amorphous silicon and compatible binders," *J Mater Chem A Mater*, vol. 1, no. 28, p. 8234, Jun. 2013, doi: 10.1039/c3ta10883j.

[55] Tekna, "Tekna.com," 2020. http://www.tekna.com/ (accessed Jun. 03, 2020).

[56] C. K. Chan *et al.*, "High-performance lithium battery anodes using silicon nanowires," *Nat Nanotechnol*, vol. 3, no. 1, pp. 31–35, Jan. 2008, doi: 10.1038/nnano.2007.411.

[57] J. K. Yoo, J. Kim, Y. S. Jung, and K. Kang, "Scalable fabrication of silicon nanotubes and their application to energy storage," *Advanced Materials*, vol. 24, no. 40, pp. 5452–5456, 2012, doi: 10.1002/adma.201201601.

[58] J. Ryu, D. Hong, S. Choi, and S. Park, "Synthesis of Ultrathin Si Nanosheets from Natural Clays for Lithium-Ion Battery Anodes," *ACS Nano*, vol. 10, no. 2, pp. 2843–2851, 2016, doi: 10.1021/acsnano.5b07977.

[59] T. Takamura, M. Uehara, J. Suzuki, K. Sekine, and K. Tamura, "High capacity and long cycle life silicon anode for Li-ion battery," *J Power Sources*, vol. 158, no. 2 SPEC. ISS., pp. 1401–1404, 2006, doi: 10.1016/j.jpowsour.2005.10.081.

[60] T. Takamura, S. Ohara, M. Uehara, J. Suzuki, and K. Sekine, "A vacuum deposited Si film having a Li extraction capacity over 2000 mAh/g with a long cycle life," *J Power Sources*, vol. 129, no. 1 SPEC. ISS., pp. 96–100, 2004, doi: 10.1016/j.jpowsour.2003.11.014.

[61] D. Mazouzi *et al.*, "Critical roles of binders and formulation at multiscales of silicon-based composite electrodes," *J Power Sources*, vol. 280, pp. 533–549, Apr. 2015, doi: 10.1016/j.jpowsour.2015.01.140.

[62] J. Zhou *et al.*, "Core-Shell Coating Silicon Anode Interfaces with Coordination Complex for Stable Lithium-Ion Batteries," *ACS Appl Mater Interfaces*, vol. 8, no. 8, pp. 5358–5365, 2016, doi: 10.1021/acsami.5b12392.

[63] N. Liu *et al.*, "A pomegranate-inspired nanoscale design for large-volume-change lithium battery anodes," *Nat Nanotechnol*, vol. 9, no. 3, pp. 187–192, Mar. 2014, doi: 10.1038/nnano.2014.6.

[64] H. Tao, L.-Z. Fan, W.-L. Song, M. Wu, X. He, and X. Qu, "Hollow core–shell structured Si/C nanocomposites as high-performance anode materials for lithium-ion batteries," *Nanoscale*, vol. 6, no. 6, pp. 3138–3142, 2014, doi: 10.1039/C3NR03090C.

[65] L. Y. Yang, H. Z. Li, J. Liu, Z. Q. Sun, S. S. Tang, and M. Lei, “Dual yolk-shell structure of carbon and silica-coated silicon for high-performance lithium-ion batteries,” *Sci Rep*, vol. 5, pp. 1–9, 2015, doi: 10.1038/srep10908.

[66] X. Li *et al.*, “Hollow core-shell structured porous Si-C nanocomposites for Li-ion battery anodes,” *J Mater Chem*, vol. 22, no. 22, pp. 11014–11017, 2012, doi: 10.1039/c2jm31286g.

[67] N. Liu, H. Wu, M. T. McDowell, Y. Yao, C. Wang, and Y. Cui, “A yolk-shell design for stabilized and scalable Li-ion battery alloy anodes,” *Nano Lett*, vol. 12, no. 6, pp. 3315–3321, 2012, doi: 10.1021/nl3014814.

[68] A. Terechshenko, A. Sanbayeva, M. R. Babaa, A. Nurpeissova, and Z. Bakenov, “Spray-pyrolysis preparation of Li 4 Ti 5 O 12 /si composites for lithium-ion batteries,” *Eurasian Chemico-Technological Journal*, vol. 21, no. 1, pp. 69–73, 2019, doi: 10.18321/ectj793.

[69] M. Liu, H. Gao, G. Hu, K. Zhu, and H. Huang, “Facile preparation of core-shell Si@Li4Ti5O12 nanocomposite as large-capacity lithium-ion battery anode,” *Journal of Energy Chemistry*, vol. 40, pp. 89–98, 2020, doi: 10.1016/j.jechem.2019.02.011.

[70] Q. Xia, A. Xu, L. Du, Y. Yan, and S. Wu, “High-rate, long-term performance of LTO-pillared silicon/carbon composites for lithium-ion batteries anode under high temperature,” *J Alloys Compd*, vol. 800, pp. 50–57, 2019, doi: 10.1016/j.jallcom.2019.06.023.

[71] J. I. Lee *et al.*, “High-performance silicon-based multicomponent battery anodes produced via synergistic coupling of multifunctional coating layers,” *Energy Environ Sci*, vol. 8, no. 7, pp. 2075–2084, 2015, doi: 10.1039/c5ee01493j.

[72] S. H. Lee, C. Huang, and P. S. Grant, “Layer-by-layer printing of multi-layered heterostructures using Li4Ti5O12 and Si for high power Li-ion storage,” *Nano Energy*, vol. 61, no. January, pp. 96–103, 2019, doi: 10.1016/j.nanoen.2019.04.044.

[73] C. H. Yim, S. Niketic, N. Salem, O. Naboka, and Y. Abu-Lebdeh, “Towards improving the practical energy density of Li-Ion batteries: Optimization & evaluation of silicon:graphite composites in full cells,” *J Electrochem Soc*, vol. 164, no. 1, pp. A6294–A6302, 2017, doi: 10.1149/2.0481701jes.

[74] F. M. Courtel and Y. Abu-Lebdeh, “Use of Xanthan Gum as an Anode Binder,” 10,483,546 B2, 2019

[75] F. M. Courtel, S. Niketic, D. Duguay, Y. Abu-Lebdeh, and I. J. Davidson, “Water-soluble binders for MCMB carbon anodes for lithium-ion batteries,” *J Power Sources*, vol. 196, no. 4, pp. 2128–2134, 2011, doi: 10.1016/j.jpowsour.2010.10.025.

[76] H. Wang *et al.*, “Key Factors for Binders to Enhance the Electrochemical Performance of Silicon Anodes through Molecular Design,” *Small*, vol. 18, no. 1, p. 2101680, Jan. 2022, doi: 10.1002/smll.202101680.

[77] X. Zhao, S. Niketic, C. H. Yim, J. Zhou, J. Wang, and Y. Abu-Lebdeh, “Revealing the Role of Poly(vinylidene fluoride) Binder in Si/Graphite Composite Anode for Li-Ion Batteries,” *ACS Omega*, vol. 3, no. 9, pp. 11684–11690, 2018, doi: 10.1021/acsomega.8b01388.

[78] Y. Lai *et al.*, “Revisit the Progress of Binders for a Silicon-Based Anode from the Perspective of Designed Binder Structure and Special Sized Silicon Nanoparticles,” *Ind Eng Chem Res*, vol. 61, no. 19, pp. 6246–6268, May 2022, doi: 10.1021/acs.iecr.2c00453.

[79] N. Delpuech *et al.*, “Critical Role of Silicon Nanoparticles Surface on Lithium Cell Electrochemical Performance Analyzed by FTIR, Raman, EELS, XPS, NMR, and BDS Spectroscopies,” *The Journal of Physical Chemistry C*, vol. 118, no. 31, pp. 17318–17331, Aug. 2014, doi: 10.1021/jp503949y.

[80] J. W. Sturman, C.-H. Yim, Z. Karkar, E. A. Baranova, M. Toupin, and Y. Abu-Lebdeh, “Investigation of Xanthan Gum and Carboxymethyl Cellulose Binders for the Silicon Anode of Lithium-Ion Batteries,” *J Electrochem Soc*, vol. 170, no. 2, p. 020534, Feb. 2023, doi: 10.1149/1945-7111/acbbf1.

[81] B. Koo, H. Kim, Y. Cho, K. T. Lee, N.-S. Choi, and J. Cho, “A Highly Cross-Linked Polymeric Binder for High-Performance Silicon Negative Electrodes in Lithium Ion Batteries,” *Angewandte Chemie International Edition*, vol. 51, no. 35, pp. 8762–8767, Aug. 2012, doi: 10.1002/anie.201201568.

[82] E. Markevich, G. Salitra, and D. Aurbach, “Fluoroethylene Carbonate as an Important Component for the Formation of an Effective Solid Electrolyte Interphase on Anodes and Cathodes for Advanced Li-Ion Batteries,” *ACS Energy Lett*, vol. 2, no. 6, pp. 1337–1345, Jun. 2017, doi: 10.1021/acsenergylett.7b00163.

[83] G. Yang *et al.*, “Robust Solid/Electrolyte Interphase (SEI) Formation on Si Anodes Using Glyme-Based Electrolytes,” *ACS Energy Lett*, vol. 6, no. 5, pp. 1684–1693, May 2021, doi: 10.1021/acsenergylett.0c02629.

[84] B. Cantor, I. T. H. Chang, P. Knight, and A. J. B. Vincent, “Microstructural development in equiatomic multicomponent alloys,” *Materials Science and Engineering A*, vol. 375–377, no. 1-2 SPEC. ISS., pp. 213–218, 2004, doi: 10.1016/j.msea.2003.10.257.

[85] J. W. Yeh *et al.*, “Nanostructured high-entropy alloys with multiple principal elements: Novel alloy design concepts and outcomes,” *Adv Eng Mater*, vol. 6, no. 5, pp. 299–303, 2004, doi: 10.1002/adem.200300567.

[86] E. J. Pickering and N. G. Jones, “High-entropy alloys: a critical assessment of their founding principles and future prospects,” *International Materials Reviews*, vol. 61, no. 3, pp. 183–202, 2016, doi: 10.1080/09506608.2016.1180020.

[87] Y. Zhang, *High-Entropy Materials*, vol. 113, no. 9. Singapore: Springer Singapore, 2019. doi: 10.1007/978-981-13-8526-1.

[88] Y. Chen *et al.*, “Opportunities for High-Entropy Materials in Rechargeable Batteries,” *ACS Mater Lett*, vol. 3, no. 2, pp. 160–170, 2021, doi: 10.1021/acsmaterialslett.0c00484.

[89] Y. Ma *et al.*, “High-entropy energy materials: Challenges and new opportunities,” *Energy Environ Sci*, vol. 14, no. 5, pp. 2883–2905, 2021, doi: 10.1039/d1ee00505g.

[90] C. M. Rost *et al.*, “Entropy-stabilized oxides,” *Nat Commun*, vol. 6, no. 1, p. 8485, Dec. 2015, doi: 10.1038/ncomms9485.

[91] M. Widom, “Modeling the structure and thermodynamics of high-entropy alloys,” *J Mater Res*, vol. 33, no. 19, pp. 2881–2898, 2018, doi: 10.1557/jmr.2018.222.

[92] M. Fu, X. Ma, K. Zhao, X. Li, and D. Su, “High-entropy materials for energy-related applications,” *iScience*, vol. 24, no. 3, p. 102177, Mar. 2021, doi: 10.1016/j.isci.2021.102177.

[93] H. Xiang *et al.*, “High-entropy ceramics: Present status, challenges, and a look forward,” *Journal of Advanced Ceramics*, vol. 10, no. 3, pp. 385–441, Jun. 2021, doi: 10.1007/s40145-021-0477-y.

[94] S. Akrami, P. Edalati, M. Fuji, and K. Edalati, “High-entropy ceramics: Review of principles, production and applications,” *Materials Science and Engineering R: Reports*, vol. 146, no. August, p. 100644, 2021, doi: 10.1016/j.mser.2021.100644.

[95] J.-W. Yeh, “Physical Metallurgy of High-Entropy Alloys,” *JOM*, vol. 67, no. 10, pp. 2254–2261, Oct. 2015, doi: 10.1007/s11837-015-1583-5.

[96] A. Sarkar *et al.*, “High entropy oxides for reversible energy storage,” *Nat Commun*, vol. 9, no. 1, p. 3400, Dec. 2018, doi: 10.1038/s41467-018-05774-5.

[97] A. Sarkar, B. Breitung, and H. Hahn, “High entropy oxides: The role of entropy, enthalpy and synergy,” *Scr Mater*, vol. 187, pp. 43–48, 2020, doi: 10.1016/j.scriptamat.2020.05.019.

[98] M. Vaidya, G. M. Muralikrishna, and B. S. Murty, “High-entropy alloys by mechanical alloying: A review,” *J Mater Res*, vol. 34, no. 5, pp. 664–686, 2019, doi: 10.1557/jmr.2019.37.

[99] Q. Wang, L. Velasco, B. Breitung, and V. Presser, “High-Entropy Energy Materials in the Age of Big Data: A Critical Guide to Next-Generation Synthesis and Applications,” *Adv Energy Mater*, vol. 11, no. 47, p. 2102355, Dec. 2021, doi: 10.1002/aenm.202102355.

[100] A. Amiri and R. Shahbazian-Yassar, “Recent progress of high-entropy materials for energy storage and conversion,” *Journal of Materials Chemistry A*, vol. 9, no. 2. pp. 782–823, 2021. doi: 10.1039/d0ta09578h.

[101] Y. Lin, N. Luo, M. Chamas, C. Hu, and S. Grasso, “Sustainable high-entropy ceramics for reversible energy storage: A short review,” *Int J Appl Ceram Technol*, vol. 18, no. 5, pp. 1560–1569, 2021, doi: 10.1111/ijac.13762.

[102] A. Sarkar *et al.*, "High-Entropy Oxides: Fundamental Aspects and Electrochemical Properties," *Advanced Materials*, vol. 31, no. 26, p. 1806236, Jun. 2019, doi: 10.1002/adma.201806236.

[103] Q. Wang *et al.*, "Multi-anionic and -cationic compounds: New high entropy materials for advanced Li-ion batteries," *Energy Environ Sci*, vol. 12, no. 8, pp. 2433–2442, 2019, doi: 10.1039/c9ee00368a.

[104] A. Sarkar *et al.*, "Nanocrystalline multicomponent entropy stabilised transition metal oxides," *J Eur Ceram Soc*, vol. 37, no. 2, pp. 747–754, 2017, doi: 10.1016/j.jeurceramsoc.2016.09.018.

[105] J. Sturman, C.-H. Yim, E. A. Baranova, and Y. Abu-Lebdeh, " Communication—Design of LiNi 0.2 Mn 0.2 Co 0.2 Fe 0.2 Ti 0.2 O 2 as a High-Entropy Cathode for Lithium-Ion Batteries Guided by Machine Learning ," *J Electrochem Soc*, vol. 168, no. 5, p. 050541, 2021, doi: 10.1149/1945-7111/ac00f4.

[106] Z. Sun, Y. Zhao, C. Sun, Q. Ni, C. Wang, and H. Jin, "High entropy spinel-structure oxide for electrochemical application," *Chemical Engineering Journal*, vol. 431, no. July, p. 133448, Mar. 2022, doi: 10.1016/j.cej.2021.133448.

[107] D. Bérardan, S. Franger, A. K. Meena, and N. Dragoe, "Room temperature lithium superionic conductivity in high entropy oxides," *J Mater Chem A Mater*, vol. 4, no. 24, pp. 9536–9541, 2016, doi: 10.1039/c6ta03249d.

[108] H. Xu *et al.*, "Nano high-entropy alloy with strong affinity driving fast polysulfide conversion towards stable lithium sulfur batteries," *Energy Storage Mater*, vol. 43, no. August, pp. 212–220, 2021, doi: 10.1016/j.ensm.2021.09.003.

[109] L. Yang *et al.*, " Multiprincipal Component P2-Na 0.6 (Ti 0.2 Mn 0.2 Co 0.2 Ni 0.2 Ru 0.2 )O 2 as a High-Rate Cathode for Sodium-Ion Batteries ," *JACS Au*, vol. 1, no. 1, pp. 98–107, 2021, doi: 10.1021/jacsau.0c00002.

[110] C. Zhao, F. Ding, Y. Lu, L. Chen, and Y. S. Hu, "High-Entropy Layered Oxide Cathodes for Sodium-Ion Batteries," *Angewandte Chemie - International Edition*, vol. 59, no. 1, pp. 264–269, 2020, doi: 10.1002/anie.201912171.

[111] A. S. Etman, J. Zhou, and J. Rosen, "Ti1.1V0.7CrxNb1.0Ta0.6C3Tz high-entropy MXene freestanding films for charge storage applications," *Electrochem commun*, vol. 137, no. February, p. 107264, 2022, doi: 10.1016/j.elecom.2022.107264.

[112] S. K. Nemani *et al.*, "High-Entropy 2D Carbide MXenes: TiVNbMoC 3 and TiVCrMoC 3," *ACS Nano*, vol. 15, no. 8, pp. 12815–12825, Aug. 2021, doi: 10.1021/acsnano.1c02775.

[113] M. Kheradmandfard *et al.*, "Ultrafast green microwave-assisted synthesis of high-entropy oxide nanoparticles for Li-ion battery applications," *Mater Chem Phys*, vol. 262, no. January, p. 124265, 2021, doi: 10.1016/j.matchemphys.2021.124265.

[114] Q. Dong *et al.*, “Rapid Synthesis of High-Entropy Oxide Microparticles,” *Small*, vol. 18, no. 11, p. 2104761, Mar. 2022, doi: 10.1002/smll.202104761.

[115] H. Guo *et al.*, “Design and fabrication of high-entropy oxide anchored on graphene for boosting kinetic performance and energy storage,” *Ceram Int*, vol. 48, no. 3, pp. 3344–3350, 2022, doi: 10.1016/j.ceramint.2021.10.109.

[116] A. Sarkar *et al.*, “Rare earth and transition metal based entropy stabilised perovskite type oxides,” *J Eur Ceram Soc*, vol. 38, no. 5, pp. 2318–2327, 2018, doi: 10.1016/j.jeurceramsoc.2017.12.058.

[117] R. Djenadic *et al.*, “Multicomponent equiatomic rare earth oxides,” *Mater Res Lett*, vol. 5, no. 2, pp. 102–109, 2017, doi: 10.1080/21663831.2016.1220433.

[118] A. Sarkar *et al.*, “Multicomponent equiatomic rare earth oxides with a narrow band gap and associated praseodymium multivalency,” *Dalton Transactions*, vol. 46, no. 36, pp. 12167–12176, 2017, doi: 10.1039/C7DT02077E.

[119] Z. Lun *et al.*, “Cation-disordered rocksalt-type high-entropy cathodes for Li-ion batteries,” *Nat Mater*, vol. 20, no. 2, pp. 214–221, 2021, doi: 10.1038/s41563-020-00816-0.

[120] Q. Wang *et al.*, “High entropy oxides as anode material for Li-ion battery applications: A practical approach,” *Electrochem commun*, vol. 100, no. January, pp. 121–125, 2019, doi: 10.1016/j.elecom.2019.02.001.

[121] H. Duncan, F. M. Courtel, and Y. Abu-Lebdeh, “ A Study of the Solid-Electrolyte-Interface (SEI) of ZnMn 2 O 4 : A Conversion-Type Anode Material for Li-Ion Batteries ,” *J Electrochem Soc*, vol. 162, no. 13, pp. A7110–A7117, 2015, doi: 10.1149/2.0141513jes.

[122] N. Qiu, H. Chen, Z. Yang, S. Sun, Y. Wang, and Y. Cui, “A high entropy oxide (Mg0.2Co0.2Ni0.2Cu0.2Zn0.2O) with superior lithium storage performance,” *J Alloys Compd*, vol. 777, pp. 767–774, 2019, doi: 10.1016/j.jallcom.2018.11.049.

[123] J. Yan *et al.*, “A high-entropy perovskite titanate lithium-ion battery anode,” *J Mater Sci*, vol. 55, no. 16, pp. 6942–6951, 2020, doi: 10.1007/s10853-020-04482-0.

[124] E. Lökçü, Ç. Toparli, and M. Anik, “Electrochemical Performance of (MgCoNiZn)1-xLixO High-Entropy Oxides in Lithium-Ion Batteries,” *ACS Appl Mater Interfaces*, vol. 12, no. 21, pp. 23860–23866, 2020, doi: 10.1021/acsami.0c03562.

[125] H. Chen, N. Qiu, B. Wu, Z. Yang, S. Sun, and Y. Wang, “A new spinel high-entropy oxide (Mg0.2Ti0.2Zn0.2Cu0.2Fe0.2)3O4 with fast reaction kinetics and excellent stability as an anode material for lithium ion batteries,” *RSC Adv*, vol. 10, no. 16, pp. 9736–9744, 2020, doi: 10.1039/d0ra00255k.

[126] D. Wang *et al.*, “Spinel-structured high entropy oxide (FeCoNiCrMn)3O4 as anode towards superior lithium storage performance,” *J Alloys Compd*, vol. 844, p. 156158, 2020, doi: 10.1016/j.jallcom.2020.156158.

[127] J. Zhao, X. Yang, Y. Huang, F. Du, and Y. Zeng, “Entropy Stabilization Effect and Oxygen Vacancies Enabling Spinel Oxide Highly Reversible Lithium-Ion Storage,” *ACS Appl Mater Interfaces*, vol. 13, no. 49, pp. 58674–58681, Dec. 2021, doi: 10.1021/acsami.1c18362.

[128] H. Xiang, H. Xie, Y. Chen, H. Zhang, and A. Mao, “materials entropy oxide as a novel high-performance anode material for lithium-ion batteries,” *J Mater Sci*, vol. 56, no. 13, pp. 8127–8142, 2021, doi: 10.1007/s10853-021-05805-5.

[129] T. X. Nguyen, J. Patra, J. K. Chang, and J. M. Ting, “High entropy spinel oxide nanoparticles for superior lithiation-delithiation performance,” *J Mater Chem A Mater*, vol. 8, no. 36, pp. 18963–18973, 2020, doi: 10.1039/d0ta04844e.

[130] T. X. Nguyen, C. C. Tsai, J. Patra, O. Clemens, J. K. Chang, and J. M. Ting, “Co-free high entropy spinel oxide anode with controlled morphology and crystallinity for outstanding charge/discharge performance in Lithium-ion batteries,” *Chemical Engineering Journal*, vol. 430, no. P1, p. 132658, 2022, doi: 10.1016/j.cej.2021.132658.

[131] C. Q. Duan *et al.*, “New spinel high-entropy oxides (FeCoNiCrMnXLi)3O4 (X = Cu, Mg, Zn) as the anode material for lithium-ion batteries,” *Ceram Int*, vol. 47, no. 22, pp. 32025–32032, 2021, doi: 10.1016/j.ceramint.2021.08.091.

[132] B. Xiao *et al.*, “High entropy oxides (FeNiCrMnX)3O4 (X=Zn, Mg) as anode materials for lithium ion batteries,” *Ceram Int*, vol. 47, no. 24, pp. 33972–33977, 2021, doi: 10.1016/j.ceramint.2021.08.303.

[133] B. Xiao *et al.*, “High-entropy oxides as advanced anode materials for long-life lithium-ion Batteries,” *Nano Energy*, vol. 95, no. November 2021, p. 106962, 2022, doi: 10.1016/j.nanoen.2022.106962.

[134] K. H. Tian *et al.*, “High-entropy chemistry stabilizing spinel oxide (CoNiZnXMnLi)3O4 (X = Fe, Cr) for high-performance anode of Li-ion batteries,” *Rare Metals*, vol. 41, no. 4, pp. 1265–1275, 2022, doi: 10.1007/s12598-021-01872-4.

[135] H. Chen, N. Qiu, B. Wu, Z. Yang, S. Sun, and Y. Wang, “Tunable pseudocapacitive contribution by dimension control in nanocrystalline-constructed (Mg0.2Co0.2Ni0.2Cu0.2Zn0.2)O solid solutions to achieve superior lithium-storage properties,” *RSC Adv*, vol. 9, no. 50, pp. 28908–28915, 2019, doi: 10.1039/c9ra05508h.

[136] X.-L. Zhang *et al.*, “Review—Pseudocapacitive Energy Storage Materials from Hägg-Phase Compounds to High-Entropy Ceramics,” *J Electrochem Soc*, vol. 168, no. 12, p. 120521, 2021, doi: 10.1149/1945-7111/ac3e49.

[137] X. Wang, S. Tang, W. Guo, Y. Fu, and A. Manthiram, “Advances in multimetallic alloy-based anodes for alkali-ion and alkali-metal batteries,” *Materials Today*, vol. 50, no. November, pp. 259–275, 2021, doi: 10.1016/j.mattod.2021.05.001.

[138] B. T. Heligman, K. J. K. III, K. P. Scanlan, R. Sun, and A. Manthiram, “Interdigitated Eutectic Alloy Anodes with High-Volumetric Capacity for Lithium-Ion Batteries,” *ECS Meeting Abstracts*, 2019, doi: 10.1149/MA2019-01/2/249.

[139] F. Xin *et al.*, “Enhanced Electrochemical Performance of Fe-Sn Alloy with Cu Additive As Anode in Lithium-Ion Batteries,” *ECS Meeting Abstracts*, 2017, doi: 10.1149/MA2017-02/4/418.

[140] Y. Cao, B. Scott, R. A. Dunlap, and M. N. Obrovac, “Mechanically Milled Si-Mn-Fe Alloys as Negative Electrodes for Li-Ion Batteries,” *ECS Meeting Abstracts*, 2018, doi: 10.1149/MA2018-01/3/393.

[141] M. Obrovac, “WO2006028583A2,” World International Property Organization, USA, WO2006028583A2, 2006.

[142] V. Pavlyuk *et al.*, “New maximally disordered – High entropy intermetallic phases (MD-HEIP) of the Gd1-xLaxSn2-ySbyMz (M=Li, Na, Mg): Synthesis, structure and some properties,” *J Alloys Compd*, vol. 838, p. 155643, Oct. 2020, doi: 10.1016/j.jallcom.2020.155643.

[143] P. Edalati *et al.*, “Scripta Materialia High-entropy alloys as anode materials of nickel - metal hydride batteries,” *Scr Mater*, vol. 209, p. 114387, 2022, doi: 10.1016/j.scriptamat.2021.114387.

[144] Z. Wang, H. Ge, S. Liu, G. Li, and X. Gao, “High-entropy alloys to activate the sulfur cathode for lithium-sulfur batteries,” *Energy & Environmental Materials*, pp. 0–2, 2022, doi: 10.1002/eem2.12358.

[145] L. Lin *et al.*, “High-Entropy Sulfides as Electrode Materials for Li-Ion Batteries,” *Adv Energy Mater*, vol. 12, no. 8, 2022, doi: 10.1002/aenm.202103090.

[146] J. Wang *et al.*, “Lithium containing layered high entropy oxide structures,” *Sci Rep*, vol. 10, no. 1, pp. 1–13, 2020, doi: 10.1038/s41598-020-75134-1.

[147] K. Walczak *et al.*, “NaMn0.2Fe0.2Co0.2Ni0.2Ti0.2O2 high-entropy layered oxide – experimental and theoretical evidence of high electrochemical performance in sodium batteries,” *Energy Storage Mater*, vol. 47, no. December 2021, pp. 500–514, May 2022, doi: 10.1016/j.ensm.2022.02.038.

[148] K. Wang *et al.*, “Synthesis of High-Entropy Layered Oxide Epitaxial Thin Films: LiCr1/6Mn1/6Fe1/6Co1/6Ni1/6Cu1/6O2,” *Cryst Growth Des*, vol. 22, no. 2, pp. 1116–1122, 2022, doi: 10.1021/acs.cgd.1c01076.

[149] Z. Y. Gu *et al.*, “An Advanced High-Entropy Fluorophosphate Cathode for Sodium-Ion Batteries with Increased Working Voltage and Energy Density,” *Advanced Materials*, vol. 34, no. 14, 2022, doi: 10.1002/adma.202110108.

[150] N. Osenciat *et al.*, “Charge compensation mechanisms in Li-substituted high-entropy oxides and influence on Li superionic conductivity,” *Journal of the American Ceramic Society*, vol. 102, no. 10, pp. 6156–6162, 2019, doi: 10.1111/jace.16511.

[151] B. Wu *et al.*, “High-Entropy NASICON Phosphates (Na3M2(PO4)3and NaMPO4Ox, M = Ti, V, Mn, Cr, and Zr) for Sodium Electrochemistry,” *Inorg Chem*, vol. 61, no. 9, pp. 4092–4101, 2022, doi: 10.1021/acs.inorgchem.1c03861.

[152] M. P. Stockham, B. Dong, and P. R. Slater, “High entropy lithium garnets – Testing the compositional flexibility of the lithium garnet system,” *J Solid State Chem*, vol. 308, no. December 2021, p. 122944, 2022, doi: 10.1016/j.jssc.2022.122944.

[153] F. Strauss *et al.*, “High-Entropy Polyanionic Lithium Superionic Conductors,” *ACS Mater Lett*, vol. 4, no. 2, pp. 418–423, 2022, doi: 10.1021/acsmaterialslett.1c00817.

[154] K. Yazhou and Y. Zhiren, “Synthesis, structure and electrochemical properties of Al doped high entropy perovskite Lix(LiLaCaSrBa)Ti1-xAlxO3,” *Ceram Int*, vol. 48, no. 4, pp. 5035–5039, 2022, doi: 10.1016/j.ceramint.2021.11.041.

[155] M. R. Chellali *et al.*, “On the homogeneity of high entropy oxides: An investigation at the atomic scale,” *Scr Mater*, vol. 166, pp. 58–63, 2019, doi: 10.1016/j.scriptamat.2019.02.039.

[156] M. Moździerz *et al.*, “Mixed ionic-electronic transport in the high-entropy (Co,Cu,Mg,Ni,Zn)1-Li O oxides,” *Acta Mater*, vol. 208, p. 116735, Apr. 2021, doi: 10.1016/j.actamat.2021.116735.

[157] B. Cheng *et al.*, “Pressure-induced tuning of lattice distortion in a high-entropy oxide,” *Commun Chem*, vol. 2, no. 1, pp. 1–9, 2019, doi: 10.1038/s42004-019-0216-2.

[158] F. Tavani, M. Fracchia, N. Pianta, P. Ghigna, E. Quartarone, and P. D’Angelo, “Multivariate curve resolution analysis of operando XAS data for the investigation of the lithiation mechanisms in high entropy oxides,” *Chem Phys Lett*, vol. 760, no. August, p. 137968, 2020, doi: 10.1016/j.cplett.2020.137968.

[159] P. Ghigna *et al.*, “Lithiation Mechanism in High-Entropy Oxides as Anode Materials for Li-Ion Batteries: An Operando XAS Study,” *ACS Appl Mater Interfaces*, vol. 12, no. 45, pp. 50344–50354, 2020, doi: 10.1021/acsami.0c13161.

[160] S. Y. Wang *et al.*, “Operando synchrotron transmission X-ray microscopy study on (Mg, Co, Ni, Cu, Zn)O high-entropy oxide anodes for lithium-ion batteries,” *Mater Chem Phys*, vol. 274, no. August, p. 125105, 2021, doi: 10.1016/j.matchemphys.2021.125105.

[161] S. Schweidler, S. L. Dreyer, B. Breitung, and T. Brezesinski, “Operando acoustic emission monitoring of degradation processes in lithium-ion batteries with a high-entropy oxide anode,” *Sci Rep*, vol. 11, no. 1, pp. 1–8, 2021, doi: 10.1038/s41598-021-02685-2.

[162] S. Schweidler, S. L. Dreyer, B. Breitung, and T. Brezesinski, “Acoustic Emission Monitoring of High-Entropy Oxyfluoride Rock-Salt Cathodes during Battery Operation,” *Coatings*, vol. 12, no. 3, p. 402, 2022, doi: 10.3390/coatings12030402.

[163] B. Breitung *et al.*, “Gassing Behavior of High-Entropy Oxide Anode and Oxyfluoride Cathode Probed Using Differential Electrochemical Mass Spectrometry,” *Batter Supercaps*, vol. 3, no. 4, pp. 361–369, 2020, doi: 10.1002/batt.202000010.

[164] J. Wang *et al.*, “Spinel to Rock-Salt Transformation in High Entropy Oxides with Li Incorporation,” *Electrochem*, vol. 1, no. 1, pp. 60–74, 2020, doi: 10.3390/electrochem1010007.

[165] C. Y. Huang *et al.*, “Atomic-scale investigation of Lithiation/Delithiation mechanism in High-entropy spinel oxide with superior electrochemical performance,” *Chemical Engineering Journal*, vol. 420, no. April, 2021, doi: 10.1016/j.cej.2021.129838.

[166] R. Witte *et al.*, “Magnetic properties of rare-earth and transition metal based perovskite type high entropy oxides,” *J Appl Phys*, vol. 127, no. 18, pp. 1–10, 2020, doi: 10.1063/5.0004125.

[167] R. Witte *et al.*, “High-entropy oxides: An emerging prospect for magnetic rare-earth transition metal perovskites,” *Phys Rev Mater*, vol. 3, no. 3, pp. 1–8, 2019, doi: 10.1103/PhysRevMaterials.3.034406.

[168] A. Sarkar, R. Kruk, and H. Hahn, “Magnetic properties of high entropy oxides,” *Dalton Transactions*, vol. 50, no. 6, pp. 1973–1982, 2021, doi: 10.1039/d0dt04154h.

[169] A. Sarkar *et al.*, “Role of intermediate 4 f states in tuning the band structure of high entropy oxides,” *APL Mater*, vol. 8, no. 5, 2020, doi: 10.1063/5.0007944.

[170] M. Anik and E. Lokcu, “Synthesis and Electrochemical Performance of the (Mg0.2Co0.2Ni0.2Zn0.2Li0.2) O High Entropy Oxide as Anode Material for Li-ion Batteries,” *The Eurasia Proceedings of Science Technology Engineering and Mathematics*, vol. 7, pp. 329–332, 2019.

# Chapter 3: Experimental Methods

## 3.1 Physical Characterization

### XRD

X-Ray Diffraction (XRD) can provide information about the crystal structure of battery electrode materials.[1] It involves the bombardment of a sample with x-rays. A certain fraction of the x-rays are diffracted by the crystallographic planes within the sample. The angle and signal intensity of the diffracted x-rays are converted into a diffractogram. This can help determine whether a sample is phase-pure or multi-phase (i.e., impurities). For powder XRD, a small amount of powder was placed into a silicone-based sample holder. The sample was flushed with the holder. For air-sensitive or post-mortem electrodes, Kapton tape was often used to cover the sample during the scan. XRD was carried out with a Bruker AXS D8 diffractometer in Bragg-Brentano configuration using Cu Kα radiation ($\lambda$= 0.154 nm) between 10° and 85° 2θ. The applied voltage and current were 40 kV and 40 mA. Bruker DIFFRAC.EVA was used for qualitative data analysis, databased sample matching, sample displacement corrections, and $K\alpha_2$ stripping for crystalline samples. Typically, the scan background was not removed. Bruker TOPAS was used to determine lattice parameters for single-phase materials when necessary.

### SEM and EDX

Scanning Electron Microscopy (SEM) is an imaging technique that can characterize micron to sub-micron particles by scanning a sample with an electron beam.[1] The electron beam interacts with the sample and emits various signals (the most notable of which are secondary electrons and backscattered electrons). The signals and their intensity are then converted into an image. SEM was carried out with a Hitachi SU5000 Field Emission microscope. Energy Dispersive X-ray Spectroscopy (EDX) is an elemental analysis technique used in conjunction with SEM. With EDX, an electron beam strikes the surface of a sample; the sample then emits x-rays of a certain energy which will depend on the sample's elemental composition. EDX allows for sub-surface elemental quantification to sample depths of around 2 µm.[1] However, EDX is unable to identify low atomic number elements like lithium. EDX was used to quantify (wt. or at. %) the approximate elemental composition of samples (e.g., oxide cathodes or Si-C composites). In addition, EDX colour maps were used to qualitatively visualize a sample's elemental distribution over a surface area of several square micrometers.

### ICP-OES Sample Preparation

Inductively Coupled Plasma-Optical Emission Spectroscopy (ICP-OES) was used to quantify the elemental distribution of metals (including lithium) in a powder sample. Metal oxide cathodes were prepared for ICP-OES analysis by digesting 0.1 g of powder into 2 mL of aqua regia. The solution was then heated gently on a hot plate for approximately 15 minutes until the cathode was dissolved. The resulting coloured acidic solution was then transferred to a volumetric flask and filled with deionized water up to a total volume of 50 mL. A successful digestion resulted in a slightly coloured but transparent solution with no precipitate. ICP-OES provided only metal compositions in ppm (by mass), and the balance was assumed to be oxygen.

### FTIR

Fourier Transform Infrared Spectroscopy (FTIR) is used primarily to identify chemical bonds and functional groups in organic/polymeric materials.[1] With FTIR, infrared radiation is applied to a sample, wherein a certain fraction is absorbed. This absorbed IR radiation is then converted into vibrational and/or rotational energy. This energy is detected and the resulting signal is converted into a spectrum (typically from 4000 to 400 $cm^{-1}$) which reflects a molecule's fingerprint. FTIR was used to confirm the presence of functional groups in biopolymer binders that can interact with the surface of silicon (Chapter 6). In addition, FTIR was used to confirm the molecular structure of SmAz in Chapter 5.

## 3.2 Electrode Preparation and Battery Assembly

### Tape-Casting

Anode and cathode films were prepared via a standard slurry/tape-casting method. Details regarding each electrode formulation have been described in the experimental sections of each publication chapter. In a typical process, the active powder was combined with an additional carbon additive (Super P/Timcal or KS4) and a binder (PVDF/HSV900, or a biopolymer). Nanosilicon powder was vacuum dried at 80 °C prior to use. Super P conductive additive and graphite were dried at 90 °C prior to use. The biopolymer binders were stored in a sealed container at room temperature to avoid any thermal degradation that may occur with long-term storage at elevated temperatures. Batch sizes of 0.5 g total dry mass were typically used. When PVDF was used as a binder, the solvent was 1-Methyl-2-pyrrolidinone (NMP). When a biopolymer was used as a binder, the solvent was deionized water with ethanol. Slurries were mixed with a Thinky planetary mixer in high-density polyethylene vials (24 mL or 35 mL) along with 5 mm diameter zirconium oxide balls. Using a notch bar with a controlled gap size, the slurry was evenly casted onto an acetone-cleaned aluminum or copper current collector for the cathode or anode, respectively. Copper is required for anodes to prevent the alloying of lithium with aluminum at low potential. The solvent was evaporated from the electrode films with room temperature air drying (for water-based slurries) or dried in a convection oven at 85 °C (for NMP-based slurries). The dried electrode films were typically calendered in a roll press at 0.5 metric ton to increase contact with the current collector and increase volumetric energy density. However, silicon-rich electrode films were usually not calendered to preserve porosity. 0.5-inch diameter (12.7 mm) electrode disks were cut from the dried films. Finally, the electrode disks were always vacuum dried at 80 ℃ overnight (18-24 hours) prior to battery assembly to remove trace moisture or solvent.

### Coin-Cell Assembly

The mass of each dried electrode disk was measured before assembly into half-cell batteries. In half-cells, the negative electrode is a Li metal foil (voltage vs $Li/Li^+$), where Li is present in great excess and serves as the counter/reference electrode. Half-cell batteries with Li metal (typically by MSE Supplies, 250 µm thickness, diameter 15.6 mm) were prepared in an argon-filled glove box using NRC-brand 2325-type coin cells (see Figure 3.2.1). The electrolyte volume was typically 74.8 µL and the separator consisted of two Celgard polypropylene membranes. The electrolytes were carbonate-based. The most common electrolyte formulations were 1M $LiPF_6$ in EC/EMC (1:1 v/v) + 10% FEC for Si-based anodes, and 1M $LiPF_6$ in EC/DEC (1:1 v/v) for cathodes. The FEC additive is known to improve cycle retention in Si-based anodes.[2] Coin cells were allowed to rest at OCV for at least 12 hours before electrochemical testing to allow for electrolyte penetration of the membranes and electrode. Certain authors replace their Li foil during cycling to extend battery life and improve the performance of reported results.[3] However, this was never done for the sealed coin cells in this thesis.

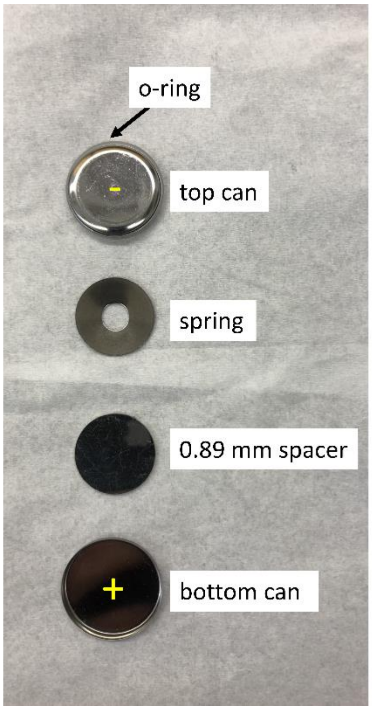

Figure 3.2.1. NRC-brand 2325-type coin cells

### Pouch Cell Assembly

Pouch cells were prepared from either commercial electrodes (MTI NMC532 or CMS graphite) or electrodes made in-house. For electrodes made in-house, the anode was composed of 90 wt% graphite, 5 wt% NaCMC (700K) or XG, and 5 wt% Super P conductive carbon; the cathode was composed of 90 wt% NMC 532 (MTI), 5 wt% PVDF, and 5 wt% Super P. The anode and cathode electrodes were cast with a 250 µm gap notch bar onto a cleaned Cu or Al foil, respectively. The electrode films were dried at 85 ℃ to evaporate the solvent. The casts were calendered. The resulting N/P ratio was around 1:35-1:4. Single-layer pouch cell electrodes were cut into films of the following dimensions: 58x45mm for the anode and 57x44 mm for the cathode, with a protruding metal tab on the right side of each electrode. The electrodes were vacuum dried at 80 ℃ overnight prior to cell assembly. A 4 mm width Ni tab with polymer tape was welded to the anode tab with a Sunstone CDDP welder. For the cathode, a 4 mm width Al tab with polymer tape was used. The electrodes were wrapped in S-configuration with a single layer of either a Celgard 3501 or a commercial separator. Pouch cells were encased in an Al-laminated film (shiny side in, 113 µm thickness) and sealed on three sides with a MTI MSK-115A vacuum sealing machine. To the pouch cell was added 0.9 mL of 1M $LiPF_6$ in EC/EMC/DMC (1:1:1 v/v) + 2 % VC electrolyte. This electrolyte was present in great excess to reduce concerns of electrolyte consumption during cycling. A final vacuum seal (degas time 30 s @ -98 kPa; 5 s seal at a temperature of 180 °C) was accomplished with the MSK-115A. Pouch cells were then held at 1.5 V for 24 hours to prevent corrosion of Cu, followed by a single formation cycle at C/20 between 4.2 V and 3.0 V. The pouch cell was then punctured in a dry room and immediately degassed and re-sealed with the MSK-115A. However, this degassing step is most relevant for multi-layer pouch cells. The pouch cell was then cycled at C/10 between 4.2 and 3.0 V. Current rates were calculated based on the loading of the cathode while assuming a theoretical capacity of 155 mAh/g.

### High-Energy Ball-Milling

High energy ball-milling with a SPEX 8000M mixer was used for alloy formation, in solid-state synthesis, or to reduce particle size prior to tape-casting. Ball-milling was carried out inside a SPEX 8007 stainless steel (SS) vial with SS ball bearings in a ball to powder ratio of 10:1. An argon atmosphere was used for air-sensitive materials. For alloy formation, hexane was used as a process control agent during ball-milling. For alloy synthesis, ball-milling was performed for 2 hours, with a 30-minute rest after 1h. For the pulverization of a pellet, ball-milling was performed for 20 minutes.

## 3.3 Electrochemical Characterization

### Galvanostatic Battery Cycling

Battery cycling was carried out in an Arbin BT2000 battery cycler at 30 °C. Typically, 2-3 coin-cells were tested for each sample to ensure reproducible results. Each coin-cell was charged and discharged over a certain number of cycles to observe capacity retention over time. The cells were charged and discharged at constant current to a potential limit, followed by a 15-minute OCV rest. Half-cell anodes were first discharged (active material lithiation) to 0.005 V and then charged to 1.5 V. This potential window is suitable for silicon (~0.4 V) and graphite (~0.2 V) lithiation, which were the primary active species in the studied anodes. For organic anodes, an upper voltage window of 3.0 V was selected. This voltage window is unusually high for anode materials and was only used in the study on organic anodes (see Chapter 5). Half-cell cathodes were first charged (active material delithiation) to 4.2-4.4 V and then discharged to 2.5 V. Important information about the electrochemical properties of battery materials can be derived from galvanostatic cycling data including: capacity retention over time, potential/voltage profiles, and differential capacity curves (dQ/dV).

Typically, C-rate currents were used, where the current was calculated based on the theoretical capacity of the active material (e.g., 1C=372 mA/g for graphite). 1C is a high current density and refers to a full charge or discharge in 1 hour. In contrast, 0.1C (or C/10) is a common laboratory standard and refers to a 10-hour charge or discharge time. Low current cycling was typically used (i.e., C/20 to C/10) to minimize diffusion limitations, unless a rate-capability test was performed. Alternatively, current densities were simply calculated in terms of an applied current per unit of active material (e.g., 50 mA/$g_{\text{ActiveMaterial}}$).

### Cyclic Voltammetry

Cyclic voltammetry (CV) is one of the most common electrochemical characterization techniques used to study redox and adsorption processes. CV involves varying the potential of a working electrode at a constant sweep-rate (mV/s) and measuring the current response that arises from electrochemical reactions.[4] This provides information that is very similar to the differential capacity plot (dQ/dV), which is derived from battery cycling data acquired at a constant current.[4] However, for battery materials, the dQ/dV plot is often preferred because it allows redox processes time to reach completion (especially at low C-rates). In contrast, with CV, there may be kinetic limitations due to the time constraint imposed by the scan rate (mV/s). CV was carried out on a Biologic potentiostat in a two-electrode configuration where Li metal served as the reference and counter electrode. CV was typically performed by scanning the voltage window from 1.5 V to 5 mV (for anodes) at scan rates between 0.2 mV/s to 1 mV/s. The electrode was scanned six times at each scan rate and only the last scan was taken for analysis. The current response ($i$) acquired with CV is known to follow the relationship below, where $a$ and $b$ are parameters and $v$ is the scan rate.

$$i = i_{capacitive} + i_{diffusive} = av^{b}$$

In general, the b-value of 0.5 is associated with diffusion-controlled processes, whereas the b-value of 1 is associated with capacitive or capacitive-like processes.[5] In hybrid materials, the b-value will be between 0.5 and 1. It should be understood that the b-value is dependent on a variety of factors such as potential window and a material’s charge-storage mechanism. [6]

### Impedance Spectroscopy

Potentiostatic Electrochemical Impedance Spectroscopy (EIS) allows for the investigation of cell resistances by applying a sinusoidal voltage signal of various frequencies and measuring a current response.[4] EIS was typically carried out in a two-electrode configuration (vs Li metal) in the frequency range from 100 kHz to 10 mHz at an amplitude of 10 mV. Impedance data for battery materials is most often presented as a Nyquist plot which consists of one or more semicircles at high-medium frequencies, and a line region at low frequencies. The line region can provide an indicator of diffusive or capacitive processes.[6] Double-layer capacitive behaviour is marked by a 90° line region, whereas typical battery behaviour is marked by a 45° line region (i.e., Warburg diffusion). Impedance from Li-ion batteries is often described in terms of an equivalent circuit model, where impedance is divided into contributions from bulk resistance, interfacial resistance, charge-transfer resistance, and Warburg diffusion.[6] However, in many experimental settings (especially 2-electrode configurations) the individual contributions are difficult to distinguish and may overlap. A 3-electrode configuration is preferred for accurate quantification and modeling of the resistances at the working electrode.

## 3.4 Operando X-Ray Diffraction

Operando X-Ray Diffraction refers to XRD characterization that is performed while the battery is operational.[4, 7] This provides information about changes in the battery electrode material’s crystal structure during charging and discharging. Operando XRD requires a specially designed electrochemical cell that has an x-ray transparent window.[4] Beryllium (Be) metal and Kapton polyimide films are commonly used windows.[4, 7] However, it should be acknowledged that these windows are not completely transparent to x-rays. Kapton is marked by a broad peak around 20°; whereas with crystalline beryllium, dominant reflections will appear around 45.8°, 50.8°, 52.8°, and 70.9°. Moreover, the intensity of the peaks from the studied electrode material will be attenuated with increasing window thickness. The operando cell can either be a single-use coin cell or a reusable battery housing. In addition, there are two main orientations for the battery material. An illustration of these orientations is shown below in Figure 3.4.1. The second design is preferred because the electrode material is in direct contact with the beryllium, which increases the intensity of the material’s diffraction peaks. After battery assembly, the operando cell is installed into a diffractometer and connected to a potentiostat to charge and discharge the battery.

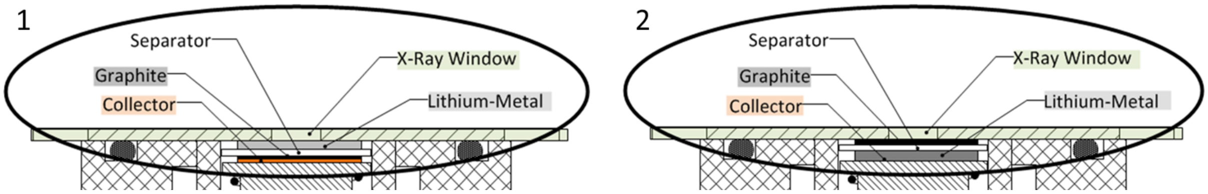

Figure 3.4.1 Popular design configurations for operando XRD [8]

Operando XRD can reveal important information about the lithiation and degradation mechanism of an electrode material. For instance, Wu et al studied NMC cathodes with XRD and discovered an irreversible phase transition at elevated temperatures, which revealed the material's failure mechanism.[9] Early work on in situ XRD with silicon was done by Hatchard and Dahn, where they observed diffraction patterns for different lithiated phases of silicon in a battery.[10] Phase diagrams had historically predicted a fully lithiated silicon phase of $Li_{22}Si_5$, which would correspond to a capacity of nearly 4200 mAh/g.[10, 11] However, a capacity this high was not reported experimentally, which led to the theory that $Li_{15}Si_4$ was the final lithiated state that was achievable electrochemically. Hatchard's study confirmed the fully lithiated state of silicon to be $Li_{15}Si_4$, which occurred below 50 mV (vs Li).[10] This phase has a theoretical capacity of 3579 mAh/g and is consistent with most experimental observations. Operando experiments have since studied the lithiated stages of graphite and silicon oxide at different potentials.[8, 12] Although silicon and graphite have been studied in their pure phases, there has been limited research surrounding operando XRD on composite electrodes.

Work on operando XRD began with efforts to use a conductive carbon coated Kapton film (0.05 mm thick) as both an electrode substrate and an x-ray window. The use of beryllium was initially undesired because of its cost and toxicity. The Kapton side of the film is insulating by nature of the polymer, but the carbon-coated side is conductive. For all single-use operando cells, the bottom can was cut with a 0.4" diameter hole to accommodate the x-ray transparent window. The carbon-coated Kapton film electrode (of 0.625" diameter) with Si-C active material was adhered to the coin cell with a thin ring of TorrSeal epoxy. The electrode disk was applied to the center of the coin cell and care was taken to ensure the application of the epoxy was clean and did not have large amounts of excess covering the exposed Kapton window or contaminating the active material of the electrode. The cell was then allowed to cure at 60 °C overnight to ensure complete setting of the hardener. A copper ring was added to the interior of the coin cell bottom can to allow electrical contact between the steel and the conductive side of the Kapton with the active material. The cell was then dried and assembled in the glove box as usual.

Early experiments with the Si-G composite were marked by very low reversible capacity. In addition, a shift in the reflection from the (002) plane of graphite was not observed during cycling. Postmortem of these failed cells revealed a highly corroded lithium foil disk with green deposits, as seen in Figure 3.4.2. The failure of these cells was also marked by a unique peak around 1.2 V in the dQ/dV plot during discharge. An investigation into the problem ruled-out the TorrSeal or copper ring. It was then determined that the Kapton film absorbed moisture and/or oxygen from the ambient air and allowed it to diffuse into the operando coin cell during testing. In these electrochemical tests, the presence of even trace moisture will compromise the experimental data. Hence, any solution to the problem should eliminate the moisture diffusion problem at the source. Several hydrophobic polymers were considered as a secondary seal (PMMA, PVC, PE, PP, PU, Mylar, etc.). However, these polymers have diffraction peaks of their own and would distort the resolution of the anode signal. It was ultimately decided to move away from Kapton and use beryllium as an x-ray transparent window and current collector.

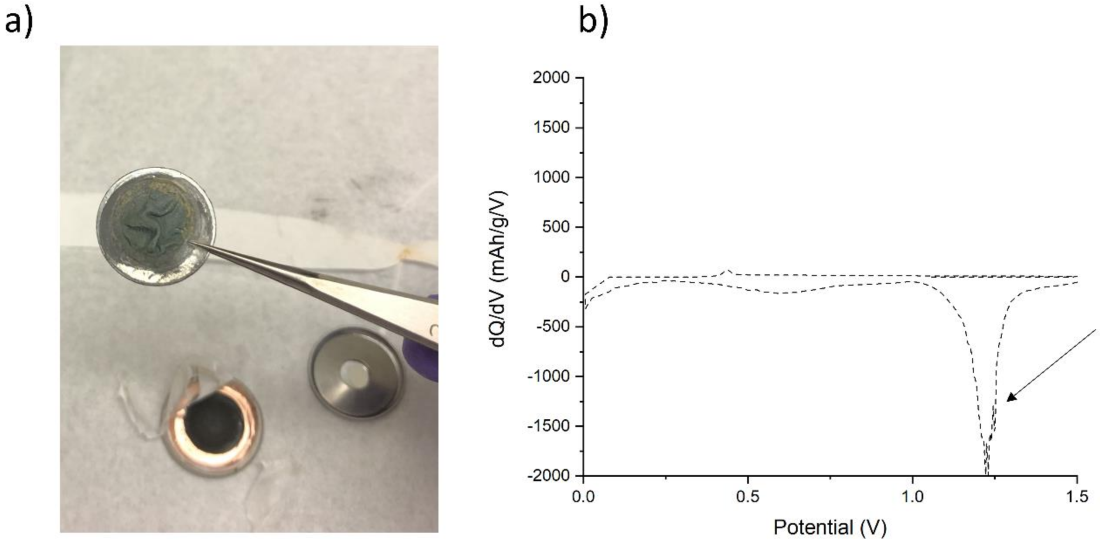

Figure 3.4.2 a) Corroded lithium foil from porous Kapton film and b) associated dQ/dV plot

Work on the beryllium operando cell began by applying a Si-G slurry to a Be disk, which was then sealed to the modified coin cell can (0.4” diameter hole) using TorrSeal, as described previously. Several Be thicknesses (25 µm, 50 µm, and 250 µm) and diameters (0.5”, 0.625”, and 0.8”) were considered. The thinner Be window allows for greater signal intensity of the active material, but these windows were very prone to fissures and leaks after cell assembly. The thicker Be window (250 µm & 0.8” diameter, in addition to a thinner internal spacer) was ultimately preferred owing to its more rigid surface and reduced propensity to leak. The single-use operando cell employing the thicker Be window was used in several successful operando experiments (see Figure 3.4.3). In a typical operando experiment, the single-use cell was placed into a special cell housing within the diffractometer, where the negative and positive electrodes were connected to a Biologic potentiostat. The operando coin cell was discharged and charged at a low current to ensure sufficient time to resolve phase transformations in the electrode material. Previous studies have reported currents between C/25 to C/50, depending on the investigated material and objective of the study.[8, 12] A 2-3 hours constant-voltage period was included at each voltage limit. The diffractometer was programmed to perform a new scan between 10-85° 2θ with a 0.03 step-size every 2 hours. A total of 25 scans were taken over a period of approximately 50 hours.

Figure 3.4.3. Single-use beryllium window coin-cell for operando XRD

The Bruker Operando cell (shown in Figure 3.4.4) is a reusable alternative to the single-use coin cell. It uses a beryllium window 29 mm in diameter and 270 µm thick, with a wider exposed surface area diameter of 0.7”. The Bruker Operando cell has no diffraction peaks between 10-40° (see Figure S5.12) ; this 2θ range allows for the investigation of several materials including the (002) plane of graphite, the (111) plane of silicon, and certain organic anodes. Peaks from the Celgard membrane may appear with thin layers of active material; the peaks appear around 13.9°, 16.7°, and 18.3° 2θ. Moreover, Li metal has a dominant reflection from the (110) plane around 36°. This peak may appear after cell assembly, or during an operando test due to Li plating onto the active material/Be window. Preferred orientation must be considered with diffraction peaks that arise from non-powder samples like Li metal, as peak intensity will vary with sample orientation. Investigated voltages should be limited to below 3.5 V (vs Li) to avoid oxidation of the Be window.[13] As the investigated electrode material is applied to the interior side of the Be window, sample displacement should be considered. A sample displacement factor was applied to the operando XRD data files by calibrating peak locations to a reference XRD scan of the pristine powder sample. For example, the (002) reflection from graphite in an operando cell was set to 26.4°, which was the 2θ at which it appeared in the powder XRD scan of pristine graphite. The Bruker Operando cell is placed inside a custom cell housing but is otherwise used with the same potentiostat and diffractometer program described with single-use coin cells. EIS was performed on the operando cell prior to cycling to confirm the total cell resistance was within an expected range.

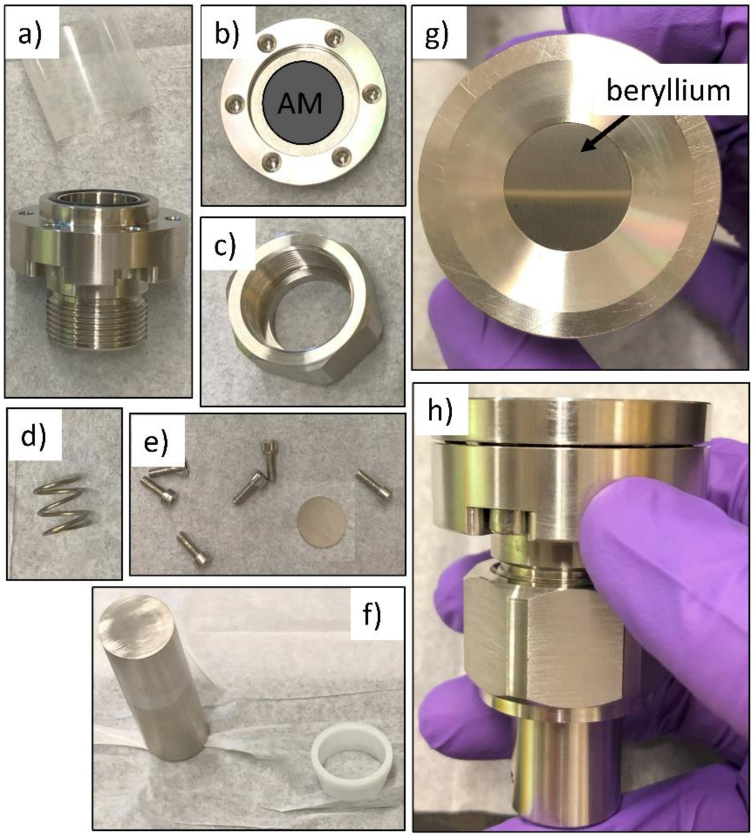

Figure 3.4.4. The Bruker Operando cell including a) the main steel housing and insulating sleeve, b) the positive electrode cover compartment with beryllium window (inc. surface area of active material [AM]), c) cap nut, d) spring, e) screws and spacer, f) negative electrode shaft and o-ring, g) assembled top and h) side images

Figure 3.4.5 shows the results of a successful operando XRD experiment on a Si-G composite electrode using the Bruker Operando cell. For graphite lithiation, there is a clear evolution in the (002) reflection from graphite. At low voltage around 0.03 V, the (002) reflection disappears, and the reflection associated with $LiC_{12}$ appears near 25°; further lithiation to 5 mV is associated with the formation of the fully lithiated graphite phase $LiC_6$ near 24°.[8] The (002) reflection from graphite reappears during delithiation to 1.5 V. For silicon, the dominant (111) reflection declines in intensity and nearly disappears during the first lithiation. The (111) reflection intensity does not return to its pristine state upon delithiation, consistent with amorphization of the bulk phase.

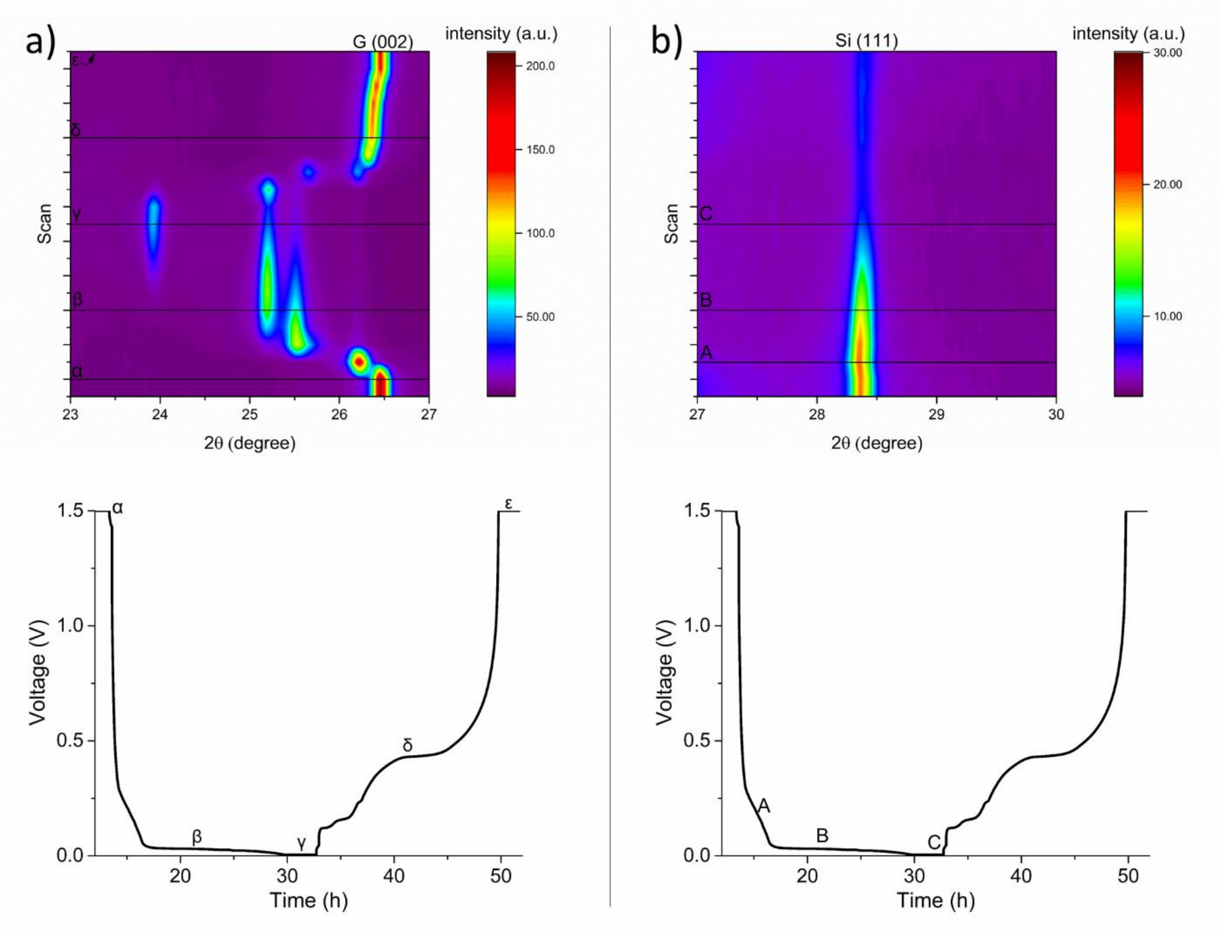

Figure 3.4.5. Operando XRD experiment on a 20 wt% Si + 60 wt% graphite composite during the first cycle (balance 10 wt% Super P, 10 wt% NaCMC binder). Image a) shows changes in the (002) graphite reflection and b) shows changes in the (111) reflection from silicon during lithiation-delithiation. As the graphite and silicon used for this test was very crystalline, the signal to background ratio is high and allows for clear identification of phase changes during cycling.

# References

[1] D. Titus, E. James Jebaseelan Samuel, and S. M. Roopan, “Nanoparticle characterization techniques,” in Green Synthesis, Characterization and Applications of Nanoparticles, Elsevier, 2019, pp. 303–319. doi: 10.1016/B978-0-08-102579-6.00012-5.

[2] M. Wetjen, D. Pritzl, R. Jung, S. Solchenbach, R. Ghadimi, and H. A. Gasteiger, “Differentiating the degradation phenomena in silicon-graphite electrodes for lithium-ion batteries,” J Electrochem Soc, vol. 164, no. 12, pp. A2840–A2852, 2017, doi: 10.1149/2.1921712jes.

[3] Y. Lai et al., “Revisit the Progress of Binders for a Silicon-Based Anode from the Perspective of Designed Binder Structure and Special Sized Silicon Nanoparticles,” Ind Eng Chem Res, vol. 61, no. 19, pp. 6246–6268, May 2022, doi: 10.1021/acs.iecr.2c00453.

[4] E. Talaie, P. Bonnick, X. Sun, Q. Pang, X. Liang, and L. F. Nazar, “Methods and Protocols for Electrochemical Energy Storage Materials Research,” Chemistry of Materials, vol. 29, no. 1, pp. 90–105, Jan. 2017, doi: 10.1021/acs.chemmater.6b02726.

[5] Y. Jiang and J. Liu, “Definitions of Pseudocapacitive Materials: A Brief Review,” Energy and Environmental Materials, vol. 2, no. 1, pp. 30–37, Mar. 2019, doi: 10.1002/eem2.12028.

[6] T. S. Mathis, N. Kurra, X. Wang, D. Pinto, P. Simon, and Y. Gogotsi, “Energy Storage Data Reporting in Perspective—Guidelines for Interpreting the Performance of Electrochemical Energy Storage Systems,” Adv Energy Mater, vol. 9, no. 39, p. 1902007, Oct. 2019, doi: 10.1002/aenm.201902007.

[7] N. Sharma, W. K. Pang, Z. Guo, and V. K. Peterson, “In Situ Powder Diffraction Studies of Electrode Materials in Rechargeable Batteries,” ChemSusChem, vol. 8, no. 17, pp. 2826–2853, 2015, doi: 10.1002/cssc.201500152.

[8] N. A. Cañas et al., “Operando X-ray diffraction during battery cycling at elevated temperatures: A quantitative analysis of lithium-graphite intercalation compounds,” Carbon N Y, vol. 116, pp. 255–263, 2017, doi: 10.1016/j.carbon.2017.02.002.

[9] Z. Wu et al., “Pre-Lithiation of Li(Ni1-x-yMnxCoy)O2 Materials Enabling Enhancement of Performance for Li-Ion Battery,” ACS Appl Mater Interfaces, vol. 8, no. 24, pp. 15361–15368, 2016, doi: 10.1021/acsami.6b03730.

[10] T. D. Hatchard and J. R. Dahn, “In Situ XRD and Electrochemical Study of the Reaction of Lithium with Amorphous Silicon,” J Electrochem Soc, vol. 151, no. 6, p. A838, 2004, doi: 10.1149/1.1739217.

[11] M. N. Obrovac and V. L. Chevrier, “Alloy negative electrodes for Li-ion batteries,” Chem Rev, vol. 114, no. 23, pp. 11444–11502, 2014, doi: 10.1021/cr500207g.

[12] J. Park, S. S. Park, and Y. S. Won, “In situ XRD study of the structural changes of graphite anodes mixed with SiOx during lithium insertion and extraction in lithium ion batteries,” Electrochim Acta, vol. 107, pp. 467–472, 2013, doi: 10.1016/j.electacta.2013.06.059.

[13] J. B. Leriche et al., “An Electrochemical Cell for Operando Study of Lithium Batteries Using Synchrotron Radiation,” J Electrochem Soc, vol. 157, no. 5, p. A606, 2010, doi: 10.1149/1.3355977.

# Chapter 4: Exploring the Design Space of High-Entropy Layered Cathodes

James Sturman[1, 2], Chae-Ho Yim[1], Elena A. Baranova[2], and Yaser Abu-Lebdeh[1, Z]

1. Energy, Mining, and Environment Research Centre, National Research Council of Canada, 1200 Montreal Road, Ottawa, Ontario K1A 0R6, Canada
2. Department of Chemical and Biological Engineering, Centre for Catalysis Research and Innovation (CCRI), University of Ottawa, 161 Louis-Pasteur, Ottawa ON, K1N 6N5, Canada

Publication status: published
Adapted from DOI 10.1149/1945-7111/ac00f4

## Abstract

The use of “high-entropy” materials in electrodes is an emerging strategy to improve the stability and electrochemical properties of lithium-ion batteries. This study reports the machine learning-driven discovery of a high-entropy $LiNi_{0.2}Mn_{0.2}Co_{0.2}Fe_{0.2}Ti_{0.2}O_2$ layered oxide cathode. Battery testing reveals a good initial capacity (160 mAh $g^{-1}$) and a stability up to 4.4 V. These materials are a promising way to expand the design space of cathode candidates while using inexpensive transition metals. However, further optimization of these materials is needed to improve battery performance relative to traditional cathodes.

## Introduction

In recent years, entropy stabilization has become an increasingly popular design strategy for lithium-ion battery electrode materials.[1] The use of five or more equimolar components in an alloy or oxide is typically classified as “high-entropy.” This is believed to reduce the transition temperature required for the formation of a single phase and increase the stability of the compound.[2] The approach is expected to expand the design space of possible cathode materials, some of which may have superior electrochemical properties to conventional layered NMC.[1,3] The high-entropy concept has economic implications as well since it may allow cobalt to be replaced with other metals. It has been shown experimentally that high-entropy oxides can be stabilized into a single phase.[2,4] Multicomponent high-entropy oxides have also been stabilized into single phase rock-salt structures by a variety of synthesis techniques at different temperatures.[5] The lithiation properties of $(Co_{0.2}Cu_{0.2}Mg_{0.2}Ni_{0.2}Zn_{0.2})O$ high-entropy oxide was studied at low potential and was shown to have a capacity around 500 mAh $g^{-1}$ at a 0.1 A $g^{-1}$ current rate.[4] The same authors later successfully used this as an anode material in a full cell while using NMC as a cathode.[6] They reported a stable capacity of 300 mAh $g^{-1}$ for 50 cycles. However, the material suffered from a large first-cycle irreversible capacity.[6] High-entropy rock-salt oxyfluorides have also been used as cathode materials for lithium-ion batteries.[3,7] One study reported an initial charge capacity of 161 mAh $g^{-1}$ at C/10, but the material had a large irreversible capacity since the first cycle discharge capacity was 120 mAh $g^{-1}$.[7] Wang et al. successfully synthesized several high-entropy layered oxides; however, they were reported to have a low capacity (~80 mAh $g^{-1}$) and a high capacity fade.[8] Recently, computational work has been reported for high-entropy disordered rock-salt cathodes.[3] Lun et al. calculated the compatibility for 7965 different compounds and reported the mixing temperature of various cation combinations. The mixing temperature is one metric used to predict the synthesizability of a single-phase compound.[3] The authors also reported an electrochemical performance of 170 mAh $g^{-1}$ at a high current rate of 2000 mA $g^{-1}$ for one of their cathodes.[3] This work reports the preparation and characterization of a layered cathode material with an average stoichiometry of $LiNi_{0.2}Mn_{0.2}Co_{0.2}Fe_{0.2}Ti_{0.2}O_2$ (denoted 11111).

## Experimental

A modified Pechini method was used to prepare the 11111 cathode. Precursor salts included $Ni(NO_3)_2 \cdot 6H_2O$ (98%), $Co(NO_3)_2 \cdot 6H_2O$ (98%), $Fe(NO_3)_3 \cdot 9H_2O$ (98%), Titanium-isopropoxide (97%), and $Mn(NO_3)_2 \cdot 4H_2O$ (97%). In a typical process, stoichiometric amounts of metal nitrate salts were dissolved in water, along with a 1:4 molar ratio of citric acid and ethylene glycol. The solution was microwaved (600 W) for 5 min at 90 °C to mix the solution, and then 5 min at 140 °C to complete the polymerization reaction. A dark-black gel was obtained. The gel was first heat treated for 1 h at 180 °C and then calcined for 10 h at 450 °C to decompose the organic matrix. The resulting powder was mixed with $LiNO_3$ (5% excess Li), pelletized, and then calcined in air at 700 °C for 10 h, followed by 850 °C for 15 h. Commercial NMC532 was purchased from MTI.

Electrodes were prepared with an active material of 80 wt%, 5 wt% PVDF binder, 7.5 wt% Super P, and 7.5 wt% KS4 carbon. The slurry was mixed for 15 min at 2000 rpm and then applied to a standard aluminum current collector. The cathode film was dried at 85 °C in a convection oven to evaporate the 1-Methyl-2-pyrrolidinone solvent. 0.5″ diameter disks were cut and vacuum dried at 80 °C overnight. Half cells (with lithium metal) were assembled in an argon-filled glove box. The electrolyte was 1 M $LiPF_6$ in EC: DEC (1:1 v/v). Two Celgard 2500 polypropylene membranes were used as a separator. Coin cells were allowed to rest for at least 12 h before testing. Galvanostatic battery cycling was done at 30 °C in an Arbin BT2000 battery cycler in the potential range between 2.5 V to 4.4 V. A 15-min open-circuit rest was included at each potential limit. The batteries were charged/discharged symmetrically at C/20 for 2 cycles, followed by 50 cycles at C/10 unless otherwise stated. A theoretical capacity of 155 mAh $g^{-1}$ was used to calculate the C-rates. X-Ray Diffraction (XRD) was done with a Bruker AXS D8 diffractometer (Cu Kα, $\lambda$ = 0.154 nm). Scanning Electron Microscopy (SEM) was used to characterize the cathode morphology. Inductively Coupled Plasma-Optical Emission Spectrometry (ICP-OES) was used to determine the experimental mass fractions of the metals in the cathode powder.

## Results and Discussion

Early work consisted of identifying transition metals that would be suitable to include in a high-entropy modification to the NMC layered oxide (i.e. $LiNi_{0.2}Mn_{0.2}Co_{0.2}X_{0.2}Y_{0.2}O_2$). The transition metal candidates for X and Y were selected based on their compatibility and economical considerations such as abundance and low cost. Machine learning was also used to identify correlations between metal pairs and energy density. First, data on more than two thousand battery materials were collected from the MaterialsProject database using the Pymatgen Python package.[9] Relevant parameters from the database were then extracted and featurized using the Matminer Python package. Finally, a random forest regression algorithm in the SciKit-Learn package was used to train the model and identify correlations between the features and the energy density. Figure 4.1 shows the energy map for various combinations of metals in equimolar proportion. Combinations selected for experiments are outlined in green. Samples with chrome or copper did not yield a single phase or had poor electrochemical performance. This communication focuses on the results of high-entropy cathodes with the combination of Ti and Fe (green arrow in Figure 4.1) since these samples had minimal impurities and had good electrochemical performance. These cathodes were calcined at 850 °C. Higher temperature calcination (850 °C vs

700 °C) was consistently observed to increase crystallinity and the features of the diffraction peaks, as well as reduce impurities. This trend has also been recently reported in the literature for cathodes synthesized via the Pechini method. Higher temperature calcination was shown to increase the particle size and crystallinity of the sample, as well as improve the electrochemical performance.[10]

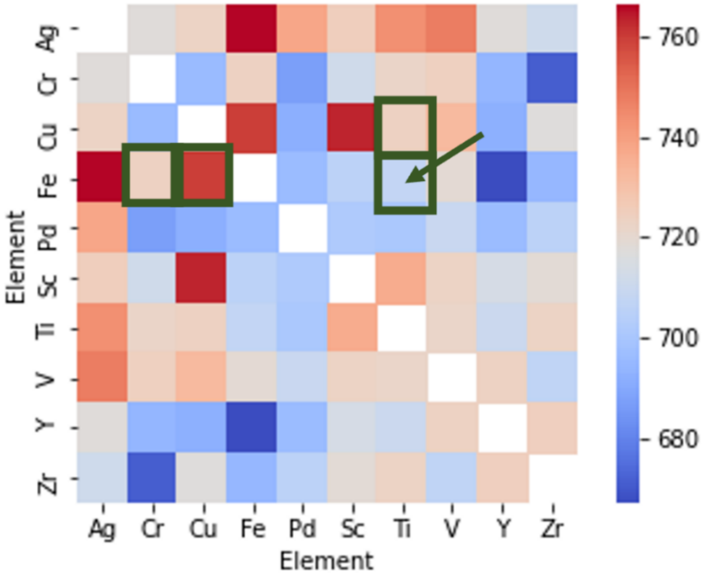

Figure 4.1. Map of estimated material energy density (Wh/kg) for different metal pairs assuming equimolar composition with Ni, Co, and Mn.

The XRD plot of Figure 4.2 shows the diffraction pattern for the 11111 cathode. The pattern is consistent with the desired R-3m layered structure, although the intensity is comparatively lower than commercial NMC. Nevertheless the relatively high intensity ratio $I_{003}/I_{104}$ suggests a low degree of cation mixing, and the clear splitting of the (108)/(110) peaks around 65° suggests a well-defined layered structure.[11,12] The splitting in the (104) peak is believed to be traces of a secondary phase.[11] Figure 4.2b shows the mass fractions for the 11111 cathode. The reported values are consistent with the expected theoretical mass fractions. SEM of the raw cathode powder is shown in Figure 4.2c and reveals the size of most particles to be below 2 µm. The pelletization of the cathode and the higher temperature synthesis resulted in a larger particle size compared to other cathodes prepared with the Pechini method (<250 nm). However, the particle size of this high-entropy cathode is still smaller than cathodes prepared via co-precipitation, where the particle size can be around 10 µm. The relatively small particle size of this 11111 cathode is also responsible for the lower reflection intensity in the XRD plot.

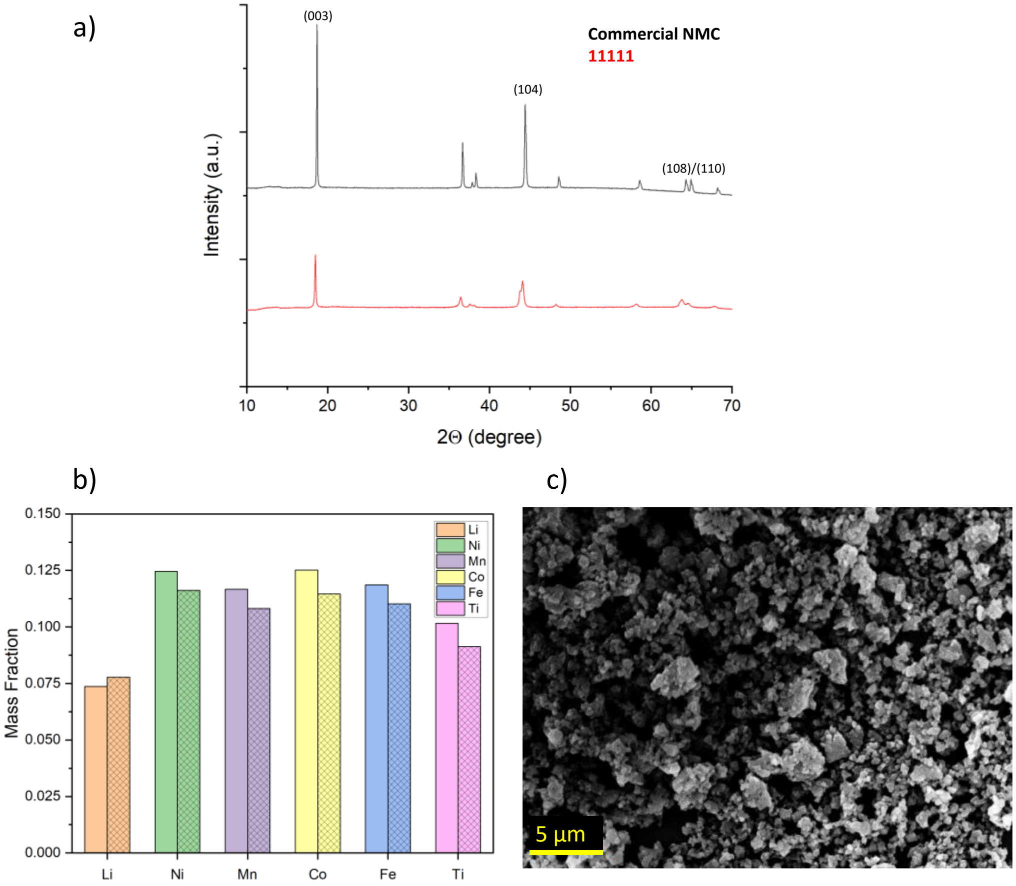

Figure 4.2. (a) XRD plot of the 11111 cathode and a commercial NMC532 baseline, (b) theoretical (solid bars) and experimental (textured bars) mass fractions and (c) SEM image of the 11111 cathode.

Figure 4.3 plots the active material charge capacity as a function of cycle number for the 11111 cathode. The first cycle capacity is consistent with typical layered cathodes. However, a large irreversible capacity was seen during the first cycle. The high-entropy sample had an initial capacity over 160 mAh $g^{-1}$ and a stable capacity of 85 mAh $g^{-1}$. The potential profile and dQ/dV plots for the 11111 cathode are seen in Figures 4.3b and c, respectively. The dQ/dV plot has a single redox peak around 4 V and may be a unique signature of the high-entropy material since a high potential has also been reported for other high-entropy layered oxides.[8] This should be contrasted with the redox peaks typically seen at lower potential in NMC cathodes (~3.7 V).

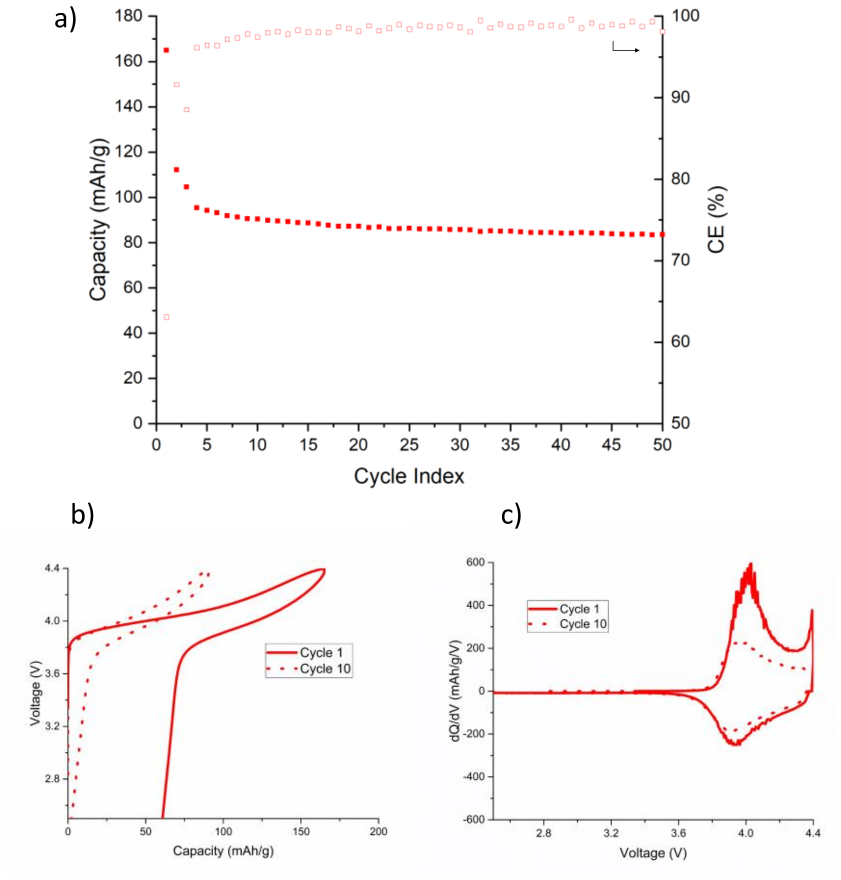

Figure 4.3. (a) Cycling data for the 11111 cathode charged to 4.4 V, (b) potential profile plots and (c) dQ/dV plots for the same coin cell.

The 11111 cathode was also cycled in an extended potential range from 1.2 V to 4.4 V. This lower potential is known to overlithiate NMC cathodes and is associated with the formation of a SEI.[13–15] Figure 4.4a shows the cycling data for the 11111 cathode and an NMC baseline. The high-entropy cathode shows a sustained capacity around 150 mAh $g^{-1}$, whereas the NMC baseline fails rapidly in this potential range. The dQ/dV plot of Figure 4.4b shows greater charge redox activity after 15 cycles compared to the cell in Figure 4.3c after only 10 cycles. The results suggest the high-entropy material may accommodate overlithiation better than traditional cathodes. At this time, these high-entropy cathodes do not have better capacity retention than conventional layered oxides. Further optimization of the synthesis conditions and careful selection of transition metal candidates is required to improve phase stability and the electrochemical performance of these cathodes.

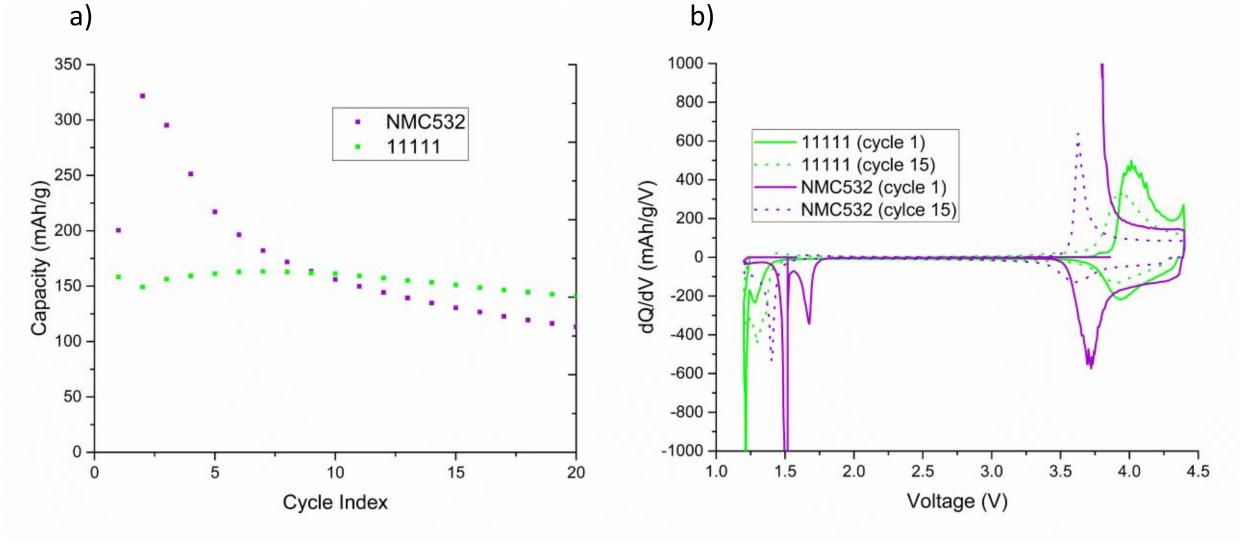

Figure 4.4. (a) Cycling data for extended potential range (1.2 V to 4.4 V) and (b) associated dQ/dV plot. Note: all cycles in this figure are cycled at C/10.

## Conclusions

This work used a data-driven approach to identify high-entropy cathode candidates for lithium-ion batteries. The best cathode $LiNi_{0.2}Mn_{0.2}Co_{0.2}Fe_{0.2}Ti_{0.2}O_2$ was prepared using a simple sol-gel technique and calcined in air. It was found the high-entropy sample provided an initial capacity of 160 mAh $g^{-1}$ and a stable capacity of 85 mAh $g^{-1}$ when charged to a high voltage of 4.4 V. This study highlights the potential of combining machine learning with entropy stabilization to design new cathodes that use inexpensive metals not typically included in layered cathodes. However, further optimization of these materials is needed to increase their reversible capacity relative to traditional cathodes.

## Acknowledgments

We would like to thank the Office of Energy Research and Development (OERD) at Natural Resources Canada for financial support. Special thanks to Shuo Yan for her help with SEM.

## Recent Developments

Later preparations of this 11111 cathode at different calcination temperatures were able to improve phase purity as marked by a reduction in the splitting of the 104 peak. However, these cathodes had similar or inferior cycling performance to the cathode reported in this chapter.

Since the publication of the work in Chapter 4, other research groups have revealed important insight into the failure mechanism of these high-entropy layered cathodes. Zheng et al studied $LiNi_{0.2}Co_{0.2}Mn_{0.2}Fe_{0.2}Al_{0.2}O_2$ with XPS and HAADF/ADF-STEM.[16] The authors revealed the formation of a $M_3O_4$ spinel phase at the surface of the layered cathode after the first delithiation. This phase blocks future lithiation and results in rapid capacity decline of the cathode. What is still unclear is how expanding the voltage range (1.2 V to 4.4 V) improved capacity retention.

## References

[1] A. Sarkar *et al.*, “High-Entropy Oxides: Fundamental Aspects and Electrochemical Properties,” *Advanced Materials*, vol. 31, no. 26, 2019, doi: 10.1002/adma.201806236.

[2] C. M. Rost *et al.*, “Entropy-stabilized oxides,” *Nat Commun*, vol. 6, 2015, doi: 10.1038/ncomms9485.

[3] Z. Lun *et al.*, “Cation-disordered rocksalt-type high-entropy cathodes for Li-ion batteries,” *Nat Mater*, 2020, doi: 10.1038/s41563-020-00816-0.

[4] A. Sarkar *et al.*, “High entropy oxides for reversible energy storage,” *Nat Commun*, vol. 9, no. 1, 2018, doi: 10.1038/s41467-018-05774-5.

[5] A. Sarkar *et al.*, “Nanocrystalline multicomponent entropy stabilised transition metal oxides,” *J Eur Ceram Soc*, vol. 37, no. 2, pp. 747–754, 2017, doi: 10.1016/j.jeurceramsoc.2016.09.018.

[6] Q. Wang *et al.*, “High entropy oxides as anode material for Li-ion battery applications: A practical approach,” *Electrochem commun*, vol. 100, no. January, pp. 121–125, 2019, doi: 10.1016/j.elecom.2019.02.001.

[7] Q. Wang *et al.*, “Multi-anionic and -cationic compounds: New high entropy materials for advanced Li-ion batteries,” *Energy Environ Sci*, vol. 12, no. 8, pp. 2433–2442, 2019, doi: 10.1039/c9ee00368a.

[8] J. Wang *et al.*, “Lithium containing layered high entropy oxide structures,” *Sci Rep*, vol. 10, no. 1, pp. 1–13, 2020, doi: 10.1038/s41598-020-75134-1.

[9] A. Jain *et al.*, “Commentary: The materials project: A materials genome approach to accelerating materials innovation,” *APL Mater*, vol. 1, no. 1, 2013, doi: 10.1063/1.4812323.

[10] M. Kunduraci, R. N. Mutlu, and A. M. Gizir, “Electrochemical behavior of LiNi0.6Mn0.2Co0.2O2 cathode in different aqueous electrolytes,” *Ionics (Kiel)*, vol. 26, no. 4, pp. 1663–1672, 2020, doi: 10.1007/s11581-020-03490-z.

[11] Y. S. Meng, Y. W. Wu, B. J. Hwang, Y. Li, and G. Ceder, “Combining Ab Initio Computation with Experiments for Designing New Electrode Materials for Advanced Lithium Batteries: LiNi[sub 1/3]Fe[sub 1/6]Co[sub 1/6]Mn[sub 1/3]O[sub 2],” *J Electrochem Soc*, vol. 151, no. 8, p. A1134, 2004, doi: 10.1149/1.1765032.

[12] P. Kalyani and N. Kalaiselvi, “Various aspects of LiNiO2 chemistry: A review,” *Sci Technol Adv Mater*, vol. 6, no. 6, pp. 689–703, 2005, doi: 10.1016/j.stam.2005.06.001.

[13] C. Usubelli *et al.*, “ Understanding the Overlithiation Properties of LiNi 0.6 Mn 0.2 Co 0.2 O 2 Using Electrochemistry and Depth-Resolved X-ray Absorption Spectroscopy ,” *J Electrochem Soc*, vol. 167, no. 8, p. 080514, 2020, doi: 10.1149/1945-7111/ab8a9d.

[14] Z. Wu *et al.*, “Prelithiation Activates Li(Ni0.5Mn0.3Co0.2)O2 for High Capacity and Excellent Cycling Stability,” *Nano Lett*, vol. 15, no. 8, pp. 5590–5596, 2015, doi: 10.1021/acs.nanolett.5b02246.

[15] Z. Wu *et al.*, “Pre-Lithiation of Li(Ni1-x-yMnxCoy)O2 Materials Enabling Enhancement of Performance for Li-Ion Battery,” *ACS Appl Mater Interfaces*, vol. 8, no. 24, pp. 15361–15368, 2016, doi: 10.1021/acsami.6b03730.

[16] Q. Zheng *et al.*, “Surface Phase Conversion in a High-Entropy Layered Oxide Cathode Material,” *ACS Appl Mater Interfaces*, vol. 15, no. 3, pp. 4643–4651, Jan. 2023, doi: 10.1021/acsami.2c16194.

# Chapter 5: Small Molecule Azaacene as an Anode Material for Lithium-ion Batteries

James W. Sturman[1,2,3], Eloi Grignon[4], Bryony T. McAllister[4], Chae-Ho Yim[3], Elena A. Baranova[1,2], Dwight S. Seferos[4] * and Yaser Abu-Lebdeh[3]*

1. Department of Chemical and Biological Engineering, Centre for Catalysis Research and Innovation (CCRI), University of Ottawa, 161 Louis-Pasteur, Ottawa ON, K1N 6N5, Canada
2. Nexus for Quantum Technologies (NexQT), University of Ottawa, Ottawa, Ontario, K1N 6N5, Canada
3. Energy, Mining, and Environment Research Centre, National Research Council of Canada, 1200 Montreal Road, Ottawa, Ontario K1A 0R6, Canada
4. Department of Chemistry, University of Toronto, Lash Miller Chemical Labs, 80 St. George Street, Toronto, Ontario M5S 2H6, Canada

Publication status: published

Adapted from DOI 10.1021/acs.energyfuels.3c01366

## Abstract

In recent years, organic electrodes have attracted much attention owing to their unique properties including low density, flexibility, and in certain cases ultra-high capacity. In this contribution, we report the synthesis of a novel small molecule azaacene (SmAz) and reveal its electrochemical performance as an anode material in Li-ion batteries. SmAz delivers a reversible capacity of around 550 mAh $g^{-1}$ at 50 mA $g^{-1}$, a value that exceeds its theoretical capacity (237 mAh $g^{-1}$). Moreover, SmAz displays an activation process in which the capacity increases with cycle time. Operando XRD suggests SmAz becomes amorphous during cycling. Greater insight into the charge storage mechanism is revealed with impedance and cyclic voltammetry and suggests the organic anode is controlled by a mixture of ion-diffusion and pseudocapacitive processes. Overall, these results reveal a new mechanistic understanding of the electrochemical behaviour in organic electrodes, as well as design features for their continued development.

## Introduction

Organic electrodes for metal-ion batteries have attracted significant research in recent years. Relative to inorganic materials, organic molecules are flexible, can be synthesized through benign low-energy and low-cost processes, and their redox ability is independent of the counter-ion, enabling their use in both Li-ion and post-Li-ion batteries.[1–6] Importantly, organic electrode materials do not contain any scarce elements, thus providing a sustainable source of energy storage that is not susceptible to supply chain issues arising from fluctuating costs or geopolitical factors.[7] Many organic cathodes can now provide a high gravimetric energy density as well as adequate cycling life, which opens the door for their application in settings where volume is not a constraint.[2] Although the majority of organic battery research is directed towards cathode materials, the development of anodes with a high energy density is also a pressing concern.[8] Recently, organic anodes displaying *superlithiation* and ultra-high capacities have emerged as an interesting class of materials.[9–16] Briefly, the superlithiation phenomenon consists of the reduction of an organic $sp^2$ framework at a voltage below 1 V vs $Li/Li^+$ such that the material uptakes many more metal ions than would be expected based on redox-active groups alone.[10, 11, 14] This was first demonstrated for $Li^+$, where 1 ion could be inserted per carbon atom, but has since been shown to also occur for $Na^+$ and $K^+$, where ionic uptake is reduced according to the size of the cation.[17–19] The 1:1 Li:C lithiation ratio of these anodes is much higher than the 1:6 observed in graphite, the traditional anode material in commercial cells.

The list of superlithiation materials spans a breadth of architectures (small molecules, polymers, frameworks) and functionalities (carboxylates, imides, imines, etc.). The first report of this phenomenon was for a small crystalline molecule, 1,4,5,8-naphthalenetetracarboxylic dianhydride, which was found to reversibly store 18 Li-ions, thereby reaching an ultra-high capacity of 1804 mAh $g^{-1}$.[19] The authors posited that the polar ends of the anhydride facilitated lithium insertion into the material. Later, other small molecule organic anodes from the well-established carboxylate family were shown to exhibit similar behavior. For instance, the conjugated structure of dilithium benzenedipropiolate, which includes sp-hybridized carbons, could be reversibly reduced to obtain superlithiation capacities of 1363 mAh $g^{-1}$.[12] Interestingly, the reduction of the triple bond in this material seems to be a precondition for superlithiation, which explains why certain carboxylates cannot reach these high capacities. Other carboxylates, such as lithium maleate[20] and dilithium thiophene-2,5-dicarboxylate[21] have also shown superlithiation behaviour, reaching 1500 mAh $g^{-1}$ and 1143 mAh $g^{-1}$, respectively.

Beyond carboxylates, both small molecule and polymeric N-containing anodes have been widely studied as superlithiation materials. In a well-known example, a conjugated azaacene-containing ladder polymer provided a remarkable discharge capacity of 1750 mAh $g^{-1}$ at 0.05C.[10] The authors of this work proposed that the backbone nitrogen atoms lowered the energetic penalty of lithium insertion, thus allowing for superlithiation. This led to the development of additional azaacene superlithiation materials[11], including the subject of this work. More recently, superlithiation has been reported in networks comprising triazines[16, 22], naphthalimides[23], and aramids [24], thus showing the diversity of structures that can lead to ultra-high capacities.

Ultra-high capacities have also been observed with other carbonaceous materials like hard carbons, porous nitrogen-containing carbons, and graphene. While these carbonaceous materials are structurally different from organic electrodes, their lithiation mechanism may be similar. Hard carbons are a form of non-graphitizable carbon with a higher capacity than graphite.[25] The Li storage mechanism in hard carbons is still the subject of research but is typically believed to involve a combination of Li adsorption, intercalation, and pore-filling.[25–27] Nitrogen-containing mesoporous carbons have been reported to have ultra-high capacities when used as anode materials for Li-ion batteries. The electrodes are typically prepared from nitrogen-containing biomass (such as egg proteins), the pyrolysis of coal tar in the presence of melamine or ammonia, or the pyrolysis of nitrogen-containing organic compounds like polyacrylonitrile and polypyrrole.[28, 29] Moreover, DFT calculations studying Li adsorption on graphene have found that certain defects (in particular edges and pyridinic defects) can increase reversible capacity compared to pristine graphene.[30, 31]

In the current contribution, we investigate a crystalline small molecule azaacene, SmAz, and report its electrochemical behaviour. SmAz was selected because it is conjugated and contains nitrogen heteroatoms, properties which are known to increase lithiation in organic anodes. SmAz displays a high specific capacity reaching up to 650 mAh $g^{-1}$ with constant current cycling, which is far superior to its theoretical capacity of 237 mAh $g^{-1}$. We use operando XRD, impedance spectroscopy, and cyclic voltammetry to show that SmAz undergoes amorphization during lithiation and is controlled by both ion-diffusion and pseudocapacitance at high voltage. Schematic 5.1 illustrates the two proposed mechanisms.

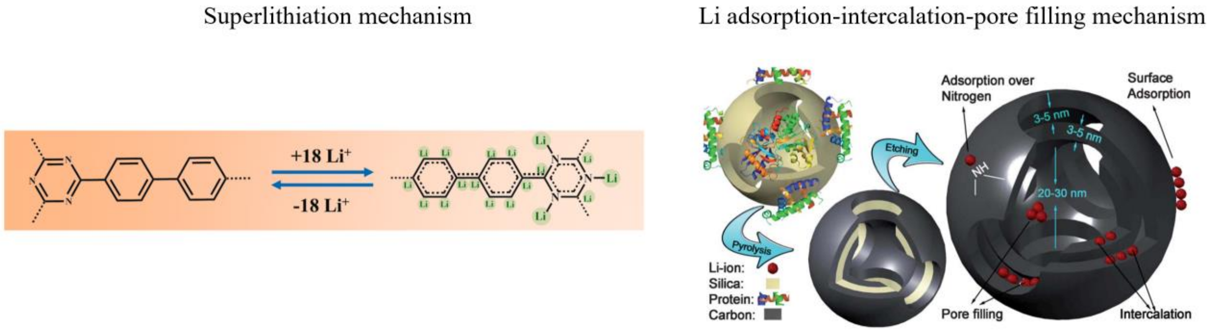

Schematic 5.1. Overview of different mechanisms for highly lithiated nitrogen-containing carbons.[15, 29]

## Experimental

Synthesis and advanced characterization of SmAz is discussed in the supporting information. Electrodes were prepared as a slurry of 40 wt% active material (either SmAz or its polymeric equivalent: P3), 50 wt% Super P conductive carbon (Timcal), and 10 wt% PVDF binder. The mixture was suspended in N-methyl-2-pyrrolidone (NMP) (120 mg/mL) and sonicated until free of agglomerates for 1-1.5 hour, with stirring every 15 minutes. The slurry was applied to an acetone-cleaned copper foil (20 µm thickness) using a 250 µm gap notch bar. The casts were then dried in a convection oven at 85 °C and then cut into 12.7 mm diameter disks, which were then vacuum dried at 80 °C overnight. Half-cell batteries with lithium metal (voltage vs. $Li/Li^+$) were prepared in an argon-filled glove box using 2325 type coin cells, 74.8 µL of electrolyte, and two 2500 Celgard polypropylene membranes. The electrolyte was 1M $LiPF_6$ in ethylene carbonate and diethyl carbonate EC:DEC (1:1 v/v) (Sigma Aldrich). All coin cells were allowed to rest at least 24 hours and were then cycled at 30 °C in an Arbin BT2000 battery cycler. All batteries were cycled between 0.005 V and 3.0 V at a 50 mA $g^{-1}$ constant current unless otherwise specified. A 15-minute open circuit rest was included at each voltage limit. Capacities and current densities were calculated based on the mass of active material (SmAz or P3).

The X-Ray Diffraction (XRD) was carried out with a Bruker AXS D8 diffractometer (Cu Kα, λ=0.154 nm) between 10° and 85° 2θ. Electrochemical Impedance Spectroscopy (EIS) was conducted in a 2-electrode configuration with a BioLogic potentiostat in the frequency range from 100 kHz to 10 mHz. Cyclic voltammetry (CV) was performed six times at each scan rate (0.2 to 1 mV/s) on the Biologic potentiostat in the voltage range of 0.005 to 3.0 V. Only the last cycle at each scan rate was taken for analysis.

A Bruker Operando cell with a beryllium (Be) window was used for Operando XRD. The Be window had a diameter of 29 mm and a thickness of 270 µm. The 40 wt% SmAz slurry in NMP was deposited on the interior side of the Be window and dried at 85 °C to evaporate the solvent, followed by 80 °C vacuum drying overnight. The Bruker Operando cell was then assembled in an argon-filled glove box with a Li metal foil, two 2500 Celgard membrane separators, and 112 µL of the aforementioned electrolyte. The cell was allowed to rest at least 24 hours before cycling at a current of 50 mA $g^{-1}$. XRD scans were taken every 2 hours during discharging and charging.

NMR spectra were recorded using a 400 MHz Bruker Avance III or a 500 MHz Agilent DD2 NMR spectrometer equipped with a $^{13}$C-sensitive cryogenically cooled probe and referenced to the residual solvent peak (DMSO or TFA). Mass spectrometry was performed using a JOEL AccuTOF JMS-T1000LC mass spectrometer equipped with a direct analysis in real-time (DART) ion source. Fourier Transform Infrared Spectroscopy (FTIR) measurements were taken on a Thermo Scientific iS50 equipped with an ATR accessory.

## Results and Discussion

The synthesis of the small molecule azaacene was similar to that of the previously reported P3 (Figure 5.1).[11] First, pyrene tetraone (PT) was obtained through the Ru-catalyzed oxidation of pyrene. Then, nitration of PT at the 2- position afforded PT-$NO_2$ in 91% yield. Finally, PT-$NO_2$ was condensed with *o*-phenylenediamine endcaps to yield the conjugated small molecule azaacene SmAz in 95% yield.[17] Following an extensive screening process, we found that SmAz was insoluble in nearly all organic solvents except trifluoroacetic acid (TFA), where it exhibited partial solubility. Taking advantage of this property, we were able to obtain an $^1$H NMR spectrum of the product (Figure S5.5), thus confirming its structure and its purity. The ability to accurately characterize SmAz distinguishes it from P3 and many other superlithiation materials, where insolubility precludes solution characterization. SmAz was also analyzed through FTIR spectroscopy (Figure S5.8). Here, a signal at 3089 $cm^{-1}$ belongs to the $sp^2$ C-H stretch, a signal at 1476 $cm^{-1}$ belongs to the aromatic C=C stretch, and signals at 1512 $cm^{-1}$ and 1341 $cm^{-1}$ belong to the nitro group. Importantly, the C=O stretch at 1672 $cm^{-1}$ of PT and PT-$NO_2$ is absent from the spectrum of SmAz, thus further confirming the purity of the final azaacene product.

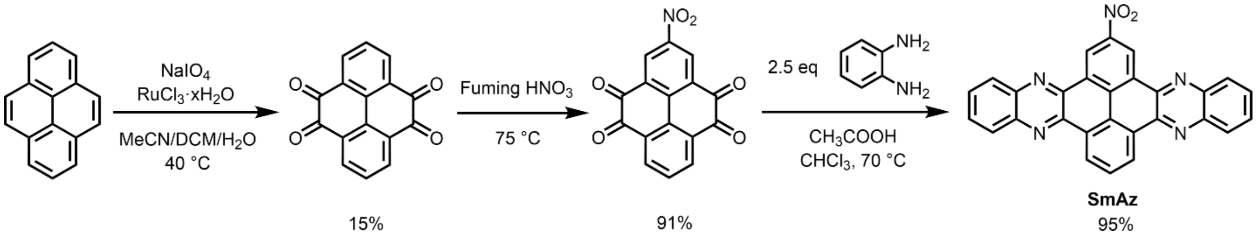

Figure 5.1. Reaction scheme for the synthesis of SmAz.

Figure 5.2a plots the capacity of SmAz and P3 based anodes cycled at 50 mA $g^{-1}$. The very high first discharge capacity is attributed primarily to irreversible side reactions and SEI formation since SmAz's first cycle coulombic efficiency (CE) was 30%. A high first cycle irreversible capacity has also been reported with other organic anodes and mesoporous N-rich carbons.[10, 28] In addition, the high surface area Super P conductive additive will also contribute to irreversible side reactions. As such, the discharge capacity of 550 mAh $g^{-1}$ on the 10th cycle is a more accurate reflection of SmAz's reversible capacity. This capacity exceeds SmAz's theoretical capacity of 237 mAh $g^{-1}$ (assuming one $Li^+$ per aromatic nitrogen).[11] The polymer equivalent P3 also had a very high first cycle irreversible capacity. However, P3's 10th cycle discharge capacity of 375 mAh $g^{-1}$ is significantly lower than SmAz.

Both electrodes displayed an activation process whereby the capacity increases with cycle number. Such an activation process has been reported extensively in the literature for carbon-based anodes. The activation process is generally attributed to gradual penetration of the electrolyte into the electrode resulting in more exposed redox-active sites (including surface pseudocapacitance), material amorphization, and reversible SEI formation and decomposition.[10, 11] In addition, highly porous nitrogen-containing carbons are believed to store Li on defect sites in addition to Li adsorption and pore filling.[29] SmAz had a clear activation period of around 40 cycles of steady capacity increase, after which the capacity plateaued around 650 mAh $g^{-1}$ and subsequently declined. Throughout this activation period, SmAz had a relatively low CE around 96%. Such a low CE is consistent with excessive electrode-electrolyte side reactions (i.e., unstable SEI) and has been observed with certain mesoporous carbons, organic anodes, and silicon.[29]

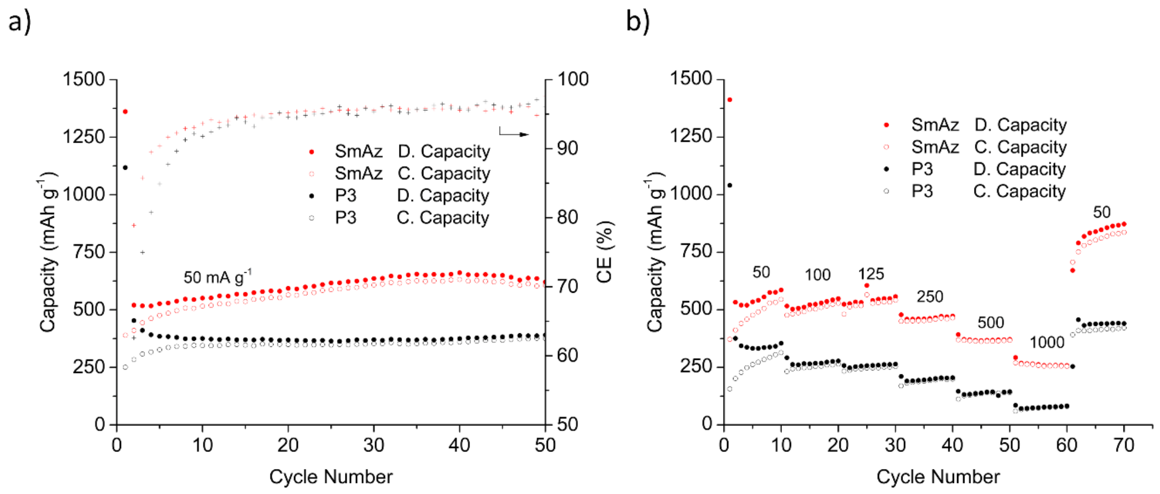

Figure 5.2. a) 50 cycles of constant-current cycling and b) rate capability test on SmAz and P3 based electrodes. It should be noted that the weighted capacity contribution of Super P (~260 mAh g$^{-1}$ at 50 mA g$^{-1}$) has been subtracted from the total capacity. A rendition of Figure 5.2b without this subtraction can be found in Figure S5.9. All current densities in mA g$^{-1}$. Cells were cycled between 0.005 V and 3.0 V.

Further rate capability tests in Figure 5.2b were conducted at current densities from 50 mA g$^{-1}$ to 1000 mA g$^{-1}$ to compare the small molecule SmAz with the polymer P3. The activation process was sustained for the P3 polymer at all current densities. However, it was not seen with the small molecule SmAz above 500 mA g$^{-1}$, as marked by a decline in capacity retention at 1000 mA g$^{-1}$. After the rate capability test, there was a capacity recovery above 400 mAh g$^{-1}$ with the P3 polymer and above 800 mAh g$^{-1}$ with SmAz. Voltage profile and differential capacitance plots in Figure 5.3 reveal a significant difference in the lithiation mechanism between SmAz and P3. Figure 5.3a reveals a sloping charge/discharge curve for the P3 electrode (without any clear redox activity above 1 V), as has been described elsewhere.[11] In contrast, the SmAz electrode has a reversible redox peak, seen around 1.0 V during discharge (lithiation) and 1.1 V during charge (delithiation). More subtle broad peaks are seen around 0.34 V (during lithiation) and 0.42 V (during delithiation). This would suggest SmAz has a significant diffusion-controlled contribution to the capacity and explains SmAz's poor performance at high current densities. However, at cycle 50 (Figure 5.3d), the redox peaks disappear, which suggests that the reaction around 1 V is not solely responsible for the high capacity observed with SmAz.

The observed redox peaks around 1 V may be attributed to lithium reactions with SmAz's four nitrogen sites, aromatic carbons, or possible complex reactions between SmAz, the binder, and the Super P.[9–12, 14, 32] The redox peaks cannot be attributed solely to the PVDF binder and Super P, as seen by the absence of notable peaks in the dQ/dV plot (blank cell in Figure S5.10). Previous studies on similar nitrogen-containing organic electrodes have attributed redox couples between 1.0 V and 1.5 V to lithium interactions with nitrogen sites.[10, 13, 14, 33] In contrast, superlithiation (lithiation of aromatic carbons) has been reported to occur in a lower voltage region (~0.1V) and has been associated with a sloping voltage profile (i.e., absence of clear plateaus).[10–12, 14, 34] However, a sloping voltage profile in the low voltage region has also been observed with other carbonaceous anodes (such as mesoporous and hard carbons); in these materials, the lithiation mechanism is often described as a combination of Li adsorption and intercalation.[25–27] It should also be noted that carbonaceous anodes are known to experience a very large first cycle irreversible capacity due to electrolyte reactions and SEI formation, which can also be associated with a sloped voltage profile.[14, 33]

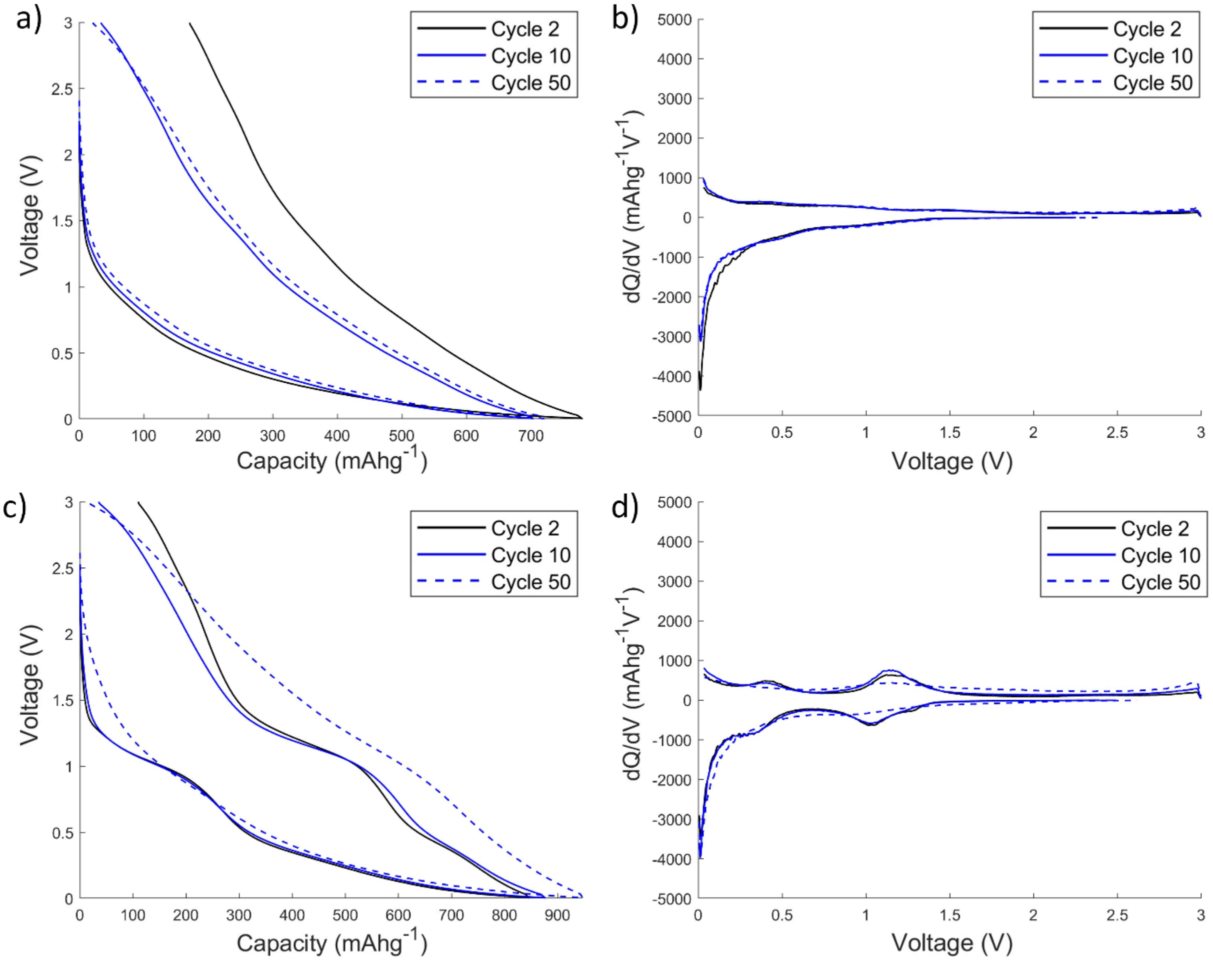

Figure 5.3. a) Voltage profile and b) differential capacitance plots for P3-based electrode. c) Voltage profile and d) differential capacitance plots for SmAz-based electrode. As capacity is a function of voltage, the Super P capacity

contribution has not been subtracted. The first cycle has been omitted to focus only on reversible redox processes. All cycles at a 50 mA $g^{-1}$ current density. Consult Figure S5.11 to see the irreversible peaks during the first cycle.

Many publications that report superlithiation or ultra-high capacities for carbon-based anodes (organic, hard carbon, or mesoporous carbons) cycle their cells to an upper voltage of 3.0 V or higher.[11–13, 25, 26, 28, 29, 32, 35] This is typically done to increase the reported capacity of the anode. However, the extent to which the upper cut-off voltage is responsible for the reported high capacity is often not discussed. Figure 5.4 plots the long-term cycling of SmAz-based electrodes in two voltage ranges. When charged to 3.0 V, SmAz delivered a discharge capacity of 550 mAh $g^{-1}$ within 10 cycles at 50 mA $g^{-1}$. Cycling at a higher current density of 500 mA $g^{-1}$ initially reduced the capacity to 350 mAh $g^{-1}$ (similar to Figure 5.2b), but the activation process was sustained for over 40 cycles. There was a low CE of ~98% throughout the fast-charging at 500 mA $g^{-1}$. Such a low CE is consistent with an unstable SEI. SmAz attained a maximum capacity around 460 mAh $g^{-1}$ and then declined to a final capacity of 375 mAh $g^{-1}$ after 200 cycles. Thus, regardless of current density, while the upper voltage was 3.0 V, SmAz displayed an ultra-high capacity above its theoretical 237 mAh $g^{-1}$.

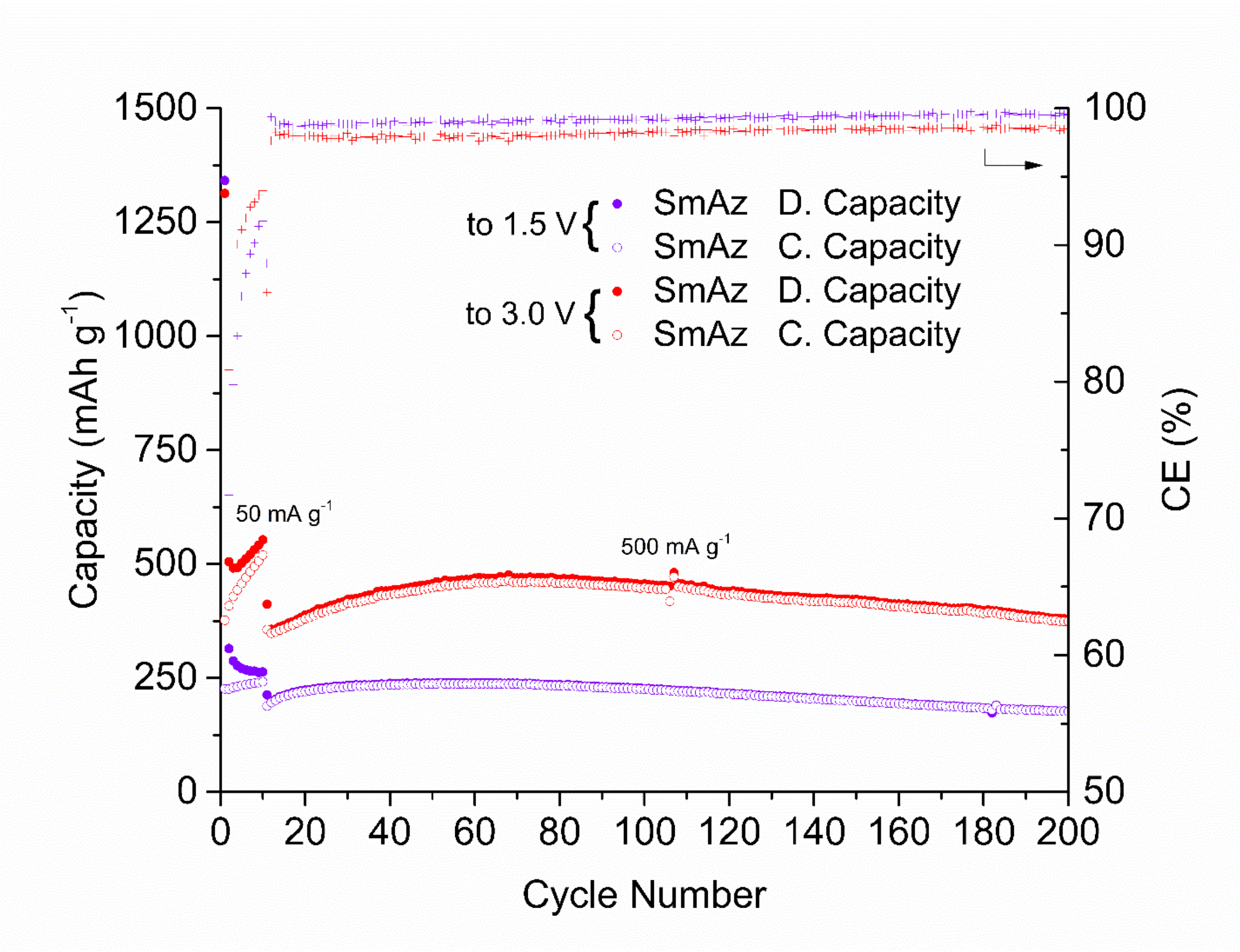

Figure 5.4. Long-term cycling of SmAz-based electrodes in two voltage ranges. The Super P capacity contribution has been subtracted.

In contrast, when SmAz was charged to only 1.5 V, it delivered a lower discharge capacity of 265 mAh g$^{-1}$ at 50 mA g$^{-1}$. This value is much closer to the theoretical capacity of SmAz (albeit slightly higher due to SEI formation and electrolyte side-reactions). Moreover, the activation process was also suppressed in the lower voltage range. The cell charged to 3.0 V had a 21% increase in capacity (from 383 to 465 mAh g$^{-1}$) between cycle 20 and cycle 60. In contrast, the cell charged to 1.5 V increased by only 7% (from 222 to 238 mAh g$^{-1}$) within the same cycle range. In addition, it had a more stable CE above 99% throughout the fast-charging at 500 mA g$^{-1}$. Therefore, SmAz's ability to deliver ultra-high capacity and its activation property are greatly dependent on the voltage window. This result is surprising since superlithiation (involving the reduction of sp$^2$ framework) is reported to occur at low voltage significantly below 1.0 V. Thus, restricting the upper cut-off voltage from 3.0 to 1.5 V should not be expected to significantly affect the material's ability to deliver an ultra-high capacity.

EIS and CV experiments were carried out to elucidate the voltage-dependent nature of SmAz's electrochemical properties. In situ EIS tests in Figure 5.5 were performed on the SmAz anode between 5 mV and 3.0 V during discharge and charge. Two features were notable: a large interfacial resistance at low voltage, and a greater pseudocapacitive contribution at high voltage. Impedance in Li-ion batteries typically consists of bulk resistance, interfacial resistance, charge-transfer resistance, and Warburg diffusion.[36–38] However, in many experimental settings these contributions are not individually distinguishable.[36]

At a voltage above 0.75 V, the total resistance was ~100 Ω, which consists of both interfacial and charge-transfer resistance as seen by the overlapping semi-circles. When the cell was discharged to 5 mV (red), two distinct semi-circles became prominent. The first semicircle in the high-medium frequency range is attributed to interfacial resistance (SEI), whereas the second semicircle in the medium-low frequency range is attributed to charge transfer resistance.[37–39] At 5mV, the resistance from SEI (~300 Ω) is greater than the total resistance seen at voltages between 0.75 – 3 V (~100 Ω). This is consistent with a change in the conductivity of the SEI during lithiation down to 5mV.[39] This observation is consistent with other impedance studies on carbon anodes while using a 2-electrode configuration.[39] Changes in SEI conductivity or growth may explain the increase in capacity seen with SmAz. For example, certain anodes (typically metal oxides) have been reported to display the property of increasing capacity with cycle time.[40, 41] In these materials, the increase in capacity is generally attributed to the formation of a polymeric gel-like film. [40, 41] In one study working with the $Cu_2Se$ anode, the reversible growth of a polymeric film was identified as the cause of capacity increase and was also associated with an increase in SEI and CT-derived impedance at low voltage.[42] However, the property of high impedance at low voltage has been observed in other anodes like graphite, where it has been attributed to electrode expansion during lithiation.[43]

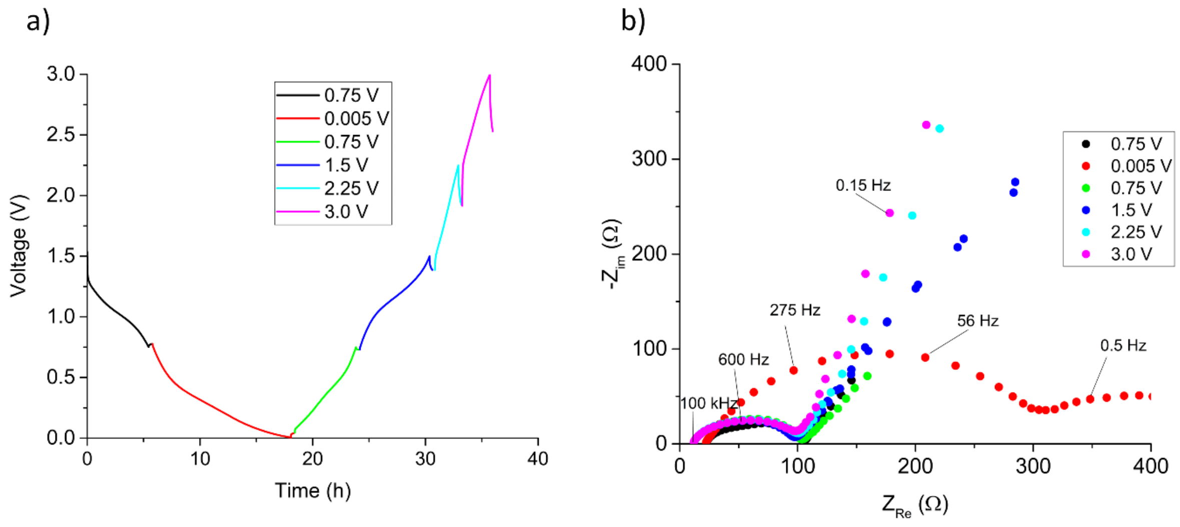

Figure 5.5. Impedance of a SmAz-based electrode at different voltage limits during cycling. a) Voltage vs time profile, and b) associated Nyquist plots for impedance measurements taken after a 15-minute rest at each voltage limit. Impedance in Figure 5.5 was conducted after 10 cycles, as such, an SEI is already assumed to have formed.

The angle between the real axis and the linear impedance in the low-frequency range can be described by a constant phase element (CPE) and used as an indicator of ion-diffusion or capacitive behaviour. The constant phase element is modeled by the following equation: $Z_{CPE}=1/Q(j2\pi f)^{\alpha}$. Where Q is a constant, j is the imaginary unit, f is the frequency, and $\alpha$ is a dimensionless parameter.[38, 44] In the special case where $\alpha=0.5$, the angle becomes 45° and describes Warburg impedance for diffusion.[38] An $\alpha=1$ results in an angle of 90° and represents an ideal capacitor.[37, 38] In Figure 5.5b, a greater angle was determined at higher voltage (73° at 3.0 V) compared to lower voltage (49° at 0.75 V), which suggests a greater pseudocapacitive contribution at the higher voltage range. The pseudocapacitive behaviour of SmAz was further analyzed with CV at different scan rates. The relationship between peak current (i) and the scan rate (v) can be expressed as a power-law equation: $i=av^{b}$, where *a* and *b* are parameters. The *b*-value is the slope of the line obtained by plotting log(i) versus log(v). The *b*-value of 0.5 occurs with diffusion-controlled Li-storage processes.[15, 45, 46] In contrast, the *b*-value of 1.0 occurs with capacitive or capacitive-like processes (such as EDLC or pseudocapacitance), or processes that are not diffusion limited (e.g., nanosized or surface-active materials).[15, 45, 46] In the field of Li-batteries, a material with a b-value near 1 is often characterized as, at least partially, *pseudocapacitive*.[46–48] The term pseudocapacitive refers to “reversible surface or near-surface Faradaic reactions”.[49]

Results of the *b*-value analysis for five regions of the CV curve is shown in Figure 5.6. Regarding the delithiation (oxidation) processes, a *b*-value of 0.77 was obtained for the delithiation peak in the low voltage range around 1 V, whereas a *b*-value of 0.85 was obtained at a higher voltage around 3.0 V. Moreover, quantification of the current contributions near the peaks 2 and 3 were estimated in Figure S5.13 and reveal a greater pseudocapacitive contribution (>50%) at 3.0 V for all scan rates. Although the anode is controlled by a mixture of diffusion-pseudocapacitive processes, there is a greater pseudocapacitive delithiation at the high voltage around 3.0 V. This Li extraction would occur at the surface of SmAz or the SEI and is likely responsible for SmAz's activation and ultra-high capacity when charged up to 3.0 V. It should be noted that reversible reactions with SEI/surface species have been suggested in certain materials.[34, 50]

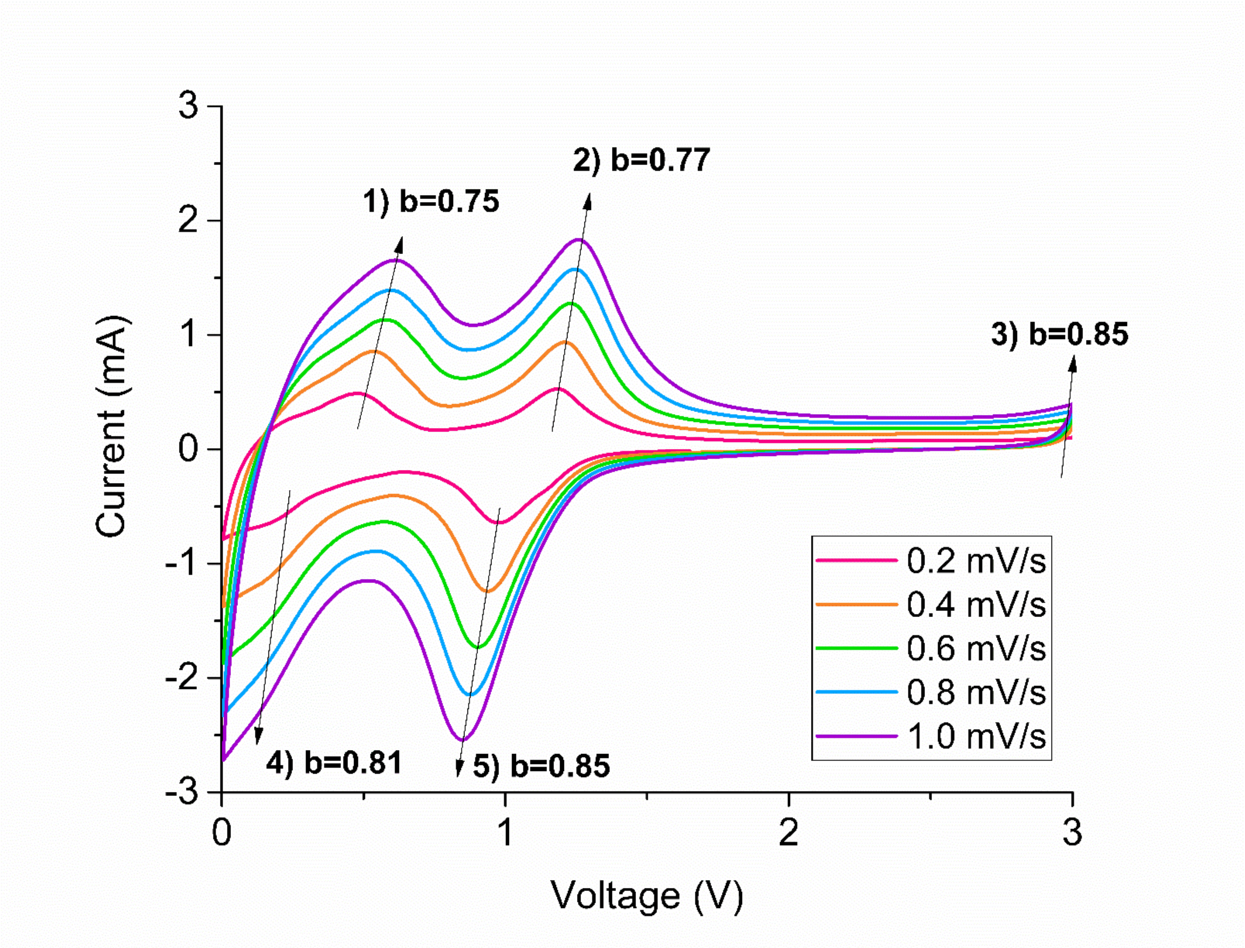

Figure 5.6. CV and b-value analysis on SmAz-based electrode.

Further insight into the lithiation of the SmAz anode was revealed with Operando XRD. Figure 5.7 shows the Operando XRD plot for the first cycle of the SmAz electrode in the 2θ range between 12-18°. In this range, there are three dominant reflections from SmAz (see Figure S5.12). The peak intensity began to decline around the first plateau above 1.5 V, and a pronounced decline in intensity was seen around the 1 V plateau. At 5 mV, the peaks became indistinguishable from the background (point C). The peaks did not return upon delithiation. This behaviour has been reported with Operando XRD for several types of anode materials. In particular, it has been seen with certain metal-oxide conversion anodes, where lithiation produces small crystallites that are not detectable with the bulk characterization method of Operando XRD.[51] It has also been seen in alloying anodes like silicon, where Si particles tend to become amorphous with extended lithiation and delithiation. Regardless, the observed reduction in crystallinity with SmAz would likely be associated with an increase in electrolyte-exposed surface area along with SEI formation. A greater amount of exposed surface area would support a transition from a bulk-redox process towards a surface-redox process.[46] This condition would be especially conducive to Li storage/extraction mechanisms involving adsorption (relevant at low voltage) and pseudocapacitance (with SmAz's surface or SEI species), and may explain SmAz's low CE, high capacity, and activation behaviour when charged to 3.0 V.[25, 26, 29, 34, 46, 52]

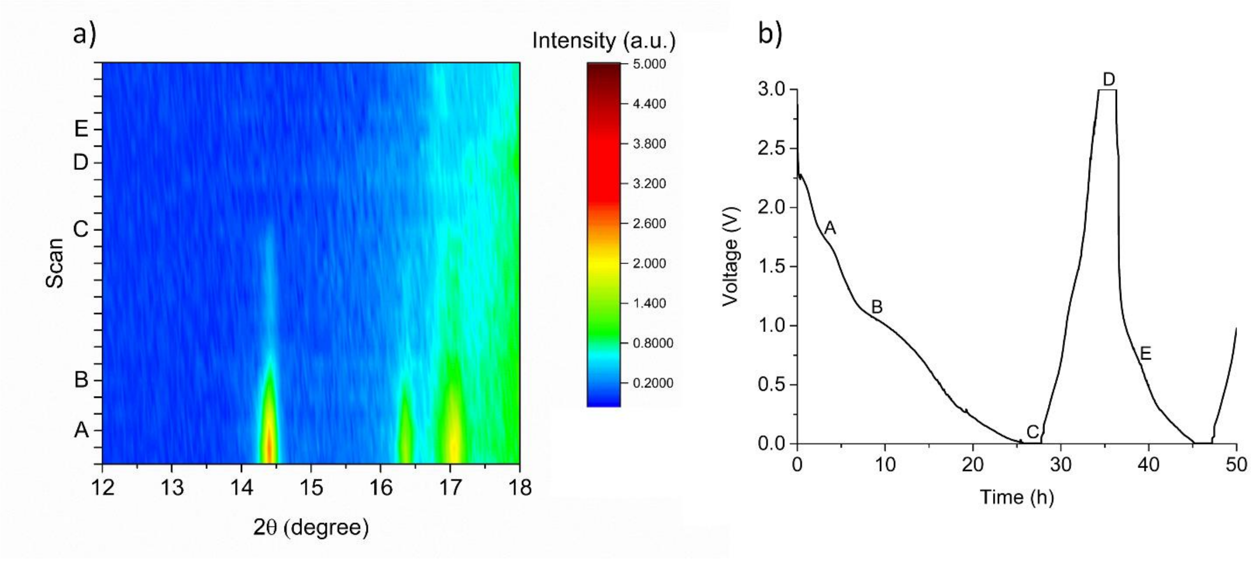

Figure 5.7. a) Operando XRD of SmAz-based electrode in the 2θ range between 12-18° and b) the voltage vs time profile of the 1st cycle during the operando experiment. Note the letters correspond to the voltage at which the XRD scan was taken in Figure a).

The characterization of SmAz supports a type of mixed redox-pseudocapacitive process that is hypothesized to involve multiple steps. Upon lithiation, there are Li reactions with nitrogen sites around 1V, followed by an adsorption-intercalation-type process in the low voltage range (~0.1V), as well as possible superlithiation of aromatic carbons. Upon delithiation, there is Li desorption-deintercalation, Li extraction from the nitrogen sites around 1V. Then, near the higher voltage of 3.0 V, there is pseudocapacitive Li extraction. This would involve reversible lithium extraction from SmAz's surface or SEI and would only occur at a high voltage.

## Conclusions

In conclusion, a crystalline small molecule azaacene (SmAz) has been synthesized and studied as an anode material in Li-ion batteries. SmAz had a reversible capacity of around 550 mAh $g^{-1}$ at 50 mA $g^{-1}$, a value that exceeds its theoretical capacity. Moreover, SmAz showed an activation process whereby the capacity increases with cycle time. Operando XRD, impedance spectroscopy, and cyclic voltammetry revealed that SmAz undergoes amorphization during lithiation and is controlled by a mixed process consisting of both ion-diffusion and pseudocapacitance at high voltage.

Author Contributions

SmAz Synthesis: EG

Electrochemical Experiments: JS, EG

Manuscript Writing: JS, EG

Consultations and Manuscript Revisions: DSS, BTM, YAL, CHY, EAB

Acknowledgements

We would like to thank the Office of Energy Research and Development (OERD) at Natural Resources Canada, the Collaboration Centre in Green Energy Materials (CC-GEM), and the Natural Sciences and Engineering Research Council of Canada (NSERC) for financial support.

## References

[1] B. Esser, F. Dolhem, M. Becuwe, P. Poizot, A. Vlad, and D. Brandell, “A perspective on organic electrode materials and technologies for next generation batteries,” *J Power Sources*, vol. 482, p. 228814, Jan. 2021, doi: 10.1016/j.jpowsour.2020.228814.

[2] P. Poizot, J. Gaubicher, S. Renault, L. Dubois, Y. Liang, and Y. Yao, “Opportunities and Challenges for Organic Electrodes in Electrochemical Energy Storage,” *Chem Rev*, vol. 120, no. 14, pp. 6490–6557, Jul. 2020, doi: 10.1021/acs.chemrev.9b00482.

[3] T. B. Schon, B. T. McAllister, P.-F. Li, and D. S. Seferos, “The rise of organic electrode materials for energy storage,” *Chem Soc Rev*, vol. 45, no. 22, pp. 6345–6404, 2016, doi: 10.1039/C6CS00173D.

[4] E. Grignon, A. M. Battaglia, T. B. Schon, and D. S. Seferos, “Aqueous zinc batteries: Design principles toward organic cathodes for grid applications,” *iScience*, vol. 25, no. 5, p. 104204, May 2022, doi: 10.1016/j.isci.2022.104204.

[5] X. Luo *et al.*, “Advanced Covalent Organic Frameworks for Multi-Valent Metal Ion Batteries,” *Chemistry – A European Journal*, vol. 29, no. 6, Jan. 2023, doi: 10.1002/chem.202202723.

[6] Z. Su *et al.*, “Multilayer structure covalent organic frameworks (COFs) linking by double functional groups for advanced K+ batteries,” *J Colloid Interface Sci*, vol. 639, pp. 7–13, Jun. 2023, doi: 10.1016/j.jcis.2023.02.012.

[7] J. Kim, Y. Kim, J. Yoo, G. Kwon, Y. Ko, and K. Kang, “Organic batteries for a greener rechargeable world,” *Nat Rev Mater*, vol. 8, no. 1, pp. 54–70, Sep. 2022, doi: 10.1038/s41578-022-00478-1.

[8] A. E. Lakraychi, F. Dolhem, A. Vlad, and M. Becuwe, “Organic Negative Electrode Materials for Metal-Ion and Molecular-Ion Batteries: Progress and Challenges from a Molecular Engineering Perspective,” *Adv Energy Mater*, vol. 11, no. 32, p. 2101562, Aug. 2021, doi: 10.1002/aenm.202101562.

[9] J. Wu *et al.*, “Nanostructured Conjugated Ladder Polymers for Stable and Fast Lithium Storage Anodes with High-Capacity,” *Adv Energy Mater*, vol. 5, no. 9, p. 1402189, May 2015, doi: 10.1002/aenm.201402189.

[10] J. Wu, X. Rui, G. Long, W. Chen, Q. Yan, and Q. Zhang, “Pushing Up Lithium Storage through Nanostructured Polyazaacene Analogues as Anode,” *Angewandte Chemie International Edition*, vol. 54, no. 25, pp. 7354–7358, Jun. 2015, doi: 10.1002/anie.201503072.

[11] B. T. McAllister *et al.*, “High-Rate Activation of Organic Superlithiation Anodes,” *ACS Appl Energy Mater*, vol. 4, no. 7, pp. 6659–6666, Jul. 2021, doi: 10.1021/acsaem.1c00714.

[12] S. Renault, V. A. Oltean, C. M. Araujo, A. Grigoriev, K. Edström, and D. Brandell, “Superlithiation of Organic Electrode Materials: The Case of Dilithium Benzenedipropiolate,” *Chemistry of Materials*, vol. 28, no. 6, pp. 1920–1926, Mar. 2016, doi: 10.1021/acs.chemmater.6b00267.

[13] Z. Lei, X. Chen, W. Sun, Y. Zhang, and Y. Wang, “Exfoliated Triazine-Based Covalent Organic Nanosheets with Multielectron Redox for High-Performance Lithium Organic Batteries,” *Adv Energy Mater*, vol. 9, no. 3, p. 1801010, Jan. 2019, doi: 10.1002/aenm.201801010.

[14] Z. Lei *et al.*, “Boosting lithium storage in covalent organic framework via activation of 14-electron redox chemistry,” *Nat Commun*, vol. 9, no. 1, p. 576, Feb. 2018, doi:

10.1038/s41467-018-02889-7.
[15] F. Jiang *et al.*, “Synthesis of biphenyl-linked covalent triazine frameworks with excellent lithium storage performance as anode in lithium ion battery,” *J Power Sources*, vol. 523, p. 231041, Mar. 2022, doi: 10.1016/j.jpowsour.2022.231041.
[16] Z. Zhang, Y. Zhou, P. Chen, S. Zeng, W. Nie, and Y. Xu, “Investigation of Capacity Increase in Schiff-Base Networks as the Organic Anode for Lithium-Ion Batteries,” *ACS Appl Energy Mater*, vol. 4, no. 11, pp. 12882–12891, Nov. 2021, doi: 10.1021/acsaem.1c02569.
[17] W. Luo, M. Allen, V. Raju, and X. Ji, “An Organic Pigment as a High-Performance Cathode for Sodium-Ion Batteries,” *Adv Energy Mater*, vol. 4, no. 15, p. 1400554, Oct. 2014, doi: 10.1002/aenm.201400554.
[18] Y. Chen *et al.*, “Organic electrode for non-aqueous potassium-ion batteries,” *Nano Energy*, vol. 18, pp. 205–211, Nov. 2015, doi: 10.1016/j.nanoen.2015.10.015.
[19] X. Han, G. Qing, J. Sun, and T. Sun, “How Many Lithium Ions Can Be Inserted onto Fused C $_6$ Aromatic Ring Systems?,” *Angewandte Chemie International Edition*, vol. 51, no. 21, pp. 5147–5151, May 2012, doi: 10.1002/anie.201109187.
[20] Y. Wang *et al.*, “Ultrahigh-Capacity Organic Anode with High-Rate Capability and Long Cycle Life for Lithium-Ion Batteries,” *ACS Energy Lett*, vol. 2, no. 9, pp. 2140–2148, Sep. 2017, doi: 10.1021/acsenergylett.7b00622.
[21] H. H. Lee, Y. Park, K.-H. Shin, K. T. Lee, and S. Y. Hong, “Abnormal Excess Capacity of Conjugated Dicarboxylates in Lithium-Ion Batteries,” *ACS Appl Mater Interfaces*, vol. 6, no. 21, pp. 19118–19126, Nov. 2014, doi: 10.1021/am505090p.
[22] F. Jiang *et al.*, “Superlithiation Performance of Covalent Triazine Frameworks as Anodes in Lithium-Ion Batteries,” *ACS Appl Mater Interfaces*, vol. 13, no. 41, pp. 48818–48827, Oct. 2021, doi: 10.1021/acsami.1c14838.
[23] F. Baskoro, A. L. Lubis, H. Q. Wong, G.-S. Liou, and H.-J. Yen, “Redox-active polynaphthalimides as versatile electrode materials for high-voltage, high-rate and long-cycle-life organic Li-ion batteries,” *J Mater Chem A Mater*, vol. 11, no. 21, pp. 11210–11221, 2023, doi: 10.1039/D3TA00596H.
[24] F. Baskoro, H.-J. Lin, C.-W. Chang, C.-L. Wang, A. L. Lubis, and H.-J. Yen, “High-performance aramid electrodes for high-rate and long cycle-life organic Li-ion batteries,” *J Mater Chem A Mater*, vol. 11, no. 2, pp. 569–578, 2023, doi: 10.1039/D2TA07651A.
[25] L. Xie *et al.*, “Hard Carbon Anodes for Next-Generation Li-Ion Batteries: Review and Perspective,” *Adv Energy Mater*, vol. 11, no. 38, Oct. 2021, doi: 10.1002/aenm.202101650.
[26] S. Huang *et al.*, “N-Doping and Defective Nanographitic Domain Coupled Hard Carbon Nanoshells for High Performance Lithium/Sodium Storage,” *Adv Funct Mater*, vol. 28, no. 10, Mar. 2018, doi: 10.1002/adfm.201706294.
[27] H. Zhang, S. Zhao, and F. Huang, “A comparative overview of carbon anodes for nonaqueous alkali metal-ion batteries,” *J Mater Chem A Mater*, vol. 9, no. 48, pp. 27140–27169, Dec. 2021, doi: 10.1039/d1ta07962j.
[28] Y. Mao *et al.*, “Lithium storage in nitrogen-rich mesoporous carbon materials,” *Energy Environ Sci*, vol. 5, no. 7, pp. 7950–7955, Jul. 2012, doi: 10.1039/c2ee21817h.
[29] Z. Li *et al.*, “Mesoporous nitrogen-rich carbons derived from protein for ultra-high capacity battery anodes and supercapacitors,” *Energy Environ Sci*, vol. 6, no. 3, pp. 871–878, Mar. 2013, doi: 10.1039/c2ee23599d.

[30] Y. X. Yu, “Can all nitrogen-doped defects improve the performance of graphene anode materials for lithium-ion batteries?,” *Physical Chemistry Chemical Physics*, vol. 15, no. 39, pp. 16819–16827, 2013, doi: 10.1039/c3cp51689j.

[31] Z. Pang, X. Shi, Y. Weia, and D. Fang, “Grain boundary and curvature enhanced lithium adsorption on carbon,” *Carbon N Y*, vol. 107, pp. 557–563, 2016, doi: 10.1016/j.carbon.2016.06.035.

[32] P. Yang *et al.*, “Superior anodic lithium storage behavior of organic pigment 2,9-dimethylquinacridone,” *Chemical Engineering Journal*, vol. 394, no. March, p. 124924, 2020, doi: 10.1016/j.cej.2020.124924.

[33] J. Xie *et al.*, “Novel Conjugated Ladder-Structured Oligomer Anode with High Lithium Storage and Long Cycling Capability,” *ACS Appl Mater Interfaces*, vol. 8, no. 26, pp. 16932–16938, 2016, doi: 10.1021/acsami.6b04277.

[34] H. Kang *et al.*, “Polyanthraquinone-Triazine - A Promising Anode Material for High-Energy Lithium-Ion Batteries,” *ACS Appl Mater Interfaces*, vol. 10, no. 43, pp. 37023–37030, 2018, doi: 10.1021/acsami.8b12888.

[35] H. Q. Wang, Z. Bin Zhao, M. Chen, N. Xiao, B. B. Li, and J. S. Qiu, “Nitrogen-doped mesoporous carbon nanosheets from coal tar as high performance anode materials for lithium ion batteries,” *Xinxing Tan Cailiao/New Carbon Materials*, vol. 29, no. 4, pp. 280–286, Aug. 2014, doi: 10.1016/S1872-5805(14)60137-2.

[36] M. Gaberšček, “Understanding Li-based battery materials via electrochemical impedance spectroscopy,” *Nat Commun*, vol. 12, no. 1, p. 6513, Nov. 2021, doi: 10.1038/s41467-021-26894-5.

[37] W. Choi, H. C. Shin, J. M. Kim, J. Y. Choi, and W. S. Yoon, “Modeling and applications of electrochemical impedance spectroscopy (Eis) for lithium-ion batteries,” *Journal of Electrochemical Science and Technology*, vol. 11, no. 1. Korean Electrochemical Society, pp. 1–13, Feb. 01, 2020. doi: 10.33961/jecst.2019.00528.

[38] N. Meddings *et al.*, “Application of electrochemical impedance spectroscopy to commercial Li-ion cells: A review,” *J Power Sources*, vol. 480, p. 228742, Dec. 2020, doi: 10.1016/j.jpowsour.2020.228742.

[39] M. Steinhauer, S. Risse, N. Wagner, and K. A. Friedrich, “Investigation of the Solid Electrolyte Interphase Formation at Graphite Anodes in Lithium-Ion Batteries with Electrochemical Impedance Spectroscopy,” *Electrochim Acta*, vol. 228, pp. 652–658, Feb. 2017, doi: 10.1016/j.electacta.2017.01.128.

[40] H. Duncan, F. M. Courtel, and Y. Abu-Lebdeh, “ A Study of the Solid-Electrolyte-Interface (SEI) of ZnMn 2 O 4 : A Conversion-Type Anode Material for Li-Ion Batteries ,” *J Electrochem Soc*, vol. 162, no. 13, pp. A7110–A7117, 2015, doi: 10.1149/2.0141513jes.

[41] Y. Xiao, X. Wang, W. Wang, D. Zhao, and M. Cao, “Engineering hybrid between MnO and N-doped carbon to achieve exceptionally high capacity for lithium-ion battery anode,” *ACS Appl Mater Interfaces*, vol. 6, no. 3, pp. 2051–2058, Feb. 2014, doi: 10.1021/am405142p.

[42] X. Li, Z. Zhang, C. Liu, and Z. Lin, “Capacity increase investigation of Cu2Se electrode by using electrochemical impedance spectroscopy,” *Front Chem*, vol. 6, no. JUN, 2018, doi: 10.3389/fchem.2018.00221.

[43] S. S. Zhang, K. Xu, and T. R. Jow, “EIS study on the formation of solid electrolyte interface in Li-ion battery,” in *Electrochimica Acta*, Jan. 2006, pp. 1636–1640. doi: 10.1016/j.electacta.2005.02.137.

[44] Y.-R. Nian and H. Teng, “Influence of surface oxides on the impedance behavior of carbon-based electrochemical capacitors,” *Journal of Electroanalytical Chemistry* , vol. 540, pp. 119–127, 2003, [Online]. Available: www.elsevier.com/locate/jelechem

[45] B. Xiao *et al.*, “High-entropy oxides as advanced anode materials for long-life lithium-ion Batteries,” *Nano Energy*, vol. 95, no. November 2021, p. 106962, 2022, doi: 10.1016/j.nanoen.2022.106962.

[46] Y. Jiang and J. Liu, “Definitions of Pseudocapacitive Materials: A Brief Review,” *Energy and Environmental Materials*, vol. 2, no. 1, pp. 30–37, Mar. 2019, doi: 10.1002/eem2.12028.

[47] O. Buyukcakir *et al.*, “Lithium Accommodation in a Redox-Active Covalent Triazine Framework for High Areal Capacity and Fast-Charging Lithium-Ion Batteries,” *Adv Funct Mater*, vol. 30, no. 36, Sep. 2020, doi: 10.1002/adfm.202003761.

[48] J. Ryu *et al.*, “Three-Dimensional Monolithic Organic Battery Electrodes,” *ACS Nano*, vol. 13, no. 12, pp. 14357–14367, Dec. 2019, doi: 10.1021/acsnano.9b07807.

[49] S. Fleischmann *et al.*, “Pseudocapacitance: From Fundamental Understanding to High Power Energy Storage Materials,” *Chem Rev*, vol. 120, no. 14, pp. 6738–6782, Jul. 2020, doi: 10.1021/acs.chemrev.0c00170.

[50] Y. Y. Hu *et al.*, “Origin of additional capacities in metal oxide lithium-ion battery electrodes,” *Nat Mater*, vol. 12, no. 12, pp. 1130–1136, Dec. 2013, doi: 10.1038/nmat3784.

[51] A. Sarkar *et al.*, “High entropy oxides for reversible energy storage,” *Nat Commun*, vol. 9, no. 1, p. 3400, Dec. 2018, doi: 10.1038/s41467-018-05774-5.

[52] J. Han, A. Mariani, S. Passerini, and A. Varzi, “A perspective on the role of anions in highly concentrated aqueous electrolytes,” *Energy Environ Sci*, 2023, doi: 10.1039/d2ee03682g.

# Chapter 6: Investigation of Xanthan Gum and Carboxymethyl Cellulose Binders for the Silicon Anode of Lithium-Ion Batteries

James W. Sturman[1, 2], Chae-Ho Yim[1], Zouina Karkar[1], Elena A. Baranova[2], Mathieu Toupin[3*], and Yaser Abu-Lebdeh[1*]

1. Energy, Mining, and Environment Research Centre, National Research Council of Canada, 1200 Montreal Road, Ottawa, Ontario K1A 0R6, Canada
2. Department of Chemical and Biological Engineering, Centre for Catalysis Research and Innovation (CCRI), University of Ottawa, 161 Louis-Pasteur, Ottawa ON, K1N 6N5, Canada
3. Automotive and Surface Transportation Research Centre, National Research Council of Canada, 75 de Mortagne Blvd. J4B 6Y4, Boucherville (QC), Canada

Publication status: published
Adapted from DOI 10.1149/1945-7111/acbbf1

**Abstract**

The binder is known to play an important role in the cycle stability of silicon-based anodes for lithium-ion batteries. Nature-derived biopolymers such as sodium carboxymethyl cellulose (NaCMC) and xanthan gum (XG) are a promising class of binders that offer several advantages over traditional polyvinylidene fluoride (PVDF). Advantages include better contact between silicon particles and the ability to process the electrodes using water as a solvent. While many studies have explored the fundamental properties of these biopolymer binders and their interaction with silicon, there has been little research on the use of these binders under practical loadings (such as ∼2 mg Si cm$^{-2}$ and <10 wt% binder). Herein, we compare the electrochemical performance of both NaCMC and XG-based silicon electrodes with a low binder content. Si-binder interactions and their role in electrode performance are revealed with XPS, SEM, and EDX. In addition, we report the results of both a high-silicon (80 wt% Si) and a practical low-silicon (20 wt% Si) composite electrode while using silicon nano powder prepared by industrial-scale synthesis. It is found that NaCMC consistently outperforms XG as a binder, which is attributable to superior cohesion within the electrode.

## Introduction

The demand for lithium-ion batteries continues to grow as the need for renewable energy increases. Over the past few decades, lithium-ion batteries have seen widespread adoption in portable electronics, and they are increasingly being used in electric vehicles. To satisfy the energy density needed for these next-generation applications, new anode materials with high-energy densities are required. Traditional graphite is a very stable intercalation-based anode, but its low capacity has driven many researchers to identify alternatives. Silicon (Si) has one of the highest gravimetric energy densities known when alloyed with lithium. Unlike graphite which is limited to 1 lithium ion per 6 carbon atoms ($LiC_6$), the lithium- silicon alloy $Li_{15}Si_4$ has nearly 4 lithium ions per silicon atom[1,2] This gives silicon a theoretical capacity of 3579 mAh $g^{-1}$, compared to the 372 mAh $g^{-1}$ for graphite. However, the problem with silicon (and most alloy anodes) is its poor stability— as the alloying of lithium and silicon is accompanied by a 300% volume expansion.[3] The continuous expansion/contraction of the silicon during lithiation/delithiation causes severe electrode pulverization, excessive SEI formation, and rapid capacity fade in a few cycles.[2]

There have been many strategies to improve the poor stability of silicon.[4–7] Those that will be considered in this paper include the use of nano-sized silicon, the use of silicon-graphite composites, and the use of aqueous binders. Based on work by Yim et al., there is a negligible increase in energy density after more than ∼20 wt% silicon in a full cell.[7] In addition, it is well-known that irreversible capacity increases with silicon content.[8] In the literature, it is common to report the performance of *silicon* electrodes while using a silicon:binder:carbon mass ratio of 6:2:2.[9–12] A survey of recent publications on polymer-based binders for the silicon anode revealed only 5 out of 25 studies used a binder content of 10% or less.[13] It should be noted that a large fraction of binder and carbon (typically Super P) will result in a composite-type electrode that will inflate the cycle stability of *silicon* and lower the overall gravimetric energy density of the electrode.[10,14] In addition, a large fraction of high surface area carbon will contribute to a large irreversible capacity from SEI during the first cycle, thus reducing feasibility in commercial cells.

The binder is known to play an important role in the cycle stability of silicon-based anodes since it is responsible for the mechanical integrity of the electrode.[15] Next-generation binders should be inexpensive, electrochemically stable, able to accommodate the expansion of silicon, and use environmentally friendly processing.[16] Natural biopolymers (such as NaCMC and xanthan gum [XG]) are a promising class of binders that offer several advantages over traditional PVDF.[15]

In particular, XG is a high molecular weight polysaccharide produced extracellularly by the bacteria *Xanthomonas campestris*.[17] It is water soluble and has proven good performance with graphite anodes.[18,19]

As seen in Figure 6.1, both XG and NaCMC are structurally similar to cellulose. In the case of NaCMC, carboxymethyl groups replace some hydroxyl groups on the cellulose backbone.[20] With XG, the cellulose backbone is linked with trisaccharide side chains (consisting of D-mannose linked to the main chain, D-glucuronic acid, and another terminal D-mannose).[10,17] The non-terminal mannose is often acetylated, and the terminal mannose can be pyruvated.[17] These complex side chains and functional groups enable XG to adopt a stiff single, double, or triple helical structure.[10,17] In addition, these side chains are known to play an important role in the electrochemical performance of XG-based electrodes.[9] As XG is a natural product, its exact molecular structure, composition of side chains, and molecular weight are dependent on fermentation conditions. Its molecular weight is typically around 1–3 million Da.[10,17] These biopolymers contain many carboxylate and hydroxyl functional groups that form noncovalent bonds with the hydroxyl groups on the surface of silicon (such as self-healing hydrogen bonds).[10,21] Charged binders offer the additional advantage of ion- dipole interactions, which can improve electrode bonding and cycle stability.[10,21] In addition, certain binders like NaCMC prepared in an acidic solution (~pH 3) are known to facilitate esterification between the –OH groups on the silicon and the –COOH groups of the binder, thus forming covalent bonds.[22] This, however, requires an additional processing step with an acidic buffer. In addition, recent results with Si–C composites have shown superior capacity retention for NaCMC-based electrodes prepared under neutral (pH 7 buffer) conditions compared to acidic conditions.[23]

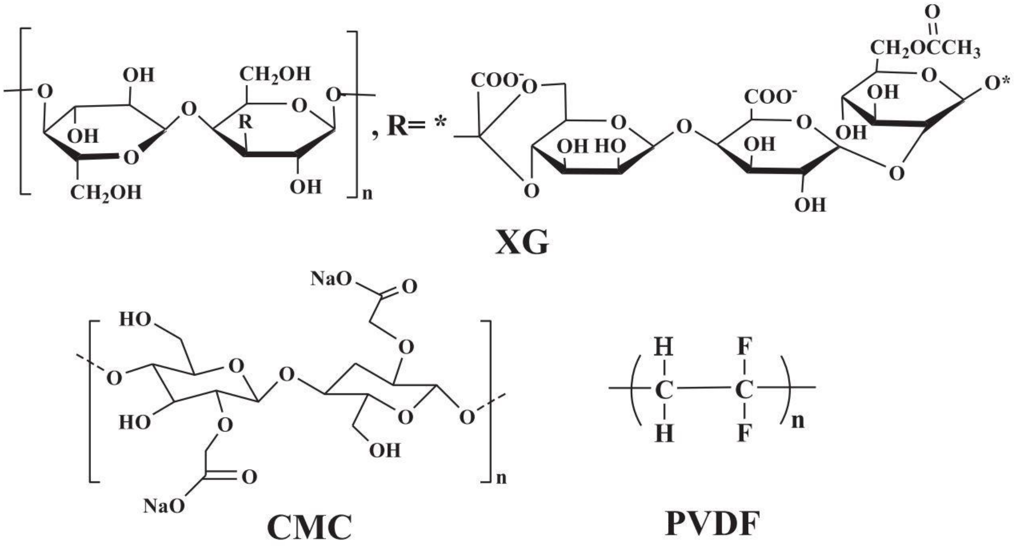

Figure 6.1. The basic structure of xanthan gum, sodium carboxymethylcellulose, and PVDF. Reproduced with permission from [20]

While existing studies have explored the fundamental properties of these biopolymer binders and their interaction with silicon, there has been little electrochemical research on the use of these binders under realistic conditions (⩽10 wt% binder). Herein, we optimize the electrochemical performance of both NaCMC and XG-based silicon electrodes with a low binder content. The scope of the work was limited to nature-derived biopolymer binders because of their low cost of production and their known self-healing hydrogen bonding mechanism. We report results for both a high-silicon (80 wt%) and a practical low-silicon (20 wt%) composite with graphite, with a special emphasis on capacity retention, silicon-binder interactions, and electrode cohesion. In addition, we use silicon nanoparticles supplied by Tekna, which uses inductively coupled plasma technology for the synthesis of industrial-scale nanosilicon powder.[24]

## Experimental

Silicon-based electrodes were prepared in 0.5 g batches of dry material. A typical composition consisted of 80 wt% silicon nano powder (Tekna N-100, ∼100 nm ave. dim.), 10 wt% Super P conductive carbon (Timcal), and 10 wt% binder. For the silicon- graphite composite electrodes, the composition consisted of 20 wt% silicon nano powder, 60 wt% graphite, 10 wt% Super P conductive carbon, and 10 wt% binder. Xanthan gum was supplied from Jungbunzlauer (FNP food and pharmaceutical grade) and sodium carboxymethyl cellulose (Mw ∼700000, d.s. 0.9) was purchased from Sigma-Aldrich. We used unmodified high molecular weight NaCMC

(700 K) to improve the mechanical properties of the electrode while also providing a closer approximation to the naturally high molecular weight of XG. High molecular weight binders are known to provide superior capacity retention, which is attributed to better rheological properties and cohesive bonding.[25]

Natural spherical graphite SPGPT803 was supplied by Targray. All silicon powder was vacuum dried at 80 °C to remove trapped moisture prior to use. 4 g of deionized water and 1 g of ethanol were added to the dry material to form a slurry. The ethanol co-solvent was used to aid in the mixing of the Super P. Sufficient mixing was then required to form a homogenous mixture between the binder, carbon, and silicon. The slurry was mixed with 4 zirconia balls in an AR-100 Thinky planetary mixer for a total of 45 min at 2000 rpm. The mixing was carried out in three 15 min sessions and included a 15 min rest after each session to prevent overheating. The slurry was cast onto an acetone-cleaned copper foil (20 $\mu$m thickness) using a 350 $\mu$m gap notch bar. The casts were air dried at room temperature. The casts were not calendered and the porosity of the resulting anodes ranged between 50%-60% as calculated according to Primo et al.[26] Calendering of Si-rich electrodes is known to reduce porosity and potentially reduce capacity retention.[2,22] 0.5-inch diameter electrode disks were cut and vacuum dried at 80 °C overnight. This standard preparation gave a relatively high active material loading of $\sim$2.2 mg cm$^{-2}$ with a standard deviation of 0.13 mg cm$^{-2}$. Half-cell batteries with lithium metal were prepared in an argon-filled glove box using 2325 type coin cells, 74.8 $\mu$l of electrolyte and two 3501 Celgard polypropylene membranes. The electrolyte was 1 M $LiPF_6$ in ethylene carbonate and ethyl methyl carbonate EC: EMC (1:1 v/v) (Sigma Aldrich) with 10 wt% fluoroethylene carbonate (FEC) additive. All coin cells were allowed to rest at least 24 h and were then cycled at 30 °C in an Arbin BT2000 battery cycler.

Current densities were calculated based on the theoretical capacity of the active material. This was 3579 mAh g$^{-1}$ (1 C = 3579 mA g$^{-1}$) for silicon and 372 mAh g$^{-1}$ for graphite. All batteries were cycled between 0.005 V and 1.5 V at a C/10 constant current rate unless otherwise specified. A 15 min open circuit rest was included at each potential limit. All reported cycling data has been replicated with at least two coin cells. Table 6.1 lists the main electrode compositions and their abbreviated ID used in this paper.

**Table 6.1. Sample nomenclature**

| Sample Composition (mass %) | Abbreviated ID |
|---|---|
| **80% silicon***, 10% XG, 10% Super P | 80Si-10XG |
| **80% silicon**, 10% NaCMC, 10% Super P | 80Si-10CMC |
| **20% silicon, 60% graphite**, 10% XG, 10% Super P | 20Si-10XG |
| **20% silicon, 60% graphite**, 10% NaCMC, 10% Super P | 20Si-10CMC |

*active material is written in bold

The morphology was characterized by Field Emission Scanning Electron Microscopy (SEM) with a Hitachi SU5000 microscope. For postmortem SEM, batteries were opened under argon in their delithiated state and the electrodes were rinsed for 1–2 min with diethyl carbonate solvent to remove bulk quantities of the Li salt, then dried under vacuum.[27] Elemental distribution was quantified with the Energy Dispersive X-ray (EDX) Spectroscopy Analyzer X-Max Oxford Instruments. The powder X-ray Diffraction (XRD) was conducted with a Bruker AXS D8 diffractometer (Cu K$\alpha$, $\lambda$ = 0.154 nm) between 10° and 85° 2$\theta$. Fourier Transform Infrared spectroscopy (FTIR) was conducted with a Thermo Fisher Nicolet 6700 spectrometer using a diamond crystal single-bounce ATR accessory. X-ray Photoelectron Spectroscopy (XPS) data was acquired from a Kratos AXIS Ultra DLD spectrometer with a monochromated Al K-alpha beam (1486.6 eV). High resolution spectra were taken at a pass energy of 20 eV.

## Results and Discussion

Figure 6.2 shows the XRD patterns of the silicon and graphite used in this study with no obvious reflections from impurities. The nano silicon is crystalline as seen with the clear reflections from all five lattice planes expected in the investigated 2θ range. For silicon, a lattice parameter of $a$ = 5.43 Å was determined by refinement using the Fd-3m space group with TOPAS software. It should be noted that a peak typically attributed to amorphous silica (broad peak around 10°) was not observed in the bulk-silicon sample.[14] This is likely due to the relatively small amount of amorphous silica on the surface. The native oxide layer (traces of silica & hydroxide) is seen as a 2–3 nm amorphous coating on the silicon surface in Figure 6.2c (yellow arrow).

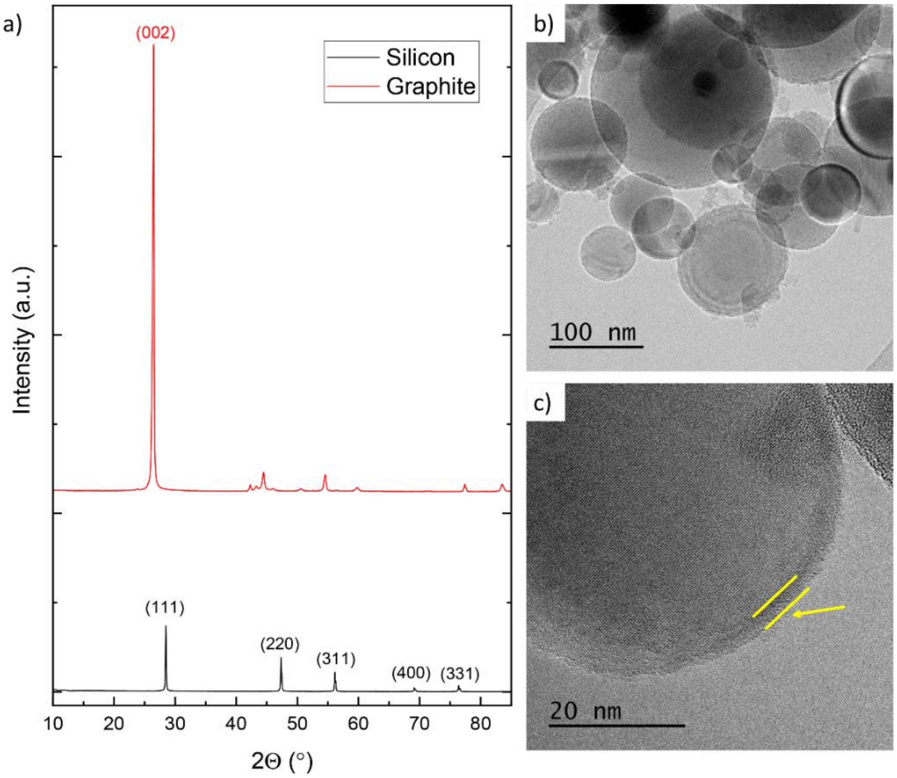

Figure 6.2. (a) Powder XRD patterns of pristine SPGPT803 graphite and N-100 silicon, (b) TEM and (c) HRTEM images of the silicon particles, showing crystalline lattice fringes in the bulk and an amorphous exterior coating.

The FTIR spectrums of the pristine binders are shown in Figure 6.3 and serve to confirm the expected structure and functional groups. Predominant signatures of these biopolymers include the large broad band between 3500–3000 cm$^{-1}$ from the stretching vibration of the O–H group, the band between 1650 to 1550 cm$^{-1}$ from stretching of the COO$^{-}$ group, and the band between 900–1100 cm$^{-1}$ attributed to stretching from the ether group.[10,20] Additional signatures include the band around 3000–2850 cm$^{-1}$ from the stretching of the C–H bonds; the band at 1244 cm$^{-1}$ from the stretching vibration of the ether C–O–C bond; and the band around 1720 cm$^{-1}$ from the stretching of the C=O bond from the acetyl group, which is absent in NaCMC.[9,14]

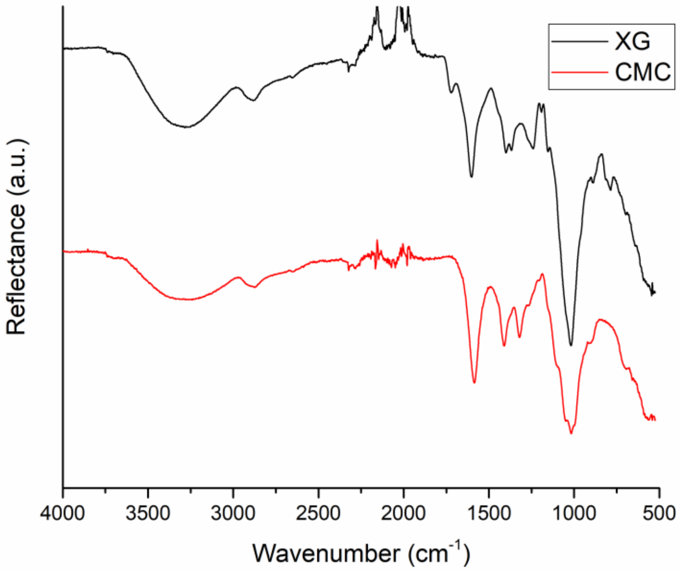

Figure 6.3. FTIR of pristine binders.

Initial electrochemical tests were performed on the Si-rich electrodes to compare the failure modes between binders in the absence of any buffering contribution from graphite. Although the rapid failure of high Si-loading electrodes makes them unsuitable for battery applications, they provide insight into any degradation behavior unique to the silicon powder and the binder. Previous studies have confirmed the thermal and electrochemical stability of NaCMC and XG in the investigated potential range; in addition, these binders are reported to have a negligible capacity contribution.[10,28] Figure 6.4 plots the active material discharge capacity vs cycle number for 80Si-10XG and 80Si-10CMC. All electrodes had an initial discharge capacity near the theoretical value for silicon (~3500 mAh $g^{-1}$). The initial coulombic efficiency (CE) for the XG and NaCMC-based electrodes were 65% and 70% respectively. Both binders' CE exceeded 98% after approximately 15 cycles. These Si-rich electrodes displayed a rapid capacity decay with over 50% capacity loss within a few cycles. The XG-based electrode failed completely after 20 cycles, whereas the NaCMC- based electrode still maintained around 300 mAh $g^{-1}$ after 100 cycles. Although the capacity retention was superior with NaCMC, it is still unsatisfactory for any practical application. This rapid failure is expected since the high mass of ~2.2 $mg_{Si}$ $cm^{-2}$ is known to be within a critical loading where mechanical strain generated by silicon is severe, as described by Karkar et al.[29] Still, trials not reported here at loadings of ~1 $mg_{Si}$ $cm^{-2}$ did not show any improvement in the capacity retention. This indicates that a close-packed arrangement of the nano silicon follows the Si-based electrode model reported by Beattie et al. This work predicts that the vol % of nano silicon cannot exceed 14% or else there is not enough free volume available to prevent particles to push on one and other when forming the $Li_xSi_y$ alloy.[30] Moreover, the relatively neutral pH of the unmodified-binder electrode slurry is less conducive to the formation of covalent bonds between Si and NaCMC.[31]

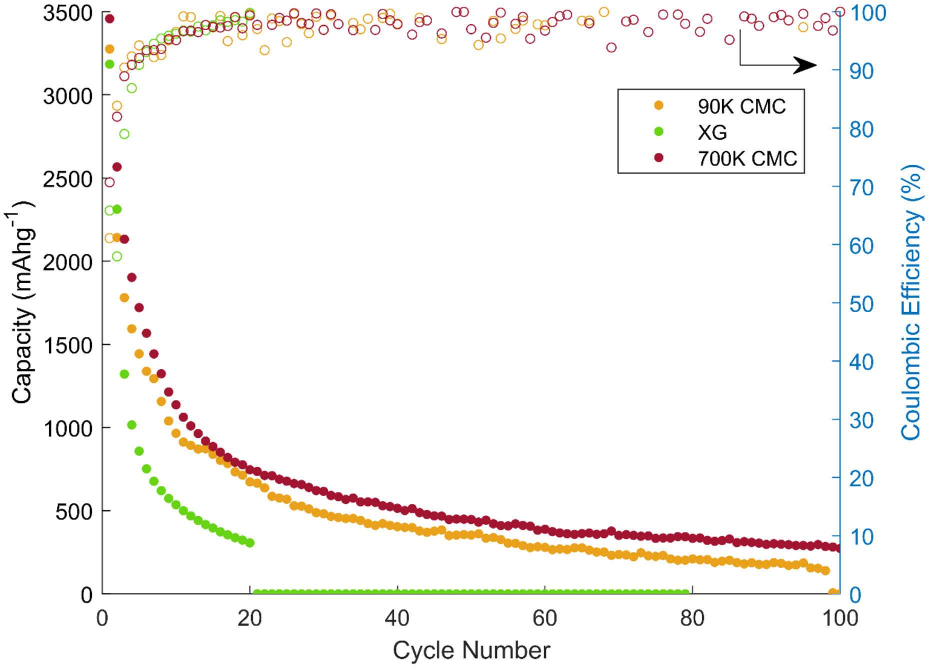

Figure 6.4. Cycle performance of 80 wt% silicon electrodes with XG and NaCMC binders (80Si-10XG and 80Si-10CMC). Si loading of ~2.2 mg cm$^{-2}$.

To confirm the superiority of a high molecular weight, an electrode prepared with low molecular weight 90 K NaCMC was also tested. Films with 90 K NaCMC were very brittle and had inferior electrochemical performance relative to 700 K NaCMC, as seen in Figure 6.4. Potential profile and dQ/dV plots in Figure 6.5 provide further insight into the electrochemical processes during silicon lithiation. These Si-rich electrodes displayed significant voltage hysteresis, which is typical of alloy anodes. The redox peaks were seen to follow the known potentials for silicon lithiation.[2,32] Figures 6.5c and d show first cycle lithiation (discharge) activity around 0.1 V (corresponding to the long plateau in the first cycle of Figures 6.5a and b) and is attributed to the formation of an amorphous-Li-Si phase.[2] Further lithiation to around 50 mV is known to form the crystalline c-$Li_{15}Si_4$ phase.[2] Upon delithiation (charge), two peaks became notable. The peak around 0.27 V is attributed to the conversion of a-$Li_{15}Si_4$ to an amorphous-$Li_2Si$ alloy.[32] The sharp peak around 0.44 V is widely attributed to the conversion of amorphous-$Li_2Si$ and the remaining c-$Li_{15}Si_4$ into amorphous Si.[2,32] After the first cycle, two broad lithiation peaks emerged around 0.25 and 0.09 V respectively showing the formation of a-$Li_2Si$ and a-$Li_{15}Si_4$. The formation of the crystalline-$Li_{15}Si_4$ at 50 mV was noticed for cycle 2 and beyond but to a lesser extent. The same delithiation peaks at 0.27 and 0.44 V remained but the intensity of the latter diminished with cycling. The intensity of these redox peaks on the 3rd cycle was greater with the NaCMC-based electrode due to its better capacity retention. The more rapid capacity decline of the XG-based electrode was accompanied with an increase in overpotential and a rapid decline in the peak associated with delithiation of $Li_{15}Si_4$ and $Li_2Si$ (0.44 V). This is a consequence of contact loss between silicon particles and an increase in electrode resistance.[33] The resulting poor electrode cohesion with XG will be confirmed later in Figures 6.6 and 6.8. With both electrodes, the faint potential well in the discharge curve of the first cycle is likely due to the passivating nature of the polymeric binder coating the silicon. However, a similar phenomenon has also been described with crystalline silicon, as well as with other alloy anodes which are known to require an overpotential to nucleate the lithiated phase during the initial stages of Li-alloy formation[34–37] The relationship between the nano silicon synthesis, crystallinity, and electrochemical performance with aqueous binders is the subject of ongoing work.

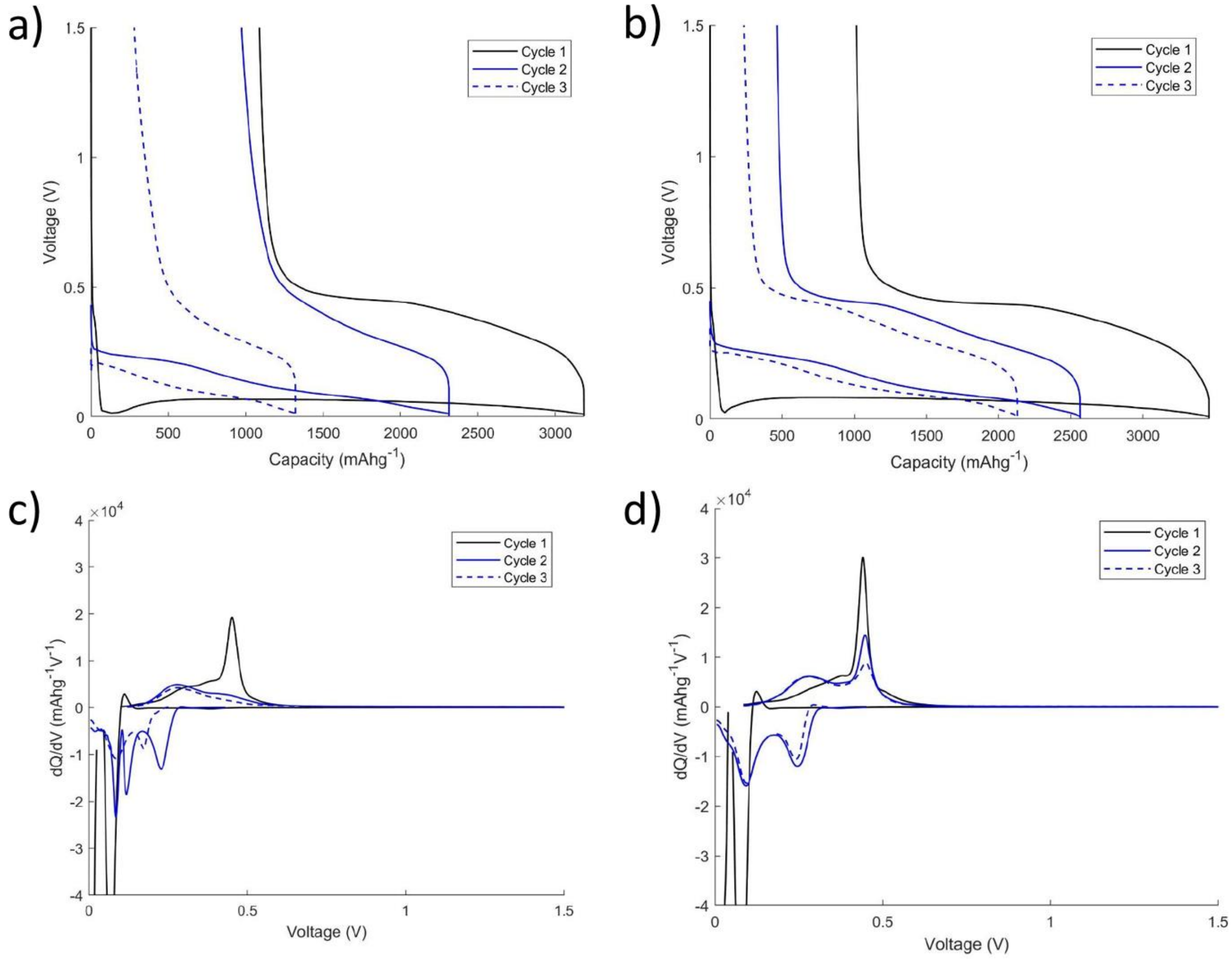

Figure 6.5. Potential profile and differential capacitance plots for 80Si-10XG (a & c) and 80Si-10CMC electrodes (b & d).

Figures 6.6 and 6.7 show SEM images of XG-based and NaCMC-based electrodes, respectively. After cycling, the SEM cross-section images of the XG-based electrode revealed a large increase in the thickness of the active layer (from 25 $\mu$m to 100 $\mu$m). A large proportion of this expansion is attributable to voids from poor cohesion and the rupture of particle-binder bonds.[38] Figures 6.6c and 6.7c reveal more cracks within the active layer with XG compared to NaCMC. The absence of prominent fractures and void spaces with NaCMC is consistent with superior cohesion within the active layer.

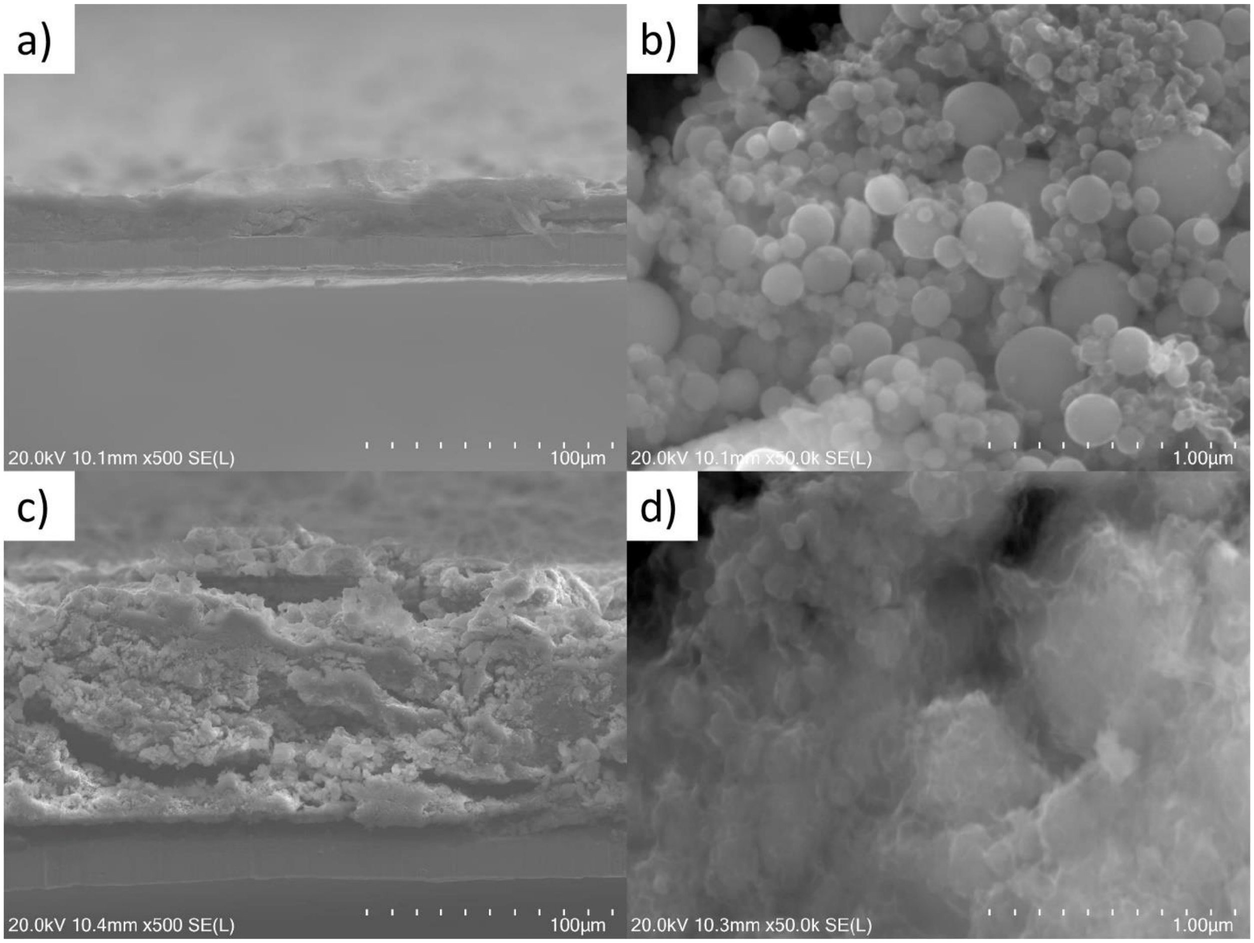

Figure 6.6. SEM cross-sections of an uncycled 80Si-10XG electrode (a & b) and an electrode after 100 cycles at C/10 (c & d).

Additional SEM images in Figure S6.2 provide further confirmation of the superior bulk electrode cohesion of NaCMC-based electrodes. However, pronounced electrode delamination between NaCMC- based electrodes and the copper was observed. Poor Cu-NaCMC adhesion has been reported both qualitatively (with the observation of postmortem delamination) and quantitatively (with film adhesion tests).[39] Previous studies have reported XG to possess superior adhesion with the Cu current collector compared to NaCMC.[10,39] SEM images in Figure S6.3 show binder-only films on copper for both binders as prepared in this study. The images confirm NaCMC has a better ability to form a freestanding film, however it delaminates easily from the copper. In contrast, the XG film shows better adhesion with the copper but with a more brittle and flake-like morphology upon drying.

Certain peel tests that have focused on the adhesion between the silicon and the binder have not revealed a clear benefit with XG compared to NaCMC.[39] Thus, the poor electrochemical performance and electrode cohesion with XG may be attributed to weaker Si-binder interactions, including a reduced ability to form ion-dipole interactions. Silicon-binder interactions are greater for charged binders as they can bind to the hydroxyl groups on silicon via ion-dipole interactions (in addition to typical hydrogen bonding).[10] XPS did not provide strong evidence that either of the binders formed covalent bonds with silicon (Figure S6.4), which supports the assumption that binding within these electrodes primarily involves strong interactions.

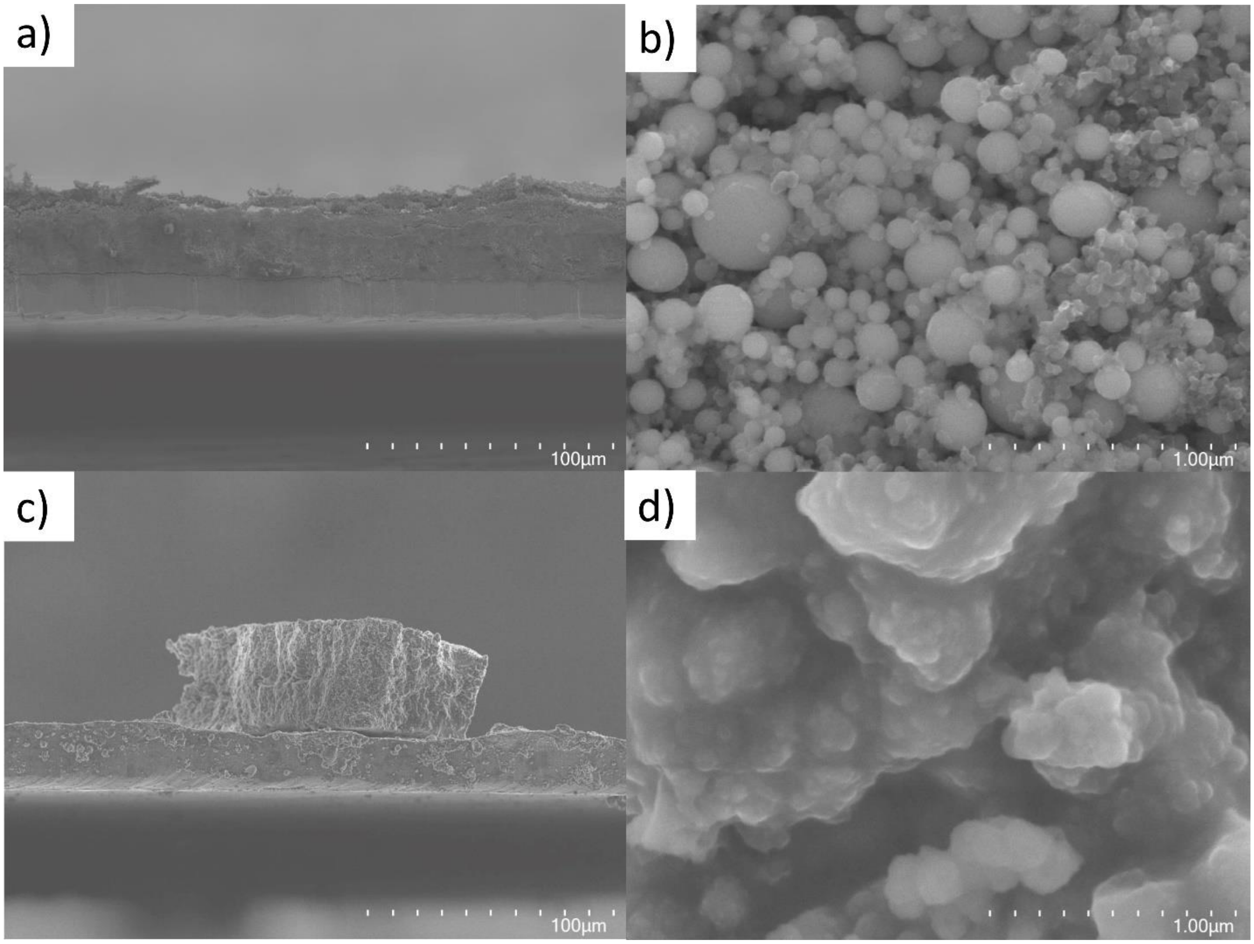

Figure 6.7. SEM cross-sections of an uncycled 80Si-10CMC electrode (a & b) and an electrode after 100 cycles at C/10 (c & d).

For both XG and NaCMC-based electrodes, the spherical silicon morphology was not well-preserved after cycling, as seen in Figures 6.6d and 6.7d. This has been described as electrochemical sintering of the nano silicon into lumps of amorphous material.[40] When comparing Figures 6.6d and 6.7d one can observe a slight difference in the morphology of the electrochemically sintered materials—where XG seems to promote a flaky material and

NaCMC more of a nodular one. SEM/EDX images of an enlarged portion of both electrodes in Figure 6.8 reveal better overall health for the NaCMC- based electrode after cycling. The NaCMC-based active layer is seen as a dense monolithic mass. EDX reveals a relatively smooth silicon surface coated with carbon, fluorine, and oxygen—which is consistent with the formation of a uniform SEI. In contrast, the XG-based active layer has numerous fissures and poor electrode cohesion. The presence of numerous isolated clusters of silicon can be inferred from the varying degree of intensity of the silicon signal. EDX of the carbon, fluorine, and oxygen reveals a greater amount of exposed surface area—which suggests more electrolyte decomposition and SEI formation. Isolation of silicon particles and excessive SEI formation within the electrode is known to impede Li-ion transfer through the cell and reduce accessible capacity.[33] Thus, these observations suggest the NaCMC-based electrode can maintain better structural integrity during cycling, resulting in a more stable SEI and superior electrochemical performance.

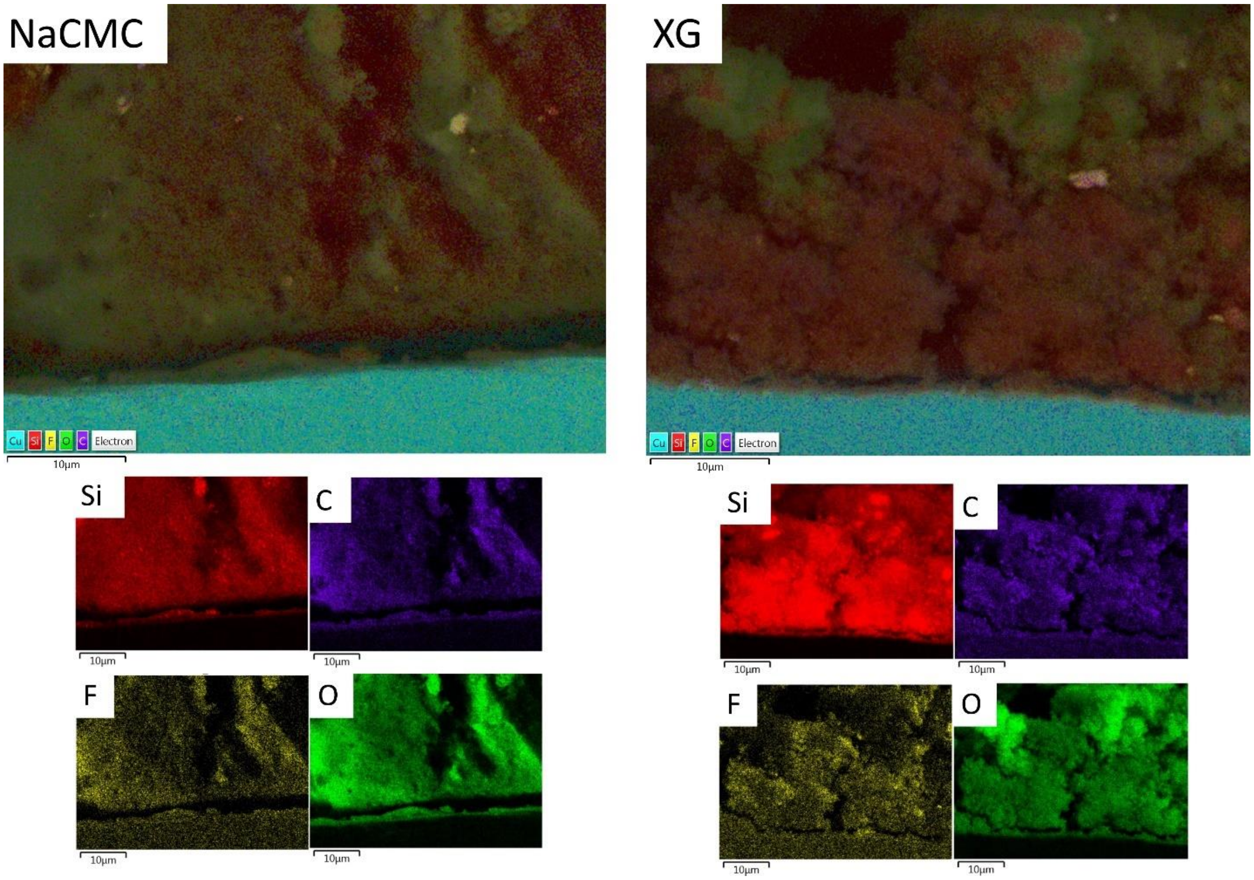

Figure 6.8. Postmortem SEM/EDX of 80Si-10CMC and 80Si-10XG electrodes. Note: blue is the signal from the copper current collector. Both images taken after 100 cycles at C/10.

The desirable XG-Cu adhesion and NaCMC-active layer cohesion inspired an attempt to combine the two binders to identify any possible synergistic effect. A Si-rich (80 wt% Si) electrode was prepared using 5 wt% XG and 5 wt% NaCMC. However, battery cycling tests in Figure S6.6 revealed no synergistic improvement in performance but rather, a compromising capacity retention profile when these two binders were combined.

Composites of silicon and graphite are a well-established economical way to buffer the volumetric expansion of silicon electrodes and hence increase capacity retention.[30,41–43] There is a natural compromise between the capacity and capacity retention of silicon-based electrodes. Electrodes with a high mass fraction of silicon will have a high inherent capacity, but this capacity will fade very quickly. In contrast, electrodes with a low mass fraction of silicon will have a lower inherent capacity, but a greater capacity retention. This allows composites to provide a high practical capacity that is greater than graphite but lower than silicon alone.[42] However, the capacity retention is greater than silicon but still less than graphite alone. Natural graphite is a naturally occurring form of graphite with flaky morphology. Its natural abundance makes it suitable for large-scale applications like electric vehicles. However, it has a low rate capability because of its high anisotropy.[44] As a result, the graphite must undergo a process called spheroidization where the particles are made into spheres. The spherical particles allow for a more uniform diffusion of Li ions, which improves the rate capability of the material, and a better packing density increases the energy density of the electrode.[44] In this study, silicon-graphite composites were prepared from spherical natural graphite SPGPT803 by Targray. Figure 6.9 shows the capacity retention of the 20 wt% Si electrodes with XG or NaCMC. The CE exceeded 90% after the first cycle, more rapidly than the Si-rich electrodes. In addition, both electrodes had a superior capacity retention as compared to the Si-rich electrodes. The NaCMC-based electrode had a capacity retention of 50% after 100 cycles, compared to only 20% retention with XG. This low retention is surprising considering the good performance previously reported with XG and graphite.[19] Nevertheless, it highlights the critical importance of silicon-binder interactions, regardless of electrode composition or silicon content.

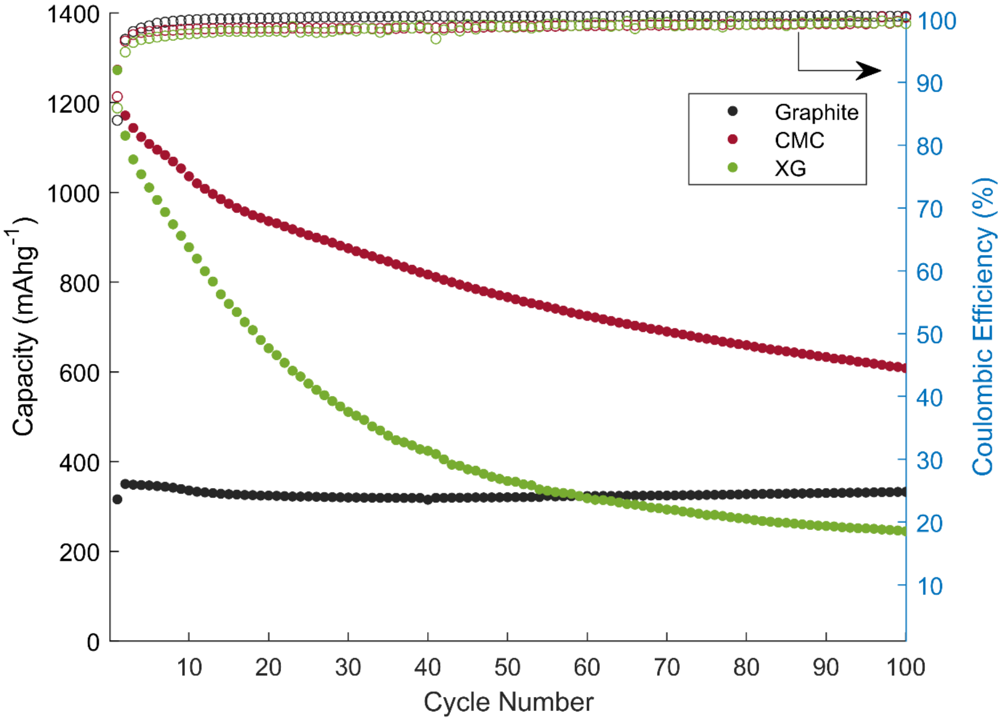

Figure 6.9. Cycling performance of 20 wt% Si + 60 wt% G with XG and NaCMC binders (20Si-10XG and 20Si-10CMC). An SPGPT803 graphite baseline with XG binder is also included. Active material (Si+G) loading of ~2.2 mg cm$^{-2}$.

Figure 6.10 shows the potential profile and dQ/dV plots for the 20Si-10XG and 20Si-10CMC composite electrodes. These electrodes had the broad peaks attributed to silicon lithiation-delithiation as described previously (albeit of reduced intensity owing to the lower Si content). Both NaCMC and XG-based electrodes had a first cycle delithiation peak at 0.43 V, which is attributed to the delithiation of c-$Li_{15}Si_4$. Additional sharp peaks at 0.2 V, 0.1 V, and 0.07 V are attributed to the lithiation of graphite. Delithiation of graphite is marked by the sharp peaks at 0.11 V, 0.15 V, and 0.22 V for both XG and NaCMC.

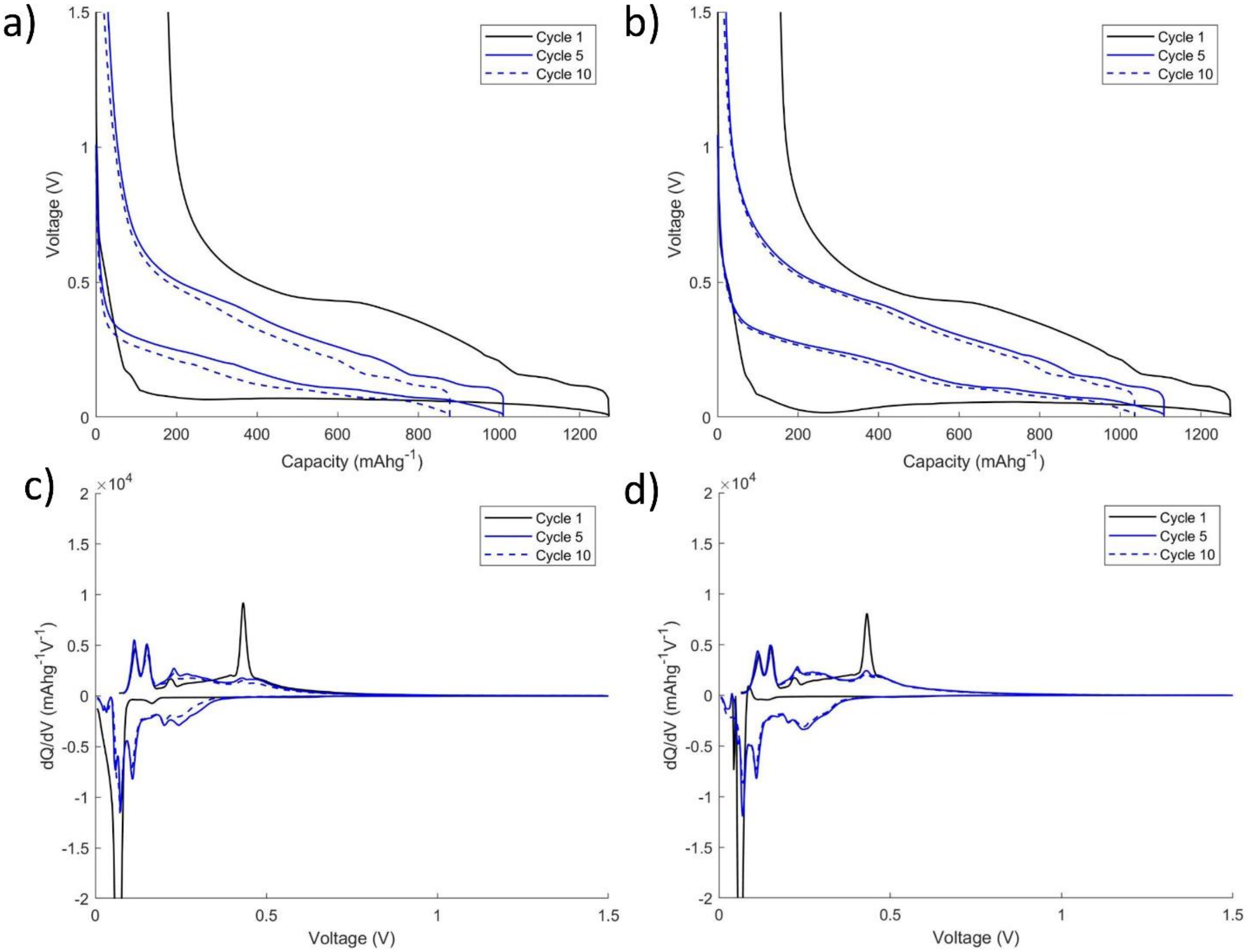

Figure 6.10. Potential profile and differential capacitance plots for 20Si-10XG (a & c) and 20Si-10CMC electrodes (b & d).

SEM images in Figures 6.11 and 6.12 show the cross-sections of pristine and cycled 20Si-10XG and 20Si-10CMC, respectively. At lower magnification the large dense-black spherical masses of graphite can be seen in the backscattered electron images (Figure S6.8). Some flake-like portions of the graphite can be seen at higher magnification (Figures 6.11b and 6.12b), likely due to shearing from the mixing. The silicon particles are distributed throughout the electrode and fill the void spaces between the larger graphite particles (Figure S6.8), contributing to an improved electronic conductivity. Postmortem images (Figures 6.11c and 6.12c) show a sustained compact electrode layer with both binders. The silicon-graphite composites consistently had less fractures and void-spaces compared to the Si-rich electrodes (Figures 6.6 and 6.7), thereby improving active material contact and reducing capacity fade. Superior electrode cohesion is expected with these composites because of the lower silicon content and the buffering contribution from the graphite. The improved electrode health of the composites was also visible to the naked eye. The Cu current collector remained smooth after cycling and should be contrasted with the welting pattern from mechanical stress observed with the Si-rich electrodes (Figure S6.9). Nevertheless, amorphization/electrochemical sintering of the silicon is still seen in Figures 6.11d and 6.12d. Additional SEM and EDX maps are available in the supporting information.

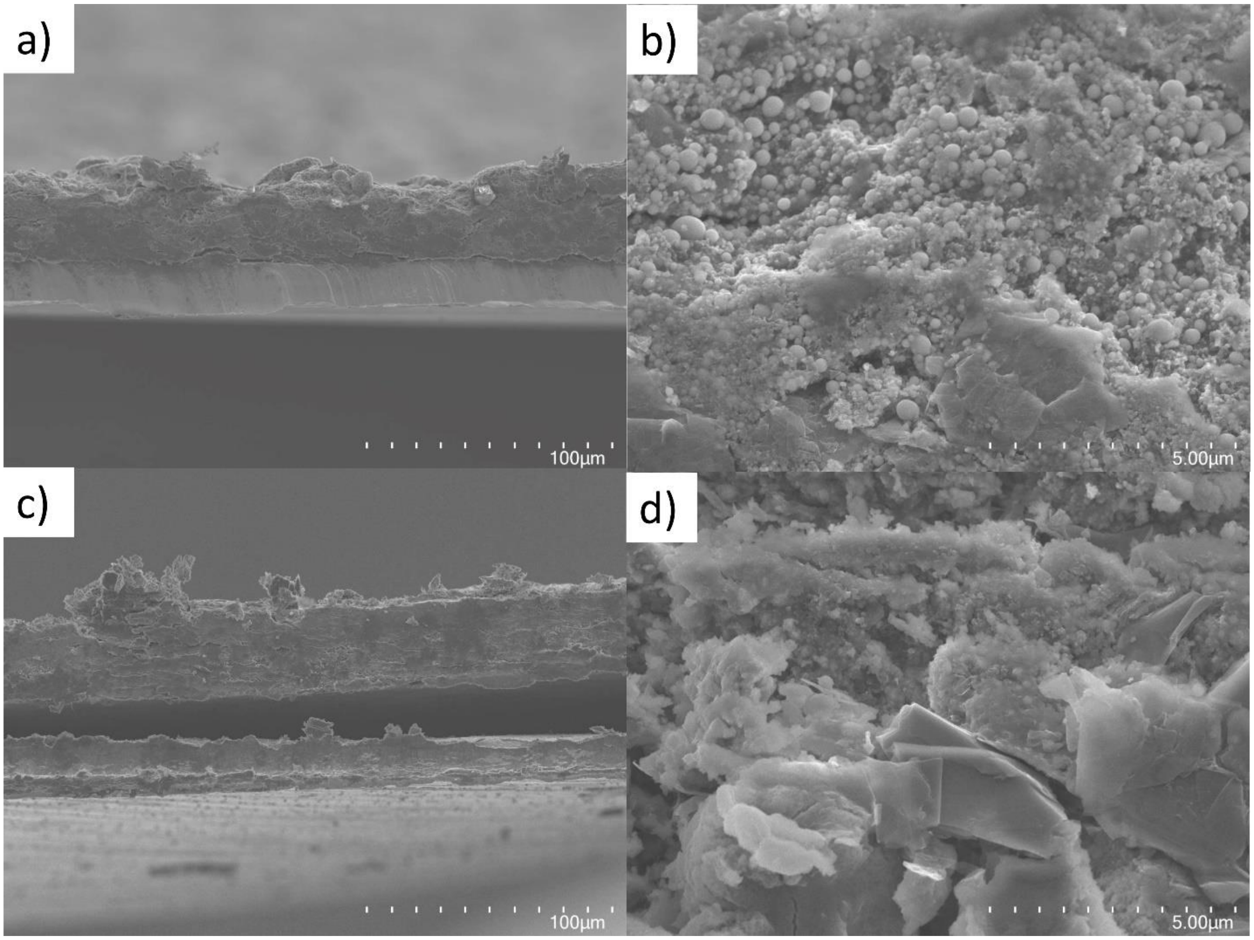

Figure 6.11. SEM cross-sections of an uncycled 20Si-10XG electrode (a & b) and an electrode after 100 cycles at C/10 (c & d). It should be noted that delamination in c) was only observed during SEM characterization.

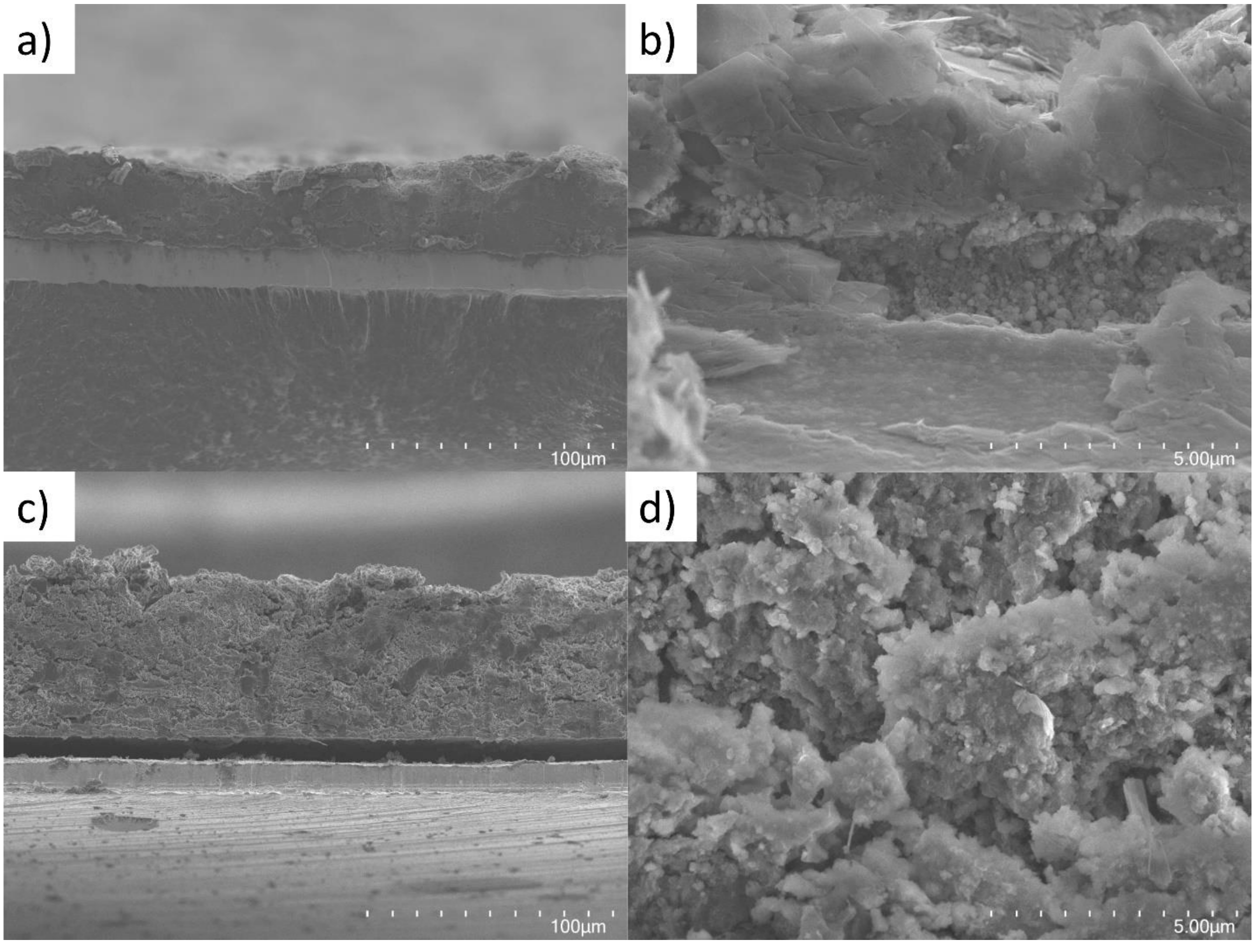

Figure 6.12. SEM cross-sections of an uncycled 20Si-10CMC electrode (a & b) and an electrode after 100 cycles at C/10 (c & d). It should be noted that delamination in c) was only observed during SEM characterization.

## Conclusions

This study compared the unmodified high molecular weight biopolymer binders XG and NaCMC in high silicon (80 wt%) and practical low silicon (20 wt%) composite electrodes. Superior capacity retention was consistently observed with NaCMC as a binder and was attributed to better active layer cohesion, as observed with SEM and EDX. Despite XG's known strong adhesion with the current collector, it was found to provide inferior capacity retention and worsen electrode cohesion. No synergistic effect was seen with a combination of the two binders. Among the best-performing electrodes, 20 wt% silicon and 60 wt% graphite with high Mw NaCMC offered a promising compromise of cost, capacity, and capacity retention and warrants further investigation. Future work will seek to elucidate the complex nature of these binder-silicon surface interactions while testing different types of nano silicon and silicon-graphite composites prepared by industrial-scale methods.

## Acknowledgments

We would like to thank the LiBTec consortium and the Office of Energy Research and Development (OERD) at Natural Resources Canada for financial support under project NRC-0301. Special thanks to Florence Perrin-Sarazin, Jeff Fraser, Oltion Kodra, and Martin Couillard for their help with SEM, XPS, and TEM.

## Author Contributions

Experiment Planning: JS, MT, YAL
Experiment Execution: JS
Manuscript Writing: JS, MT
Consultations and Manuscript Revisions: MT, YAL, ZK, EB, CHY

## References

[1] N. Nitta, F. Wu, J. T. Lee, and G. Yushin, “Li-ion battery materials: Present and future,” *Materials Today*, vol. 18, no. 5, pp. 252–264, 2015, doi: 10.1016/j.mattod.2014.10.040.

[2] M. N. Obrovac and V. L. Chevrier, “Alloy Negative Electrodes for Li-Ion Batteries,” *Chemical Reviews*, vol. 114, no. 23, pp. 11444–11502, Dec. 2014, doi: 10.1021/cr500207g.

[3] N. Liu, H. Wu, M. T. McDowell, Y. Yao, C. Wang, and Y. Cui, “A Yolk-Shell Design for Stabilized and Scalable Li-Ion Battery Alloy Anodes,” *Nano Letters*, vol. 12, no. 6, pp. 3315–3321, Jun. 2012, doi: 10.1021/nl3014814.

[4] M. Wetjen, D. Pritzl, R. Jung, S. Solchenbach, R. Ghadimi, and H. A. Gasteiger, “Differentiating the degradation phenomena in silicon-graphite electrodes for lithium-ion batteries,” *Journal of the Electrochemical Society*, vol. 164, no. 12, pp. A2840–A2852, 2017, doi: 10.1149/2.1921712jes.

[5] X. Zuo, J. Zhu, P. Müller-Buschbaum, and Y. J. Cheng, “Silicon based lithium-ion battery anodes: A chronicle perspective review,” *Nano Energy*, vol. 31, no. October 2016, pp. 113–143, 2017, doi: 10.1016/j.nanoen.2016.11.013.

[6] C.-H. Yim, F. M. Courtel, and Y. Abu-Lebdeh, “A high capacity silicon–graphite composite as anode for lithium-ion batteries using low content amorphous silicon and compatible binders,” *Journal of Materials Chemistry A*, vol. 1, no. 28, p. 8234, Jun. 2013, doi: 10.1039/c3ta10883j.

[7] C.-H. Yim, S. Niketic, N. Salem, O. Naboka, and Y. Abu-Lebdeh, “Towards Improving the Practical Energy Density of Li-Ion Batteries: Optimization and Evaluation of Silicon:Graphite Composites in Full Cells,” *Journal of The Electrochemical Society*, vol. 164, no. 1, pp. A6294–A6302, 2017, doi: 10.1149/2.0481701jes.

[8] V. G. Khomenko and V. Z. Barsukov, “Characterization of silicon- and carbon-based composite anodes for lithium-ion batteries,” *Electrochimica Acta*, vol. 52, no. 8, pp. 2829–2840, Feb. 2007, doi: 10.1016/j.electacta.2006.11.006.

[9] Y. Chen, Z. Gong, J. Liu, L. Gan, and L. Lin, “Journal of Physics and Chemistry of Solids Investigation of the Different Structures of Xanthan Gum on the Performance of Silicon Anodes in Lithium-ion batteries,” *Journal of Physics and Chemistry of Solids*, vol. 165, no. February, p. 110656, 2022, doi: 10.1016/j.jpcs.2022.110656.

[10] Y. K. Jeong, T. Kwon, I. Lee, T.-S. Kim, A. Coskun, and J. W. Choi, “Millipede-inspired structural design principle for high performance polysaccharide binders in silicon anodes,” *Energy & Environmental Science*, vol. 8, no. 4, pp. 1224–1230, 2015, doi: 10.1039/C5EE00239G.

[11] D. Wang *et al.*, “A universal cross-linking binding polymer composite for ultrahigh-loading Li-ion battery electrodes,” *Journal of Materials Chemistry A*, vol. 8, no. 19, pp. 9693–9700, 2020, doi: 10.1039/d0ta00714e.

[12] L. Wei and Z. Hou, “High performance polymer binders inspired by chemical finishing of textiles for silicon anodes in lithium ion batteries,” *Journal of Materials Chemistry A*, vol. 5, no. 42, pp. 22156–22162, 2017, doi: 10.1039/c7ta05195f.

[13] Z. Wang, T. Huang, Z. Liu, and A. Yu, “Dopamine-modified carboxymethyl cellulose as an improved aqueous binder for silicon anodes in lithium-ion batteries,” *Electrochimica Acta*, vol. 389, p. 138806, 2021, doi: 10.1016/j.electacta.2021.138806.

[14] S. Li *et al.*, “A compared investigation of different biogum polymer binders for silicon anode of lithium-ion batteries,” *Ionics*, vol. 27, no. 4, pp. 1829–1836, 2021, doi:

10.1007/s11581-021-03944-y.

[15] X. Zhao, S. Niketic, C.-H. Yim, J. Zhou, J. Wang, and Y. Abu-Lebdeh, “Revealing the Role of Poly(vinylidene fluoride) Binder in Si/Graphite Composite Anode for Li-Ion Batteries,” *ACS Omega*, vol. 3, no. 9, pp. 11684–11690, Sep. 2018, doi: 10.1021/acsomega.8b01388.

[16] J. Niu, S. Kang, S.-T. Myung, C.-H. Jo, A. Konarov, and E. Kendrick, *Future Lithium-ion Batteries*. London: The Royal Society of Chemistry, 2019. doi: 10.1039/9781788016124.

[17] A. Palaniraj and V. Jayaraman, “Production , recovery and applications of xanthan gum by Xanthomonas campestris,” *Journal of Food Engineering*, vol. 106, no. 1, pp. 1–12, 2011, doi: 10.1016/j.jfoodeng.2011.03.035.

[18] F. M. Courtel and Y. Abu-Lebdeh, “Use of Xanthan Gum as an Anode Binder,” 10,483,546 B2, 2019

[19] F. M. Courtel, S. Niketic, D. Duguay, Y. Abu-Lebdeh, and I. J. Davidson, “Water-soluble binders for MCMB carbon anodes for lithium-ion batteries,” *Journal of Power Sources*, vol. 196, no. 4, pp. 2128–2134, 2011, doi: 10.1016/j.jpowsour.2010.10.025.

[20] J. He, H. Zhong, J. Wang, and L. Zhang, “Investigation on xanthan gum as novel water soluble binder for LiFePO4 cathode in lithium-ion batteries,” *Journal of Alloys and Compounds*, vol. 714, pp. 409–418, 2017, doi: 10.1016/j.jallcom.2017.04.238.

[21] Y. Lai *et al.*, “Revisit the Progress of Binders for a Silicon-Based Anode from the Perspective of Designed Binder Structure and Special Sized Silicon Nanoparticles,” *Industrial and Engineering Chemistry Research*, 2022, doi: 10.1021/acs.iecr.2c00453.

[22] Z. Karkar *et al.*, “How silicon electrodes can be calendered without altering their mechanical strength and cycle life,” *Journal of Power Sources*, vol. 371, 2017, doi: 10.1016/j.jpowsour.2017.10.042.

[23] A. Roland, B. Delarre, J.-B. Ledeuil, N. Louvain, H. Martinez, and L. Monconduit, “Silicon-based electrodes formulation in buffered solution for enhanced electrode-electrolyte interfaces,” *Journal of Power Sources*, vol. 489, p. 229465, 2021, doi: https://doi.org/10.1016/j.jpowsour.2021.229465.

[24] Tekna, “Tekna.com,” 2020.

[25] N. Lingappan, L. Kong, and M. Pecht, “The significance of aqueous binders in lithium-ion batteries,” *Renewable and Sustainable Energy Reviews*, vol. 147, no. April, p. 111227, 2021, doi: 10.1016/j.rser.2021.111227.

[26] E. N. Primo, M. Chouchane, M. Touzin, P. Vazquez, and A. A. Franco, “Understanding the calendering processability of Li(Ni0.33Mn0.33Co0.33)O2-based cathodes,” *Journal of Power Sources*, vol. 488, p. 229361, Mar. 2021, doi: 10.1016/j.jpowsour.2020.229361.

[27] T. Waldmann *et al.*, “Review—Post-Mortem Analysis of Aged Lithium-Ion Batteries: Disassembly Methodology and Physico-Chemical Analysis Techniques,” *Journal of The Electrochemical Society*, vol. 163, no. 10, pp. A2149–A2164, Aug. 2016, doi: 10.1149/2.1211609jes.

[28] N. Cuesta, A. Ramos, I. Cameán, C. Antuña, and A. B. García, “Hydrocolloids as binders for graphite anodes of lithium-ion batteries,” *Electrochimica Acta*, vol. 155, pp. 140–147, 2015, doi: 10.1016/j.electacta.2014.12.122.

[29] Z. Karkar, D. Mazouzi, C. R. Hernandez, D. Guyomard, L. Roué, and B. Lestriez, “Threshold-like dependence of silicon-based electrode performance on active mass loading and nature of carbon conductive additive,” *Electrochimica Acta*, vol. 215, pp. 276–288, 2016, doi: 10.1016/j.electacta.2016.08.118.

[30] S. D. Beattie, D. Larcher, M. Morcrette, B. Simon, and J.-M. Tarascon, “Si Electrodes for Li-Ion Batteries—A New Way to Look at an Old Problem,” *Journal of The Electrochemical Society*, vol. 155, no. 2, p. A158, 2008, doi: 10.1149/1.2817828.

[31] D. Mazouzi *et al.*, “Critical roles of binders and formulation at multiscales of silicon-based composite electrodes,” *Journal of Power Sources*, vol. 280, pp. 533–549, 2015, doi: 10.1016/j.jpowsour.2015.01.140.

[32] M. J. Loveridge *et al.*, “Towards High Capacity Li-ion Batteries Based on Silicon-Graphene Composite Anodes and Sub-micron V-doped LiFePO 4 Cathodes,” *Scientific Reports*, vol. 6, no. March, pp. 1–11, 2016, doi: 10.1038/srep37787.

[33] N. A. Dunlap, S. Kim, J. J. Jeong, K. H. Oh, and S.-H. Lee, “Simple and inexpensive coal-tar-pitch derived Si-C anode composite for all-solid-state Li-ion batteries,” *Solid State Ionics*, vol. 324, pp. 207–217, Oct. 2018, doi: 10.1016/j.ssi.2018.07.013.

[34] A. Ulvestad *et al.*, “Crystallinity of Silicon Nanoparticles: Direct Influence on the Electrochemical Performance of Lithium Ion Battery Anodes,” *ChemElectroChem*, vol. 7, no. 21, pp. 4349–4353, 2020, doi: 10.1002/celc.202001108.

[35] C. Y. Wang, Y. S. Meng, G. Ceder, and Y. Li, “Electrochemical Properties of Nanostructured Al[sub 1−x]Cu[sub x] Alloys as Anode Materials for Rechargeable Lithium-Ion Batteries,” *Journal of The Electrochemical Society*, vol. 155, no. 9, p. A615, 2008, doi: 10.1149/1.2943215.

[36] N. S. Hudak and D. L. Huber, “Size Effects in the Electrochemical Alloying and Cycling of Electrodeposited Aluminum with Lithium,” *Journal of The Electrochemical Society*, vol. 159, no. 5, pp. A688–A695, 2012, doi: 10.1149/2.023206jes.

[37] Y. Kim, S. Sim, and S. W. Lee, “Nucleation and Growth of Lithium–Silicon Alloy on Crystalline Silicon,” *Advanced Engineering Materials*, vol. 21, no. 5, pp. 1–5, 2019, doi: 10.1002/adem.201800520.

[38] N. Dimov, S. Kugino, and M. Yoshio, “Mixed silicon–graphite composites as anode material for lithium ion batteries: Influence of preparation conditions on the properties of the material,” *Journal of Power Sources*, vol. 136, no. 1, pp. 108–114, 2004, doi: https://doi.org/10.1016/j.jpowsour.2004.05.012.

[39] L. Zhang, X. Jiao, Z. Feng, B. Li, Y. Feng, and J. Song, “A nature-inspired binder with three-dimensional cross-linked networks for silicon-based anodes in lithium-ion batteries,” *Journal of Power Sources*, vol. 484, no. November 2020, p. 229198, 2021, doi: 10.1016/j.jpowsour.2020.229198.

[40] N. Li, Hong; Huang, Xuejie; Chen, Liquan; Zhou, Guangwen; Zhang, Ze; Yu, Dapeng; Mo, Yu Jun; Pei, “The crystal structure evolution of nano-Si anode caused by lithium insertion and extraction at room temperature,” *Solid State Ionics*, vol. 135, no. 1, pp. 181–191, 2000.

[41] S. Chae, M. Ko, K. Kim, K. Ahn, and J. Cho, “Confronting Issues of the Practical Implementation of Si Anode in High-Energy Lithium-Ion Batteries,” *Joule*, vol. 1, no. 1. Cell Press, pp. 47–60, Sep. 06, 2017. doi: 10.1016/j.joule.2017.07.006.

[42] D. J. Pereira, J. W. Weidner, and T. R. Garrick, “The Effect of Volume Change on the Accessible Capacities of Porous Silicon-Graphite Composite Anodes,” *Journal of The Electrochemical Society*, vol. 166, no. 6, pp. A1251–A1256, 2019, doi: 10.1149/2.1211906jes.

[43] M. Wetjen *et al.*, “Monitoring the Lithium Concentration across the Thickness of Silicon-Graphite Electrodes during the First (De-)Lithiation,” *Journal of The Electrochemical*

*Society*, vol. 166, no. 8, pp. A1408–A1411, 2019, doi: 10.1149/2.0581908jes.
[44] M. Yoshio, R. J. Brodd, and A. Kozawa, "Lithium-Ion Batteries," New York: Springer US, 2009, p. 50.

# Chapter 7: Composites of Silicon@$Li_4Ti_5O_{12}$ and Graphite for High-Capacity Lithium-Ion Battery Anode Materials

James Sturman[1, 2], Yong Zhang[3], Chae-Ho Yim[1], Svetlana Niketic[1], Mathieu Toupin[4], Elena A. Baranova[2], and Yaser Abu-Lebdeh[1, Z]

1. Energy, Mining, and Environment Research Centre, National Research Council of Canada, 1200 Montreal Road, Ottawa, Ontario K1A 0R6, Canada
2. Department of Chemical and Biological Engineering, Centre for Catalysis Research and Innovation (CCRI), University of Ottawa, 161 Louis-Pasteur, Ottawa ON, K1N 6N5, Canada
3. School of Materials Science and Engineering, Hefei University of Technology, 193 Tunxi Road, Hefei, Anhui, 230009, China
4. Automotive and Surface Transportation Research Centre, National Research Council of Canada, 75 de Mortagne Blvd. J4B 6Y4, Boucherville (QC), Canada

Publication status: published
Adapted from DOI 10.1149/1945-7111/abda05

## Abstract

Silicon (Si) is a promising anode material for lithium-ion batteries owing to its high theoretical capacity. However, it suffers from poor capacity retention during cycling due to mechanical stresses, pulverization, and an unstable solid electrolyte interface. One practical approach to mitigate the problem is a coating design, where nano-sized silicon is encapsulated within a selected protective layer. In this study, silicon nanoparticles have been coated with a protective layer of $Li_4Ti_5O_{12}$ (LTO) ceramic and prepared using a water-based sodium alginate binder. It is found that the Si@LTO composites can be combined with graphite to improve battery performance further. The composite electrodes have been tested in half cells at C/10 and 1C rates. The best Si@LTO and graphite composite has an initial high capacity (~900 mAh $g^{-1}$ at C/10 and ~600 mAh $g^{-1}$ at 1C) and good capacity retention. It is found that this capacity retention is superior to Si@LTO alone and a binary composite of silicon with graphite. These Si@LTO + graphite composites are a promising way to integrate silicon into the development of stable and high-

energy-density lithium-ion batteries.

## Introduction

Lithium-ion batteries for long-range electric automobiles require anode materials with a higher specific capacity than traditional graphite (G).[1] Next-generation materials should have both a high gravimetric capacity and capacity retention upon cycling.[1] Silicon (Si) is a promising material for the anode as it has a theoretical capacity nearly 10 times greater than graphite (3579 mAh $g^{-1}$ for $Li_{15}Si_4$).[2,3] However, pure silicon suffers from severe volumetric expansion (up to 300%) and pulverization during lithiation and delithiation.[4] Unlike intercalation-based anodes like graphite, the alloying of silicon and lithium is responsible for such a large change in volume.[5] This expansion increases the surface area of the material and leads to the production of new Solid Electrolyte Interface (SEI) during each cycle.[6,7] This not only consumes the electrolyte but also reduces the capacity of the silicon over time and makes it difficult to commercialize full cells.[8] Therefore, much of the current work surrounding silicon anodes consists of improving capacity retention through composite electrodes and morphological changes to the material.[9,10] One example is 0D silicon nanoparticles with a high specific surface area.[11,12] Silicon nanoparticles are known to exhibit better capacity retention owing to a reduction in the pulverization of the individual particles relative to micron-silicon.[9] Some other low dimensional silicon microstructures have been investigated as well. For example, 1D silicon nanotubes and nanowires facilitate electron transport and possess superior strain relaxation because of their high aspect ratio.[9,13–15] 2D silicon nanosheets and films have been studied because of their high surface area and suppressed volume expansion.[16,17] Finally, 3D matrix architectures with carbon or metal oxides have accumulated interest owing to their robust structure and long-term cyclability.[4,18–20] Nevertheless, most of the work involving 1D and 2D structures require complex synthesis techniques that are not well-suited for large-scale production.[9] Silicon nanoparticles, as well as silicon-carbon matrix composites, offer the most scalable solutions to improve the technology readiness level of the silicon anode.

Construction of a core–shell architecture is a proven solution to buffer some of the volumetric expansion of silicon and improve cyclability.[21–24] Historically, carbon has been employed as a shell to coat silicon nanoparticles.[9] However, the carbon can also suffer from poor mechanical stability upon expansion of the silicon.[22] Coating silicon with ceramics like $TiO_2$ and

$Al_2O_3$ have shown a reduction in silicon fracture during cycling and a reduction in electrode-electrolyte side-reactions.[25,26] This protective effect facilitates the formation of a stable SEI and improves capacity retention over time.[25,26] Another metal oxide, $Li_4Ti_5O_{12}$ (LTO), has been used as an anode material for lithium-ion batteries owing to its high rate capability and low volumetric expansion upon lithiation.[27] However, pristine LTO has a low energy density (capacity of 175 mAh $g^{-1}$) and a high redox potential (1.5 V vs Li), which has restricted its capability in high-energy-density applications.[5] When LTO is combined with silicon, the resulting composite benefits from the high-capacity associated with silicon and the protective effects of LTO.[28–32] Silicon and LTO can be prepared in a coating design, as shown in Figure 7.1. The LTO may be formed at the silicon surface by a sol-gel approach, spray-pyrolysis, or the silicon and LTO can simply be combined with ball milling.[28,30,31] However, previous studies have required a high loading of binder (20 wt%) or made composites with expensive active materials like carbon nanotubes.[30,31] In this study, a sol-gel technique was used to coat silicon nanoparticles with LTO (denoted Si@LTO) by modifying a procedure described previously.[31] Active material was fixed at 80 wt% and only 10 wt% binder was used. Improvement to the cycle stability of the electrode was achieved by adding low-cost graphite or pitch-source carbon to the composite. The graphite provides capacity, improves conductivity, and serves as an additional measure to buffer some of the volumetric expansion of the silicon-rich electrode.[33] The combination of graphite and Si@LTO, together with a simple water-based sodium alginate binder, is shown to be an economical and application-oriented approach to increase the energy density of lithium-ion batteries.

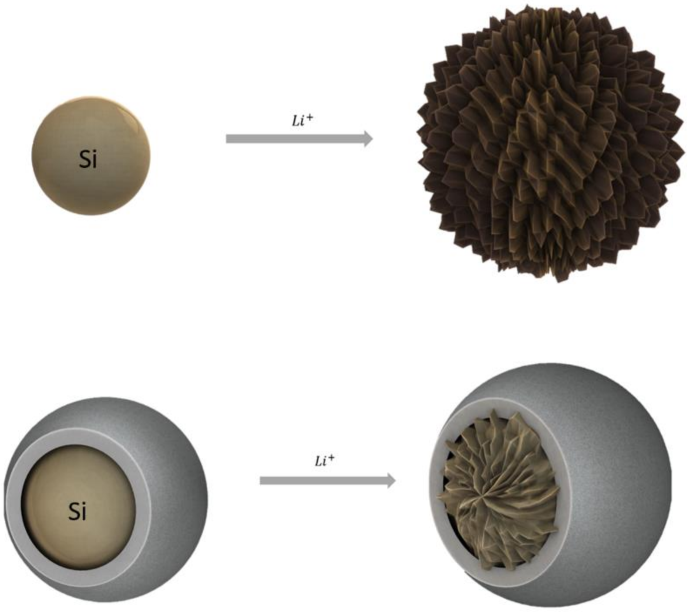

Figure 7.1. Animation of a silicon particle (top) and an ideal Si@LTO particle (bottom) upon lithiation

## Experimental

### Materials

Silicon nanopowder 99.9% (average diameter: 100 nm) was obtained from CW nano. Titanium isopropoxide (95%), sodium alginate, lithium acetate dihydrate (99.99%) were purchased from Aladdin and Sigma-Aldrich. Graphite powder (1000 mesh) was obtained from XF Nano. Natural pitch and Super P were obtained from Guangdong Canrd New Energy Technology Co. Ltd. Hydrogen peroxide (30%) was obtained from SCR Chemicals Ltd. and Sigma-Aldrich. MAGD artificial spherical graphite was obtained from Hitachi. Silicon nanopowder (average diameter: 50 nm) was purchased from Nanostructured and Amorphous Materials Inc.

### Preparation of the Si@LTO anode material

The Si@LTO synthesis method and the Si-LTO ratios were modified from a procedure described previously.[31] Silicon nanoparticles were vacuum dried at 80 °C overnight to remove trapped moisture. The sample with the Si:Li:Ti stoichiometric ratio of 17:2:1.25 is denoted *thin Si@LTO*, whereas the sample with the ratio of 17:8:5 is denoted *thick Si@LTO*. The silicon nanoparticles were added to a beaker with 15 ml of 30% $H_2O_2$. The hydrogen peroxide treatment activates the surface of the silicon with a hydroxyl group which facilitates the mixing of the silicon particles with the Li and Ti precursors.[31] The mixture was sonicated for 15 min to reduce agglomeration and then dried at 70 °C. The dried particles were ground and transferred to a beaker with the lithium acetate and 10 ml of ethanol. The mixture was sonicated for 10 s and then stirred for 1 h. Finally, titanium isopropoxide was added to the solution and sonicated for 10 s. After 2 h of stirring, the solution was dried at 70 °C for 3 h until all the ethanol had evaporated. The dried powder was ground and transferred to a tube furnace that was then purged with argon. The powder was calcined under argon for 12 h at 610 °C and then cooled to room temperature under argon. A light brown powder was obtained.

### Preparation of Si@LTO@C anode material

The pitch sample was known to produce a carbon residue of ∼60 wt% of its initial mass after the pyrolysis treatment used in this study. The Si@LTO powder was coated with approximately 20 wt% carbon residue using the pitch source. The pitch was dissolved in N-Methyl-2-pyrrolidone solvent. The solution was combined with Si@LTO and stirred overnight. The solution was then dried to evaporate NMP, and the resulting powder was calcined for 5 h at 600 °C in an atmosphere consisting of argon with 5% $H_2$. A black powder was obtained. This low temperature was selected to avoid reducing the LTO and limit the formation of silicon carbide, which is known to be inactive for lithiation.[34] Pitch has previously been shown to carbonize at 600°C.[35]

### Electrode assembly

The mass percent of active material in all electrodes was fixed at 80 wt%. This includes the mass of either Si + G, Si@LTO, Si@LTO@C, or x·Si@LTO + y·graphite ($x = 0.6$ or $0.4$, $y = 0.8 - x$). The remaining electrode mass consisted of 10 wt% sodium alginate binder and 10 wt% Super P. Sodium alginate was selected as a binder because it is environmentally friendly and has proven good cycle performance with nano silicon.[12] Water was used as a solvent, and the solution was mixed with a mortar and pestle until a homogeneous slurry was formed. The slurry was then applied to a sheet of copper foil using a notch bar. The electrode material was then vacuum dried at 80 °C overnight. Individual electrode disks were cut (12.5 mm diameter). The active material loading was between 1.25–2 mg $cm^{-2}$. Coin cell assembly was done in an argon-filled glove box ($O_2$ < 0.1 ppm, $H_2O$ < 0.1 ppm) using 2032 type coin cells. A lithium metal foil was used as a reference and counter electrode. The electrolyte was 1 M $LiPF_6$ in EC:EMC (1:1 v/ v) + 10%

FEC unless otherwise stated. One polypropylene membrane (Celgard 2500) was used as a separator. Coin cells were allowed to rest for at least 12 h before testing.

Physicochemical characterization

Galvanostatic experiments were done at 30 °C in either a Landt or Arbin BT2000 battery cycler in the potential range of 0.005 V to 1.5 V. This potential window is suitable for silicon and graphite lithiation, which are the primary electrochemically active species in the electrode.[33] A 15-minute open-circuit rest was included at each potential limit. The batteries were charged/discharged symmetrically at C/10 for the first 10 cycles, followed by 90–100 cycles at 1C. The specific capacity at C/10 was used to calculate the charging rates of each composite electrode. The term *capacity retention* refers only to the capacity retention at 1C and does not include the sudden decline in capacity when the charging rate was increased from C/10 to 1C. Impedance measurements in the frequency range from 100 kHz to 10 mHz were done with a Biologic Potentiostat. The morphology was characterized by Field Emission Scanning Electron Microscopy (SEM) with a Hitachi SU8020 or SU5000 microscope. Transmission Electron Microscopy (TEM) was done with a JEM-2100F or FEI Titan-3 80–300 microscope. Elemental distribution was quantified with the Energy Dispersive X-ray (EDX) Spectroscopy Analyzer X-Max Oxford Instruments. The powder X-Ray Diffraction (XRD) was done with a Bruker AXS D8 diffractometer (Cu Kα, $\lambda = 0.154$ nm) between 10° and 85° 2θ.

## Results and Discussion

The names of the different samples are summarized in Table 7.1. First, the thick (Si@LTO-1) and thin (Si@LTO-2) coatings were tested. Second, graphite (either 20 or 40 wt%) was added to the thick (Si@LTO-3a and b) and thin (Si@LTO-4a and b) coatings. Pyrolysis with pitch was also used to embed the thick (Si@LTO- 5) and thin (Si@LTO-6) Si@LTO in a carbon matrix. The cycling data for these trials can be found in supplemental information.

Table 7.1: Sample Nomenclature

| Sample ID | Composition |
|---|---|
| B1 | Nano Si |
| B2 | 40% Si + 40% G |
| B3 | Graphite |
| B4 | 20% Si + 60% G |

| | |
|---|---|
| Si@LTO-1 | Thick Si@LTO |
| Si@LTO-2 | Thin Si@LTO |
| Si@LTO-3a | Thick 60% Si@LTO + 20% G |
| Si@LTO-3b | Thick 40% Si@LTO + 40% G |
| Si@LTO-4a | Thin 60% Si@LTO + 20% G |
| Si@LTO-4b | Thin 40% Si@LTO + 40% G |
| Si@LTO-4b* | Improved Thin 40% Si@LTO + 40% G |
| Si@LTO-5 | Thick Si@LTO@C |
| Si@LTO-6 | Thin Si@LTO@C |

### Physical characterization

The XRD pattern of the raw powder for Si@LTO-2 is shown in Figure 7.2. The presence of both Si and LTO is observed. Diffraction peaks of silicon are seen with the 2θ at 28°, 47°, 56°, 69°, and 76°, while peaks attributed to LTO are seen at 18°, 36°, 43°, and 63°. The standard cards for both LTO (COD #1001098) and silicon (COD #4104917) are included from the Crystallographic Open Database.[36] Diffraction peaks around 24° and 33° are attributed to the presence of trace lithium silicate and are described elsewhere.[31] Lithium silicate is also part of the coating design and has been reported to be electrochemically stable, aid in the prevention of silicon fractures, and facilitate a stable SEI.[31] The peak at 41° is possibly a Li-Si alloy and is currently being investigated further. During the synthesis, it was important to perform the calcination of the Si@LTO precursor in an inert atmosphere. Failure to do this will oxidize the material to $SiO_2$ and $TiO_2$. As a result, the oxygen for the formation of LTO must be derived solely from the native $SiO_2$ layer on the silicon nanoparticles, and the lithium and titanium organic precursors. SEM of the raw powders of Si@LTO-1 and Si@LTO-2 particles are seen in Figure 7.3. The micron-sized particles had an irregular texture as a result of the different agglomerations of Si@LTO particles. Better resolution of the silicon nanoparticle morphology is seen with the Si@LTO-2 coating because of the smaller quantity of LTO in the material (Figure 7.3b). Agglomeration was reduced in later experiments, described in the Improved Synthesis section. EDX of the Si@LTO-2 raw powder in Figure 7.4 revealed a uniform distribution of silicon, titanium, and oxygen. This observation is consistent with the desired design as the titanium and oxygen are coating silicon particles.[29] Some carbon signals were also detected due to residue carbon from the precursors after calcination. TEM was done to further confirm the coating design. Figure 7.5 is a TEM image of the Si@LTO-1 sample and shows a silicon particle encapsulated in an LTO coating. The FFT and HRTEM images confirm the presence of LTO and silicon. A TEM image of Si@LTO-2 is also seen in Figure S7.1. EDX spectrum results of Si@LTO-1 in Figure S7.2 was also used to confirm the coating architecture. It reveals the dark center phase to be silicon rich, and the light coating phase to be titanium and oxygen rich.

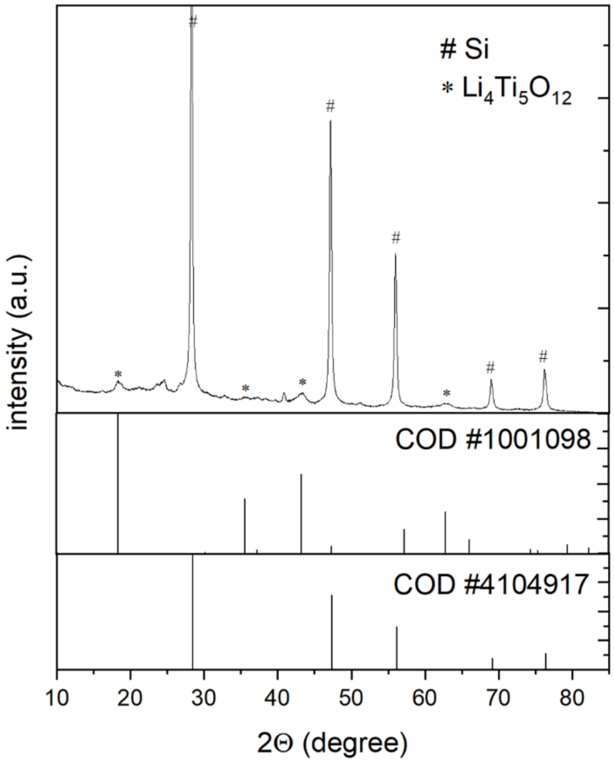

Figure 7.2. XRD pattern of the raw powder of Si@LTO-2

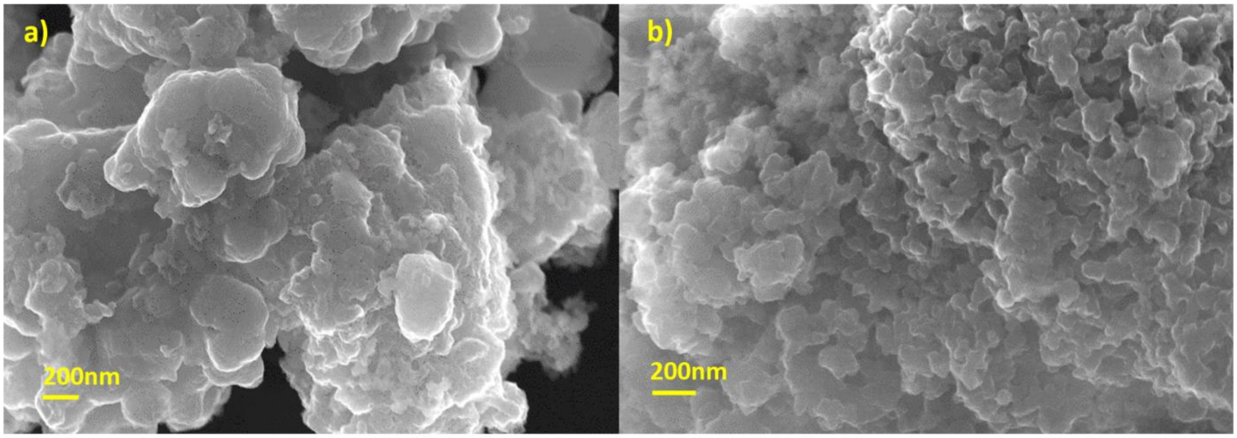

Figure 7.3. SEM of raw powders of (a) Si@LTO-1 and (b) Si@LTO-2

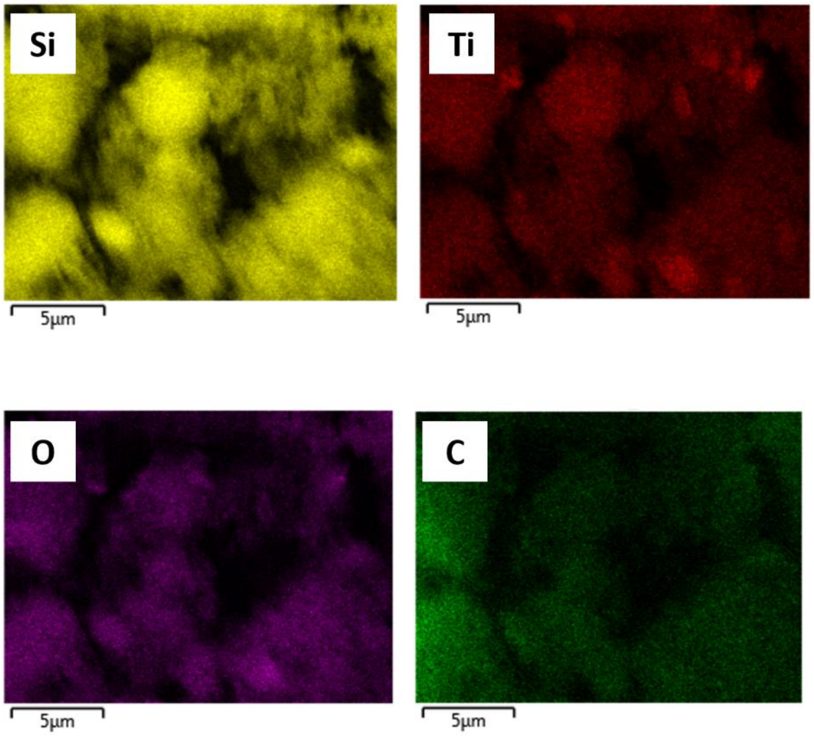

Figure 7.4. EDX of the raw powder of Si@LTO-2. Note: lithium not distinguishable with EDX analysis

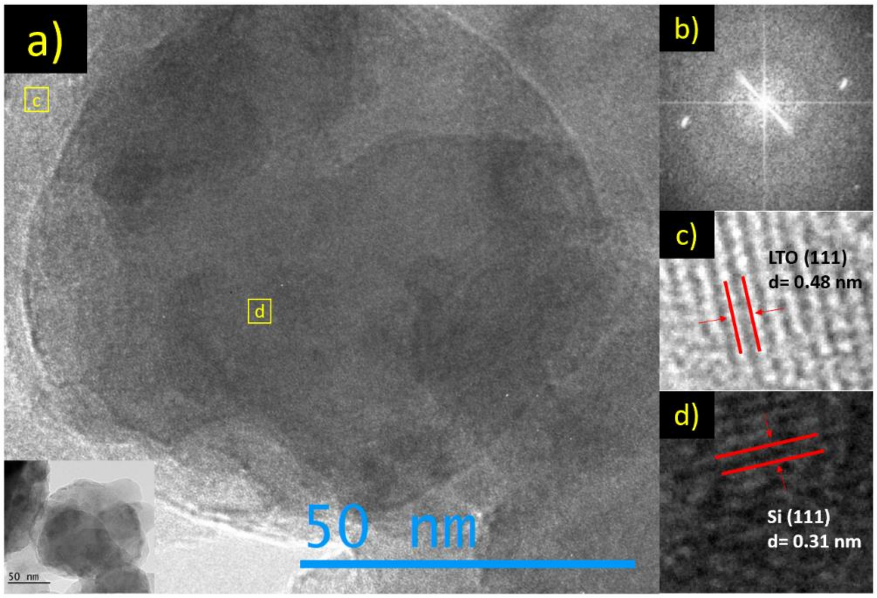

Figure 7.5. (a) TEM of the raw powder of Si@LTO-1. (b) FFT of the LTO phase for (c) HRTEM image of LTO lattice fringes. (d) HRTEM of Si lattice fringes. Thick Si@LTO was imaged to observe greater resolution of the coating.

Electrochemical characterization

The electrochemical data presented in this section plots the active material delithiation capacity as a function of cycle number. The coulombic efficiency for each cycle is plotted as hollow squares. The first 10 cycles are at a rate of C/10 and were used to precondition the coin cell. Thereafter, the charging rate was increased to 1C to study the capacity retention of the composite at a high current density. Figure 7.6a shows the baseline values for Si@LTO-1 and Si@LTO-2 electrodes. A nano silicon baseline trial (B1) is also present, which is seen to fail within 10 cycles. Si@LTO-2 material has a higher inherent capacity because it has a smaller LTO content and hence, a greater specific mass fraction of silicon. Although this composite has an initial high capacity of 1200 mAh $g^{-1}$, it shows poor capacity retention at C/10 and rapid failure at 1C. The performance was nevertheless superior to the uncoated nano silicon baseline. In contrast, Si@LTO-1 has a greater specific mass fraction of LTO, which lowers the silicon content and reduces the inherent capacity. However, this sample was found to increase the capacity retention of the electrode, as marked by the superior performance at 1C. These trends are consistent with a previous study of Si@LTO by Lee et al. and suggest the LTO coating can help buffer some of the volumetric expansion of the silicon.[31]

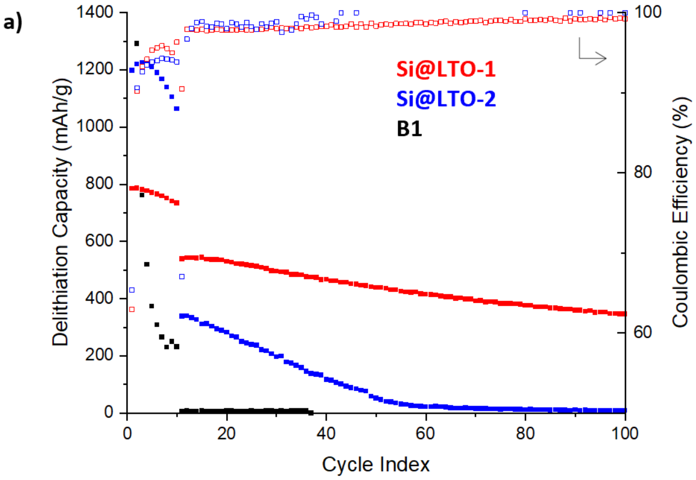

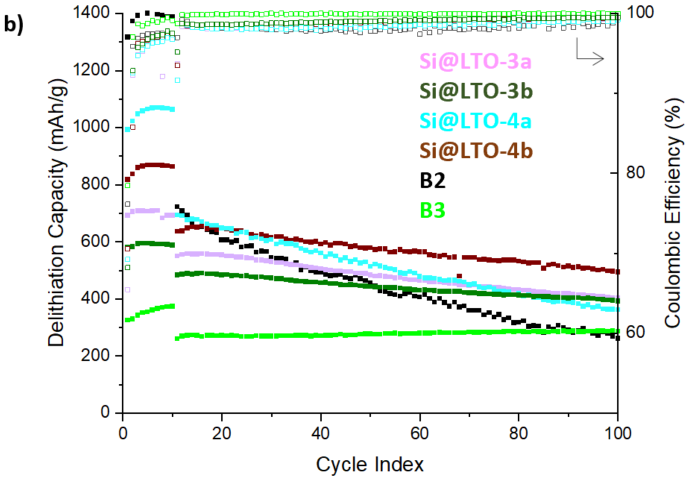

Figure 7.6. (a) Galvanostatic cycling of Si@LTO-1 and Si@LTO-2 composites and (b) Si@LTO-3 and Si@LTO-4 composites. A baseline trial consisting of 80 wt% graphite is shown as B3. A baseline trial of 40 wt% nano Si with 40 wt% graphite is also included as B2. First 10 cycles at a charge rate of C/10, followed by 1C.

To evaluate capacity and capacity retention of the composites, Si@LTO-1 and Si@LTO-2 were combined with graphite (denoted Si@LTO + G) to identify an ideal trade-off between these two measures of performance. Composites of silicon and graphite are a well-established economical way to buffer the volumetric expansion of the silicon and reduce delamination from the current collector.[8,37,38] This allows the composites to provide a high practical capacity that is greater than graphite but lower than silicon alone.[37] For example, an active material capacity of 1170 mAh $g^{-1}$ is expected with 20 wt% Si and 60 wt% graphite. However, the capacity retention is greater than silicon but less than graphite alone. Four different combinations of

Si@LTO + G were tested (Si@LTO-3a and b, and Si@LTO-4a and b from Table 7.1). The graphite content was either 20 or 40 wt% for both the thick and thin Si@LTO. Figure S7.3 shows the XRD patterns for all four composites and confirms the presence of the silicon, LTO, and graphite. Figure S7.4 shows SEM and EDX images of the cross section of Si@LTO-4b and illustrates the morphology of the prepared composite electrode. Figure 7.6b shows the electrochemical performance of the different Si@LTO electrodes with graphite. A baseline silicon-graphite composite electrode (denoted B2) showed an initial stable performance at C/10. However, a capacity retention of 35% was observed after 90 cycles at 1C. All Si@LTO + G composites had a higher capacity and capacity retention after 90 cycles compared to the B2 baseline and the Si@LTO baselines (from Figure 7.6a). This confirms the stabilizing benefit of graphite as applied to the Si@LTO. Special attention should be given to Si@LTO-4b, which had a high final capacity (~500 mAh $g^{-1}$) and capacity retention of 75% after 90 cycles at 1C. SEM of the electrode disks before and after cycling for Si@LTO-4b and the B2 baseline are shown in Figure S7.5. The images confirm a reduction in electrode pulverization and expansion for the Si@LTO-4b electrode relative to the simple binary Si-G composite (B2).

The use of a carbon matrix was also employed to improve the stability of the Si@LTO material. The pyrolysis of pitch with Si@LTO can give rise to a uniform distribution of carbon throughout the electrode material (denoted Si@LTO@C). It was thought this might buffer the volumetric expansion better than graphite. Pitch was selected as a carbon source because it is abundant and can produce soft carbon upon pyrolysis.[35] Soft carbon is a graphitizable form of carbon that consists of layers of crystalline carbon and typically has a higher specific capacity than hard carbons.[39] Cycling data for the carbon treated samples can be found in supplementary information of Figure S7.6. Both Si@LTO-5 and Si@LTO-6 had better capacity and capacity retention after 90 cycles as compared to their baselines without carbon treatment (e.g. 72% retention for thick Si@LTO@C vs 63% for thick Si@LTO). However, this cyclability improvement is comparable to trials with the simple addition of graphite. As a result, subsequent experiments focused only on composites of Si@LTO with graphite.

### Improved synthesis and characterization

An alternative synthesis method was employed to reduce particle agglomeration and improve cycle performance. The electrode composition of sample Si@LTO-4b from Table 7.1 was selected for subsequent experiments and will be denoted Si@LTO-4b* henceforward. This composite showed the best compromise between electrochemical performance and scalability. First, a thin LTO coating gives a greater inherent capacity and requires less organic lithium and titanium precursors. Second, the direct addition of graphite to an electrode slurry is more scalable than a pyrolysis treatment to embed the Si@LTO in a carbon matrix. In the following experiments, the average diameter of the nanoparticles was reduced to ∼50 nm to increase surface area and reduce pulverization, and MAGD spherical graphite was used due to its proven electrochemical performance and widespread availability. The electrode slurry was also mixed for 45 min at 2000 rpm in a Thinky planetary mixer to improve the homogeneity of the slurry. The silicon stoichiometric ratio was reduced to Si:Li:Ti 16:2:1.25 to account for the different silicon nanoparticles. SEM images in Figures S7.7 and S7.8 confirm a reduction in agglomeration for the raw powder of Si@LTO-2 particles synthesized by this alternative method. It should be acknowledged that changes in the silicon and graphite type have contributed to slight changes in cycle behaviour between the coin cells in this section and those in Figure 7.6. AC Impedance Spectroscopy was used to compare the internal resistance of the Si@LTO-4b* and a baseline B4 composite. The Nyquist plot in the frequency range from 100 kHz to 10 mHz is seen in Figure 7.7 Impedance measurements were on cycled cells in potentiostatic mode at their open circuit potential of ∼0.5 V. The lower resistance in Si@LTO-4b* relative to B4 is attributed to a reduced SEI.[31] This is consistent with a reduction in the pulverization of the silicon particles and supports the stabilizing contribution of LTO to the composite.[19,31]

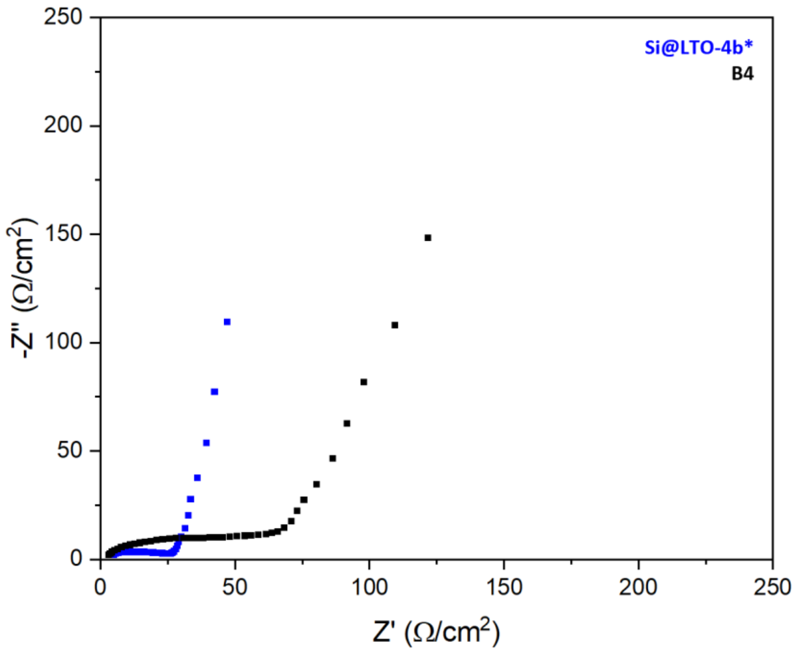

Figure 7.7. Nyquist plot for the impedance of Si@LTO-4b* and B4. The graphite mass fraction of B4 has been adjusted to ensure the specific capacity of both samples was normalized to ~1000 mAh/g. Impedance was on cycled cells at a potential of 0.5V.

Figure 7.8 shows long-term cyclability of the Si@LTO-4b* composite with 1 M $LiPF_6$ in EC:DEC (1:1 v/v) + 10% FEC electrolyte. This electrolyte showed better long-term cyclability compared to the EMC electrolyte used in prior tests. The sample shows an initial capacity around 900 mAh $g^{-1}$ at C/10. Upon cycling at 1C, the capacity was maintained around 600 mAh $g^{-1}$ for a period of 40 cycles. After 100 cycles at 1C, a stable capacity of 800 mAh $g^{-1}$ was still observed at C/10. The material showed a relatively high initial coulombic efficiency of 75%. The initial coulombic efficiency of a silicon-rich electrode is typically between 65% and 85%.[9]

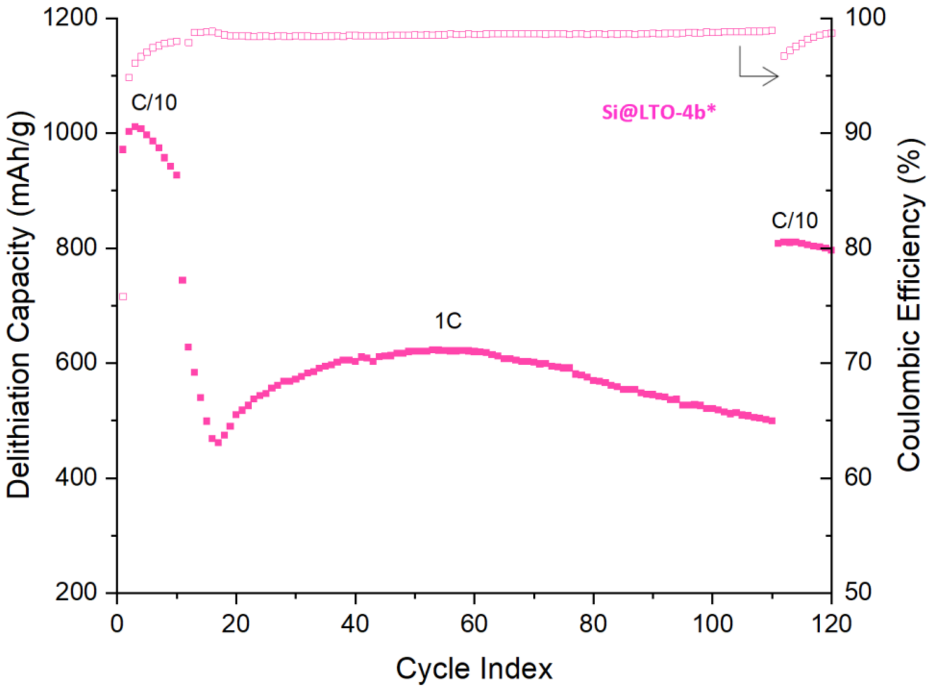

Figure 7.8. Galvanostatic cycling of the Si@LTO-4b* composite. First 10 cycles at a charge rate of C/10, followed by 1C.

However, during cycling, the coulombic efficiency never exceeded 99% in all the Si@LTO composites. The differential capacitance and potential profile for this sample are seen in Figure 7.9a and b, respectively. These plots serve to confirm the presence of both electrochemically active graphite and silicon. The broad redox peaks in Figure 7.9a indicated by the red arrows are attributed to the lithiation/delithiation of silicon.[2] Upon delithiation of the first cycle, a pronounced sharp peak is seen at 0.44 V (as indicated by the blue arrow) and is attributed to the conversion of $Li_{15}Si_4$ into an amorphous Li-Si alloy.[40] The solid line data taken at C/10 shows the presence of two sharp peaks below 0.2 V, indicating the lithiation of graphite.[2] At 1C, the peaks attributed to silicon became broader and much less pronounced due to the reduction in the rate of lithiation. The peaks attributed to the lithiation of graphite were nearly absent at 1C, suggesting most of the capacity contribution is derived from silicon at this high charge rate. The associated decline in capacity is clearly seen with the dashed line in Figure 7.9b. Since the graphite is primarily intended to act as a buffer, this capacity loss at 1C is an acceptable compromise. However, a slower charging rate should be selected in instances where energy density is favoured over power density.

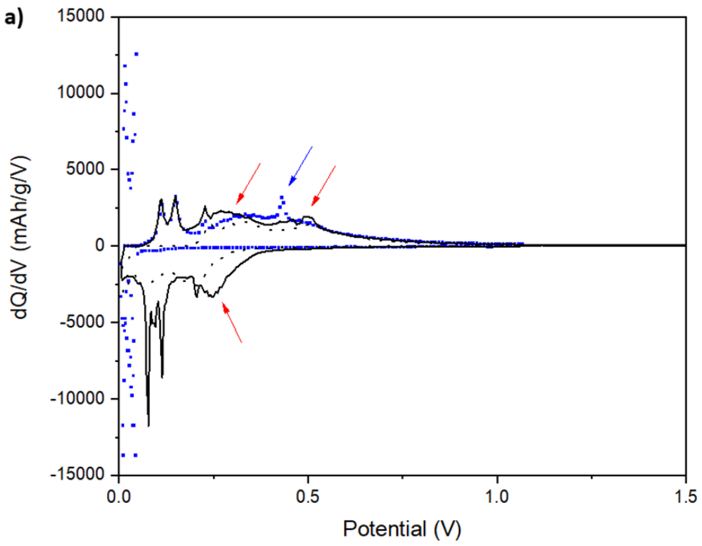

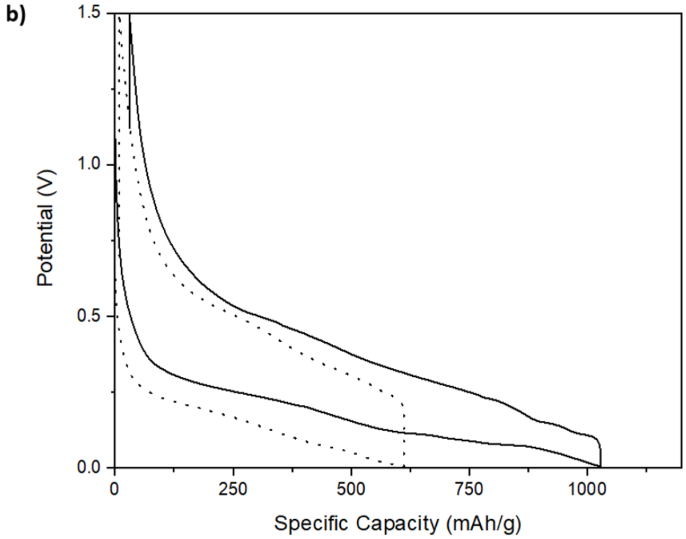

Figure 7.9. (a) dQ/dV plot (b) potential profile. Data taken from same coin cell as Figure 7.8: Si@LTO-4b*. Blue data points are from the first cycle. Solid line data taken at C/10; dashed line data taken at 1C.

## Conclusions

This study reports the preparation and characterization of LTO-coated silicon anodes by application-oriented techniques. These techniques include the addition of graphite to improve capacity retention and the use of a water-based sodium alginate binder. The capacity and capacity retention of different ratios of Si@LTO with graphite were studied at C/10 and 1C. Electrochemical performance showed that Si@LTO composites with graphite had higher capacity and capacity retention at 1C relative to baselines of nano silicon, Si@LTO alone, and a binary silicon-graphite composite. It was found that the best composite was 40 wt% Si@LTO + 40 wt% graphite, which had a high capacity at both C/10 and 1C (~900 mAh $g^{-1}$ at C/10 and ~600 mAh $g^{-1}$ at 1C). The results suggest that these Si@LTO + graphite composites have the potential to increase the practical energy density of lithium-ion batteries.

## Acknowledgments

We would like to thank the Office of Energy Research and Development (OERD) at Natural Resources Canada for financial support. We would also like to thank Sun Mao Kuan, De-Yuan Wang, Tang Song Zhang, Oltion Kodra, and Martin Couillard for their advice and help with material characterization.

## References

[1] G. E. Blomgren, “The Development and Future of Lithium Ion Batteries,” *Journal of The Electrochemical Society*, vol. 164, no. 1, pp. A5019–A5025, 2017, doi: 10.1149/2.0251701jes.

[2] M. Wetjen, D. Pritzl, R. Jung, S. Solchenbach, R. Ghadimi, and H. A. Gasteiger, “Differentiating the degradation phenomena in silicon-graphite electrodes for lithium-ion batteries,” *Journal of the Electrochemical Society*, vol. 164, no. 12, pp. A2840–A2852, 2017, doi: 10.1149/2.1921712jes.

[3] M. N. Obrovac and V. L. Chevrier, “Alloy negative electrodes for Li-ion batteries,” *Chemical Reviews*, vol. 114, no. 23, pp. 11444–11502, 2014, doi: 10.1021/cr500207g.

[4] Y. Xu, Y. Zhu, and C. Wang, “Mesoporous carbon/silicon composite anodes with enhanced performance for lithium-ion batteries,” *Journal of Materials Chemistry A*, vol. 2, no. 25, pp. 9751–9757, 2014, doi: 10.1039/c4ta01691b.

[5] N. Nitta, F. Wu, J. T. Lee, and G. Yushin, “Li-ion battery materials: Present and future,” *Materials Today*, vol. 18, no. 5, pp. 252–264, 2015, doi: 10.1016/j.mattod.2014.10.040.

[6] F. Zhang *et al.*, “Boosting the initial coulombic efficiency in silicon anodes through interfacial incorporation of metal nanocrystals,” *Journal of Materials Chemistry A*, vol. 7, no. 29, pp. 17426–17434, 2019, doi: 10.1039/c9ta05340a.

[7] T. Yoon, C. C. Nguyen, D. M. Seo, and B. L. Lucht, “Capacity Fading Mechanisms of Silicon Nanoparticle Negative Electrodes for Lithium Ion Batteries,” *Journal of The Electrochemical Society*, vol. 162, no. 12, pp. A2325–A2330, 2015, doi: 10.1149/2.0731512jes.

[8] S. Chae, M. Ko, K. Kim, K. Ahn, and J. Cho, “Confronting Issues of the Practical Implementation of Si Anode in High-Energy Lithium-Ion Batteries,” *Joule*, vol. 1, no. 1, pp. 47–60, 2017, doi: 10.1016/j.joule.2017.07.006.

[9] X. Zuo, J. Zhu, P. Müller-Buschbaum, and Y. J. Cheng, “Silicon based lithium-ion battery anodes: A chronicle perspective review,” *Nano Energy*, vol. 31, no. October 2016, pp. 113–143, 2017, doi: 10.1016/j.nanoen.2016.11.013.

[10] S. Y. Kim, J. Lee, B. H. Kim, Y. J. Kim, K. S. Yang, and M. S. Park, “Facile Synthesis of Carbon-Coated Silicon/Graphite Spherical Composites for High-Performance Lithium-Ion Batteries,” *ACS Applied Materials and Interfaces*, vol. 8, no. 19, pp. 12109–12117, 2016, doi: 10.1021/acsami.5b11628.

[11] P. Fan *et al.*, “Amorphous carbon-encapsulated Si nanoparticles loading on MCMB with sandwich structure for lithium ion batteries,” *Electrochimica Acta*, vol. 306, pp. 590–598, 2019, doi: 10.1016/j.electacta.2019.03.154.

[12] C. H. Yim, S. Niketic, N. Salem, O. Naboka, and Y. Abu-Lebdeh, “Towards improving the practical energy density of Li-Ion batteries: Optimization & evaluation of silicon:graphite composites in full cells,” *Journal of the Electrochemical Society*, vol. 164, no. 1, pp. A6294–A6302, 2017, doi: 10.1149/2.0481701jes.

[13] J. K. Yoo, J. Kim, Y. S. Jung, and K. Kang, “Scalable fabrication of silicon nanotubes and their application to energy storage,” *Advanced Materials*, vol. 24, no. 40, pp. 5452–5456, 2012, doi: 10.1002/adma.201201601.

[14] Z. Lu, T. Wong, T. W. Ng, and C. Wang, “Facile synthesis of carbon decorated silicon nanotube arrays as anode material for high-performance lithium-ion batteries,” *RSC Advances*, vol. 4, no. 5, pp. 2440–2446, 2014, doi: 10.1039/c3ra45439h.

[15] T. D. Bogart, D. Oka, X. Lu, M. Gu, C. Wang, and B. A. Korgel, “Lithium ion battery

peformance of silicon nanowires with carbon skin," *ACS Nano*, vol. 8, no. 1, pp. 915–922, 2014, doi: 10.1021/nn405710w.

[16] J. Ryu, D. Hong, S. Choi, and S. Park, "Synthesis of Ultrathin Si Nanosheets from Natural Clays for Lithium-Ion Battery Anodes," *ACS Nano*, vol. 10, no. 2, pp. 2843–2851, 2016, doi: 10.1021/acsnano.5b07977.

[17] T. Takamura, M. Uehara, J. Suzuki, K. Sekine, and K. Tamura, "High capacity and long cycle life silicon anode for Li-ion battery," *Journal of Power Sources*, vol. 158, no. 2 SPEC. ISS., pp. 1401–1404, 2006, doi: 10.1016/j.jpowsour.2005.10.081.

[18] Z. Yu *et al.*, "Lithium Titanate Matrix-Supported Nanocrystalline Silicon Film as an Anode for Lithium-Ion Batteries," *ACS Applied Materials and Interfaces*, vol. 11, no. 1, pp. 534–540, 2019, doi: 10.1021/acsami.8b13878.

[19] T. Mu *et al.*, "Scalable submicron/micron silicon particles stabilized in a robust graphite-carbon architecture for enhanced lithium storage," *Journal of Colloid and Interface Science*, vol. 555, pp. 783–790, 2019, doi: 10.1016/j.jcis.2019.07.110.

[20] J. Y. Li *et al.*, "Rational Design of Robust Si/C Microspheres for High-Tap-Density Anode Materials," *ACS Applied Materials and Interfaces*, vol. 11, no. 4, pp. 4057–4064, 2019, doi: 10.1021/acsami.8b20213.

[21] L. Y. Yang, H. Z. Li, J. Liu, Z. Q. Sun, S. S. Tang, and M. Lei, "Dual yolk-shell structure of carbon and silica-coated silicon for high-performance lithium-ion batteries," *Scientific Reports*, vol. 5, pp. 1–9, 2015, doi: 10.1038/srep10908.

[22] H. Tao, L. Z. Fan, W. L. Song, M. Wu, X. He, and X. Qu, "Hollow core-shell structured Si/C nanocomposites as high-performance anode materials for lithium-ion batteries," *Nanoscale*, vol. 6, no. 6, pp. 3138–3142, 2014, doi: 10.1039/c3nr03090c.

[23] X. Li *et al.*, "Hollow core-shell structured porous Si-C nanocomposites for Li-ion battery anodes," *Journal of Materials Chemistry*, vol. 22, no. 22, pp. 11014–11017, 2012, doi: 10.1039/c2jm31286g.

[24] N. Liu, H. Wu, M. T. McDowell, Y. Yao, C. Wang, and Y. Cui, "A yolk-shell design for stabilized and scalable Li-ion battery alloy anodes," *Nano Letters*, vol. 12, no. 6, pp. 3315–3321, 2012, doi: 10.1021/nl3014814.

[25] Y. Bai *et al.*, "Core-shell Si@TiO2 nanosphere anode by atomic layer deposition for Li-ion batteries," *Journal of Power Sources*, vol. 308, pp. 75–82, 2016, doi: 10.1016/j.jpowsour.2016.01.049.

[26] Y. He, X. Yu, Y. Wang, H. Li, and X. Huang, "Alumina-coated patterned amorphous silicon as the anode for a Lithium-Ion battery with high Coulombic efficiency," *Advanced Materials*, vol. 23, no. 42, pp. 4938–4941, 2011, doi: 10.1002/adma.201102568.

[27] Y. J. Hao, Q. Y. Lai, D. Q. Liu, Z. U. Xu, and X. Y. Ji, "Synthesis by citric acid sol-gel method and electrochemical properties of Li4Ti5O12 anode material for lithium-ion battery," *Materials Chemistry and Physics*, vol. 94, no. 2–3, pp. 382–387, 2005, doi: 10.1016/j.matchemphys.2005.05.019.

[28] A. Terechshenko, A. Sanbayeva, M. R. Babaa, A. Nurpeissova, and Z. Bakenov, "Spray-pyrolysis preparation of Li 4 Ti 5 O 12 /si composites for lithium-ion batteries," *Eurasian Chemico-Technological Journal*, vol. 21, no. 1, pp. 69–73, 2019, doi: 10.18321/ectj793.

[29] M. Liu, H. Gao, G. Hu, K. Zhu, and H. Huang, "Facile preparation of core-shell Si@Li4Ti5O12 nanocomposite as large-capacity lithium-ion battery anode," *Journal of Energy Chemistry*, vol. 40, pp. 89–98, 2020, doi: 10.1016/j.jechem.2019.02.011.

[30] Q. Xia, A. Xu, L. Du, Y. Yan, and S. Wu, "High-rate, long-term performance of LTO-

pillared silicon/carbon composites for lithium-ion batteries anode under high temperature," *Journal of Alloys and Compounds*, vol. 800, pp. 50–57, 2019, doi: 10.1016/j.jallcom.2019.06.023.

[31] J. I. Lee *et al.*, "High-performance silicon-based multicomponent battery anodes produced via synergistic coupling of multifunctional coating layers," *Energy and Environmental Science*, vol. 8, no. 7, pp. 2075–2084, 2015, doi: 10.1039/c5ee01493j.

[32] S. H. Lee, C. Huang, and P. S. Grant, "Layer-by-layer printing of multi-layered heterostructures using Li4Ti5O12 and Si for high power Li-ion storage," *Nano Energy*, vol. 61, no. January, pp. 96–103, 2019, doi: 10.1016/j.nanoen.2019.04.044.

[33] C. H. Yim, F. M. Courtel, and Y. Abu-Lebdeh, "A high capacity silicon-graphite composite as anode for lithium-ion batteries using low content amorphous silicon and compatible binders," *Journal of Materials Chemistry A*, vol. 1, no. 28, pp. 8234–8243, 2013, doi: 10.1039/c3ta10883j.

[34] A. M. Wilson, G. Zank, K. Eguchi, W. Xing, and J. R. Dahn, "Pyrolysed silicon-containing polymers as high capacity anodes for lithium-ion batteries," *Journal of Power Sources*, vol. 68, no. 2, pp. 195–200, 1997, doi: 10.1016/S0378-7753(96)02551-7.

[35] X. Y. Zhao *et al.*, "Fabrication of MnO/C composites utilizing pitch as the soft carbon source for rechargeable Li-ion batteries," *New Journal of Chemistry*, vol. 40, no. 12, pp. 9986–9992, 2016, doi: 10.1039/c6nj02309f.

[36] S. Gražulis *et al.*, "Crystallography Open Database (COD): An open-access collection of crystal structures and platform for world-wide collaboration," *Nucleic Acids Research*, vol. 40, no. D1, pp. 420–427, 2012, doi: 10.1093/nar/gkr900.

[37] D. J. Pereira, J. W. Weidner, and T. R. Garrick, "The Effect of Volume Change on the Accessible Capacities of Porous Silicon-Graphite Composite Anodes," *Journal of The Electrochemical Society*, vol. 166, no. 6, pp. A1251–A1256, 2019, doi: 10.1149/2.1211906jes.

[38] M. Wetjen *et al.*, "Monitoring the Lithium Concentration across the Thickness of Silicon-Graphite Electrodes during the First (De-)Lithiation," *Journal of The Electrochemical Society*, vol. 166, no. 8, pp. A1408–A1411, 2019, doi: 10.1149/2.0581908jes.

[39] Z. Ogumi and M. Inaba, "Carbon Anodes," in *Advances in Lithium-Ion Batteries*, W. van Schalkwijk and B. Scrosati, Eds., New York: Kluwer Academic Publishers, 2002, pp. 79–101. doi: 10.1007/0-306-47508-1_3.

[40] T. D. Hatchard and J. R. Dahn, "In Situ XRD and Electrochemical Study of the Reaction of Lithium with Amorphous Silicon," *Journal of The Electrochemical Society*, vol. 151, no. 6, p. A838, 2004, doi: 10.1149/1.1739217.

# Chapter 8: Critical Investigation of Metal-Organic-Frameworks to Improve the Silicon Anode of Lithium-ion Batteries

James W. Sturman[1,2,3], Mohamed S. E. Houache[1], Walace Doti do Pim[4], Elena A. Baranova[2,3] Muralee Murugesu[4], and Yaser Abu-Lebdeh[1,Z]

1. Energy, Mining and Environment Research Centre, National Research Council of Canada, 1200 Montreal Road, Ottawa, Ontario K1A 0R6, Canada
2. Department of Chemical and Biological Engineering, Centre for Catalysis Research and Innovation (CCRI), University of Ottawa, 161 Louis-Pasteur, Ottawa ON, K1N 6N5, Canada
3. Nexus for Quantum Technologies (NexQT), University of Ottawa, Ottawa, Ontario, K1N 6N5, Canada
4. Department of Chemistry and Biomolecular Sciences, University of Ottawa, Ottawa ON, K1N 6N5, Canada

Publication status: accepted manuscript

## Abstract

The poor capacity retention of the silicon (Si) anode has hindered its widespread use in lithium-ion batteries. Metal-Organic-Frameworks (MOF) may offer the structural and functional tunability needed to alleviate some of the longstanding problems associated with silicon pulverization. Herein, MOF-74 (Co-based) and MOF-199 (Cu-based) were implemented in different design configurations for high-Si loading electrodes. Multi-layer *sandwich* configurations provided a modest improvement in capacity retention. However, greatest improvements in capacity retention were observed when the MOF was synthesized onto the silicon surface (Si@MOF) and subsequently pyrolyzed. The best performing high-loading 0.5Si@MOF-c sample delivered a high capacity of 1000 mAh/g and retained 60% capacity after 100 cycles, surpassing a standard silicon-graphite composite.

## Introduction

Silicon is an alloying-based anode with a theoretical capacity of 3579 mAh/g, which is 10-times greater than traditional graphite. [1,2] This high-energy density makes it a promising electrode material for next-generation lithium-ion batteries. Unfortunately, the alloying of Li and Si causes electrode volume expansion and a cascade of well-known problems including severe electrode pulverization, continuous Solid-Electrolyte Interphase (SEI) formation, electrode delamination, and rapid capacity fade.[3] As a result, researchers have implemented various strategies to minimize the problems associated with silicon lithiation. The use of nano-sized silicon (average diameter around 150 nm) can reduce particle fractures, and composite strategies where silicon is combined with graphite can buffer electrode expansion. More recently, Metal Organic Frameworks (MOF) have been reported to improve capacity retention in various Si-based anodes. [4-6]

MOFs are a class of porous materials that consist of a network of organic linkers connected to metallic secondary building units. They can adopt a variety of different structures depending on the type of metal ion (Co, Zn, Cu, Al, etc.) and linker. [7] MOFs have been investigated in numerous fields and are particularly well-suited for applications that require a high surface area, such as gas adsorption and separation, [8] biological applications, [9] and catalysis. [10] For Li-ion batteries, MOFs have been involved in two main design strategies: a multi-layer *sandwich* design and an encapsulation design where the MOF surrounds the silicon (Si@MOF). [11,12]

Major benefits could result from the development of specific composite configurations with homogeneous encapsulation of Si nanostructures into a MOF-derived carbon matrix. While the Si nanoparticles offer high capacity, the MOF-carbon matrix can efficiently alleviate the volume change of Si. Moreover, the uniformly distributed metal centers within the porous carbon structure could enhance electrode conductivity and improve the storage capacity. Finally, the matrix's built-in open channels are advantageous for $Li^+$ transportation and facilitate rate performance. [7]

In 2015, Y. Han prepared a multi-layer sandwich design in which a layer of Super P (SP) & binder was applied to a Cu current collector, followed by a layer of Si, followed by a layer of MOF.[11] The authors reported a relatively stable areal capacity of 600 μAh $cm^{-2}$ for a SP-nano Si-MOF anode. In addition, these anodes outperformed a baseline of carbon-Si-carbon after ~ 25 cycles. Y. Han prepared the Si@MOF encapsulation design using carbonized Zn-based MOF.[4] They reported a capacity of 1020 mAh/g after 50 cycles for their low-Si (~10 wt%) anode.

Recently, Gao et al also prepared Si@MOF, with silicon encapsulated in a carbonized Co-based ZIF-67 (type of MOF).[12] They reported a capacity of 820 mAh/g after 1000 cycles at a high current density.

Although these results are promising, more work is needed to differentiate the factors that contribute to the reportedly improved electrochemical performance. Some of these studies used a relatively low silicon loading with a high binder content. In addition, these studies have only tested a particular MOF in either a sandwich or encapsulation configuration. Herein, two different MOFs were implemented in different design configurations for high-Si loading electrodes as illustrated in Figure 8.1. A multi-layer *sandwich* configuration provided a modest improvement in capacity retention. However, greatest improvements in capacity retention were observed when the MOF was synthesized in situ onto the silicon surface (Si@MOF) and subsequently pyrolyzed. The best-performing high-loading Si@MOF-c sample delivered a high capacity of around 1000 mAh/g and retained 60% capacity after 100 cycles.

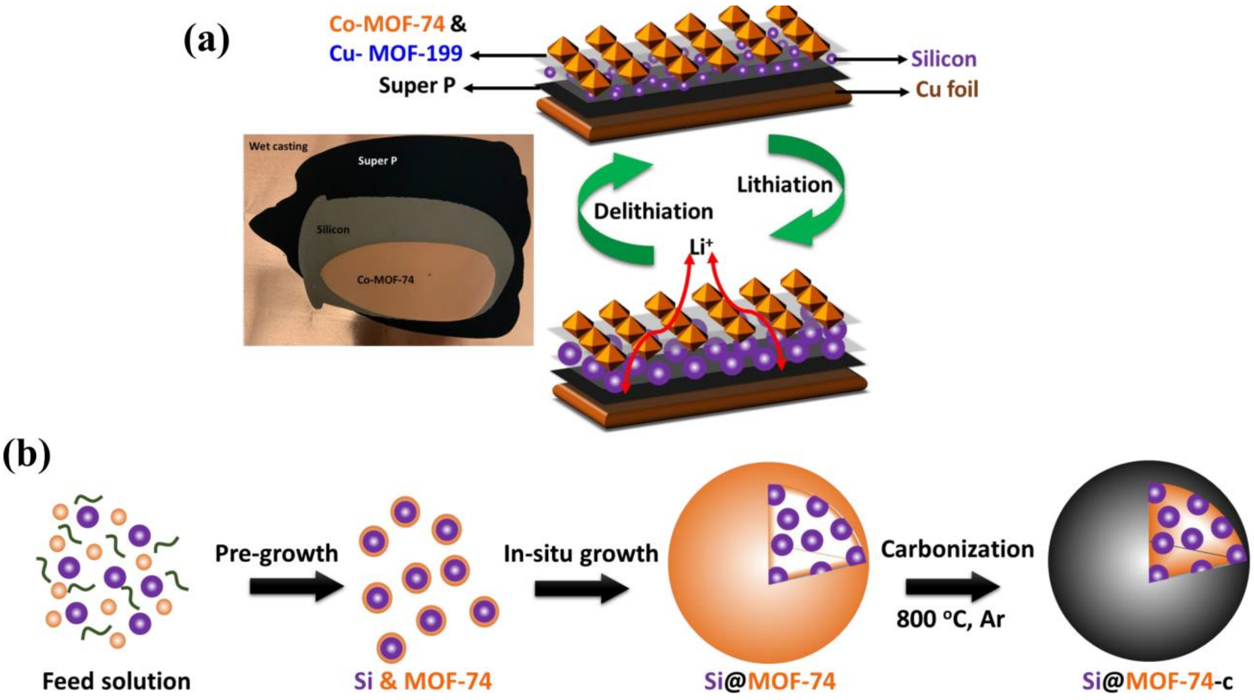

Figure 8.1. Schematic illustration of synthesis of (a) multilayer Sandwich and (b) Carbonized composite matrix “encapsulation” configurations.

## Experimental

Two main design configurations as well as several baselines were used in this study. The first configuration is referred to as the multilayer or *sandwich* design and consists of a cushion layer of Super P, followed by a layer of 80% silicon, followed by a layer of MOF (either MOF-74 or MOF-199). The loading of the silicon layer was dependent on the notch bar gap (450 µm for *thick* or 150 µm for *thin*). The loading of silicon for a thick or thin film corresponded to ~1.2 mg $cm^{-2}$ or ~0.5 mg $cm^{-2}$, respectively. The second configuration involved the encapsulation of nano silicon within a matrix composed of MOF-derived carbon (only MOF-74 was used). To help differentiate the performance contributions, we also tested several suitable baselines including: a high-Si (80% Si) electrode and a low-Si (20% Si 60% graphite) composite, a SP-cushion layer with Si, and a simple composite design in which the MOF was added directly to the slurry containing the silicon, binder and Super P. Table 8.1 below summarizes the different electrode compositions, design configurations, and abbreviated names used in this paper.

Table 8.1. Detailed nomenclature of the various studied designs.

| ***Design Configuration*** | ***Sample Composition (wt%)*** | ***Abbreviated ID*** |
|---|---|---|
| ***Baselines*** | **80% silicon***, 10% NaCMC, 10% Super P<br>**20% silicon + 60% graphite**, 10% NaCMC, 10% Super P | 80Si-10CMC<br>20Si-10CMC |
| ***Multi-layer Sandwich*** | (70% Super P + 30% Na-alginate)-cushion +<br>(**80% silicon**, 10% NaCMC, 10% Super P) +<br>(90% MOF-74/MOF-199 + 10% PVDF) | SP-Si-MOF |
| ***Simple Composite with Uncarbonized MOF*** | **65% silicon**, 15% MOF-74, 10% Na-alginate, 10% Super P | Si-MOF |
| ***Carbonized Matrix Composite*** | **80% 0.5Si@MOF-74-c**, 10% NaCMC, 10% Super P | 0.5Si@MOF-c[#] |
| ***Carbonized Matrix Composite*** | **80% 1.0Si@MOF-74-c**, 10% NaCMC, 10% Super P | 1.0Si@MOF-c |

* Active material is written in bold

\# Inclusion of "-c" indicates after carbonization, absence of "-c" indicates before carbonization

Silicon nano powder was supplied by Tekna. Water-based slurries were typically prepared from 80 wt% active material, 10 wt% binder (700 K Mw sodium carboxymethyl cellulose [NaCMC], Sigma-Aldrich), and 10 wt% Super P carbon (Timcal). The Super P-cushion slurries were prepared using 70 wt% Super P and 30 wt% Na-Alginate binder (Sigma-Aldrich). The solvent was a 4:1 mass ratio of deionized water to ethanol (EtOH). Silicon-based slurries were mixed in three 15-minute sessions at 2000 rpm in a Thinky AR-100 planetary mixer with 4 zirconia balls (5mm diameter). A 15-minute rest was included after each mixing session. The MOF slurry was composed of 90 wt% MOF and 10 wt% polyvinylidene fluoride (PVDF) in N-Methyl-2-pyrrolidone solvent. The Super P, Si, and MOF slurries were applied to a cleaned copper foil using a notch bar gap of variable thickness. The Si@MOF-c slurries were always applied to copper foil with a 350 µm gap notch bar. The casts were allowed to dry at room temperature. Then, 0.5-inch diameter electrode disks were cut and vacuum dried at 80 °C overnight. The loading of active material for the Si@MOF-c composites was approximately 2.2 mg $cm^{-2}$.

### Battery testing

Half-cell batteries with lithium metal (voltage vs $Li/Li^+$) were prepared in an argon-filled glove box using 2325-type coin cells, 74.8 µL of electrolyte and two 3501 Celgard polypropylene membranes. The electrolyte was 1M $LiPF_6$ in ethylene carbonate and ethyl methyl carbonate EC:EMC (1:1 v/v) (Sigma Aldrich) with 10 wt% fluoroethylene carbonate (FEC) additive. All coin cells were allowed to rest at least 24 hours and were then cycled at 30°C in an Arbin BT2000 battery cycler. Current densities were calculated based on the theoretical capacity of the active material. This was 3579 mAh/g (1C = 3579 mA/g) for silicon. For electrode materials that did not have a capacity known *a priori* (i.e., Si@MOF-c), a sacrificial cell was used to determine the experimental active material capacity. This value was then used to calculate a C/10 current rate in subsequent cells. All batteries were cycled between 0.005 V and 1.5 V at a C/10 constant current rate unless otherwise specified. A 15-minute open circuit rest was included at each voltage limit. It should be noted that previous publications have used a higher upper limit voltage cut off near 3.0 V, which is known to provide an additional boost in capacity (especially in the presence of a high carbon content as is the case with these samples). [11,12] Since our study focused only on the faradaic capacity of the bulk silicon and carbon, the upper voltage limit of 1.5 V was selected.

### Synthesis of MOF and Matrix Composite

For pristine MOF-74, 0.5 g of polyvinylpyrrolidone (PVP) was suspended in 30 mL of EtOH and kept under stirring at 50 °C for 24 h. After this time, the suspension was transferred to a glass bottle, and 50 mL of THF and 50 mL of water were added into the suspension. Subsequently, 3.736 g of cobalt(II) acetate tetrahydrate and 1.49 g of 2,5-dihydroxy-1,4-benzenedicarboxylic acid ($H_4DOBDC$) were incorporated in the system, which was sonicated for 1.5 h. The system was then heated at 110 °C for 72 h. The brown solid was centrifuged (9000 rpm) for 20 min, the supernatant was discarded and the solid was soaked in EtOH for 24 h. This last step was repeated twice to assure the washing of the starting materials trapped in the pores of the

MOF. Finally, the material was dried overnight in the oven at 80 °C. While for Si@MOF samples, a similar methodology was performed by in situ synthesizing MOF-74 onto the silicon surface by adding either 0.5 or 1 g of Si nanoparticles (0.5Si@MOF and 1.0Si@MOF, respectively). All other parameters were kept constant. Then, Si@MOF samples were pyrolyzed at 800 °C for 3 h under argon. The resulting samples are denoted Si@MOF-c. Carbonization is necessary to ensure electrochemical lithiation of silicon is possible.[4]

Physical Characterization

The morphology was characterized by Field Emission Scanning Electron Microscopy (SEM) using a Hitachi SU5000 microscope. Field Emission Transmission Electron Microscopy (TEM) was carried out with a JEOL JEM 2100F operating at 200 kV. For postmortem SEM, electrodes were opened under argon in their delithiated state and were washed for 1-2 minutes with diethyl carbonate solvent to remove bulk quantities of the Li salt.[13] Elemental distribution was quantified with the Energy Dispersive X-ray (EDX) Spectroscopy Analyzer X-Max Oxford Instruments. The powder X-Ray Diffraction (XRD) was carried out with a Bruker AXS D8 diffractometer (Cu Kα, $\lambda$=0.154 nm) between 10° and 85° 2θ. X-ray Photoelectron Spectroscopy (XPS) data was acquired from a Kratos AXIS Ultra DLD spectrometer with a monochromated Al K-alpha beam (1486.6 eV) under high vacuum. Thermogravimetric Analysis (TGA) curves were collected on a TA Instruments Q5000 TGA analyzer from room temperature to 800 °C in a nitrogen atmosphere (25 mL min$^{-1}$), with a heating rate of 10 °C min$^{-1}$.

## Results and Discussion

Figure 8.2a shows the XRD plot of the crystalline nano silicon with clear reflections (JCPDF: 895012).[14] TEM images in Figure 8.2a reveal a wide size distribution of nano silicon with a 2-3 nm thick amorphous coating. Co-MOF-74 and Cu-MOF-199 were confirmed to be isostructural via comparison of the calculated and experimental XRD patterns (Figure 8.2b &c). The $2\theta$ positions for all peaks in the patterns suggests good crystallinity and the diffraction peaks matched well with existing published XRD patterns of phase-pure MOFs. [15,16] MOF structures were further confirmed using TEM, by visualizing the formation of polyhedral rods approximately 250 nm thick, as well as pyramidal-shaped particles with MOF-199.

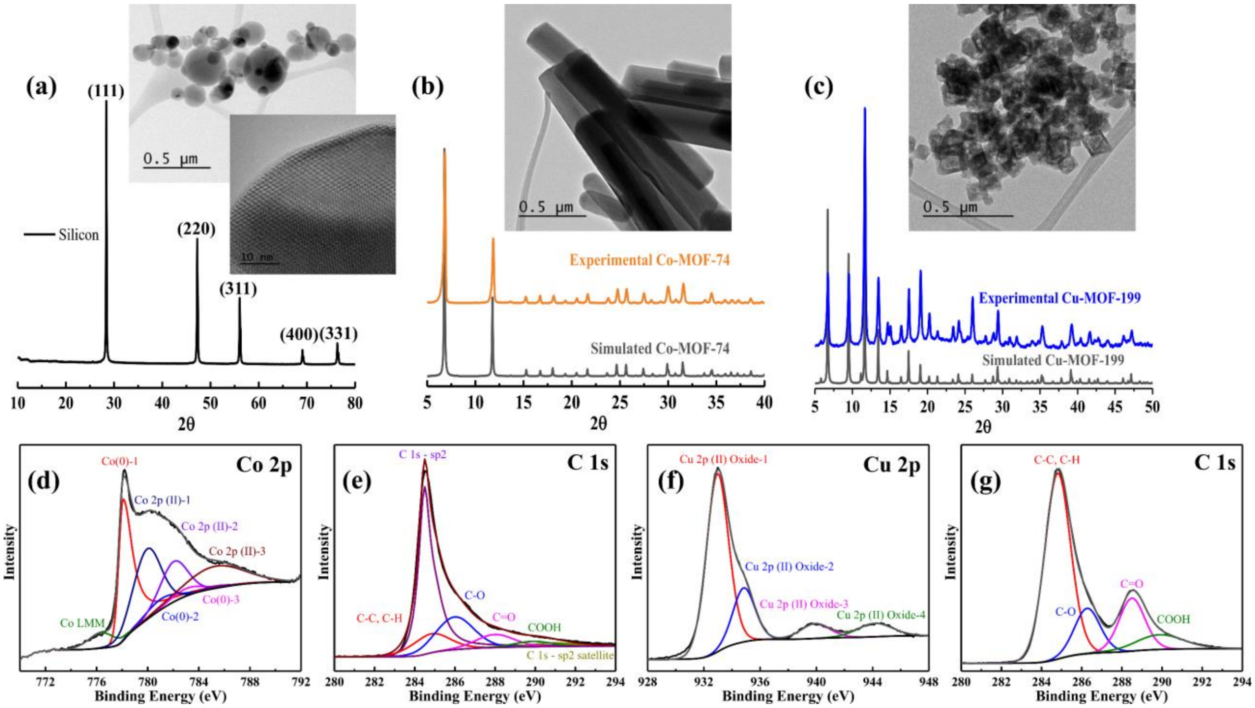

Figure 8.2. XRD and TEM of a) pristine silicon nano powder, b) pristine MOF-74 and c) pristine MOF-199 compared to the simulated patterns from XRD data. (d) XPS spectrum of Co 2p, (e) C 1s for MOF-74. (f) XPS spectrum of Cu 2p, (g) C 1s for MOF-199.

The surface chemistry environment of the fabricated MOFs was further characterized by XPS. Results of the peak fittings to the observed XPS spectra are listed in Table S8.1. Figure 8.2d presents the asymmetrical Co $2p_{3/2}$ XPS spectra of the MOF-74 decoupled into eight Gaussian curves. The binding energy (BE) peaks at ∼776, 778-783 and 779-785 eV were assigned to Co LMM Auger peak, $Co^0$ metal and $Co^{2+}$ of the $Co_3O_4$ and/or CoO. [17] The deconvolution of the C 1s core level spectrum for MOF-74 was carried out with six Gaussian curves (Figure 8.2e), which correspond to the $sp^2$ carbon bonding and satellite ($sp^2$), C C-C/C-H bonding, C-O bonding, C=O bonding and COOH bonding. [18] In the Cu 2p area (Figure 8.2f), two dominant peaks at 931.38 eV (Cu $2p_{3/2}$) and 933.25 eV (Cu $2p_{3/2}$) represent the formation of $Cu^0$ and/or $Cu^+$ (predominately in the +2-oxidation state). The peaks at 938.33 eV and 942.57 eV (Cu $2p_{3/2}$-satellite) are attributed to the CuO characteristic peaks. [19] For the C 1s, the binding energy at 284.80 eV, 286.27 eV, 288.50 eV and 289.88 eV correspond to the C-C/C-H, C-O, C=O and COOH, respectively as shown in Figure 8.2g.

Figure 8.3 and S8.1 show the MOF-encapsulated silicon particles used to prepare the Si@MOF samples before and after carbonization. The 0.5Si@MOF sample had aggregated clusters of polyhedral MOF structures and minimal free-standing silicon, demonstrating that the majority of silicon nano particles were fully covered by the MOF-74. The 1.0Si@MOF sample also had clusters of polyhedral Co-MOF, but with a greater amount of unencapsulated or free-standing silicon nanoparticles. Thus, the 1.0Si@MOF sample should be considered as a composite consisting of MOF-encapsulated Si in addition to some free-flowing Si. An attempt was made to prepare a higher silicon containing Si@MOF composite (1.5Si@MOF); however, SEM images in Figure S8.2 revealed an unsuccessful synthesis as marked by inhomogeneous agglomerations, a large quantity of unencapsulated silicon, and a poorly defined MOF morphology.

Figure 8.4a illustrates the XRD patterns of 0.5Si@MOF before and after carbonization. The main diffraction peaks of 0.5Si@MOF corresponded to the MOF-74 and Si (111) facets, with the absence of any impurity peaks. After carbonization, broadening diffraction peaks of low intensity illustrates an amorphous structure of 0.5Si@MOF-c with a single peak from the Si (111) facet.

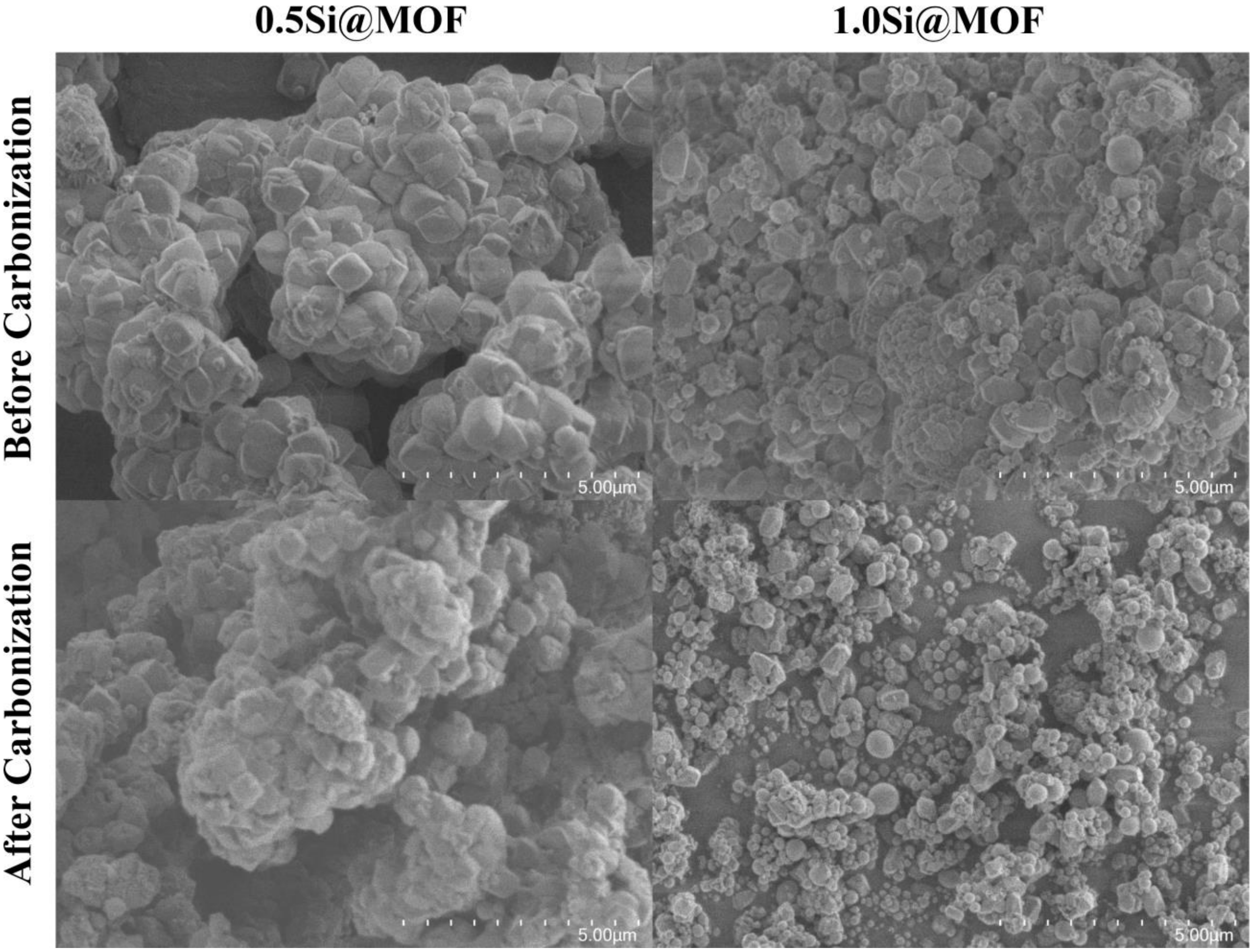

Figure 8.3. SEM images of 0.5Si@MOF and 1.0 Si@MOF samples before and after carbonization.

A thermal conversion test was performed to study thermal decomposition. Figure 8.4b is the TGA analysis of the composite in comparison with the pristine MOF-74. Clearly, the first step of weight loss occurred before 100 °C, corresponding to the moisture and solvent removal in Co-MOF-74 and another step was observed around 300 °C, attributed to the degradation of organic linkers which may result in the collapse of the MOF structure.[20] TGA analysis shows that the Co-MOF was stable until 305 °C as reported in literature.[21] When the temperature increased beyond 500 °C, no mass change occurred, demonstrating that Co-MOF-74 had been entirely decomposed.[17] However, for Si@MOF, the attachment of Si to the Co-MOF led to mass variation after 580 °C, which is attributed to silicon reactions. Comparison of the Si@MOF composites before and after carbonization suggests that the 0.5Si@MOF-c composite has a higher thermal stability than 0.5Si@MOF.  TEM and EDX mapping in Figure 8.4c show the 0.5Si@MOF sample (prior to carbonization) and reveals that cobalt and oxygen are distributed homogeneously throughout the MOF structures. In contrast, the silicon particles primarily occupy the center of the larger MOF structures. Moreover, the encapsulation of Si within the MOF-derived carbon matrix appears to be well-preserved even after the 0.5Si@MOF sample was pyrolyzed and prepared in an electrode with Super P and binder. Figure S8.3 illustrates an electrode prepared with 0.5Si@MOF-c and reveals relatively few free-standing Si nanoparticles.

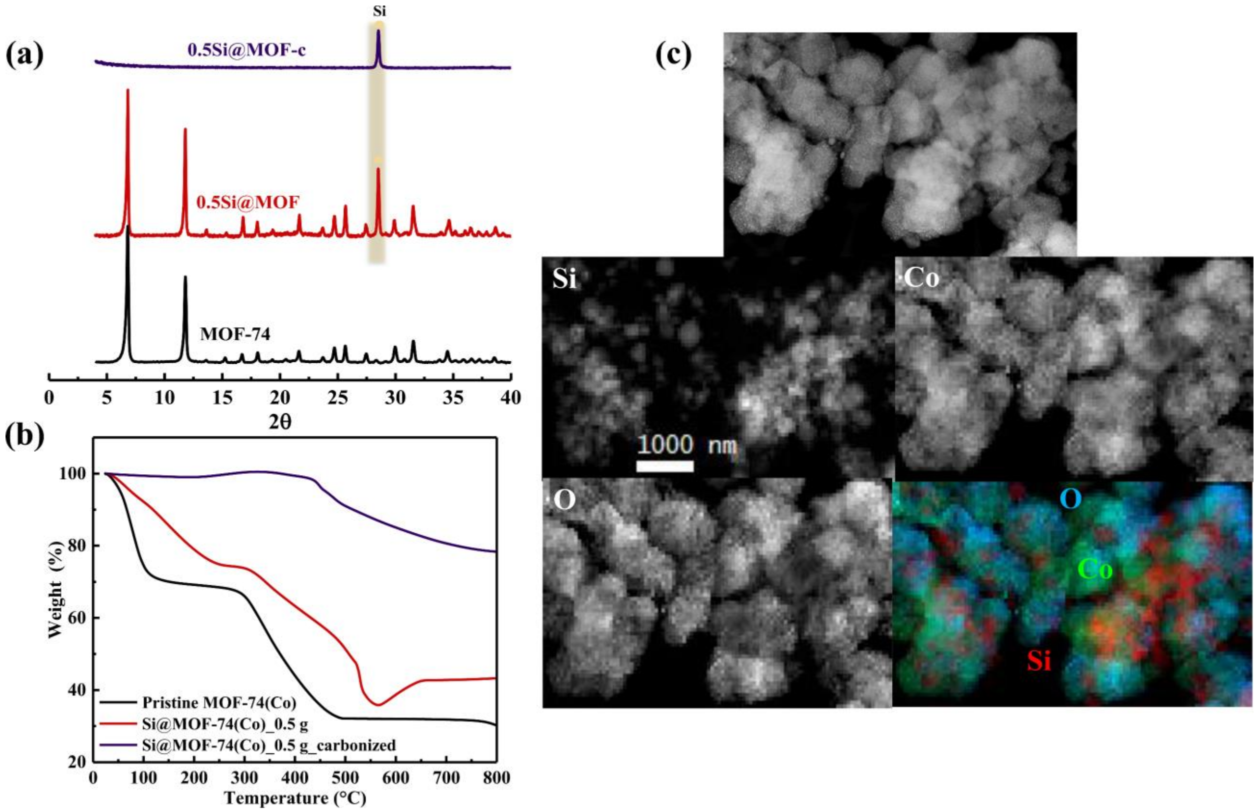

Figure 8.4. (a & b) XRD and TGA curves in an $N_2$ atmosphere for MOF-74 at different composites before and after carbonization. (c) TEM and EDX mapping images of 0.5Si@MOF before carbonization.

To further study the chemical composition of the prepared composite matrix, XPS characterization of 0.5Si@MOF and 0.5Si@MOF-c were carried out. The survey XPS spectra in Figure 8.5a, presents the asymmetrical Co $2p_{3/2}$ XPS spectra of both composite matrices decoupled into four Gaussian curves. The binding energy (BE) peaks at ∼781-788 eV was assigned to Co2$^+$ of the $Co_3O_4$ and/or CoO. The functional groups associated with carbonate, defect sites and oxygenated organic species are identified from the deconvolution of the C 1s core level spectrum in Figure 8.5b. The peak fitting shows four dominant peaks at 284.80 eV (C C-C/C-H bonding) 286.27 eV (C-O bonding), 288.50 eV (C=O bonding) and 289.88 eV (COOH bonding).

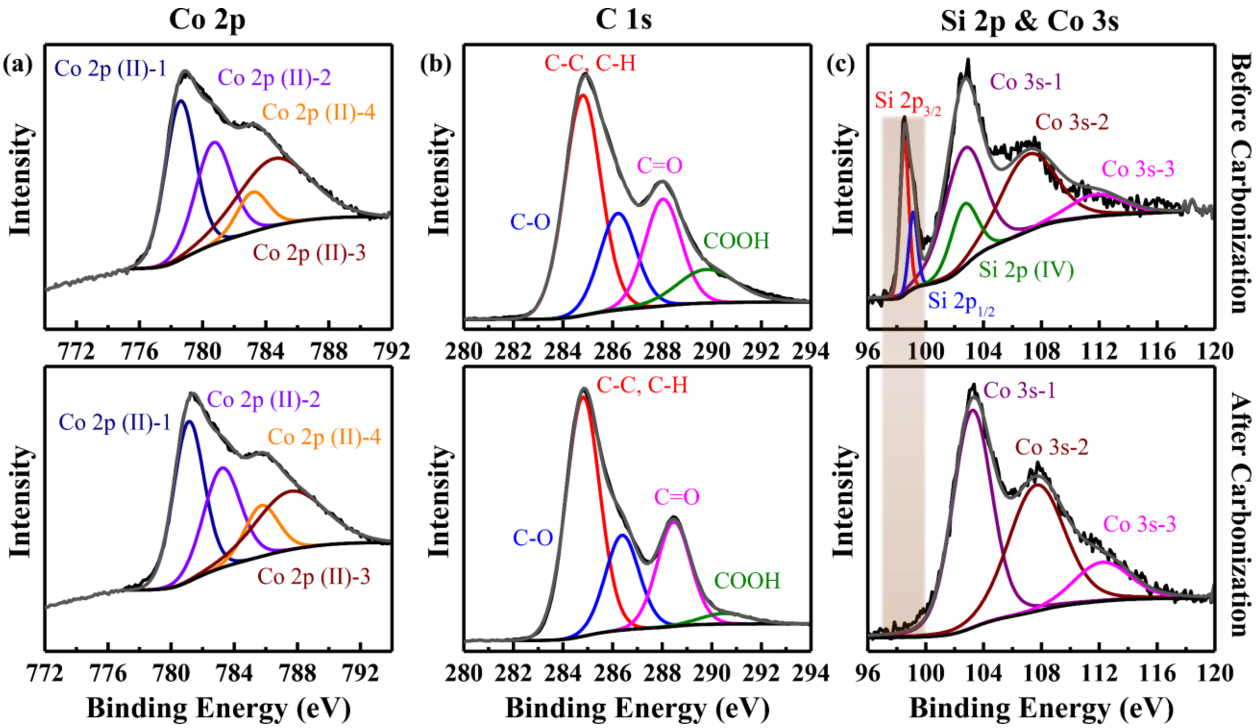

Figure 8.5. XPS spectra of (a) Co 2p, (b) C 1s and (c) Si 2p & Co 3s for 0.5Si@MOF before and after carbonization.

Figure 8.5c illustrates Gaussian curves with the binding energy of 98.53, 99.13 and 102.63 eV in the Si 2p spectrum for the 0.5Si@MOF interfacial region. The bands at 98.53 and 99.13 eV are associated to the spin–orbit doublet of elemental silicon, denoted as $2p_{3/2}$ and $2p_{1/2}$ electronic levels. [22] While the peak at 102.63 eV is the unswerving evidence for the existence of $SiO_x$. [23] However, the absence of Si peaks in 0.5Si@MOF-c indicates a negligible amount of Si on the surface of the composite matrix (primarily located in the core). It is noteworthy that Co 3s component was also included. With these components, the spectrum of the Si window comprises of a convolution of $Si2p_{3/2}$, $Si2p_{1/2}$, Si2p-oxide transitions and Co3s, which is not so unusual. [24]

Figure 8.6a displays the active material discharge capacity over 100 cycles for half-cells of electrodes of the sandwich configuration, including several baselines. In these electrodes, the protective MOF layer was quite large (~8 mg/cm$^2$) and served as an upper limit in the investigation. The Super P cushion is intended to provide a conductive buffering layer between the silicon and current collector. It should be noted that Super P has a capacity of ~240 mAh/g and will contribute to the total capacity of the cell. However, the contribution from Super P is most relevant during the first cycle, where the high-surface area carbon is known to contribute a large irreversible capacity due to SEI formation, as seen in Figure 8.6a (grey). After the first cycle, the weighted contribution from Super P is negligible as it amounts to approximately 5% of the total capacity contribution (e.g., 0.23 mAh out of a total of 4.5 mAh). The SP-Si-MOF sample maintained the highest capacity of 1980 mAh/g after 100 cycles at C/10. However, its 100-cycle capacity retention of 53% is similar to the SP-Si-cushion. Capacity retentions for the SP-Si-cushion and standard Si baselines were 56% and 21%, respectively. This would suggest the Super P protective cushion is the most significant factor for extending cycle life in the sandwich configuration. A protective Super P layer will buffer the mechanical stress from silicon expansion, thereby reducing damage to the copper current collector while preserving electrical conductivity during cycling. Figure S8.4 in SI shows an absence of welting on the Cu foil of a postmortem cell for the SP-Si-MOF composite. In contrast, the MOF layer may provide an additional surface-protective contribution that may facilitate a stable SEI. Further insight into SEI formation can be found in the coulombic efficiency (CE) of the different electrodes. The SP-Si-MOF sandwich configuration attained a stable CE most rapidly (above 98% within 5 cycles). In contrast, the baseline SP-Si-cushion required 10 cycles, and the standard silicon baseline had a more unstable CE. A rapidly stable CE is consistent with a reduction in irreversible side reactions and the formation of a stable SEI.[12]

Differential capacity and voltage curves in Figures 8.6b-c and S8.5 correspond to the SP-Si-MOF and the SP-Si baseline. The first cycle has been omitted due to the large irreversible capacity from SEI formation involving the high-surface area carbon. The dQ/dV plots reveal two lithiation peaks and two delithiation peaks, which are typical of silicon and have been described elsewhere.[14] No new peaks appear to be attributable to the MOF.

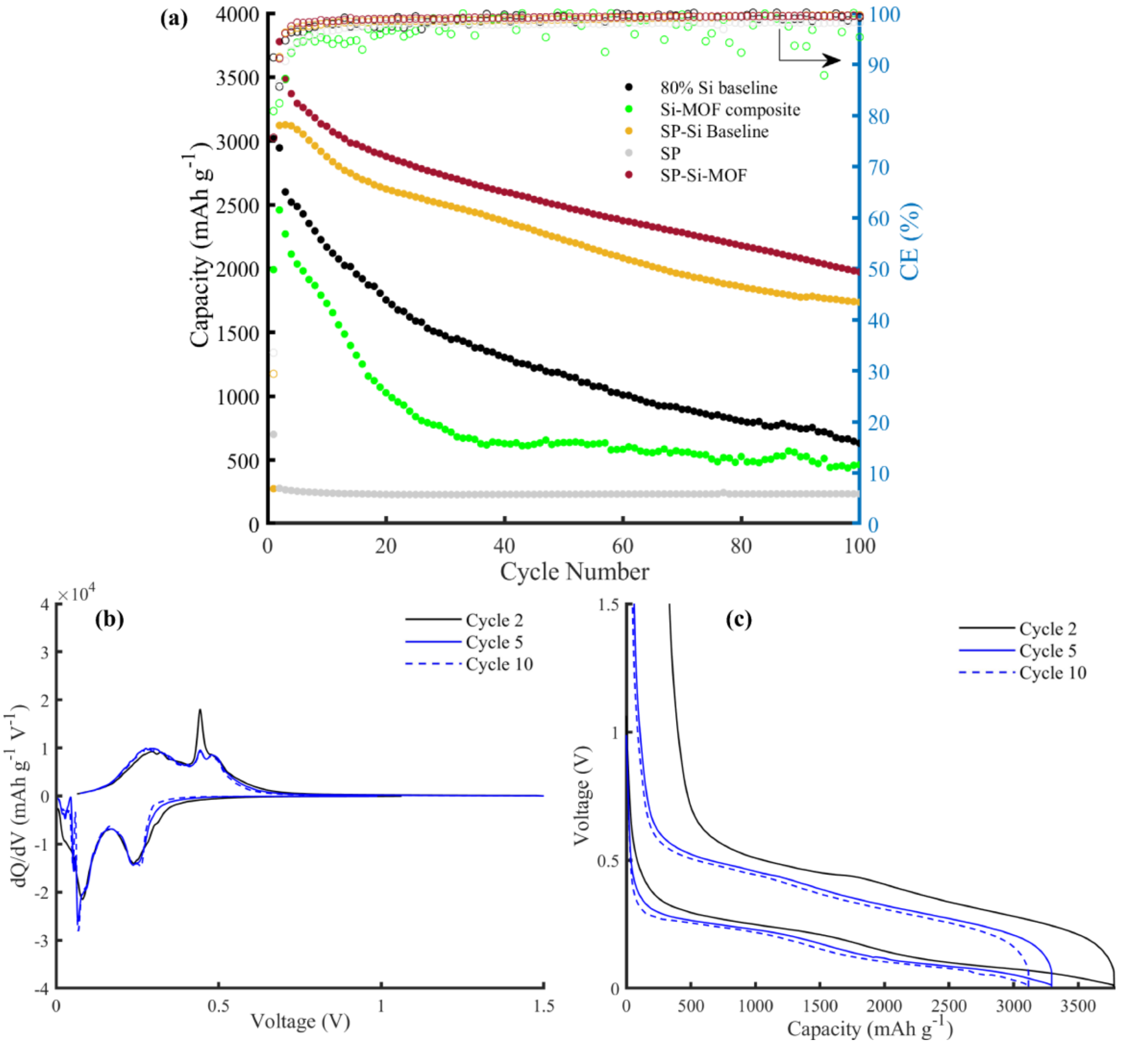

Figure 8.6. a) Active material discharge capacity for sandwich configuration electrodes with a thick Si loading. MOF-74 used for all electrodes. dQ/dV plot and potential profile for (b & c) the SP-Si-MOF sandwich.

We further evaluated the SP-Si-MOF sandwich configuration with the aim of differentiating silicon layer thickness and MOF type. Figure S8.6 shows the cycling result of SP-Si-MOF electrodes with a thick or thin SP and Si layer, while using either MOF-74 or MOF-199. In addition, these electrodes had a protective MOF layer that was reduced to ~1.5-2 mg cm$^{-2}$ to study a more economical loading of MOF. The sample with the silicon layer cast using a 450 µm or 150 µm gap notch bar is denoted *thick* or *thin*, respectively. In addition, SP-Si-cushion baselines have been included without the MOF layer. Interestingly, the capacity retention decay profile was relatively similar for all electrodes. A thin Si-loading consistently maintained a higher capacity during the first 20 cycles. Electrode sandwich designs employing MOF-199 consistently had more severe capacity decay relative to MOF-74. However, it should be noted that all MOF-74-based electrodes (including corresponding SP-Si-cushion baselines) had a capacity retention between 55 and 40% after 100 cycles and thus any benefit from the MOF layer is modest.

The cycling performance for a simple Si-MOF composite is also shown in Figure 8.6a. This electrode was prepared with 15 wt% pristine MOF (without carbonization). The Si-MOF composite had a rapid capacity decline, retaining 25% of its initial capacity after only 30 cycles. In addition, the Si-MOF composite had a very unstable CE, as marked by the fluctuations between 90-100% during cycling. The poor performance and unstable cycling of MOFs while implemented in a simple composite design is consistent with the known low conductivity of metal-organic frameworks. This low conductivity is one bottleneck to their application in fields such as electrocatalysis.[25] Other authors have reported very low reversible capacity (100 mAh/g) with similar MOF-coated silicon nanoparticles.[4] As such, it is essential that the integration of MOF into silicon electrodes employ design configurations that ensure sufficient conductivity and silicon lithiation.

Investigation into the causes of failure for the sandwich SP-Si-MOF electrodes revealed typical expansion and cracks within the active layer. Figure 8.7a & b shows the electrode cross sections for the SP-Si-MOF electrode before and after cycling. For the postmortem electrode, vertical cracks within the silicon-rich active material are prominent. These cracks likely developed as a consequence of mechanical stress accumulation within the silicon layer between the Super P and MOF layers. However, the layers remain distinct after cycling, and no evidence of cobalt migration from the MOF layer can be seen within the silicon layer, suggesting good bulk structural integrity despite silicon expansion.

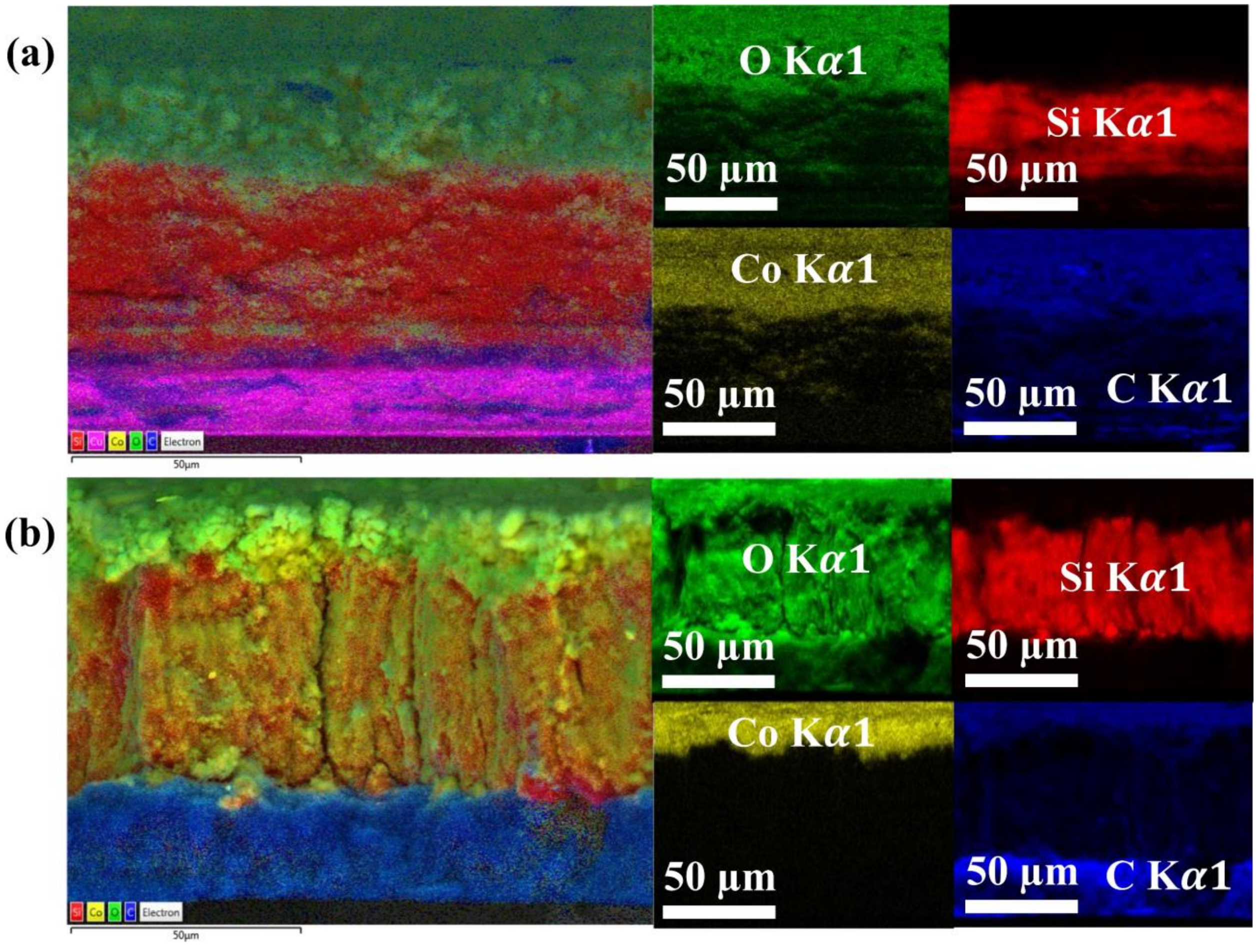

Figure 8.7. EDX maps of a) uncycled electrode cross section for thick SP-Si-MOF sandwich and b) cross section of the electrode after 100 cycles. Note: sample b) was placed onto carbon tape due to postmortem delamination from the Cu. It is recommended to compare only the silicon or MOF layer.

To further mitigate damage within the active layer of the electrode and increase capacity retention, MOF was implemented in an encapsulation design with silicon. It is known that silicon expansion and capacity fade are reduced in composite-type electrode configurations with a lower silicon content. As a result, the MOF was synthesized in situ onto the silicon surface and subsequently pyrolyzed. Figure 8.8a displays the active material discharge capacity of the Si@MOF-c electrodes with two different silicon fractions. The discussion regarding capacity and capacity retention has omitted the first-cycle to focus only on the reversible capacity. However, it should be acknowledged that these Si@MOF-c composites have a large first-cycle irreversible capacity, which is attributable to SEI formation due to the high carbon content as well as possible irreversible lithiation of traces of Co-oxides at low voltage. The 0.5Si@MOF-c composite delivered an initial reversible capacity around 1000 mAh/g, whereas 1.0Si@MOF-c delivered an initial reversible capacity around 1900 mAh/g. Moreover, the capacity retention for the

0.5Si@MOF-c electrode was 60% after 100 cycles, superior to a standard silicon-graphite composite baseline (20Si-10CMC) which retained only 40% initial capacity after 100 cycles. Considering the high active material loading (~2.2 mg $cm^{-2}$) of these electrodes, the capacity retention of 0.5Si@MOF-c is quite high. In contrast, the high-Si 1.0Si@MOF-c electrode retained only 25% of its initial capacity after 100 cycles and also had a very poor coulombic efficiency (< 97%). This capacity retention is in fact inferior to the standard silicon-graphite baseline. Thus, for 1.0Si@MOF-c, the excessive SEI from the carbon in the first cycle, and subsequent SEI and pulverization from the high-Si content vitiates any stabilizing contribution from the MOF-derived carbon matrix. Nevertheless, the performance of 1.0Si@MOF-c is still superior to a similar Si@MOF-c composite reported previously.[4] The authors prepared a Zn-based Si@MOF-c composite with an initial capacity of 1800 mAh/g, however the electrode only retained 300 mAh/g after 20 cycles. In contrast, our Co-based 1.0Si@MOF-c had a similar initial capacity and retained over 1200 mAh/g after 20 cycles. This provides some evidence that MOFs with non-alloying Co reduce capacity decay better than MOFs with alloying metals (Zn). Differential capacity and voltage curves in Figures 8.8b & c reveal the typical lithiation/delithiation behaviour of silicon without additional reversible peaks, suggesting the silicon and non-graphitic carbon are the primary electrochemically active species within Si@MOF-c. This should be contrasted with the additional peaks due to graphite lithiation/delithiation observed at low voltage with the 20Si-10CMC baseline in Figure S8.7.

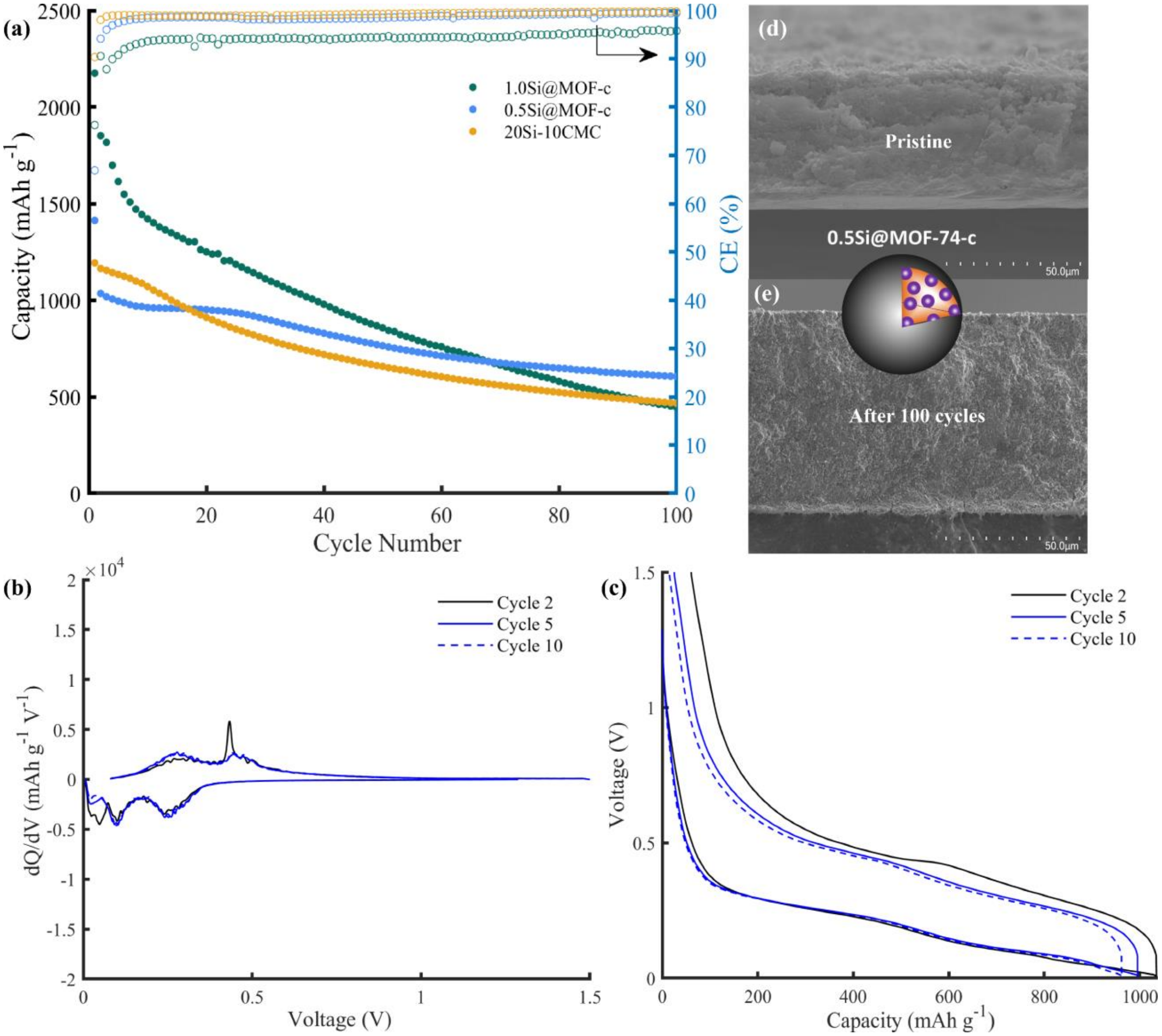

Figure 8.8. a) Active material discharge capacity for carbonized Si@MOF-c electrodes over 100 cycles. dQ/dV plot and potential profile for (b & c) 0.5Si@MOF-c. SEM cross-sections of a 0.5Si@MOF-c electrode d) pristine and e) after 100 cycles (also on carbon tape).

Moreover, the rate capability of the best-performing 0.5Si@MOF-c electrode in Figure S8.8 shows the discharge capacities at different current rates from C/10 to 2C. The electrode had a very good rate capability until the current of 2C. Upon return to C/10, the electrode delivered a high capacity around 800 mAh/g, albeit with a more rapid decline in capacity. Additional cross-section images in Figure 8.8d & e of a 0.5Si@MOF-c electrode before and after cycling confirm good active layer cohesion with no large cracks.

The kinetics of the best-performing 0.5Si@MOF-c anode was studied with b-value analysis on CV scans at different scan rates as shown in Figure S8.9. It is known that the relationship between current (i) and scan rate ($v$) follows the power-law equation below, where a and b are coefficients [26]:

$$i = av^{b}\ (0.5 \leq b \leq 1)$$

$$\log i = blog\ v + \log a$$

The b-value is determined from the slope of the line obtained by plotting log(i) vs. log(v). Semi-infinite linear diffusion is described by a b-value of 0.5, whereas a capacitive-dominated process is described by a b-value of 1.0.[27] The b-value for the anodic peak associated with $Li_xSi_y$ delithiation was 0.67, which suggests a predominantly diffusion-controlled process and is consistent with other Si-based anodes.[12,28]

To further elucidate the superior performance of 0.5Si@MOF-c, electrode surface images of postmortem electrodes for both the sandwich and the 0.5Si@MOF-c configurations are shown in Figure 8.9. The SP-Si-MOF electrode developed large fissures, consistent with the vertical cracks of Figure 8.7b. In contrast, the 0.5Si@MOF-c electrode remained relatively uniform with some small fissures. The lower degree of bulk-electrode damage within the Si@MOF-c sample is consistent with its composite-like design, lower silicon content, and superior capacity retention.

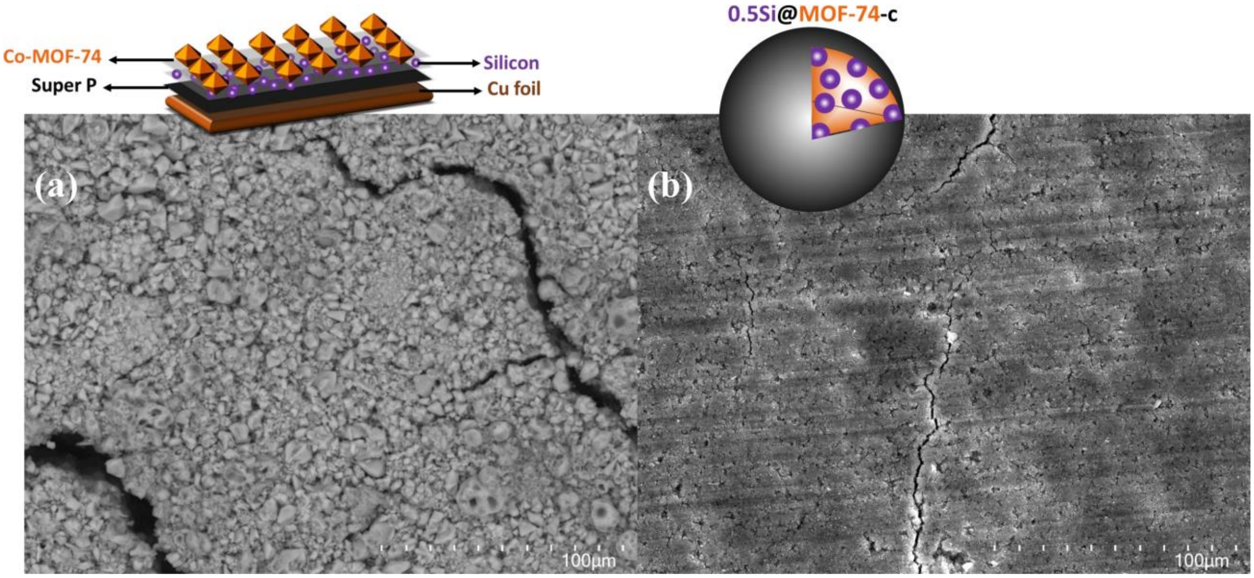

Figure 8.9. Postmortem electrode surface images of a) SP-Si-MOF and b) 0.5Si@MOF-c.

## Conclusions

In conclusion, MOF-74 (Co-based) and MOF-199 (Cu-based) were tested in different configurations with the silicon anode of lithium-ion batteries using a high-Si loading. SP-Si-MOF sandwich configurations provided a modest improvement in capacity retention. The improvement was primarily attributed to the cushion Super P layer. When tested in a sandwich configuration, MOF-74 was found to provide superior capacity retention to MOF-199. Greatest improvements in capacity retention were observed when the MOF was synthesized in situ onto the silicon surface and subsequently pyrolyzed. The best performing 0.5Si@MOF-c electrode delivered a high capacity of 1000 mAh/g and retained 60% capacity after 100 cycles, surpassing a standard silicon-graphite composite. Future studies should focus on identifying any Si-MOF interactions that may facilitate a stable SEI while critically assessing the economic feasibility of these composites.

Author Contributions

Electrochemical testing & physicochemical characterizations: JS, MH

XPS: MH

Manuscript writing: JS, MH

MOF synthesis: WDP

Consultations and suggestions: MM, EB, YAL

Acknowledgements

We would like to thank the LiBTec consortium and the Office of Energy Research and Development (OERD) at Natural Resources Canada for financial support. Special thanks to Jeff Fraser, Oltion Kodra, and Martin Couillard for their help with SEM, XPS, and TEM.

## References

[1] Cheng; Z.; Jiang; H.; Zhang; X.; Cheng; F.; Wu; M.; & Zhang; H. Fundamental Understanding and Facing Challenges in Structural Design of Porous Si-Based Anodes for Lithium-Ion Batteries. *Advanced Functional Materials*; **2023**; 2301109.

[2] Houache; M. S.; Yim; C. H.; Karkar; Z.; Abu-Lebdeh; Y. On the Current and Future Outlook of Battery Chemistries for Electric Vehicles—Mini Review. *Batteries*; **2022**; *8*(7); 70.

[3] Choi; J. W.; & Aurbach; D. Promise and reality of post-lithium-ion batteries with high energy densities. *Nature reviews materials*; **2016**; *1*(4); 1-16.

[4] Han; Y.; Qi; P.; Feng; X.; Li; S.; Fu; X.; Li; H.; ... & Wang; B. In situ growth of MOFs on the surface of Si nanoparticles for highly efficient lithium storage: Si@ MOF nanocomposites as anode materials for lithium-ion batteries. *ACS Applied Materials & Interfaces*; **2015**; *7*(4); 2178-2182.

[5] Malik; R.; Loveridge; M. J.; Williams; L. J.; Huang; Q.; West; G.; Shearing; P. R.; ... & Walton; R. I. Porous metal–organic frameworks for enhanced performance silicon anodes in lithium-ion batteries. *Chemistry of Materials*; **2019**; *31*(11); 4156-4165.

[6] Zhang; L.; Lin; Y.; Peng; X.; Wu; M.; & Zhao; T. A High-Capacity Polyethylene Oxide-Based All-Solid-State Battery Using a Metal–Organic Framework Hosted Silicon Anode. *ACS applied materials & interfaces*; **2022**; *14*(21); 24798-24805.

[7] Ou; H.; Peng; Y.; Sang; X.; Zhong; H.; Zhou; J. E.; Lin; X.; ... & Wu; Y. Recent advances in silicon-based composite anodes modified by metal-organic frameworks and their derivatives for lithium-ion battery applications. *Journal of Alloys and Compounds*; **2023**; 170713.

[8] Wang; Y.; Jin; H.; Ma; Q.; Mo; K.; Mao; H.; Feldhoff; A.; ... & Jiang; Z. A MOF glass membrane for gas separation. *Angewandte Chemie*; **2020**; *132*(11); 4395-4399.

[9] Cheng; H.; Liu; Y.; Hu; Y.; Ding; Y.; Lin; S.; Cao; W.; ... & Wei; H. Monitoring of heparin activity in live rats using metal–organic framework nanosheets as peroxidase mimics. *Analytical chemistry*; **2017**; *89*(21); 11552-11559.

[10] Senthil Raja; D.; Cheng; C. C.; Ting; Y. C.; & Lu; S. Y. NiMo-MOF-Derived Carbon-Armored Ni4Mo Alloy of an Interwoven Nanosheet Structure as an Outstanding pH-Universal Catalyst for Hydrogen Evolution Reaction at High Current Densities. *ACS Applied Materials & Interfaces*; **2023;** *15*(16); 20130-20140.

[11] Han; Y.; Qi; P.; Zhou; J.; Feng; X.; Li; S.; Fu; X.; ... & Wang; B. Metal–organic frameworks (Mofs) as sandwich coating cushion for silicon anode in lithium-ion batteries. *ACS applied materials & interfaces*; **2015**; *7*(48); 26608-26613.

[12] Gao; R.; Tang; J.; Yu; X.; Tang; S.; Ozawa; K.; Sasaki; T.; & Qin; L. C. In situ synthesis of MOF-derived carbon shells for silicon anode with improved lithium-ion storage. *Nano Energy*; **2020**; *70*; 104444.

[13] Waldmann; T.; Iturrondobeitia; A.; Kasper; M.; Ghanbari; N.; Aguesse; F.; Bekaert; E.; ... & Wohlfahrt-Mehrens; M. Post-mortem analysis of aged lithium-ion batteries: Disassembly methodology and physico-chemical analysis techniques. *Journal of The Electrochemical Society*; **2016**;*163*(10); A2149.

[14] Sturman; J. W.; Yim; C. H.; Karkar; Z.; Baranova; E. A.; Toupin; M.; & Abu-Lebdeh; Y. Investigation of Xanthan Gum and Carboxymethyl Cellulose Binders for the Silicon Anode of Lithium-Ion Batteries. *Journal of The Electrochemical Society*; **2023**; *170*(2); 020534.

[15] Pliekhov; O.; Pliekhova; O.; Štangar; U. L.; & Logar; N. Z. The Co-MOF-74 modified with N; N′-Dihydroxypyromellitimide for selective; solvent free aerobic oxidation of toluene. *Catalysis Communications*; **2018**;*110*; 88-92.

[16] Armstrong; M. R.; Senthilnathan; S.; Balzer; C. J.; Shan; B.; Chen; L.; & Mu; B. Particle size studies to reveal crystallization mechanisms of the metal organic framework HKUST-1 during sonochemical synthesis. *Ultrasonics sonochemistry*; **2017**;*34*; 365-370.

[17] Lu; Y. H.; Li; J. H.; Xu; Z. F.; Liu; J. M.; Liu; S. J.; & Wang; R. X. Metal–organic framework derived porous nanostructured Co 3 O 4 as high-performance anode materials for lithium-ion batteries. *Journal of Materials Science*; **2021**; *56*; 2451-2463.

[18] Xu; H.; Wang; Q.; Xiao; H.; Li; X.; Su; X.; Tang; M.; ... & Li; S. In situ preparation of C–SiC x O y coatings with controllable composition on continuous oxygen-enriched SiC fibres. *RSC advances*; **2019**; *9*(3); 1319-1326.

[19] Han; R.; Zhao; M.; Li; X.; Cui; S.; & Yang; J. N-doped regular octahedron MOF-199 derived porous carbon for ultra-efficient adsorption of oxytetracycline. *Separation and Purification Technology*; **2022**; *302*; 121960.

[20] Liu; G.; Wang; Y.; Xue; Q.; Wen; Y.; Hong; X.; & Ullah; K. TiO 2/Cu-MOF/PPy composite as a novel photocatalyst for decomposition of organic dyes. *Journal of Materials Science: Materials in Electronics*; **2021**; *32*; 4097-4109.

[21] Rani; R.; Deep; A.; Mizaikoff; B.; & Singh; S. Enhanced hydrothermal stability of Cu MOF by post synthetic modification with amino acids. *Vacuum*; **2019**;*164*; 449-457.

[22] Niu; P.; Zhou; Y.; Li; Z.; Xiao; Y.; Su; M.; Zhou; S.; ... & Liu; Y. Synergetic design of a coralline-like Si/Ni/C anode material with microstructure and gradient interface for lithium-ion batteries. *Journal of Alloys and Compounds*; **2023**; *933*; 167785.

[23] Zatsepin; D. A.; Zatsepin; A. F.; Boukhvalov; D. W.; & Gavrilov; N. V. Bi-doped silica glass: A combined XPS–DFT study of electronic structure and pleomorphic imperfections. *Journal of Alloys and Compounds*; **2020**; *829*; 154459.

[24] García-Méndez; M.; Castillón; F. F.; Hirata; G. A.; Farıas; M. H.; & Beamson; G. XPS and HRTEM characterization of cobalt–nickel silicide thin films. *Applied surface science*; **2000**;*161*(1-2); 61-73.

[25] Li; C.; Zhang; H.; Liu; M.; Lang; F. F.; Pang; J.; & Bu; X. H. Recent progress in metal–organic frameworks (MOFs) for electrocatalysis. *Industrial Chemistry & Materials*; **2023**; 1; 9-38.

[26] Ryu; J.; Chen; T.; Bok; T.; Song; G.; Ma; J.; Hwang; C.; ... & Park; S. Mechanical mismatch-driven rippling in carbon-coated silicon sheets for stress-resilient battery anodes. *Nature communications*; **2018**; *9*(1); 2924.

[27] An; Y.; Tian; Y.; Zhang; Y.; Wei; C.; Tan; L.; Zhang; C.; ... & Qian; Y. Two-Dimensional Silicon/Carbon from Commercial Alloy and CO2 for Lithium Storage and Flexible Ti3C2T x MXene-Based Lithium–Metal Batteries. *ACS nano*; **2020**; *14*(12); 17574-17588.

[28] Jiang; Y.; & Liu; J. Definitions of pseudocapacitive materials: a brief review. *Energy & Environmental Materials*; **2019**; *2*(1); 30-37.

# Chapter 9: Conclusions and Future Recommendations

The demand for Li-ion batteries continues to grow in tandem with the demand for portable and renewable energy. One of the most promising ways to accommodate this demand is to increase the energy density and cycle life of battery electrode materials. While many materials offer high energy density (i.e., silicon, $LiNiO_2$), this energy density is often not sustained with repeated charging and discharging. Design strategies like silicon-graphite composites and high-entropy oxides have been shown to improve the stability of certain materials. Such multicomponent electrodes can balance the advantages and disadvantages of different components to offer an attractive compromise of cost, energy density, and lifetime. This thesis has investigated various aspects of multicomponent electrodes with a special emphasis on silicon-based anodes and high-entropy materials.

The high-entropy design strategy has created new families of diverse and largely unexplored oxides and alloys with great potential as electrode materials. Moreover, they may reduce reliance on any single element. Chapter 4 reported the synthesis and electrochemical cycling of the $LiNi_{0.2}Mn_{0.2}Co_{0.2}Fe_{0.2}Ti_{0.2}O_2$ HE layered cathode. The cathode was shown to deliver a high capacity of 160 mAh/g during the first cycle and a stable capacity of around 80 mAh/g when charged to the high potential of 4.4 V. Although the cathode had a capacity retention that was inferior to traditional NMC cathodes, the study highlights the potential of the high-entropy strategy to the design of new cathodes that use inexpensive metals not typically included in layered cathodes.

In Chapter 5, a novel small molecule azaacene (SmAz) was synthesized and tested as an anode in Li-ion batteries. SmAz delivered an ultra-high capacity of  550 mAh/g at 50 mA/g, exceeding its theoretical capacity of 237 mAh/g. Like other carbon-rich and organic anodes, SmAz displayed an activation process whereby the capacity increases with cycle time when charged to the upper voltage limit of 3.0 V. These properties were elucidated with Operando XRD, impedance, and cyclic voltammetry. In particular, SmAz's lithiation mechanism was revealed to be controlled by a mixture of ion-diffusion and pseudocapacitance. Operando XRD suggested that SmAz becomes amorphous after the first cycle. The associated increase in electrolyte-exposed surface area during cycling is likely responsible for pseudocapacitive lithium extraction when charged to 3.0 V.

In Chapter 6, the role of the binder in the cohesion of silicon electrodes was investigated, including failure mechanisms. Contrary to many publications on water-soluble binders, our work used a low binder content of 10 wt% and a high Si loading. Nature-derived and water-soluble XG and NaCMC were used as a binder in high-loading electrodes prepared with either 80 wt% Si or 20 wt% Si + 60 wt% G. Electrochemical testing revealed the NaCMC binder provided superior capacity retention in both formulations. SEM/EDX and XPS suggested that while both binders help via non-covalent bonding, the NaCMC binder provided superior electrode cohesion in cycled cells. No synergistic improvement in capacity retention was observed when XG and NaCMC were simply combined in equal proportion. However, an improvement in capacity retention was achieved when a thin carbon-XG cushion layer was added to the Cu followed by a Si-NaCMC electrode layer.

In Chapter 7, silicon nanoparticles were surface modified with $Li_4Ti_5O_{12}$ to reduce capacity decay. A relatively thin $Li_4Ti_5O_{12}$ coating was found to marginally reduce capacity decay relative to unmodified nanosilicon. However, greatest improvements in battery performance were observed when the Si@LTO composite was combined with graphite or pitch-derived carbon. It was found that the best composite was 40 wt% Si@LTO + 40 wt% graphite, which had a high capacity at both C/10 and 1C (~900 mAh/g at C/10 and ~600 mAh/g at 1C). Improvements in performance were attributed to the LTO surface protective effect and the additional buffering contribution from the graphite. Postmortem SEM images revealed suppressed electrode expansion with Si@LTO+G relative to a simple binary composite of silicon and graphite.

Later, another surface-modified silicon composite was prepared with metal organic frameworks in Chapter 8. Unlike the brittle $Li_4Ti_5O_{12}$ ceramic, MOFs are a broad family which may offer the structural and functional tunability needed to alleviate some of the problems associated with silicon expansion. Two design configurations were critically investigated with different MOFs: a multilayer sandwich design and an encapsulation design. The sandwich design provided a modest improvement in capacity retention that was primarily attributed to the cushion Super P layer. In the sandwich configuration, the MOF-74 was found to provide superior capacity retention relative to MOF-199. Greatest improvements in capacity retention were observed when the MOF was synthesized onto the silicon surface and subsequently pyrolyzed. The resulting 0.5Si@MOF-c composite delivered a high capacity of 1000 mAh/g and retained 60% capacity after 100 cycles, surpassing a standard silicon-graphite composite.

Silicon is a promising anode that is already being used in commercial cells in small quantities. However, much academic work on silicon is done at a low TRL level. Future work on silicon is recommended to be carried out in full cells at the pouch-cell level to acquire data which is more relevant to practical applications. In these configurations, greater attention to manufacturability and failure-mode analysis are encouraged. Moreover, future morphological or encapsulation strategies involving silicon should critically consider the extent to which their battery performance is superior to simple silicon-graphite composites (while also using inexpensive preparation methods and materials). It is encouraged to cycle half-cell anode materials to an upper cut-off voltage not exceeding 1.5 V. For anodes, redox peaks that occur at higher potential, or carbonaceous anodes which are cycled up to 3.0 V, are unsuitable in full-cell configurations. A detailed investigation into the Faradaic/non-Faradaic contributions to capacity in organic anodes is suggested. Considering that recent studies have confirmed and investigated the poor cycle-life of high-entropy layered cathodes, it is recommended to study alternative high-entropy structures; in particular, spinel and disordered rocksalt cathodes, as well as metallic alloy anodes. It is further recommended to use characterization methods like operando XRD, EIS, and XPS to provide insight into bulk and interfacial material stability.

# Supplementary Information and Appendix

## Supplementary Information for Chapter 2

Table S2.4.1. Select Publications on High-Entropy Oxides for Li-ion Batteries

| **Primary Composition** | **First Author and Year** | **Synthesis Method** | **Structure** | **Battery Performance** | **Reference*** |
|---|---|---|---|---|---|
| (MgNiCoCuZn)O | Rost, 2015 | Solid-state | Rock-salt | Fundamental characterization | [90] |
| (CeLaPrSmY)O | Djenadic, 2017 | Nebulized spray pyrolysis (NSP) | $CaF_2$-type | Fundamental characterization on rare earth HEO | [117] |
| (CoCuMgNiZn)O | Sarkar, 2017 | (NSP)<br>flame spray pyrolysis (FSP)<br>reverse co-precipitation (RCP) | Rock-salt | Investigation of synthesis methods | [104] |
| $(CeLaPrSmY)O_{2-\delta}$ | Sarkar, 2017 | NSP | Fluorite type | Fundamental characterization | [118] |
| $(Co_{0.2}Cu_{0.2}Mg_{0.2}Ni_{0.2}Zn_{0.2})O$ | Sarkar, 2018 | NSP | Rock-salt | Anode. 500 mAh/g at 0.1 A/g | [96] |
| $(Gd_{0.2}La_{0.2}Nd_{0.2}Sm_{0.2}Y_{0.2})(Co_{0.2}Cr_{0.2}Fe_{0.2}Mn_{0.2}Ni_{0.2})O_3$ | Sarkar, 2018 | NSP | Perovskite | Fundamental characterization | [116] |
| $(Mg_{0.2}Co_{0.2}Ni_{0.2}Zn_{0.2}Li_{0.2})O$ | Anik, 2019 | Solid State | Rock-salt | Anode. 720 mAh/g after 10 cycles at 0.1A/g | [170] |
| $(Mg_{0.2}Co_{0.2}Ni_{0.2}Cu_{0.2}Zn_{0.2}O)$ | Qiu, 2019 | Solid State | Rock-salt | Anode. 920 mAh/g after 300 cycles at 0.1 A/g | [122] |
| $(Li_x(Co_{0.2}Cu_{0.2}Mg_{0.2}Ni_{0.2}Zn_{0.2})OF_x)$ | Wang, 2019 | Coprecipitation and ball milling | Rock-salt oxyfluoride | Cathode. 90 mAh/g after 100 cycles at C/10 | [103] |
| $Gd(Co_{0.2}Cr_{0.2}Fe_{0.2}Mn_{0.2}Ni_{0.2})O_3$ | Witte, 2019 | NSP | Perovskite | Investigation of magnetic properties | [167] |
| $(Co_{0.2}Cu_{0.2}Mg_{0.2}Ni_{0.2}Zn_{0.2})O$ | Wang, 2019 | NSP | Rock-salt | Anode in full cell. 300 mAh/g after 50 cycles at 0.12A/g | [120] |
| Multiple HEOs | Chellali, 2019 | NSP | Rock-salt, fluorite, and perovskite | Fundamental characterization with atom probe tomography | [155] |
| $(Ce_{0.2}La_{0.2}Pr_{0.2}Sm_{0.2}Y_{0.2})O_{2-\delta}$ | Cheng, 2019 | NSP | $CaF_2$-type | High-pressure characterization | [157] |

| | | | | | |
|---|---|---|---|---|---|
| $(Mg_{0.2}Co_{0.2}Ni_{0.2}Cu_{0.2}Zn_{0.2})O$ | Chen, 2019 | Solid State | Rock-salt | Studied pseudocapacitive contribution. Anode. 900 mAh/g after 150 cycles at 0.2A/g | [135] |
| $(FeCoNiCrMn)_3O_4$ | Wang, 2020 | Solid State | Spinel | Anode. 402 mAh/g after 300 cycles at 0.5 A/g | [126] |
| $(Mg_{0.2}Ti_{0.2}Zn_{0.2}Cu_{0.2}Fe_{0.2})_3O_4$ | Chen, 2020 | Solid State | Spinel | Anode. 504 mAh/g after 300 cycles at 0.1 A/g | [125] |
| Non-equimolar cations with Cr, Mn, Fe, Co, and Ni | Nguyen, 2020 | Hydrothermal method | Spinel | Anode. 500 mAh/g at 2 A/g | [129] |
| $(MgCoNiZn)_{0.65}Li_{0.35}O$ | Lökçü, 2020 | Solid State | Rock-salt | Anode. 610 mAh/g after 130 cycles at 1A/g | [124] |
| $[(Bi,Na)_{1/5}(La,Li)_{1/5}(Ce,K)_{1/5}Ca_{1/5}Sr_{1/5}]TiO_3$ | Yan, 2020 | Solid state | Perovskite | Anode. 85 mAh/g after 50 cycles at 0.1A/g. | [123] |
| $Li_x(NiFeMnCrCo)_yO$ | Wang, 2020 | NSP | Spinel and Rock-salts | Investigation of spinel to rock-salt transformation | [164] |
| $LiNa(NiCoMnAlFe)_1O_2$ | Wang, 2020 | NSP | Layered | Cathode. 75 mAh/g after 15 cycles at C/10 | [146] |
| $(Ce_{0.2}La_{0.2}Pr_{0.2}Sm_{0.2}Y_{0.2})O_{2-\delta}$ | Sarkar, 2020 | Reverse coprecipitation | Fluorite | Fundamental characterization | [169] |
| $Mg_{0.2}Co_{0.2}Ni_{0.2}Cu_{0.2}Zn_{0.2}O$ | Ghigna, 2020 | Solid State | Rock-salt | Anode. 600 mAh/g at 0.1 C.<br>Mechanism investigation with operando XAS | [159] |
| $(Gd_{0.2}La_{0.2}Nd_{0.2}Sm_{0.2}Y_{0.2})CoO_3$ | Witte, 2020 | NSP | Perovskite | Investigation of magnetic properties | [166] |
| $(Mg_{0.2}Co_{0.2}Ni_{0.2}Cu_{0.2}Zn_{0.2})O$ | Tavani, 2020 | Solid State | Rock-salt | Mechanism investigation | [158] |
| $(Co_{0.2}Cu_{0.2}Mg_{0.2}Ni_{0.2}Zn_{0.2})O$ and $Li(Co_{0.2}Cu_{0.2}Mg_{0.2}Ni_{0.2}Zn_{0.2})OF$ | Breitung, 2020 | NSP and solid state | Rock-salt | Investigation of gassing behavior | [163] |
| $Li_{1.3}Mn^{2+}{}_{0.1}Co^{2+}{}_{0.1}Mn^{3+}{}_{0.1}Cr^{3+}{}_{0.1}Ti_{0.1}Nb_{0.2}O_{1.7}F_{0.3}$ | Lun, 2021 | Solid State | Disordered Rock-salts | Cathode. Initially 307 mAh/g at a rate of 20 mA/g | [119] |
| $(MgCuNiCoZn)O$ | Kheradmandfard, 2021 | Microwave | Rock-salt | Anode. 325 mAh/g after 1000 cycles at 1 A/g | [113] |
| $(CrMnFeCoNi)_3O_4$ | Huang, 2021 | Hydrothermal and sintering | Spinel | Atomic-scale investigation of mechanism | [165] |
| $(Al_{0.2}CoCrFeMnNi)_{0.58}O_{4-d}$ | Xiang, 2021 | Solution | Spinel | Anode. 554 mAh/g after 500 cycles at 0.2 A/g | [128] |

|  |  |  |  |  |  |
|---|---|---|---|---|---|
|  |  | Combustion |  |  |  |
| $(Co_{0.2}Cu_{0.2}Mg_{0.2}Ni_{0.2}Zn_{0.2})O$ | Schweidler, 2021 | NSP | Rock-salt | Acoustic emission investigation of mechanism | 161 |
| $(Co_{0.2}Cr_{0.2}Fe_{0.2}Mn_{0.2}Ni_{0.2})_3O_4$ | Zhao, 2021 | Solution Combustion | Spinel | Anode. 980 mAh/g after 50 cycles at 0.1 A/g | 127 |
| $Li(Ni_{0.2}Co_{0.2}Mn_{0.2}Ti_{0.2}Fe_{0.2})O_2$ | Sturman, 2021 | Sol-gel | Layered | Cathode. 85 mAh/g after 50 cycles at C/10 | 105 |
| $(CoCuMgNiZn)_{0.8}Li_{0.2}O$ | Moździerz, 2021 | Solid State | Rock-salt | Fundamental characterization | 156 |
| $(FeNiCrMnZn)_3O_4$ | Xiao, 2021 | Solid State | Spinel | Anode. 386 mAh/g after 185 cycles at 0.5 A/g | 132 |
| $(FeCoNiCrMnXLi)_3O_4$ (X=Cu, Mg, Zn) | Duan, 2021 | Solid State | Spinel | Anode. 522 mAh/g after 100 cycles at 0.5 A/g | 131 |
| (MgCoNiCuZn)O | Wang, 2021 | Solid State | Rock-salt | Anode. 550 mAh/g after 100 cycles at 0.1 A/g | 160 |
| Co-free $(CrMnFeNiCu)_3O_4$ | Nguyen, 2022 | Hydrothermal | Spinel | Anode. 755 mAh/g at 50 mA/g | 130 |
| $(Mg_{0.2}Co_{0.2}Ni_{0.2}Cu_{0.2}Zn_{0.2})O$ | Guo, 2022 | Solid State | Rock-salt | Anode. 950 mAh/g after 200 cycles at 0.1 A/g | 115 |
| $(MnFeCoNiCuZn)_3O_{4-x}$ | Dong, 2022 | Rapid Heating | Spinel | Anode. 600 mAh/g at 130 mA/g | 114 |
| $(CoNiZnXMnLi)_3O_4$ (X=Fe, Cr) | Tian, 2022 | Solid State | Spinel | Anode. 260 mAh/g after 100 cycles at 500 mA/g | 134 |
| $LiCr_{1/6}Mn_{1/6}Fe_{1/6}Co_{1/6}Ni_{1/6}Cu_{1/6}O_2$ | Wang, 2022 | Pulsed laser deposition | Layered | Cathode. 40 mAh/g at 5 µA/cm$^2$ | 148 |
| $Ti_{1.1}V_{0.7}Cr_xNb_{1.0}Ta_{0.6}C_3T_z$ | Etman, 2022 | Solid state and solution based | MXene | Anode. 40 mAh/g after 1000 cycles at 1A/g | 111 |

Rock-salt: Fm-3m Spinel: Fd-3m Layered: R-3m

*References from Chapter 2

## Supplementary Information for Chapter 5

### Materials and Instrumentation

Pyrene (98%), sodium periodate (>99%), ruthenium (III) chloride hydrate, fuming nitric acid, glacial acetic acid and *o*-phenylenediamine (99.5%) were purchased from Sigma-Aldrich and used as received. All solvents were purchased from Sigma-Aldrich and used as received.

NMR spectra were recorded using a 400 MHz Bruker Avance III or a 500 MHz Agilent DD2 NMR spectrometer equipped with a $^{13}C$-sensitive cryogenically cooled probe and referenced to the residual solvent peak (DMSO or TFA). Mass spectrometry was performed using a JOEL AccuTOF JMS-T1000LC mass spectrometer equipped with a direct analysis in real-time (DART) ion source. Fourier Transform Infrared Spectroscopy (FTIR) measurements were taken on a Thermo Scientific iS50 equipped with an ATR accessory.

### Methods

Pyrene-4,5,9,10-tetraone (PTO)

The synthesis of PTO was adapted from a similar procedure.[1]

Pyrene (10 g, 49.4 mmol) was dissolved in dichloromethane (200 mL) and MeCN (200 mL) in a large round-bottom flask. While stirring vigorously, water (250 mL), sodium periodate (84.5 g, 395.2 mmol), and ruthenium (III) chloride hydrate (1.23 g, 5.93 mmol) were sequentially added, and the mixture was left to stir overnight at 40 $^{o}$C. Following the reaction, the dark mixture was cooled to room temperature and the organic solvents were evaporated. The mixture was then filtered through a fritted funnel and washed extensively with water to afford the crude product as a green solid. The crude product was dried in a vacuum oven at 40 $^{o}$C, ground using a mortar and pestle, and purified by column chromatography (silica gel, dichloromethane) to afford PTO as a crystalline orange solid (1.94 g, 15%).

$^{1}H$ NMR (500 MHz, DMSO-$d_6$): δ/ppm: 8.33 (4H, d), 7.74 (2H, t); $^{13}C$ NMR (125.7 MHz, DMSO-$d_6$): δ/ppm: 177.3, 134.4, 133.9, 131.6, 130.4. MS (DART) m/z: calcd for $C_{16}H_7O_4$ $[M + H]^+$: 263.03; found: 263.04.

2-Nitropyrene-4,5,9,10-tetraone (PTO-$NO_2$)

Pyrene-4,5,9,10-tetraone (1.44 g, 5.49 mmol,) was added in increments to fuming nitric acid (20 mL) and left to stir at 75 °C for 20 mins. A blast shield and butyl rubber gloves were used as a precaution. The reaction mixture was then poured into 350 mL of ice water, covered with foil and left to stir for 45 mins. The suspension was filtered and the precipitate was dried under vacuum to afford PT-$NO_2$ a bright yellow solid (yield: 1.53 g, 91%). No further purification was required.

$^1$H NMR (500 MHz, DMSO-$d_6$): δ/ppm: 8.83 (2H, s), 8.41 (2H, d), 7.86 (1H, t); $^{13}$C NMR (125.7 MHz, DMSO-$d_6$): δ/ppm: 176.2, 175.3, 148.1, 138.0, 134.0, 133.3, 132.2, 132.1, 131.8, 131.7, 126.3. MS (DART) m/z: calcd for $C_{16}H_6NO_6$ $[M + H]^+$: 308.02; found: 308.03.

SmAz

The synthesis of SmAz was adapted from a similar procedure.[2]

2-Nitropyrene-4,5,9,10-tetraone (460 mg, 1.50 mmol) and o-phenylenediamine (405 mg, 3.75 mmol) were suspended in chloroform (7.8 mL) and glacial acetic acid (31.5 mL) and heated at 70 °C under argon for 18 h. Following the reaction, the suspension was cooled to room temperature and filtered. The precipitate was washed with methanol and hot chloroform, and dried under vacuum to afford SmAz as a dark yellow powder (yield: 643.1 mg, 95 %). No further purification was required.

$^1$H NMR (500 MHz, trifluoroacetic acid-d): δ/ppm: 10.78 (2H, s), 10.02 (2H, d), 8.85 (2H, d), 8.79 (2H, d), 8.71 (1H, t), 8.46 (4H, m); $^{13}$C NMR (125.7 MHz, trifluoroacetic acid-d): δ/ppm: 150.3, 143.3, 142.3, 140.4, 138.4, 138.1, 136.8, 134.3, 134.1, 133.0, 130.7, 130.1, 129.9, 126.7, 126.6, 125.4. MS (DART) m/z: calcd for $C_{28}H_{13}N_5O_2$ $[M + H]^+$: 452.11; found: 452.12.

## Supporting Figures

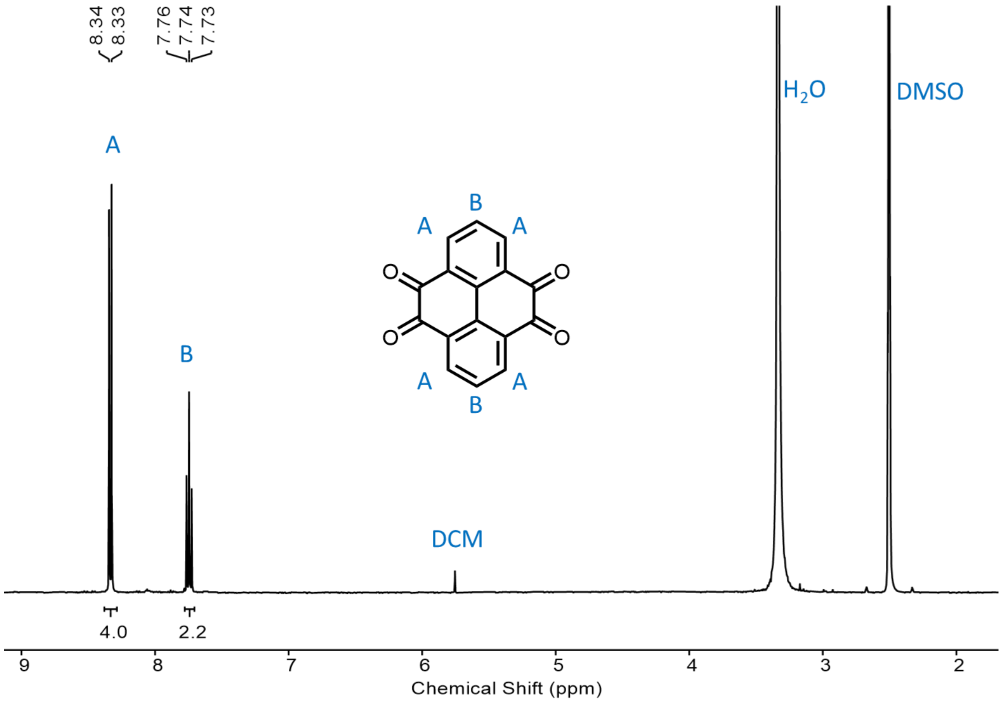

Figure S5.1. $^1$H-NMR (400 MHz, DMSO-d$_6$) of PTO.

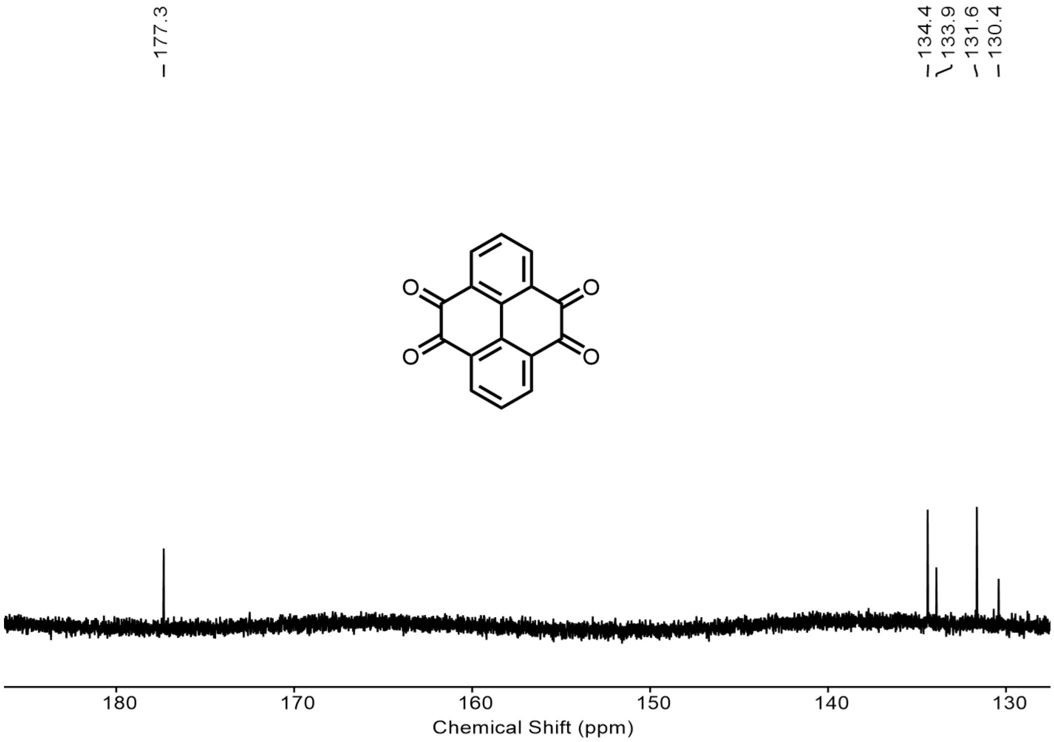

Figure S5.2. $^{13}$C-NMR (125 MHz, DMSO-$d_6$) of PTO.

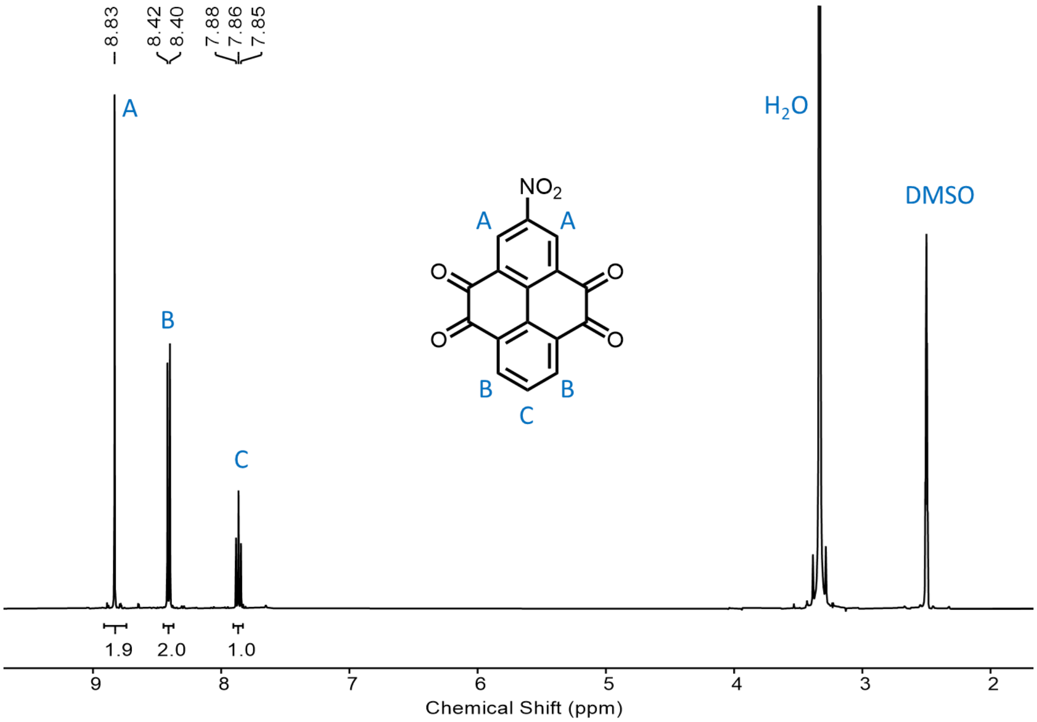

Figure S5.3. $^1$H-NMR (400 MHz, DMSO-$d_6$) of PTO-$NO_2$.

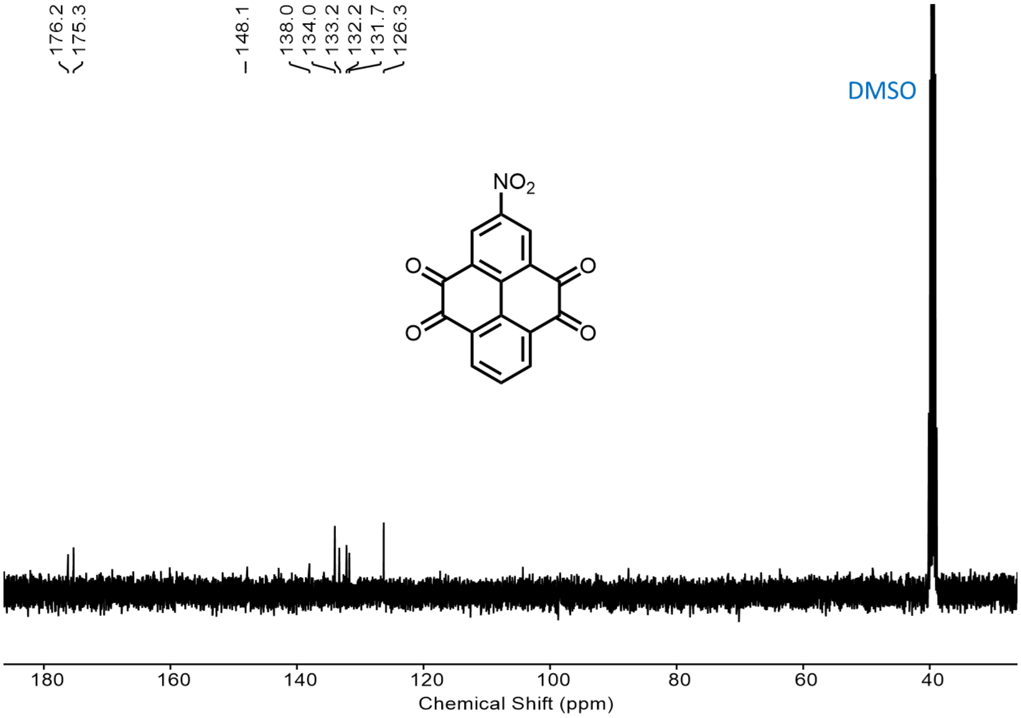

Figure S5.4. $^{13}$C-NMR (125 MHz, DMSO-$d_6$) of PTO-$NO_2$.

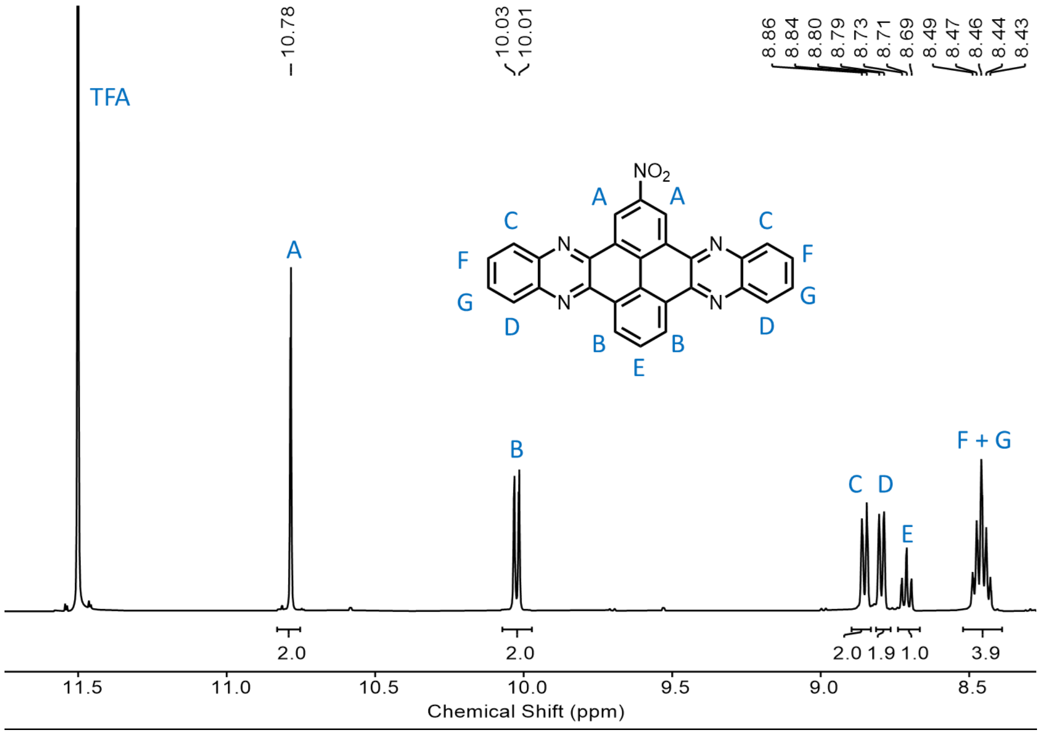

Figure S5.5. $^1$H-NMR (500 MHz, trifluoroacetic acid-d) of SmAz.

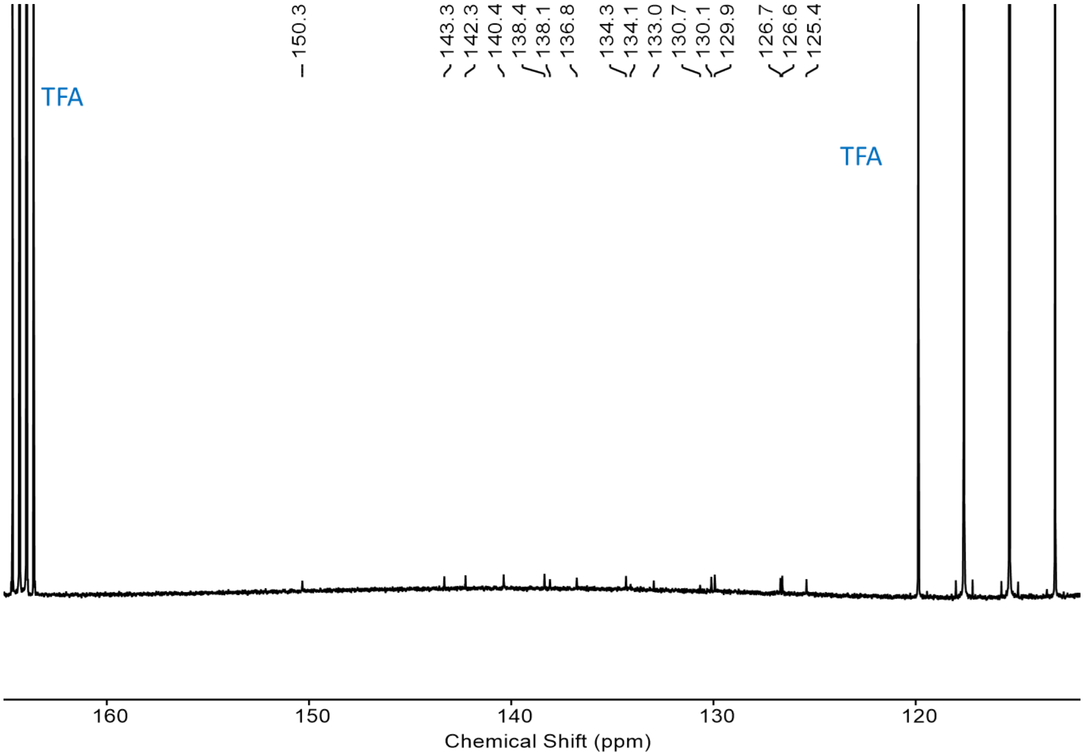

Figure S5.6. $^{13}$C-NMR (125 MHz, trifluoroacetic acid-d) of SmAz.

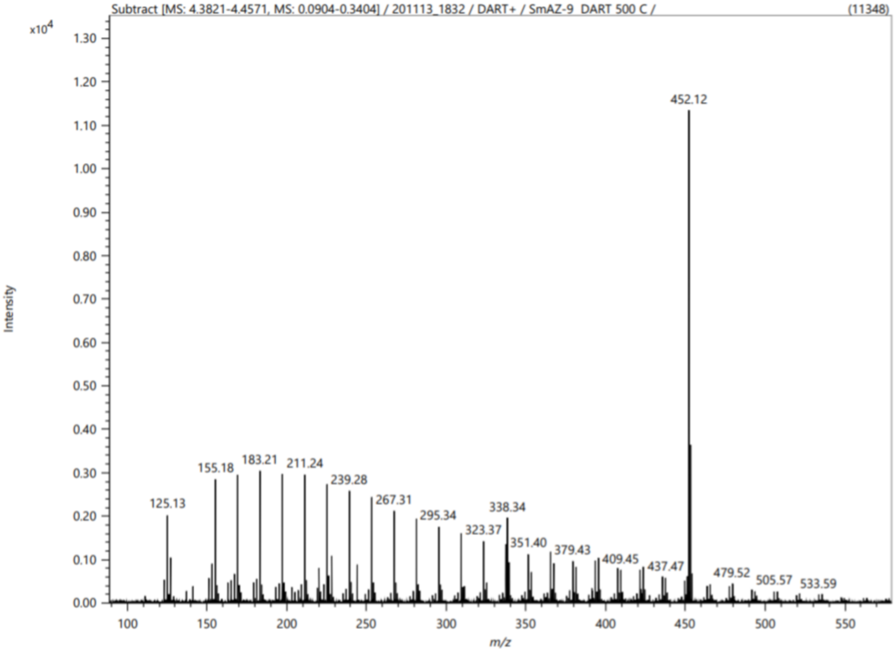

Figure S5.7. DART mass spectrum of SmAz. The molecular weight of SmAz is 451 g/mol.

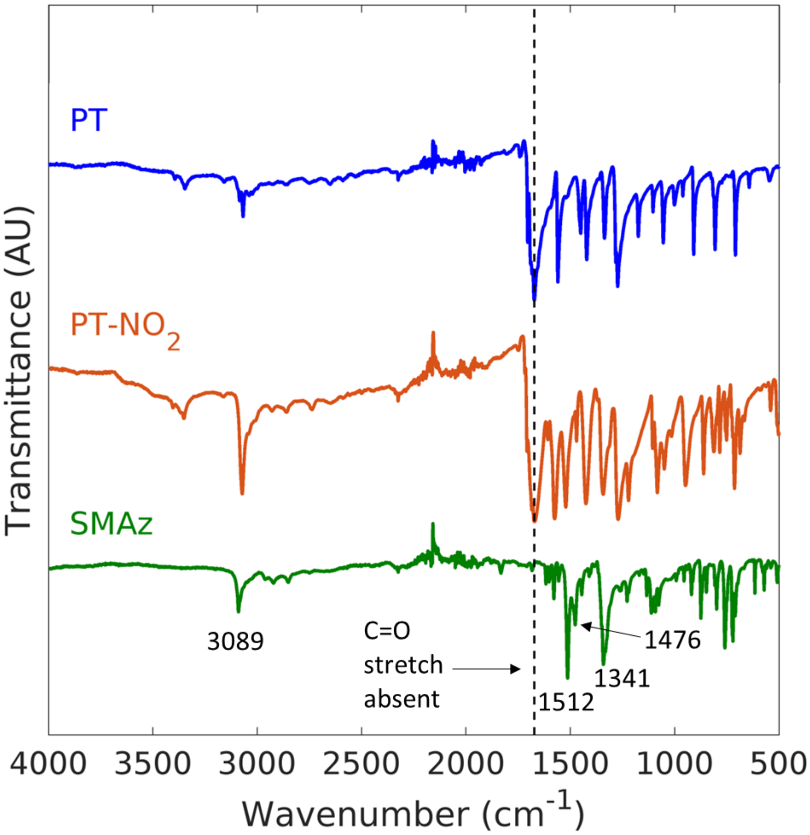

Figure S5.8. FTIR spectra of PT, PT-NO$_2$, and SmAz.

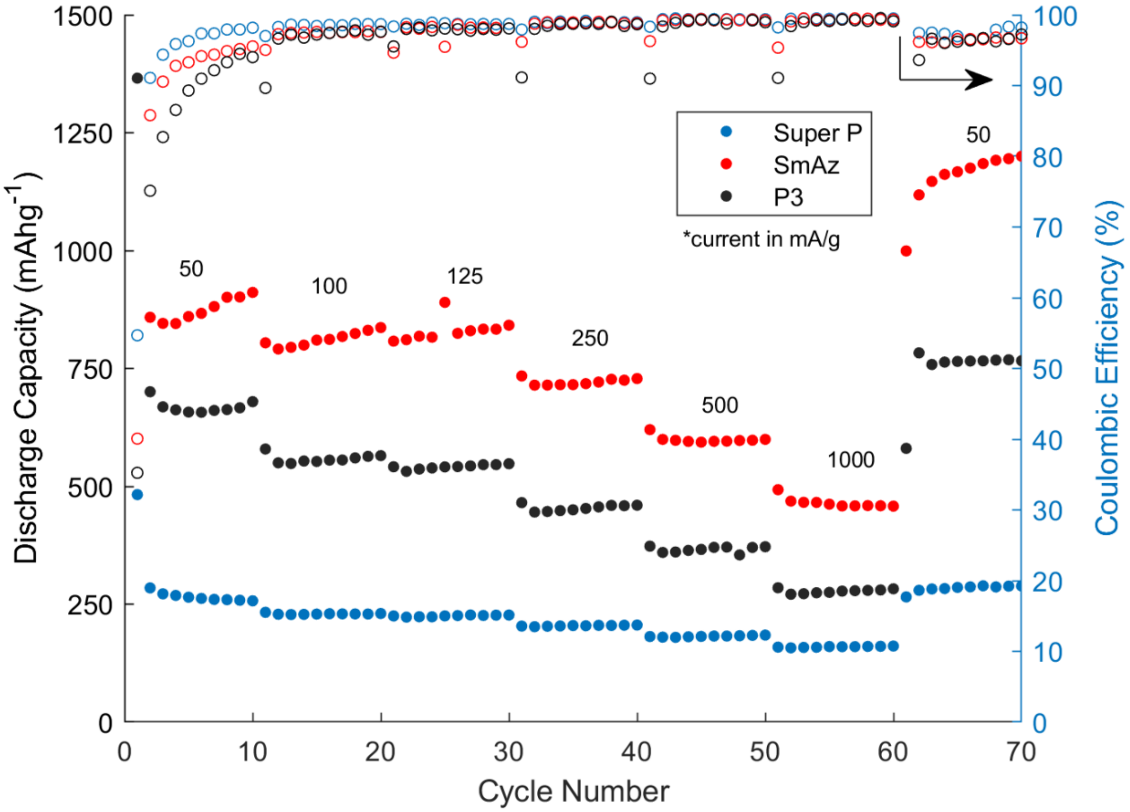

Figure S5.9. Rate capability test of SmAz and P3 without the subtraction of the Super P. The capacities were calculated such that the total mAh contribution was divided by the mass of either SmAz or P3. A Super P baseline is also included.

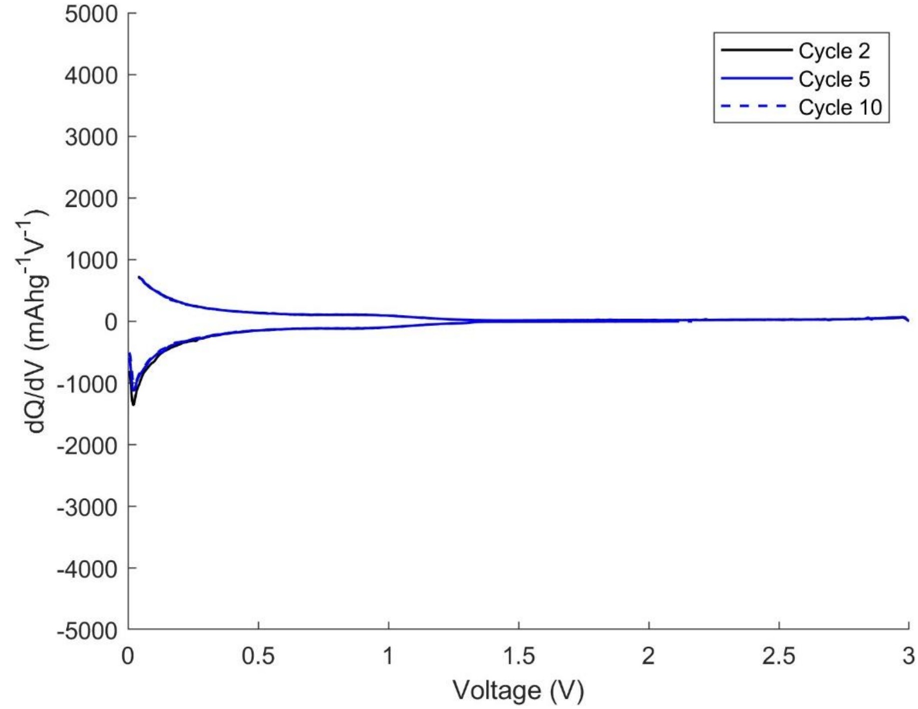

Figure S5.10. Differential capacitance plot of an electrode composed of 70% Super P and 30% PVDF binder.

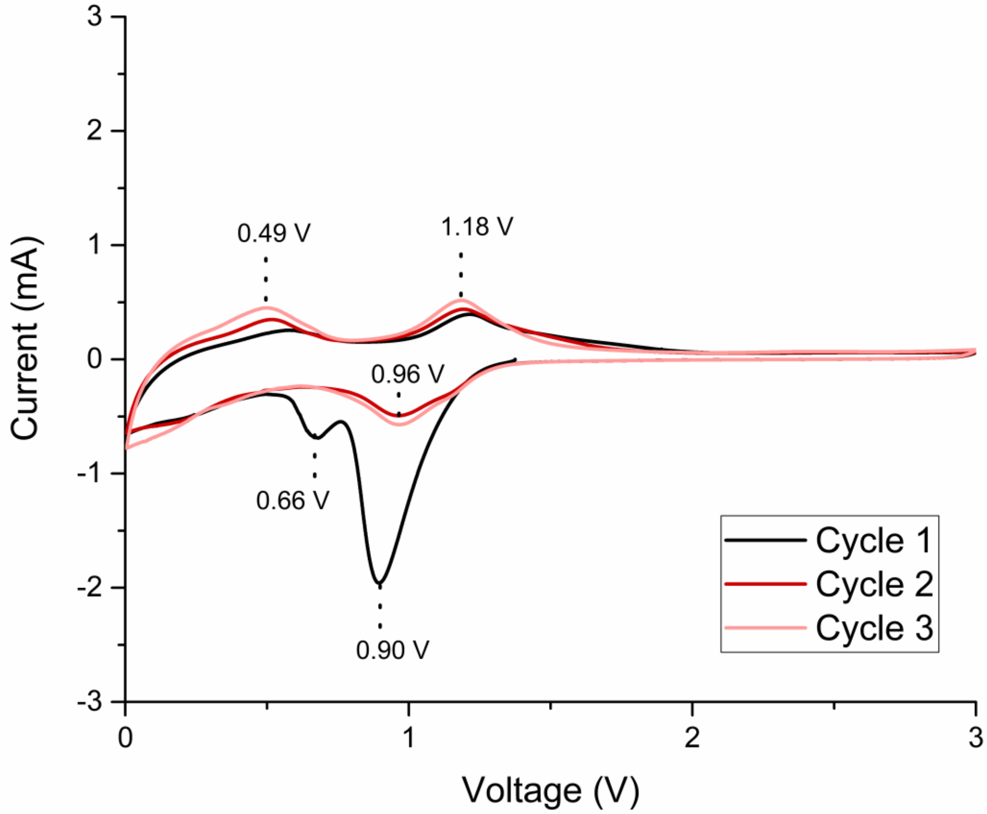

Figure S5.11. CV of the first three cycles of a SmAz-based electrode at a scan rate of 0.2 mV/s. Notice the large irreversible peaks in the first cycle, which are typically attributed to lithium reactions with nitrogen groups as well as SEI formation. Note: peak locations will change slightly depending on scan rate or current density.

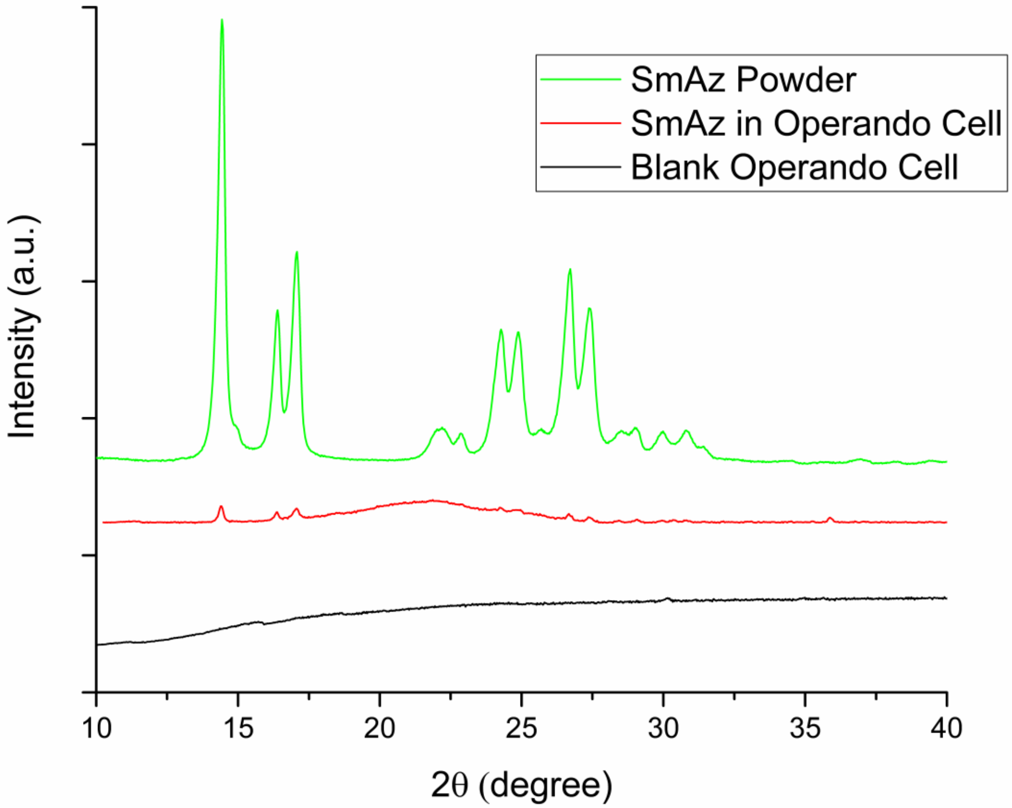

Figure S5.12. XRD plot of bulk powder SmAz, a small amount of SmAz on the Be window, and a reference scan of the operando cell holder (including Be window). For the operando cell, note the absence of reflections in the investigated 2θ range. For the SmAz, note the 3 dominant reflections in the 2θ range between 12-18°.

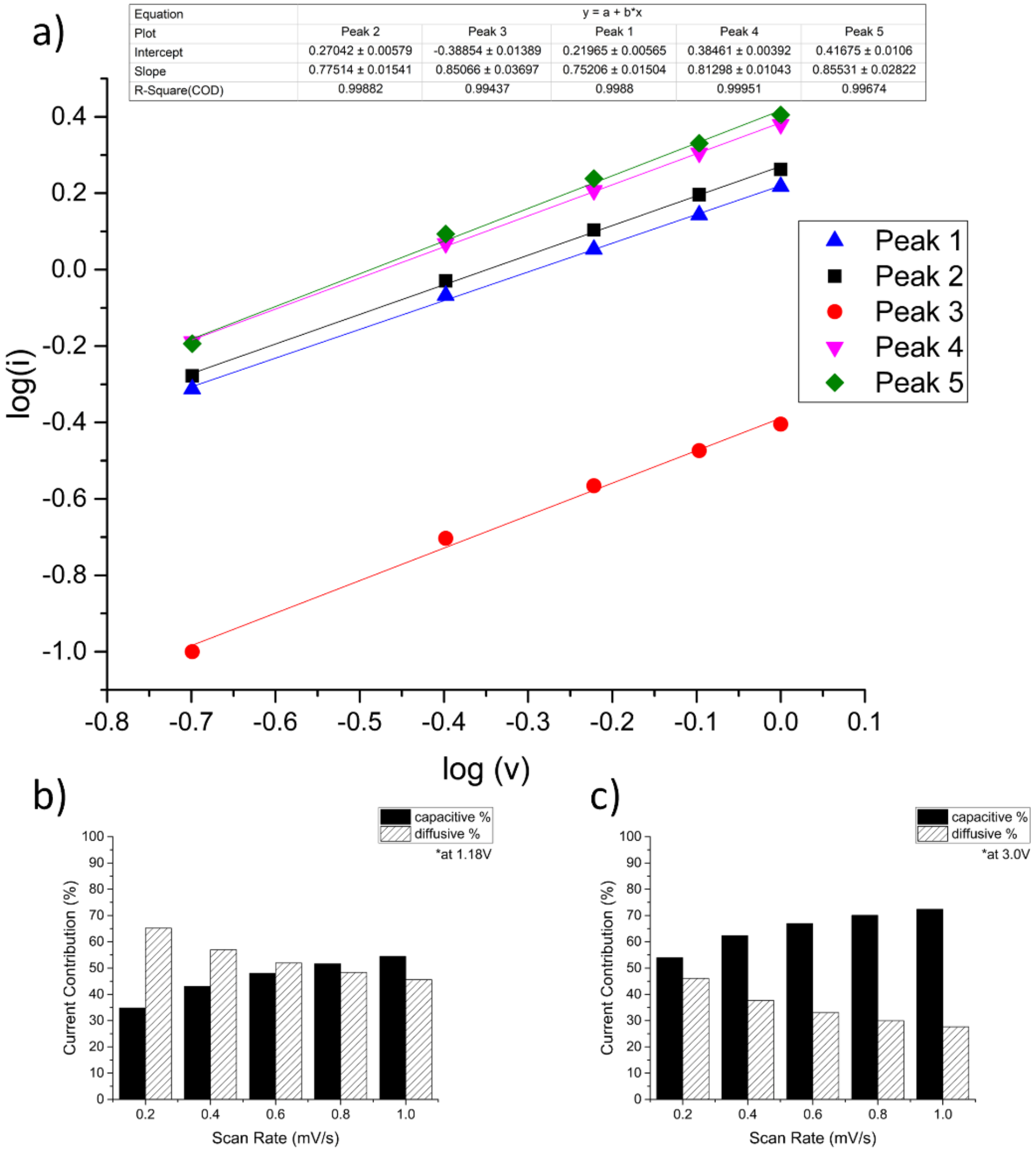

| Equation | y = a + b*x | | | | |
|---|---|---|---|---|---|
| Plot | Peak 2 | Peak 3 | Peak 1 | Peak 4 | Peak 5 |
| Intercept | 0.27042 ± 0.00579 | -0.38854 ± 0.01389 | 0.21965 ± 0.00565 | 0.38461 ± 0.00392 | 0.41675 ± 0.0106 |
| Slope | 0.77514 ± 0.01541 | 0.85066 ± 0.03697 | 0.75206 ± 0.01504 | 0.81298 ± 0.01043 | 0.85531 ± 0.02822 |
| R-Square(COD) | 0.99882 | 0.99437 | 0.9988 | 0.99951 | 0.99674 |

Figure S5.13. a) b-value analysis at the 5 peak locations in Figure 5.6. Figures b) & c) show the capacitive and diffusive contributions to the current at a fixed voltage. The current (i) at a fixed voltage (V) can be described as a combination of capacitive ($k_1 v$) and diffusive ($k_2 v^{0.5}$) contributions with the equation $i(V)=k_1 v + k_2 v^{0.5}$, where $k_1$ and $k_2$ are constants and $v$ is the scan rate.[3] This analysis was used to estimate oxidation current contributions at the voltages of 1.18 V (b) and 3.0 V (c).

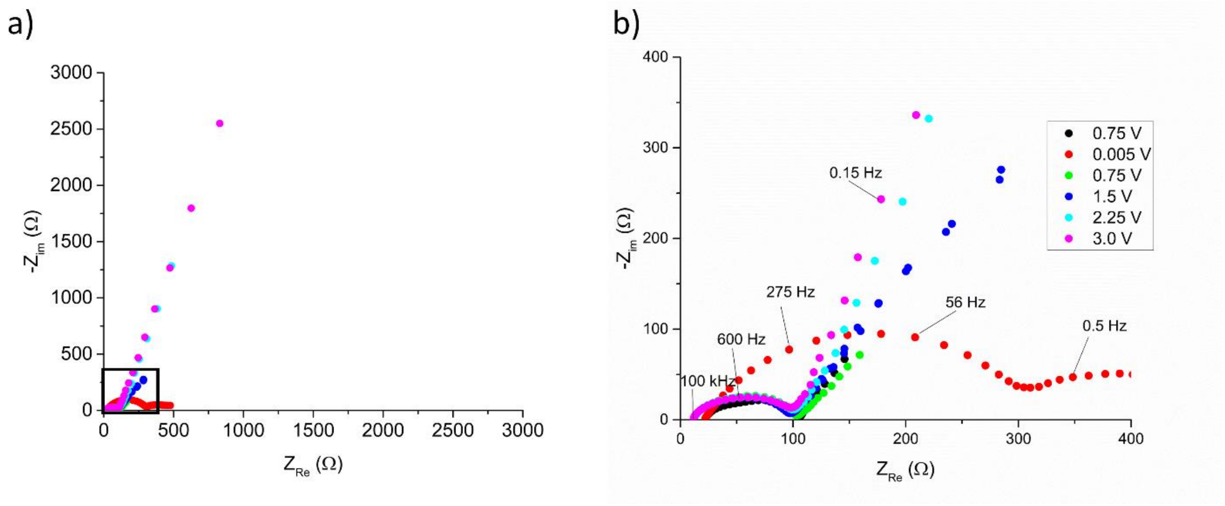

Figure S5.14. Impedance of SmAz-based electrode at different potential limits.

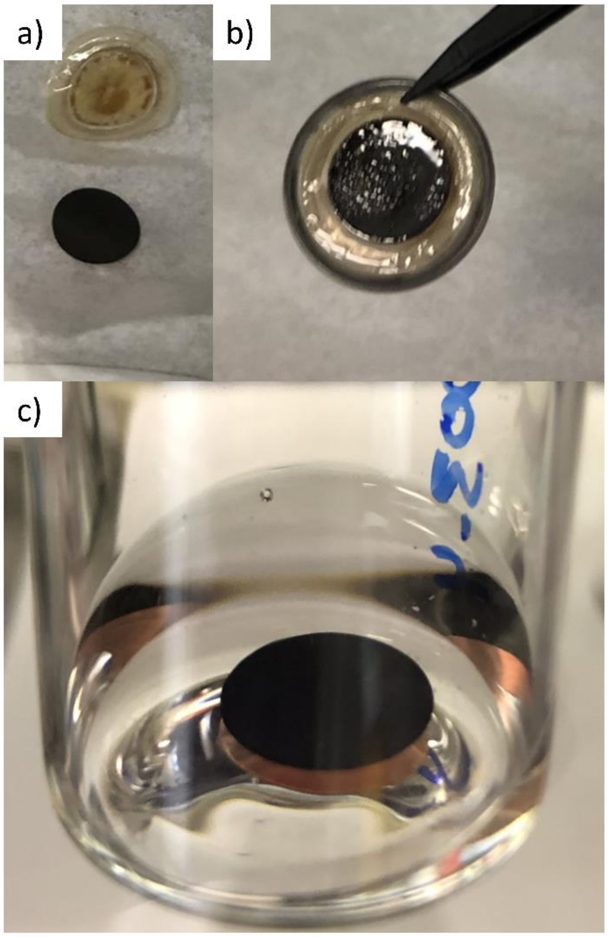

Figure S5.15. Postmortem images of the delithiated SmAz-based electrodes that were charged to 3.0 V in Figure 5.4. Images a) and b) reveal a uniform electrode and a membrane which is still wet after cycling. Image c) shows no obvious dissolution of the electrode after resting for 24 hours in the electrolyte.

## References

[1] Hu, J.; Zhang, D.; Harris, F. W. Ruthenium(III) Chloride Catalyzed Oxidation of Pyrene and 2,7-Disubstitued Pyrenes: An Efficient, One-Step Synthesis of Pyrene-4,5-Diones and Pyrene-4,5,9,10-Tetraones. J Org Chem 2005, 70 (2), 707–708. https://doi.org/10.1021/jo048509q.

[2] Kohl, B.; Bohnwagner, M. V.; Rominger, F.; Wadepohl, H.; Dreuw, A.; Mastalerz, M. Attractive Dispersion Interactions Versus Steric Repulsion of Tert -Butyl Groups in the Crystal Packing of a D 3 h -Symmetric Tris(Quinoxalinophenanthrophenazine). Chemistry - A European Journal 2016, 22 (2), 646–655. https://doi.org/10.1002/chem.201503863.

[3] Wang, J.; Polleux, J.; Lim, J.; Dunn, B. Pseudocapacitive Contributions to Electrochemical Energy Storage in TiO 2 (Anatase) Nanoparticles. The Journal of Physical Chemistry C 2007, 111 (40), 14925–14931. https://doi.org/10.1021/jp074464w.

## Supplementary Information for Chapter 6

For the silicon-rich electrodes (≥80 wt% Si), a suppressed capacity was sometimes seen during the first few cycles, similar to what is described by Takamura et al and Yim et al.[1, 2] This is likely due to the resistance associated with the high silicon content and the insulating nature of the polymeric binder. The nucleation overpotential required for the lithiation of silicon may also be responsible.[3–6] To ensure the supressed capacity was not due to the native oxide layer on the Cu current collector, the Cu foil was washed with a 2.5 % solution of HCl, rinsed with distilled water, then dried before applying the electrode slurry. This was done for both XG and NaCMC based electrodes. Cycling data in Figure S6.1 shows that the acid wash had no effect on the presence of an initial suppressed capacity.

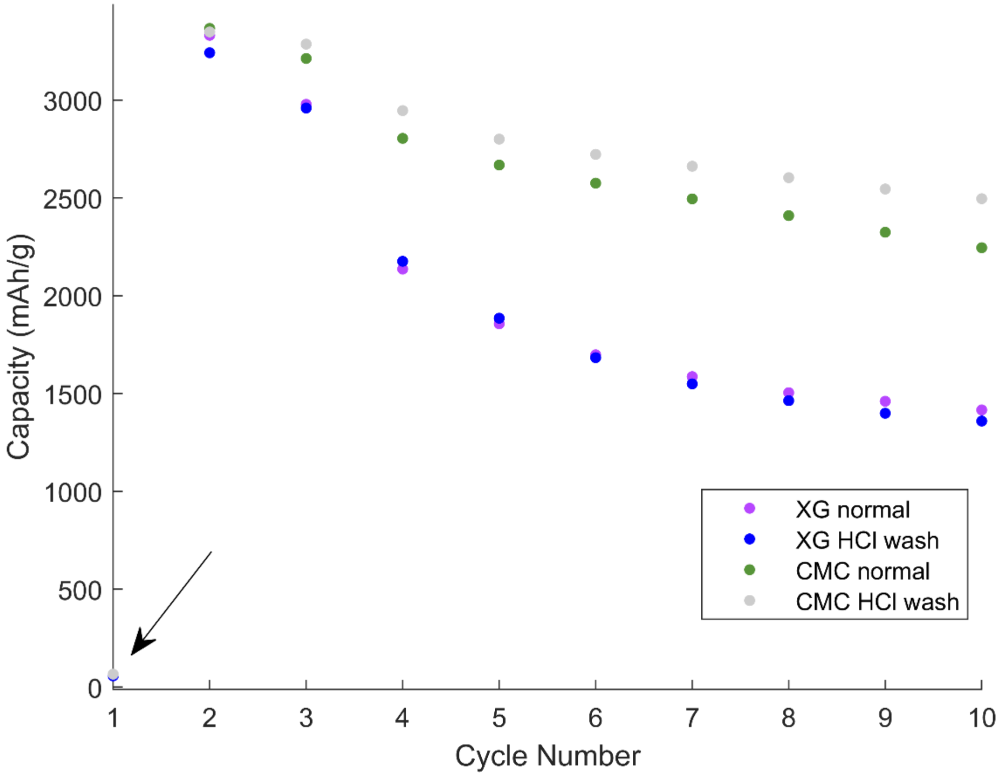

Figure S6.1. Discharge capacity vs cycle number for the study regarding HCl wash of copper foil. Note all selected trials had a first cycle suppressed capacity regardless of HCl wash. All batteries cycled at C/10. Note: Tekna N-100 silicon was not used in this test.

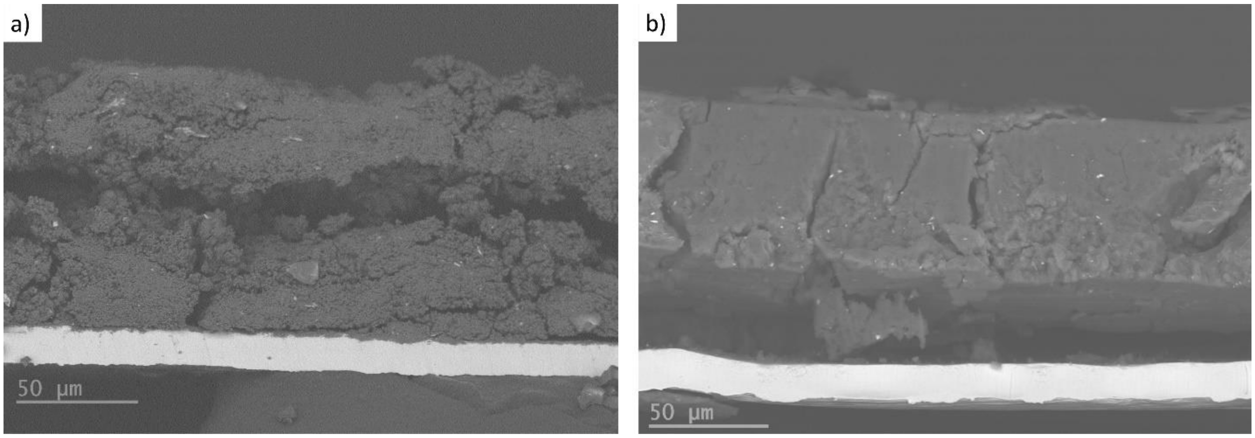

Figure S6.2. Postmortem SEM-BSE of cross sections of a) 80Si-10XG and b) 80Si-10CMC. The XG-based active layer expanded to 100 µm, whereas the CMC-based active layer remained relatively compact and expanded to only 60 µm. All images taken after 100 cycles at C/10.

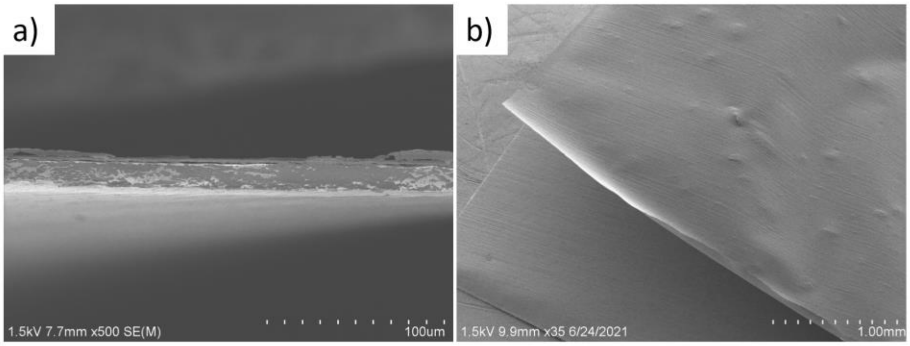

Figure S6.3. SEM images of binder-only films for XG on Cu (a, cross section) and NaCMC (b, bird’s-eye view). Note the inability to acquire a cross section image with NaCMC as a result of delamination from Cu.

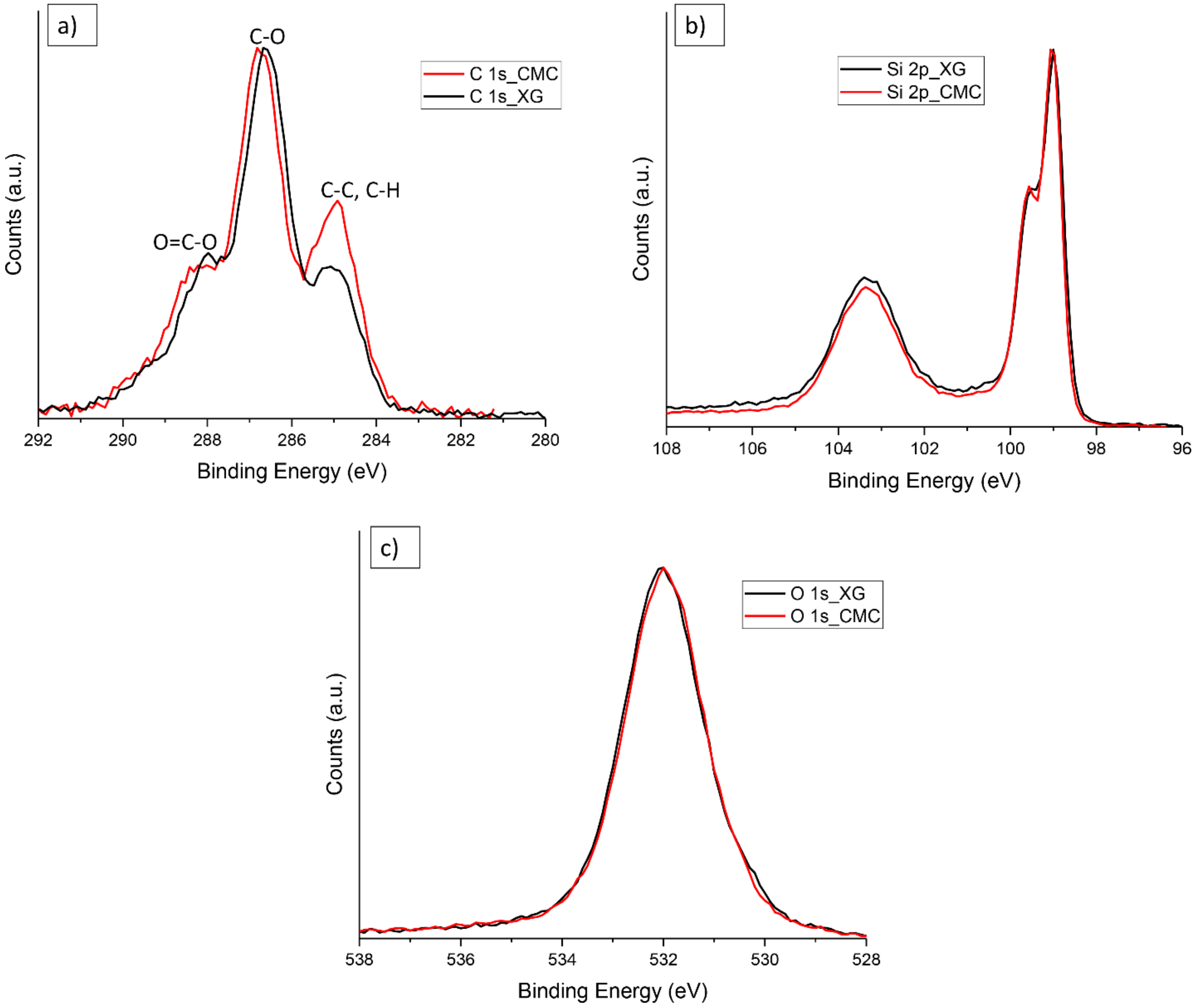

Figure S6.4. XPS spectra of a) C 1s, b) Si 2p, and c) O 1s for both uncycled Si-XG and Si-NaCMC films. Note: Super P carbon and copper were omitted in these samples.

The C1s region of polymeric carbon shows a difference in the proportion of C-C bonds (285 eV) compared to C-O bonds (286.5 eV). In addition, the lower peak intensity of the C-C bond with XG is consistent with its molecular structure. CMC-based silicon electrodes prepared under acidic conditions have previously been suggested to contain ester-type (R-**C**(=O)-O-Si-) bonds around 289.1 eV. [7] As there is no evidence of such a peak around 289.1 eV, there is no direct evidence of chemical binding between the silicon surface and the binders. As such, silicon-binder interactions in this study are believed to be predominantly non-covalent (i.e., hydrogen or ion dipole). Data for the O1s peak is unremarkable as both signals for Si-XG and Si-NaCMC overlap. Table S6.1 below provides a reference of different binding energies reported in publications on aqueous binders.

**Table S6.1.** Binding Energies (eV) for C and Si bonds from papers using polymeric binders.

| | **Roland** [8] | **D. Wang** [9] | **Wei** [10] | **Z. Wang** [11] **(citing Shanming Hu)** | **Shanming Hu** [12] |
|---|---|---|---|---|---|
| **C 1s** | 285 is C-C and C-H<br>286.5 is C-O<br>288.5 is COO | 284.8 is C–C<br>286.3 is C–OH<br>287.8 is C=O<br>289.0 is COOH | Used XPS to identify SEI around C1s ($Li_2CO_3$) | 284.8 is C–C and C –H<br>286.4 is C–OH<br>288.2 is -COONa | 284.6 is C-C and C-H<br>286.4 is C-O-<br>288.0 is -O-C=O |
| **Si 2p** | Si: 99 and 101<br>Si-Oxide: 102 and 106 | | | | <u>Si only</u><br>98.6 is Si-Si<br>100.9 is Si-O-H<br><u>Si with binder</u><br>99.9 is Si-Si<br>104.0 is Si-O-O (R) |

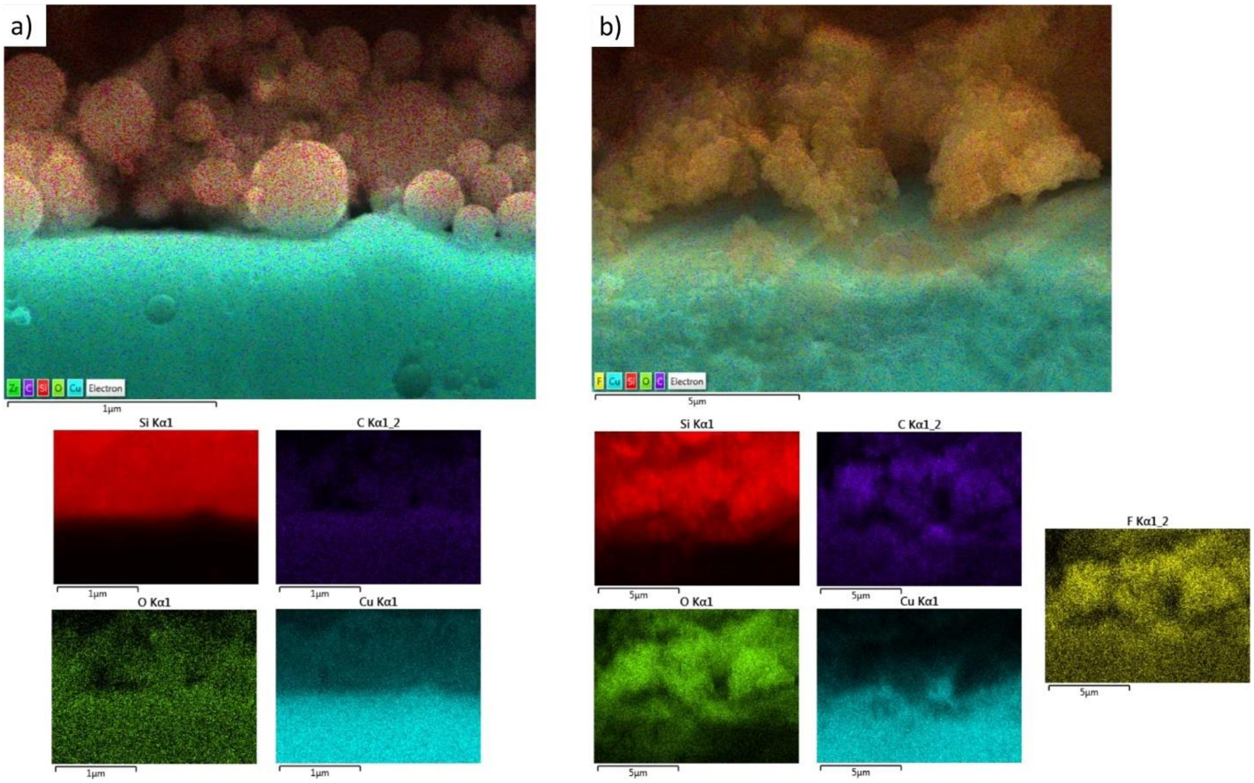

Figure S6.5. EDX maps of the cross-section of a) pristine and b) cycled 80Si-10XG electrodes.

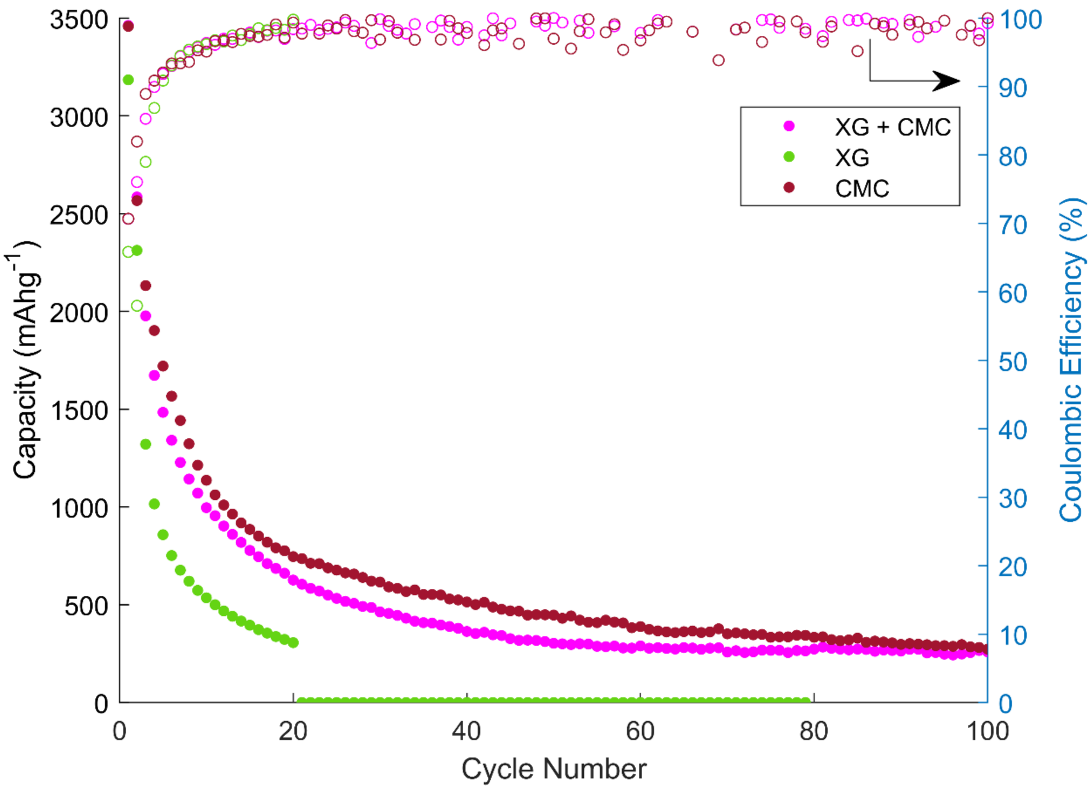

Figure S6.6. Cycling performance for 80 wt% silicon electrodes with 5 wt% XG and 5 wt% NaCMC.

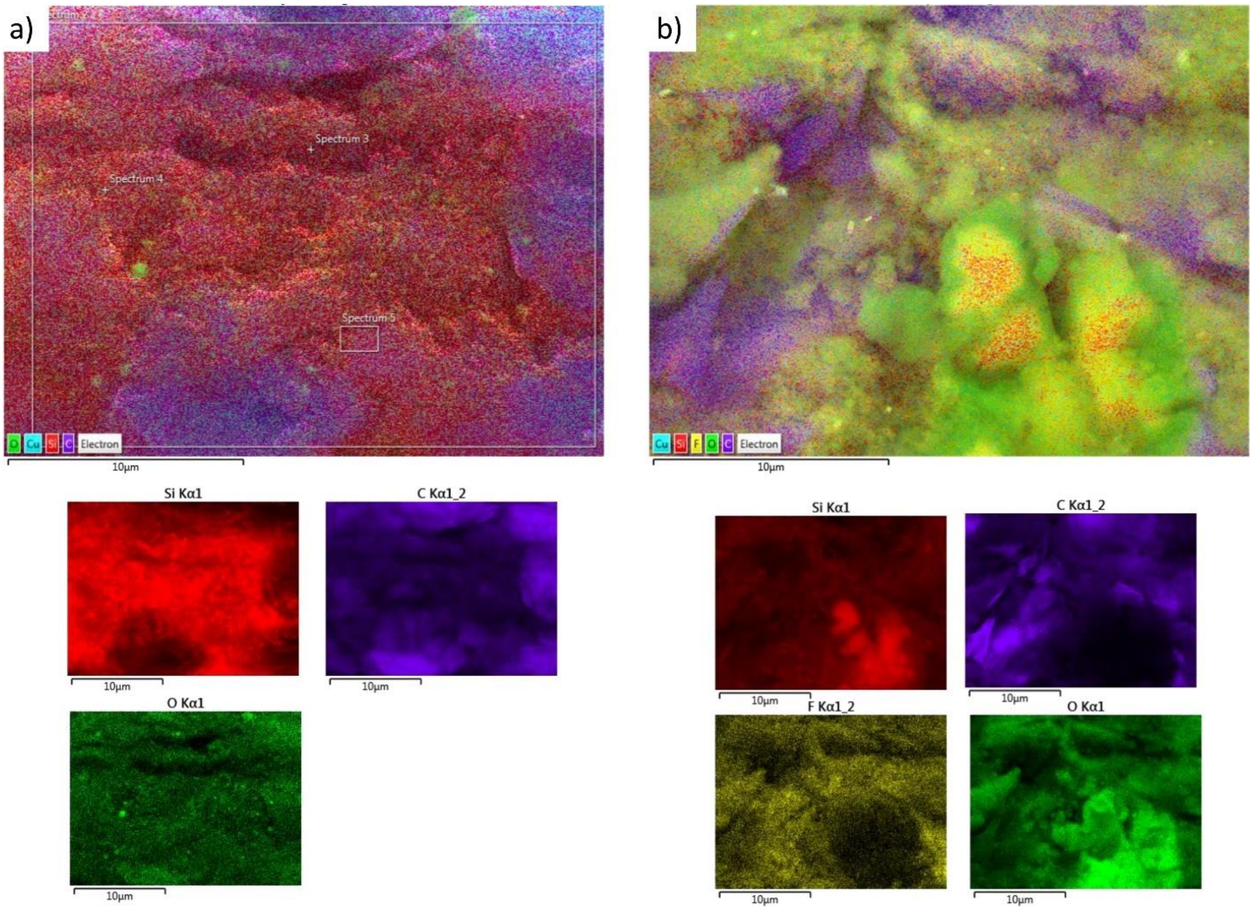

Figure S6.7. EDX maps of a) pristine and b) cycled 20Si-10XG electrodes. Note the 10 µm scale bar was necessary to observe greater resolution of graphite.

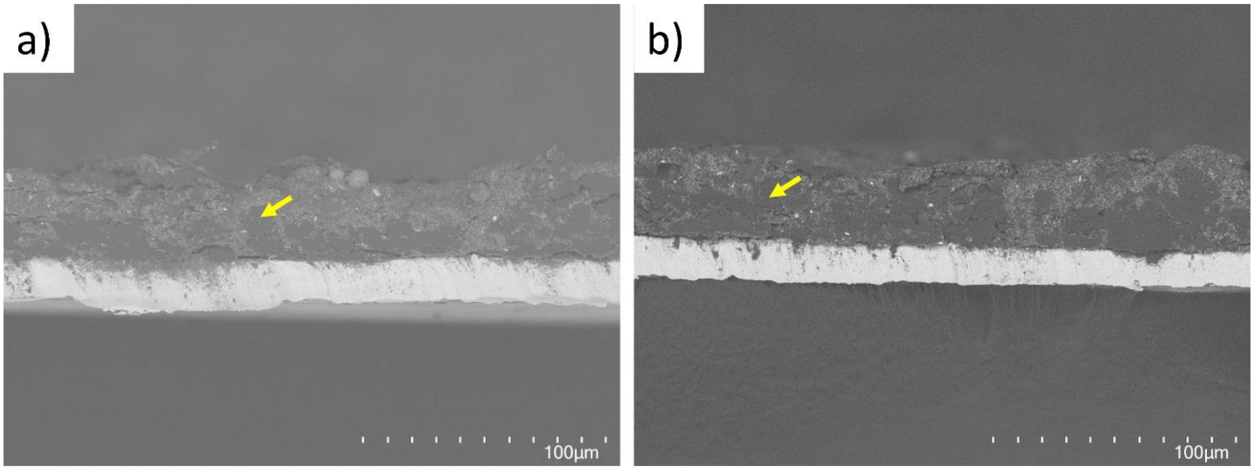

Figure S6.8. SEM-BSE of cross sections of pristine a) 20Si-10XG and b) 20Si-10CMC electrodes. Yellow arrows point out darker spherical graphite.

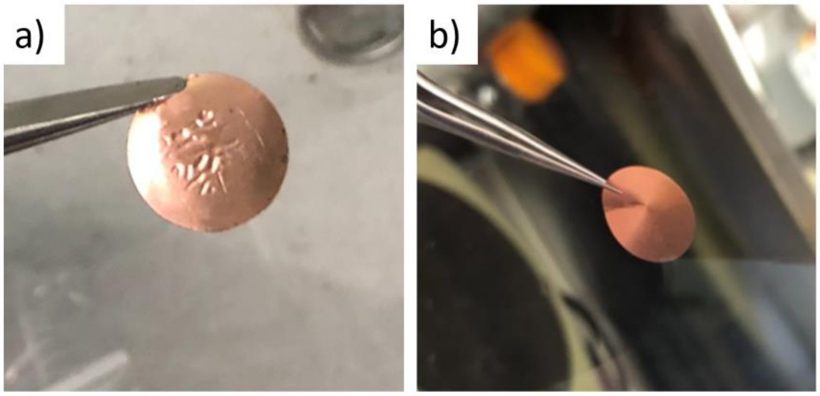

Figure S6.9. Cu-side of electrodes after 100 cycles for a) 80Si-10CMC and b) 20Si-10CMC.

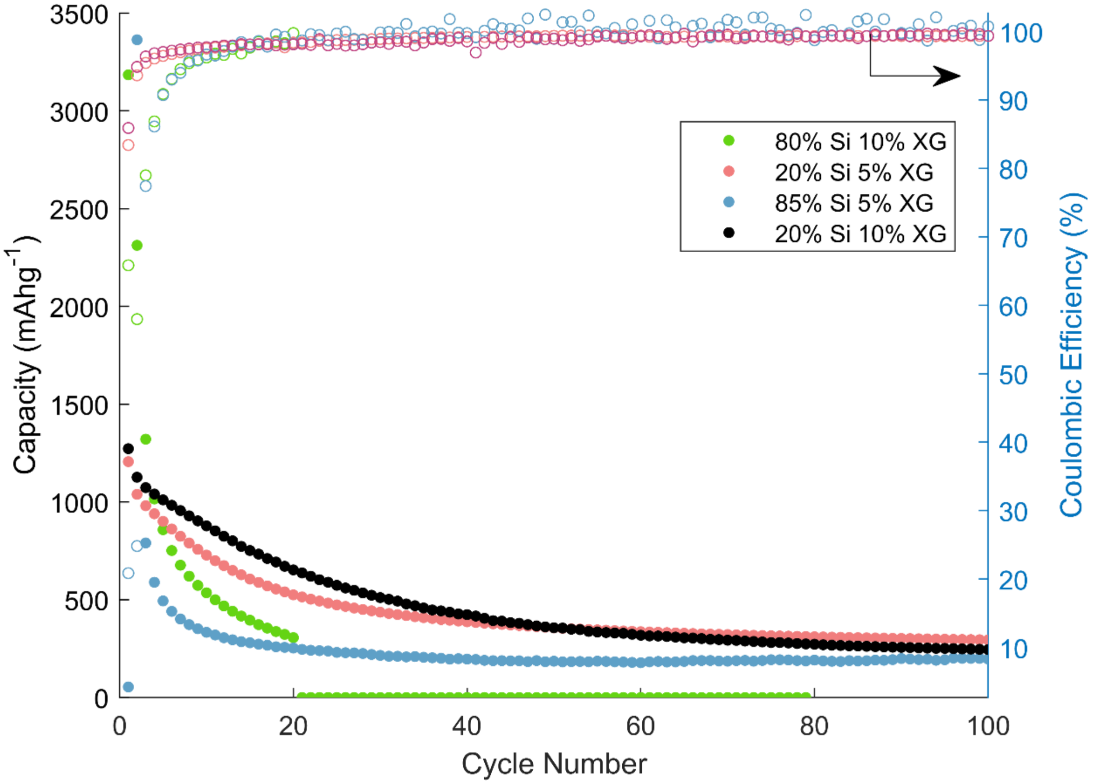

Figure S6.10. Cycling performance of 20 wt% Si and 80 wt% Si electrodes with 10 wt% or 5 wt% XG binder.

Commercial batteries typically use a binder content of 5 wt% or less to maximize the energy density of the whole cell. Figure S6.10 shows the half-cell testing results for high-silicon and low-silicon anodes formulated with an XG quantity of 5 or 10 wt%. The observation made is aligned with the general trend that a lower binder content lowers the capacity retention due to the deterioration of the mechanical strength of the electrode.

References

[1] T. Takamura, S. Ohara, M. Uehara, J. Suzuki, and K. Sekine, “A vacuum deposited Si film having a Li extraction capacity over 2000 mAh/g with a long cycle life,” *J Power Sources*, vol. 129, no. 1 SPEC. ISS., pp. 96–100, 2004, doi: 10.1016/j.jpowsour.2003.11.014.

[2] C. H. Yim, F. M. Courtel, and Y. Abu-Lebdeh, “A high capacity silicon-graphite composite as anode for lithium-ion batteries using low content amorphous silicon and compatible binders,” *J Mater Chem A Mater*, vol. 1, no. 28, pp. 8234–8243, 2013, doi: 10.1039/c3ta10883j.

[3] A. Ulvestad *et al.*, “Crystallinity of Silicon Nanoparticles: Direct Influence on the Electrochemical Performance of Lithium Ion Battery Anodes,” *ChemElectroChem*, vol. 7, no. 21, pp. 4349–4353, 2020, doi: 10.1002/celc.202001108.

[4] C. Y. Wang, Y. S. Meng, G. Ceder, and Y. Li, “Electrochemical Properties of Nanostructured Al[sub 1−x]Cu[sub x] Alloys as Anode Materials for Rechargeable Lithium-Ion Batteries,” *J Electrochem Soc*, vol. 155, no. 9, p. A615, 2008, doi: 10.1149/1.2943215.

[5] N. S. Hudak and D. L. Huber, “Size Effects in the Electrochemical Alloying and Cycling of Electrodeposited Aluminum with Lithium,” *J Electrochem Soc*, vol. 159, no. 5, pp. A688–A695, 2012, doi: 10.1149/2.023206jes.

[6] Y. Kim, S. Sim, and S. W. Lee, “Nucleation and Growth of Lithium–Silicon Alloy on Crystalline Silicon,” *Adv Eng Mater*, vol. 21, no. 5, pp. 1–5, 2019, doi: 10.1002/adem.201800520.

[7] D. Mazouzi *et al.*, “CMC-citric acid Cu(II) cross-linked binder approach to improve the electrochemical performance of Si-based electrodes,” *Electrochim Acta*, vol. 304, no. August, pp. 495–504, 2019, doi: 10.1016/j.electacta.2019.03.026.

[8] A. Roland, B. Delarre, J. B. Ledeuil, N. Louvain, H. Martinez, and L. Monconduit, “Silicon-based electrodes formulation in buffered solution for enhanced electrode-electrolyte interfaces,” *J Power Sources*, vol. 489, no. November 2020, 2021, doi: 10.1016/j.jpowsour.2021.229465.

[9] D. Wang *et al.*, “A universal cross-linking binding polymer composite for ultrahigh-loading Li-ion battery electrodes,” *J Mater Chem A Mater*, vol. 8, no. 19, pp. 9693–9700, 2020, doi: 10.1039/d0ta00714e.

[10] L. Wei and Z. Hou, “High performance polymer binders inspired by chemical finishing of textiles for silicon anodes in lithium ion batteries,” *J Mater Chem A Mater*, vol. 5, no. 42, pp. 22156–22162, 2017, doi: 10.1039/c7ta05195f.

[11] Z. Wang, T. Huang, Z. Liu, and A. Yu, “Dopamine-modified carboxymethyl cellulose as an improved aqueous binder for silicon anodes in lithium-ion batteries,” *Electrochim Acta*, vol. 389, p. 138806, 2021, doi: 10.1016/j.electacta.2021.138806.

[12] S. Hu, Z. Cai, T. Huang, H. Zhang, and A. Yu, “A Modified Natural Polysaccharide as a High-Performance Binder for Silicon Anodes in Lithium-Ion Batteries,” *ACS Appl Mater Interfaces*, vol. 11, no. 4, pp. 4311–4317, 2019, doi: 10.1021/acsami.8b15695.

## Supplementary Information for Chapter 7

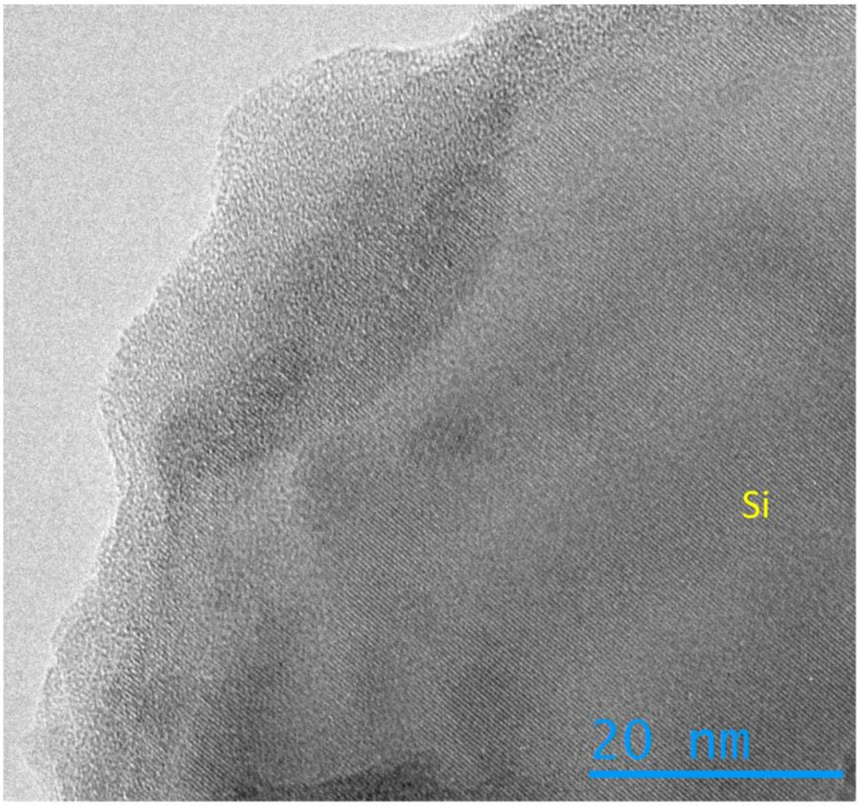

Figure S7.1. TEM of a Si@LTO-2 particle

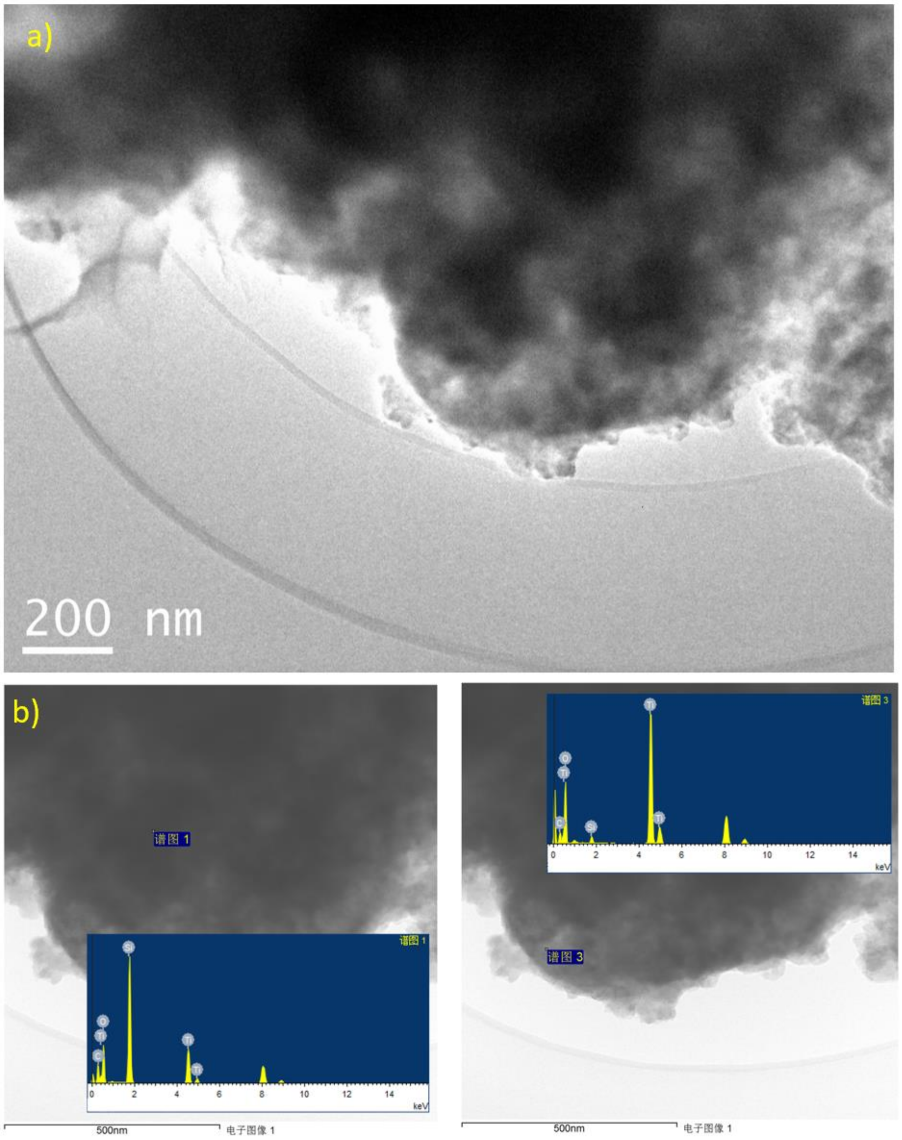

Figure S7.2. (a) TEM of Si@LTO-1 particles and (b) EDX of the inner core (left) and outer coating (right) of a particle.

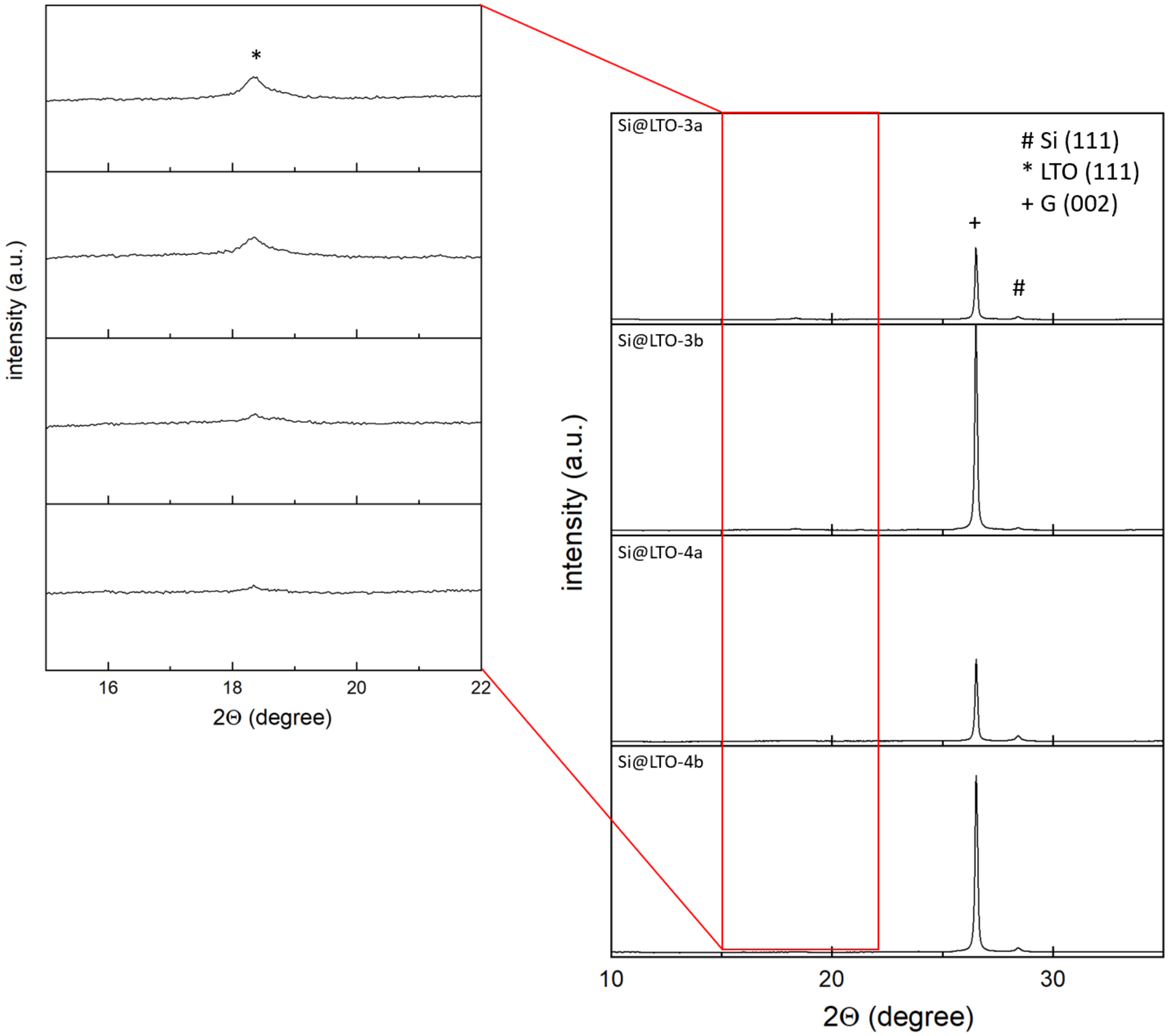

Figure S7.3. XRD of all four Si@LTO + G electrode disks. Dominant peaks from silicon, graphite, and LTO are marked.

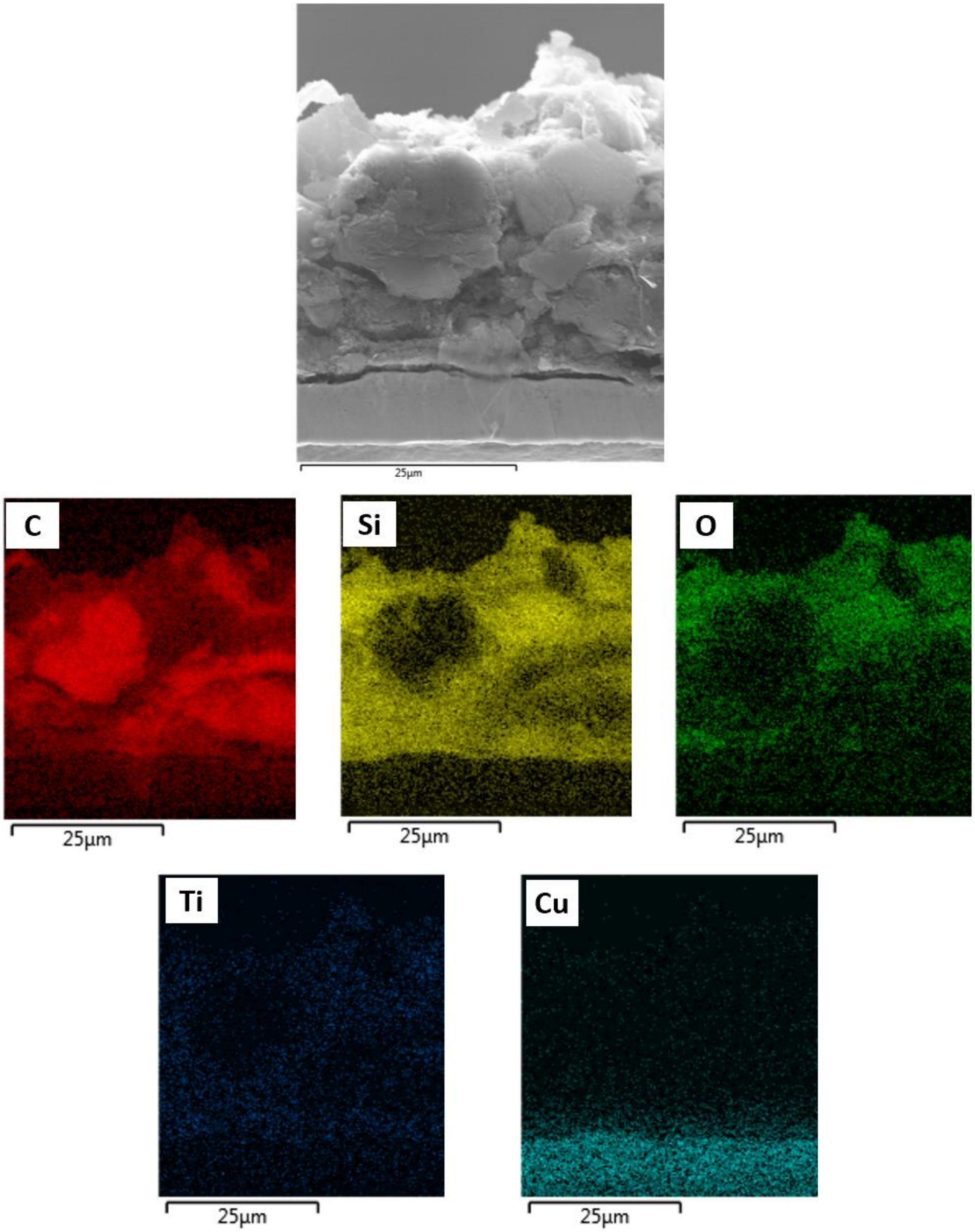

Figure S7.4. SEM and EDX images of the cross section of an uncycled Si@LTO-4b electrode disk. A micron-sized graphite particle is seen along with the uniformly distributed Si-O-Ti from the Si@LTO.

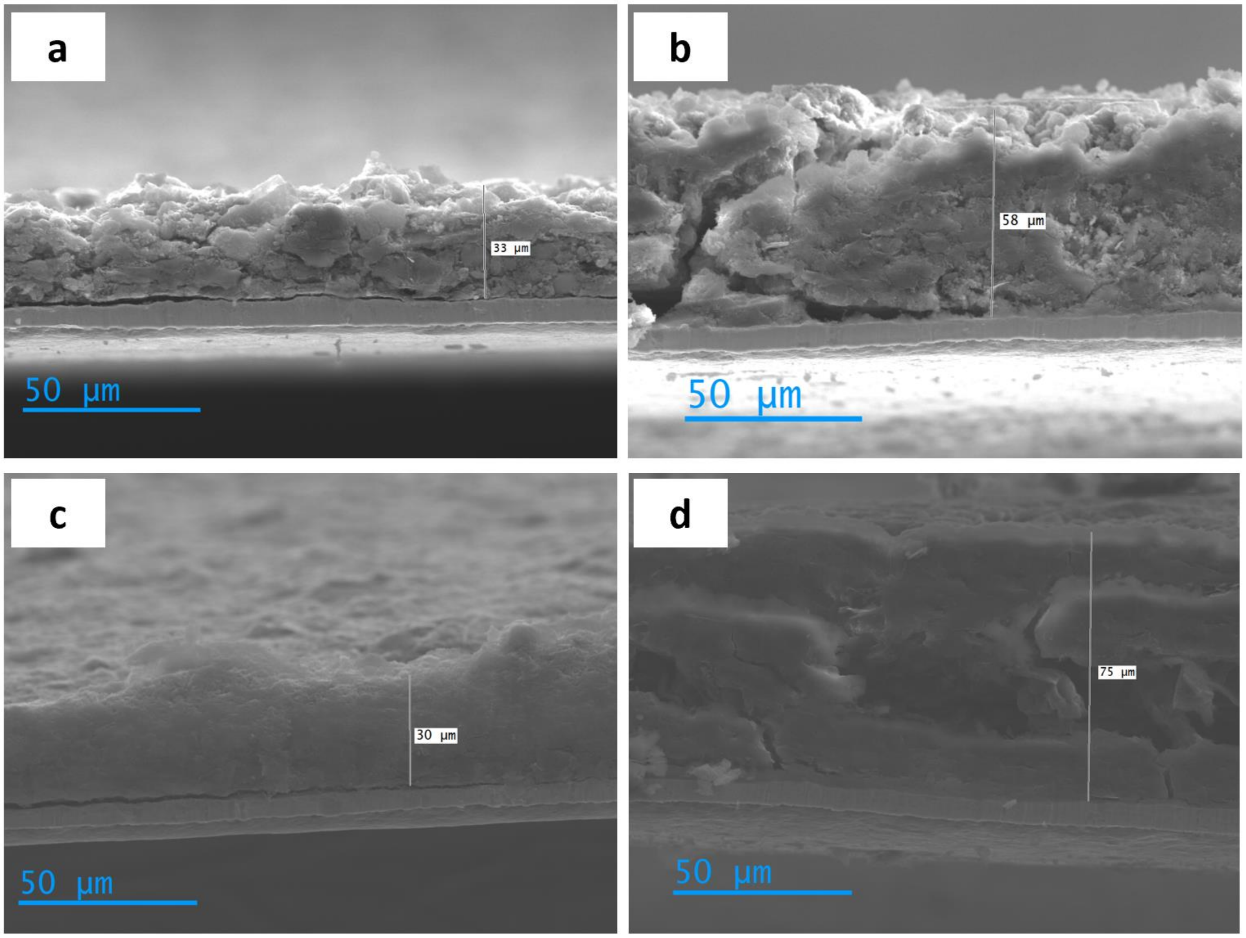

Figure S7.5. SEM images of the cross section of electrode disks. (a) Uncycled Si@LTO-4b. (b) Cycled Si@LTO-4b. (c) uncycled B2 baseline. (d) cycled B2 baseline. Si@LTO-4b shows an expansion of about 75% after 100 cycles. B2 shows an expansion of about 150% after 100 cycles and severe pulverization.

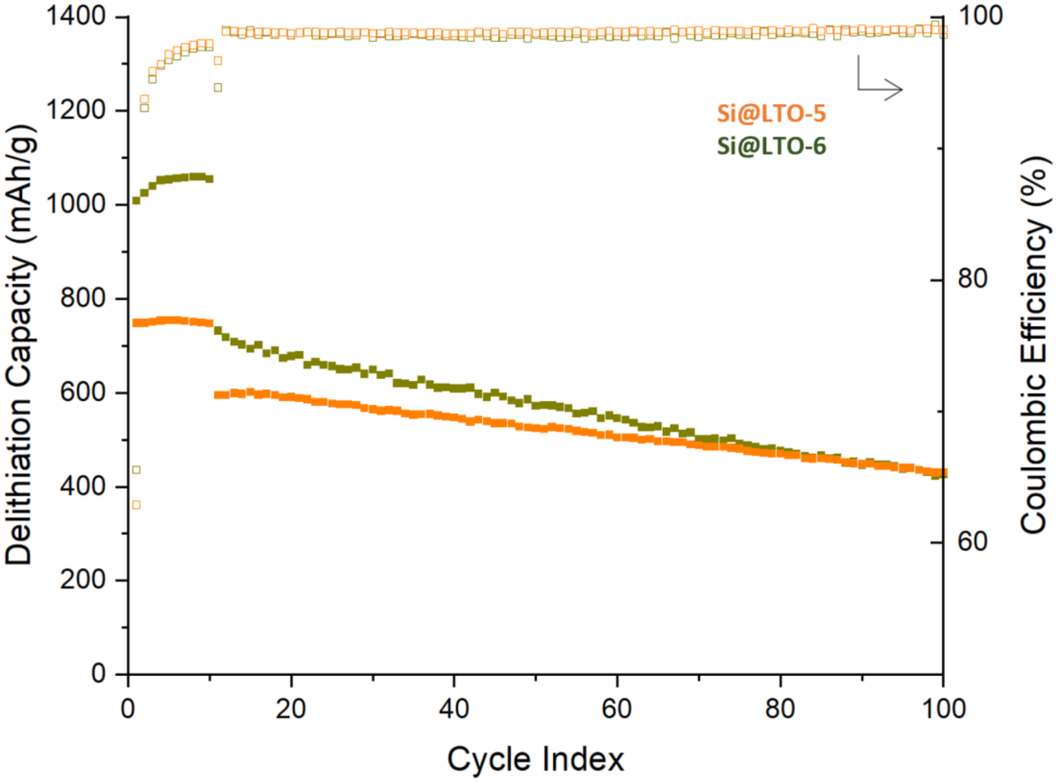

Figure S7.6. Galvanostatic cycling of carbon-treated Si@LTO composites. First 10 cycles at a charge rate of C/10, followed by 1C

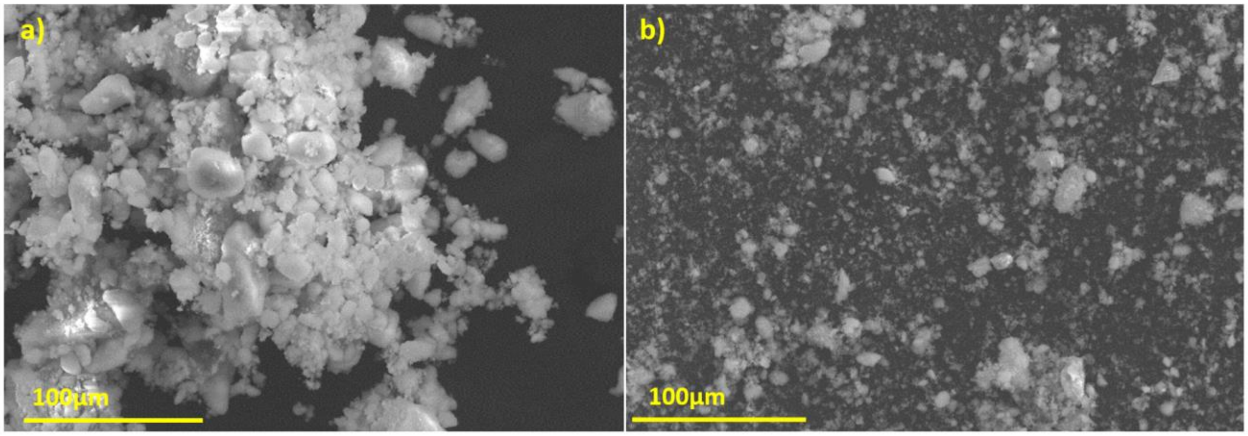

Figure S7.7. SEM images of the raw powder of (a) Si@LTO-2 and (b) Si@LTO-2 with the new synthesis—these particles were used to prepare Si@LTO-4b* electrodes

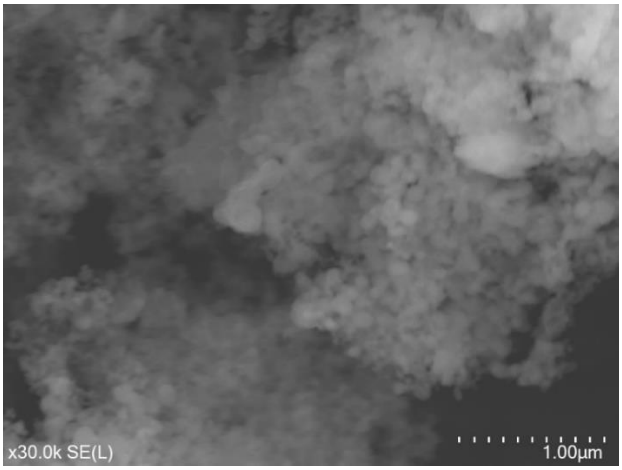

Figure S7.8. Enlarged SEM of the particles in Figure S7.7 (b)

## Supplementary Information for Chapter 8

Table S8.1. Results of peak fittings to XPS spectra shown in Figure 8.2 and 8.5 for MOF-74, MOF-199, 0.5Si@MOF and 05Si@MOF-c.

| **Co-MOF-74** | | | | | |
|---|---|---|---|---|---|
| **Peaks in Figure 8.2d (Co2p)** | | | **Peaks in Figure 8.2e (C 1s)** | | |
| **Name** | **Position** | **%Area** | **Name** | **Position** | **%Area** |
| Co (0)-1 | 778.06 | 30.4 | C-C, C-H | 284.8 | 13.94 |
| Co (0)-2 | 781.06 | 4.32 | C-O | 286 | 24.12 |
| Co (0)-3 | 783.06 | 3.07 | C=O | 288.8 | 9.63 |
| Co LMM | 776.38 | 5.29 | COOH | 289.89 | 3.96 |
| Co (II)-1 | 779.96 | 25.30 | C1s- sp2 | 284.5 | 45.21 |
| Co (II)-2 | 782.06 | 14.47 | C1s- sp2 satellite | 290.91 | 3.14 |
| Co (II)-3 | 785.16 | 0.79 | | | |
| Co (II)-4 | 785.31 | 16.35 | | | |
| **Cu-MOF-199** | | | | | |
| **Peaks in Figure 8.2f ($Cu2p_{3/2}$)** | | | **Peaks in Figure 8.2g (C 1s)** | | |
| **Name** | **Position** | **%Area** | **Name** | **Position** | **%Area** |
| Cu(II) Oxide-1 | 932.96 | 65.49 | C-C, C-H | 284.80 | 59.42 |
| Cu(II) Oxide-2 | 934.84 | 19.61 | C-O | 286.27 | 14.50 |
| Cu(II) Oxide-3 | 939.91 | 7.14 | C=O | 288.50 | 16.89 |
| Cu(II) Oxide-4 | 944.16 | 7.76 | COOH | 289.88 | 9.19 |
| **0.5Si@MOF** | | | | | |
| **Peaks in Figure 8.5a (Co2p)** | | | **Peaks in Figure 8.5b (C 1s)** | | |
| **Name** | **Position** | **%Area** | **Name** | **Position** | **%Area** |
| Co (II)-1 | 778.59 | 33.15 | C-C, C-H | 284.8 | 45.84 |
| Co (II)-2 | 780.69 | 25.23 | C-O | 286.22 | 20.11 |
| Co (II)-3 | 783.16 | 8.37 | C=O | 288.03 | 22.2 |
| Co (II)-4 | 784.53 | 33.26 | COOH | 289.79 | 11.85 |
| **Peaks in Figure 8.5c (Si 2p & Co 3s)** | | | | | |
| **Name** | **Position** | **%Area** | | | |
| Si $2p_{3/2}$ (0) | 98.53 | 6.12 | | | |
| Si $2p_{1/2}$ (0) | 99.13 | 3.06 | | | |
| Si 2p (IV) | 102.63 | 7.7 | | | |
| Co 3s-1 | 102.65 | 39.06 | | | |
| Co 3s-2 | 107.09 | 34.32 | | | |
| Co 3s-3 | 111.78 | 9.74 | | | |
| **0.5Si@MOF-c** | | | | | |
| **Peaks in Figure 8.5a (Co2p)** | | | **Peaks in Figure 8.5b (C 1s)** | | |
| **Name** | **Position** | **%Area** | **Name** | **Position** | **%Area** |
| Co (II)-1 | 781.12 | 34.17 | C-C, C-H | 284.8 | 52.67 |
| Co (II)-2 | 783.22 | 25.63 | C-O | 286.39 | 20.91 |

|  |  |  |  |  |  |
|---|---|---|---|---|---|
| Co (II)-3 | 785.72 | 11.92 | C=O | 288.47 | 22.95 |
| Co (II)-4 | 787.55 | 28.28 | COOH | 290.52 | 3.47 |
| **Peaks in Figure 8.5c (Si 2p & Co 3s)** |  |  |  |  |  |
| **Name** | **Position** | **%Area** |  |  |  |
| Co 3s-1 | 103.21 | 48 |  |  |  |
| Co 3s-2 | 107.65 | 39.76 |  |  |  |
| Co 3s-3 | 112.2 | 12.25 |  |  |  |

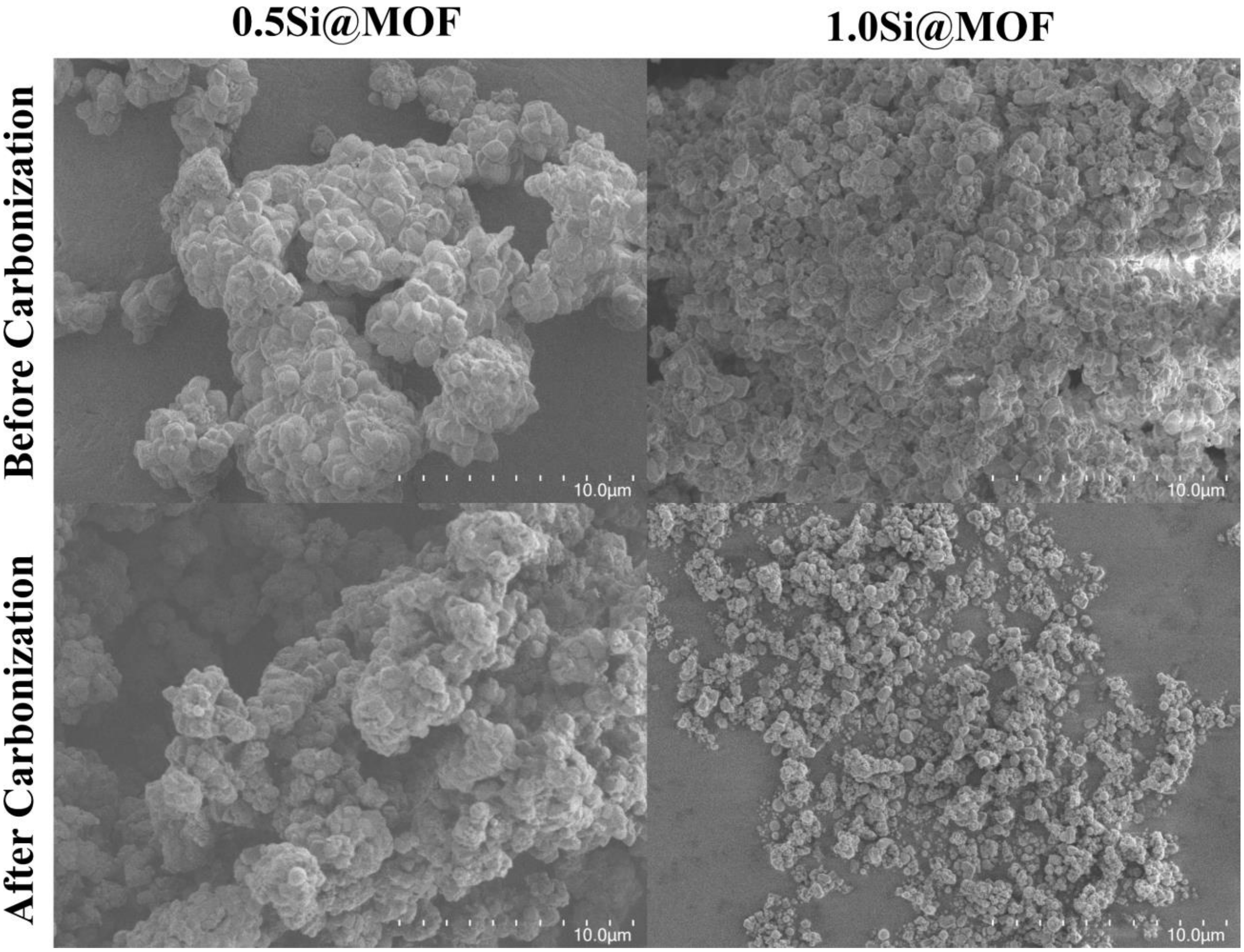

Figure S8.1. SEM images of 0.5Si@MOF and 1.0Si@MOF samples before and after carbonization.

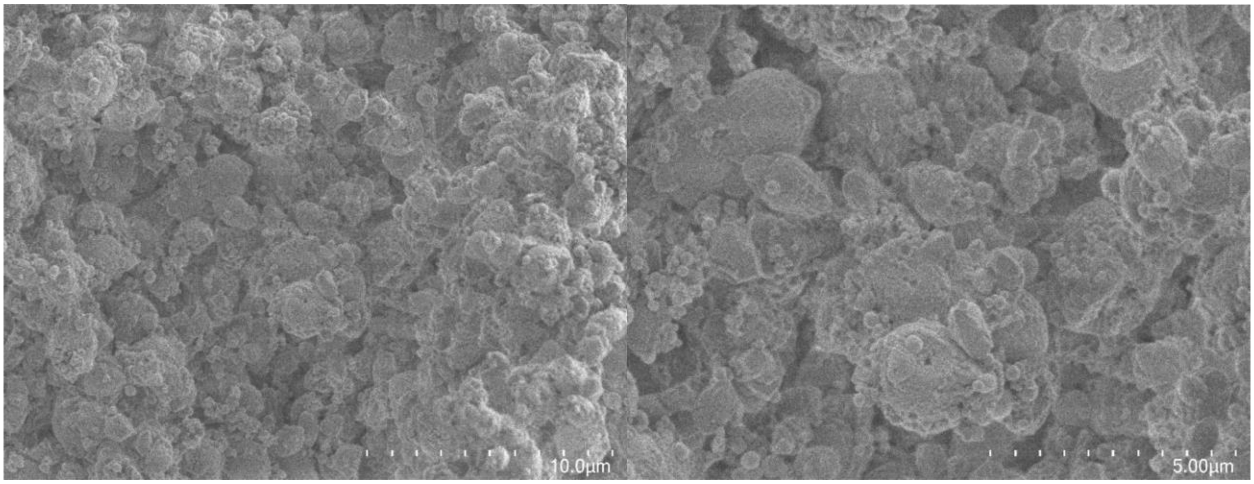

Figure S8.2. SEM images of the unsuccessful 1.5Si@MOF sample prior to carbonization. Notice the severe agglomeration of particles of different irregular morphology due to a large fraction of unencapsulated nano Si.

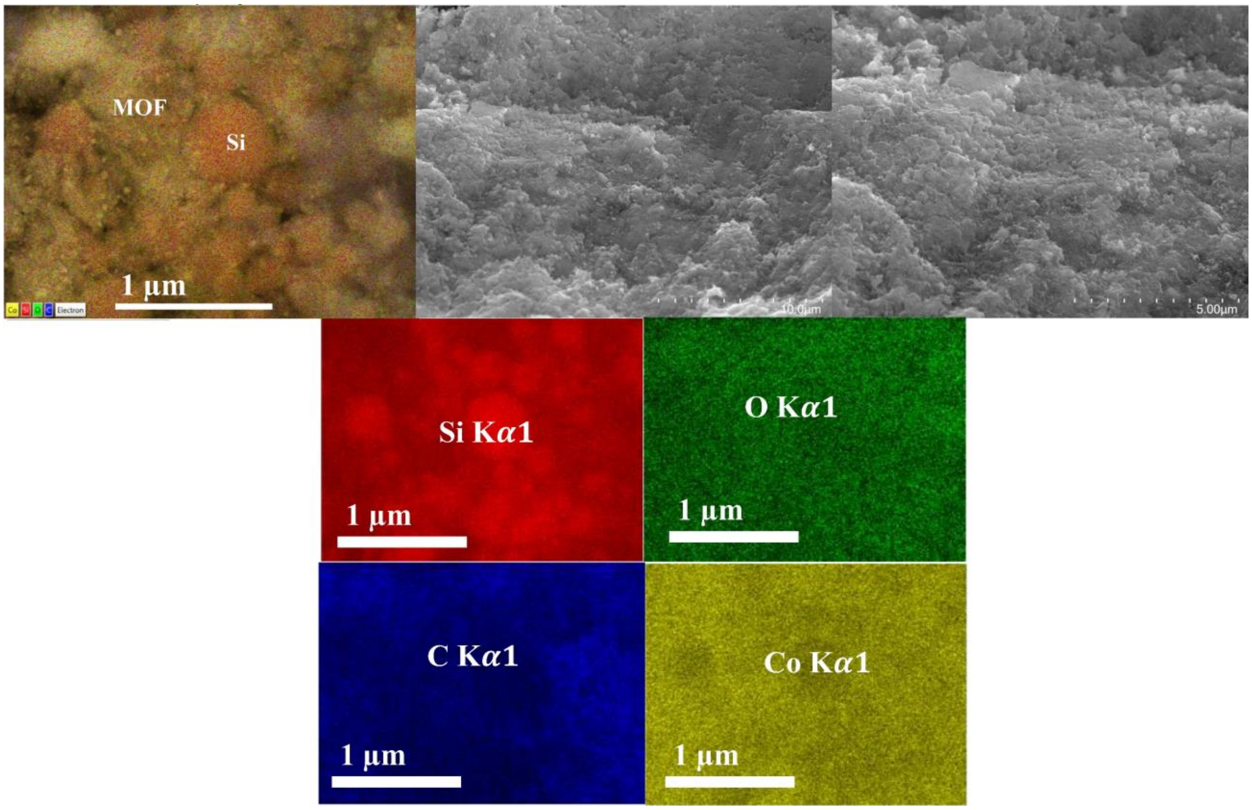

Figure S8.3. EDX map and SEM images of the bulk active material within an uncycled 0.5Si@MOF-c electrode.

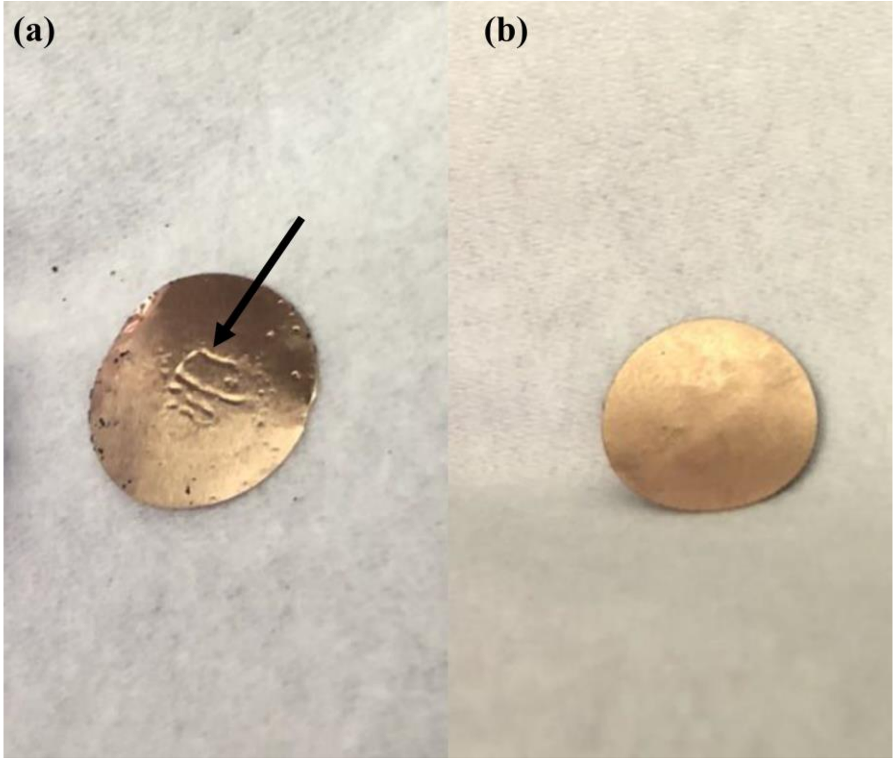

Figure S8.4. Postmortem images of the Cu-side for a) Si-rich electrode and b) SP-Si-MOF (MOF-74) electrode. Notice the welting pattern on the Si-rich baseline electrode.

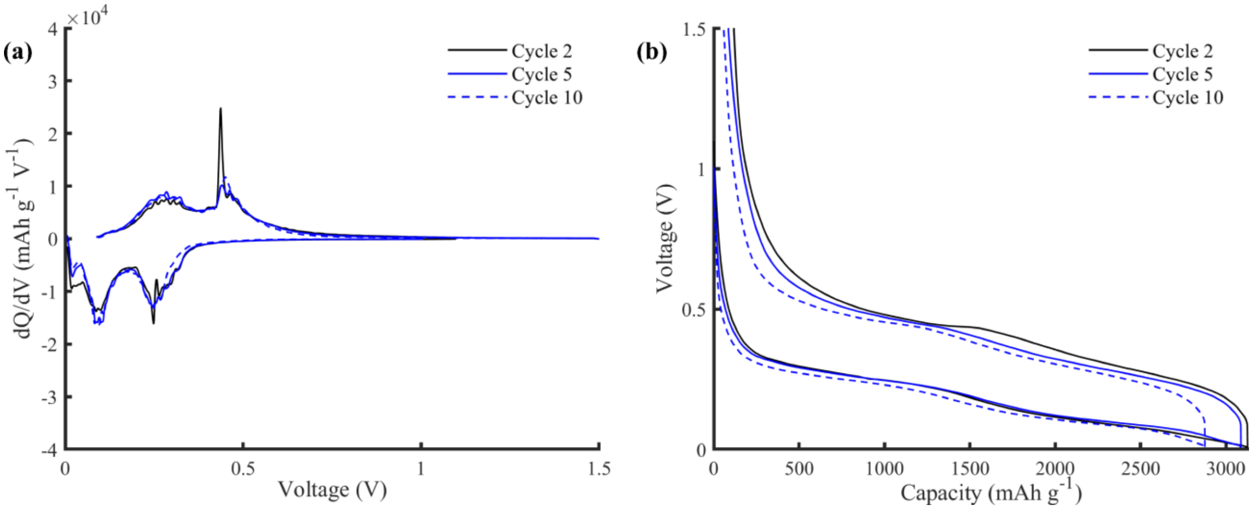

Figure S8.5. (a) dQ/dV plot and (b) potential profile for the SP-Si-cushion.

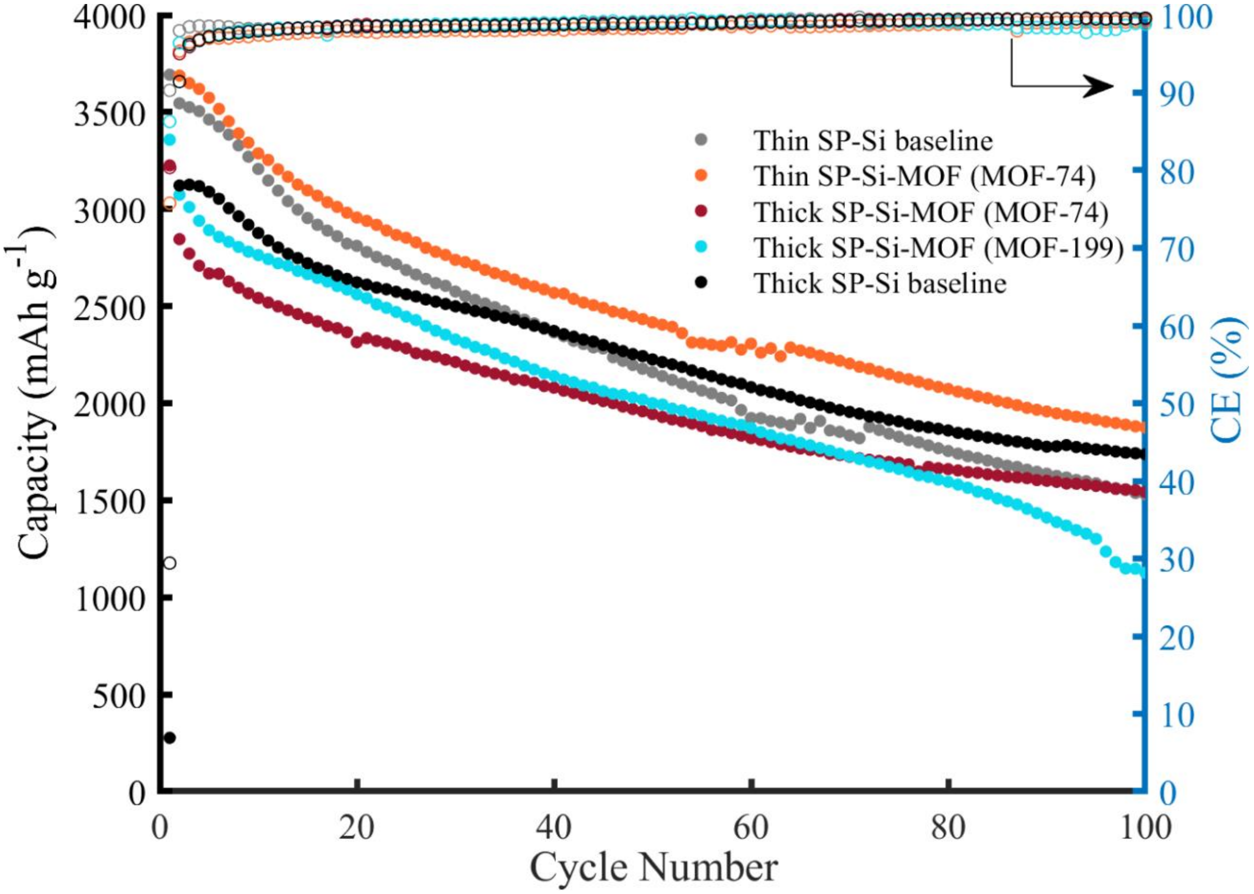

Figure S8.6. Active material discharge capacity for sandwich configuration electrodes of varied thickness and MOF type.

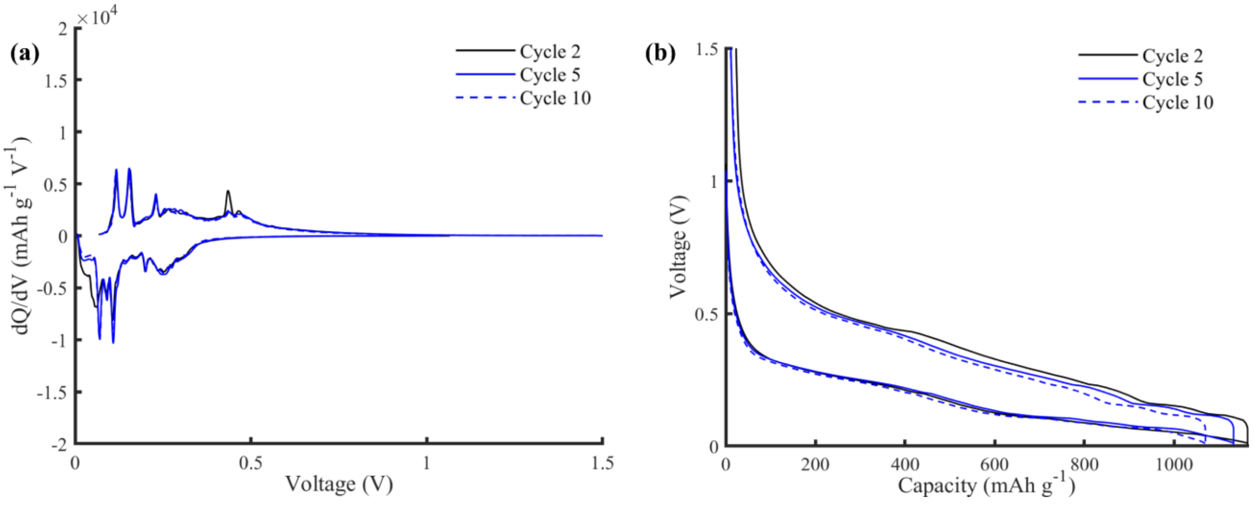

Figure S8.7. (a) dQ/dV plot and (b) potential profile for the 20Si-10CMC baseline.

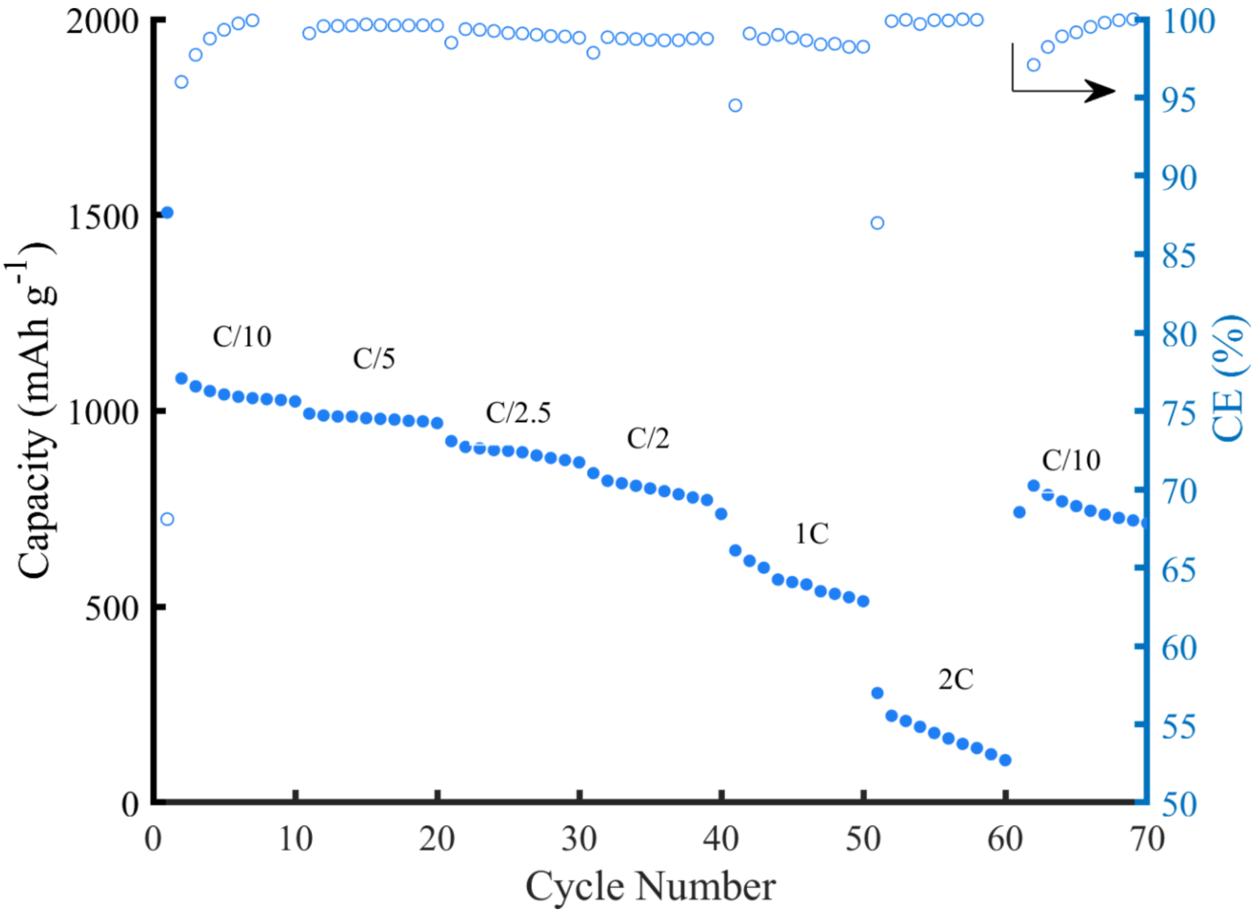

Figure S8.8. Active material discharge capacity during rate capability test on the best-performing 0.5Si@MOF-c electrode.

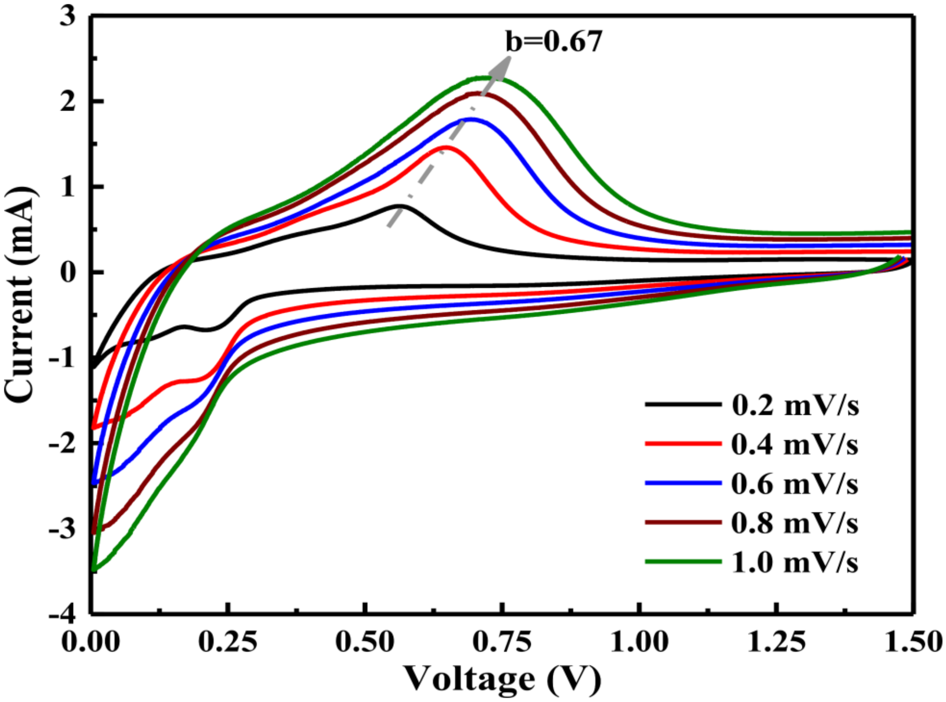

Figure S8.9. CVs at various scan rates on a 0.5Si@MOF-c electrode. Notice the high current, consistent with the high active material loading used in this study.

## Appendix A: High-Entropy Alloy Anodes

The possible advantages of multicomponent or high-entropy alloys as anode materials have been discussed in Chapter 2. It is known that the lithiation behaviour of multicomponent alloys can be different from the lithiation of the individual constituent elements (e.g., lithiation of Mg-Si phases). Some preliminary work was done to explore the feasibility of the HEAs listed in Table A1 below.

Table A1. HEAs tested as anode materials.

| Sample | Composition | Preparation |
|---|---|---|
| **JSHEA008** | $Bi_{0.2}Ge_{0.2}Sn_{0.2}Sb_{0.2}Ag_{0.2}$ | Heating under argon to 1150 °C |
| **JSHEA009** | $Si_{0.2}Al_{0.2}Sn_{0.2}Ag_{0.2}Cu_{0.2}$ | Ball-milling followed by heating under argon to 1150 °C |
| **JSHEA010** | $Si_{0.3}Al_{0.3}Sn_{0.15}Ag_{0.15}Cu_{0.1}$ | Ball-milling followed by heating under argon to 1150 °C |

Metals were stored in an Argon-filled glove box to minimize oxidation from moisture and air. Anodes were prepared with a standard tape-casting method. The dry powder consisted of 80 wt% alloy, 10 wt% PVDF binder, and 10 wt% Super P. NMP was used as a solvent. Water-based binders were not used in these anodes due to the concern of over-oxidation of the metals in the presence of water. The slurry was cast onto a cleaned Cu foil.

Figure A1 plots the discharge capacity of the alloy electrodes and reveals a very rapid capacity decay, with all samples delivering a capacity less than graphite after only 20 cycles. There is some evidence that the presence of non-alloying Cu (JSHEA009 & JSHEA010) reduces capacity fade relative to alloys composed entirely of Li-alloying metals (JSHEA008). Another disadvantage of these alloys is the high potential (vs Li) at which the alloying reactions take place. Figure A2 shows the differential capacitance plot for the JSHEA010 alloy. This property is expected as elements like Sn (0.76 V) are known to alloy with Li at much higher potential than graphite (0.125 V) or silicon (0.4 V). However, such a high potential at the anode is undesirable in full cells because it reduces the total cell voltage and hence power output of the cell. It does not appear that the prepared alloys offer any advantage relative to graphite or simple mixtures of each metal.

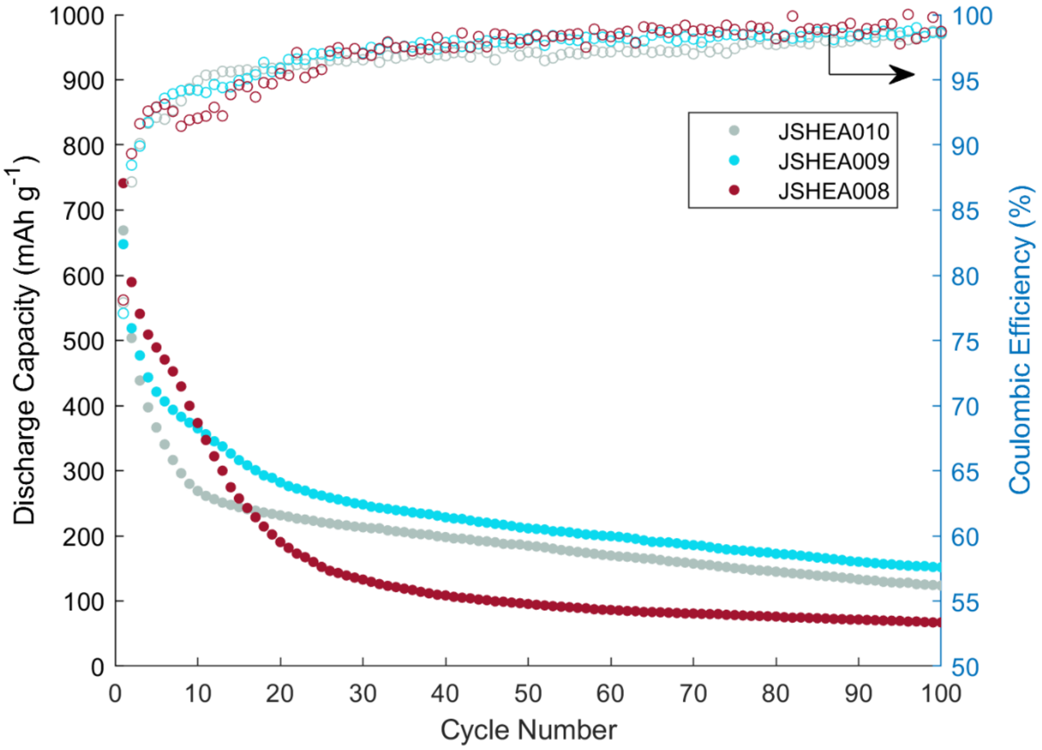

Figure A1. Active material discharge capacity of half-cell anodes prepared with different HEAs. Electrode composition was 80 wt% HEA, 10 wt% Super P, and 10 wt% PVDF binder.

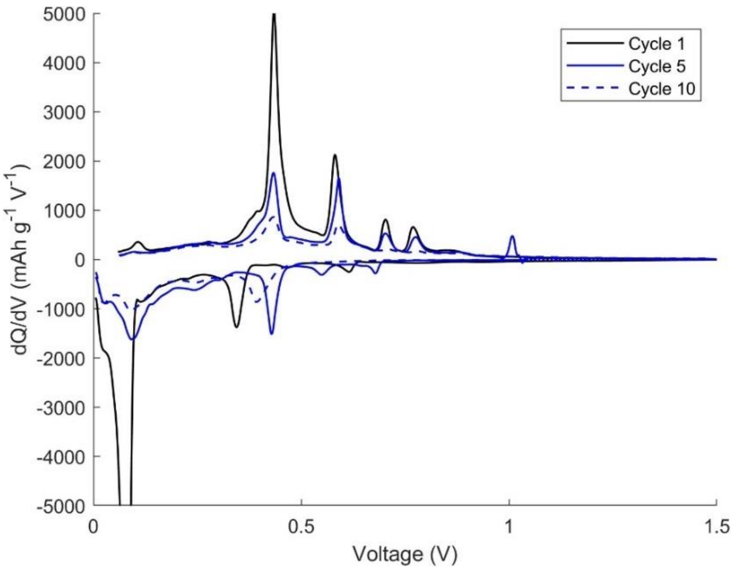

Figure A2. Differential capacitance plot for an electrode made of 80 wt% JSHEA010, 10 wt% Super P, and 10 wt% PVDF binder.

## Appendix B: Additional Comments on Silicon-Binder work

Previous experiments in Chapter 6 have suggested no synergistic effect when XG and CMC are simply combined in equal proportion. However, since XG is believed to help primarily through Cu adhesion, and NaCMC is believed to help through electrode cohesion, the binders were combined in a manner to exploit their respective properties. A thin cushion layer consisting of SP and XG was applied to a Cu foil, followed by a slurry composed of 80 wt% nanosilicon. Half-cell anodes cycled in Figure B1 reveal a very good capacity retention, superior to a baseline without such an XG/SP layer, as seen in Figure 8.6.

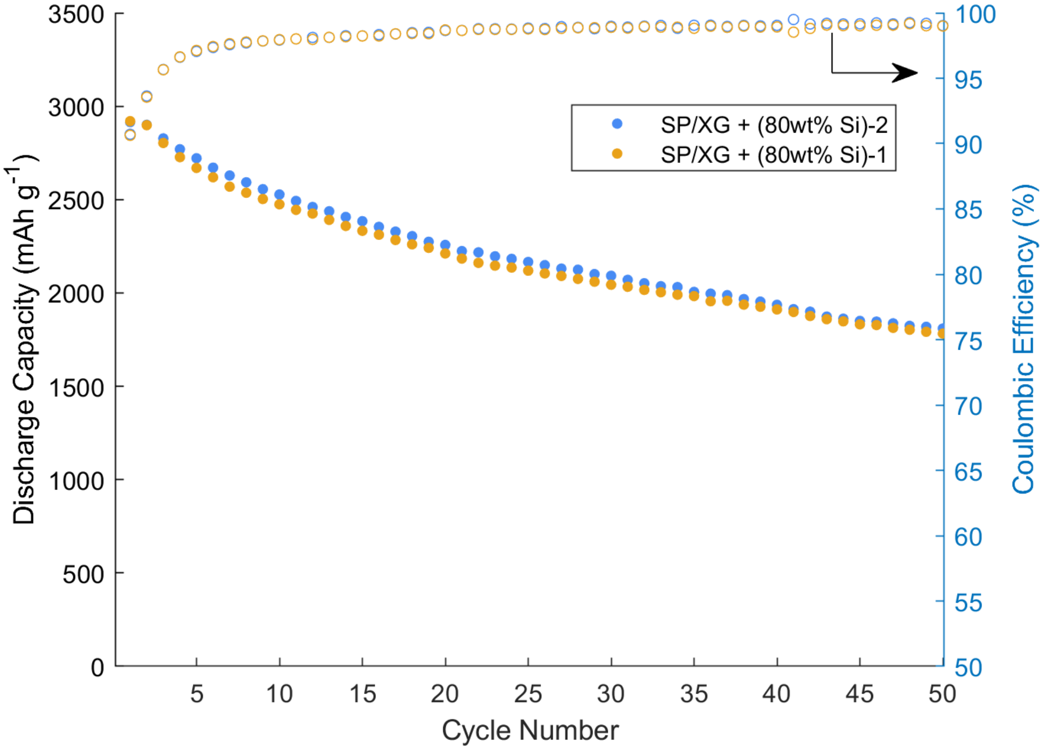

Figure B1. Active material (Si only) discharge capacity of an electrode consisting of a thin SP/XG layer, followed by a standard layer of 80 wt% Si (balance 10 wt% Super P, 10 wt% NaCMC binder).

## Licence Agreement Forms

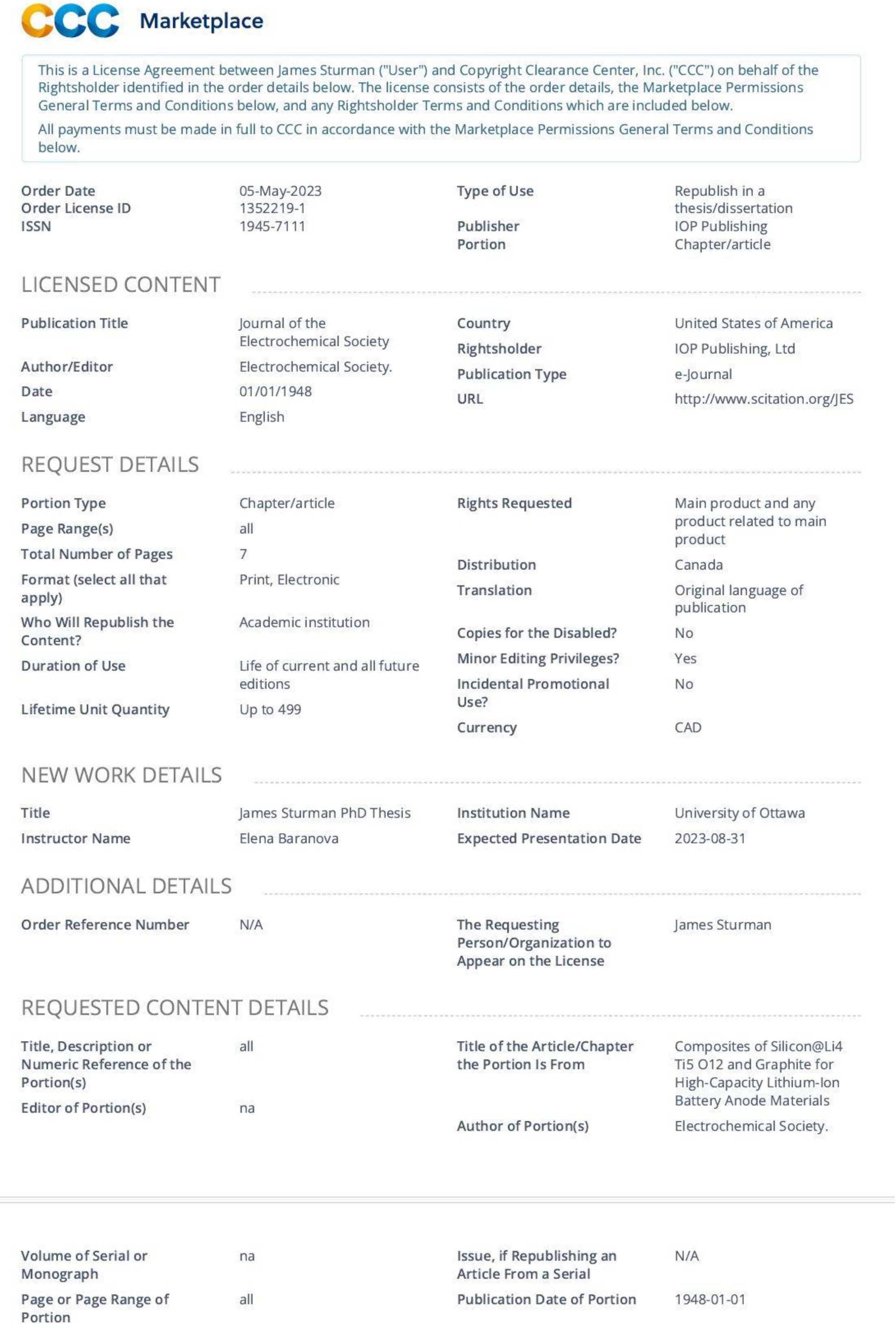

CCC Marketplace

This is a License Agreement between James Sturman ("User") and Copyright Clearance Center, Inc. ("CCC") on behalf of the Rightsholder identified in the order details below. The license consists of the order details, the Marketplace Permissions General Terms and Conditions below, and any Rightsholder Terms and Conditions which are included below.

All payments must be made in full to CCC in accordance with the Marketplace Permissions General Terms and Conditions below.

| | | | |
|---|---|---|---|
| **Order Date** | 05-May-2023 | **Type of Use** | Republish in a thesis/dissertation |
| **Order License ID** | 1352219-1 | **Publisher** | IOP Publishing |
| **ISSN** | 1945-7111 | **Portion** | Chapter/article |

LICENSED CONTENT

| | | | |
|---|---|---|---|
| **Publication Title** | Journal of the Electrochemical Society | **Country** | United States of America |
| **Author/Editor** | Electrochemical Society. | **Rightsholder** | IOP Publishing, Ltd |
| **Date** | 01/01/1948 | **Publication Type** | e-Journal |
| **Language** | English | **URL** | http://www.scitation.org/JES |

REQUEST DETAILS

| | | | |
|---|---|---|---|
| **Portion Type** | Chapter/article | **Rights Requested** | Main product and any product related to main product |
| **Page Range(s)** | all | **Distribution** | Canada |
| **Total Number of Pages** | 7 | **Translation** | Original language of publication |
| **Format (select all that apply)** | Print, Electronic | **Copies for the Disabled?** | No |
| **Who Will Republish the Content?** | Academic institution | **Minor Editing Privileges?** | Yes |
| **Duration of Use** | Life of current and all future editions | **Incidental Promotional Use?** | No |
| **Lifetime Unit Quantity** | Up to 499 | **Currency** | CAD |

NEW WORK DETAILS

| | | | |
|---|---|---|---|
| **Title** | James Sturman PhD Thesis | **Institution Name** | University of Ottawa |
| **Instructor Name** | Elena Baranova | **Expected Presentation Date** | 2023-08-31 |

ADDITIONAL DETAILS

| | | | |
|---|---|---|---|
| **Order Reference Number** | N/A | **The Requesting Person/Organization to Appear on the License** | James Sturman |

REQUESTED CONTENT DETAILS

| | | | |
|---|---|---|---|
| **Title, Description or Numeric Reference of the Portion(s)** | all | **Title of the Article/Chapter the Portion Is From** | Composites of Silicon@Li4 Ti5 O12 and Graphite for High-Capacity Lithium-Ion Battery Anode Materials |
| **Editor of Portion(s)** | na | **Author of Portion(s)** | Electrochemical Society. |
| **Volume of Serial or Monograph** | na | **Issue, if Republishing an Article From a Serial** | N/A |
| **Page or Page Range of Portion** | all | **Publication Date of Portion** | 1948-01-01 |

**CCC Marketplace**

This is a License Agreement between James Sturman ("User") and Copyright Clearance Center, Inc. ("CCC") on behalf of the Rightsholder identified in the order details below. The license consists of the order details, the Marketplace Permissions General Terms and Conditions below, and any Rightsholder Terms and Conditions which are included below.

All payments must be made in full to CCC in accordance with the Marketplace Permissions General Terms and Conditions below.

| | | | |
|---|---|---|---|
| **Order Date** | 16-May-2023 | **Type of Use** | Republish in a thesis/dissertation |
| **Order License ID** | 1355625-2 | **Publisher** | IOP Publishing |
| **ISSN** | 1945-7111 | **Portion** | Chapter/article |

## LICENSED CONTENT

| | | | |
|---|---|---|---|
| **Publication Title** | Journal of the Electrochemical Society | **Country** | United States of America |
| **Author/Editor** | Electrochemical Society. | **Rightsholder** | IOP Publishing, Ltd |
| **Date** | 01/01/1948 | **Publication Type** | e-Journal |
| **Language** | English | **URL** | http://www.scitation.org/JES |

## REQUEST DETAILS

| | | | |
|---|---|---|---|
| **Portion Type** | Chapter/article | **Rights Requested** | Main product and any product related to main product |
| **Page Range(s)** | all | **Distribution** | Canada |
| **Total Number of Pages** | 4 | **Translation** | Original language of publication |
| **Format (select all that apply)** | Print, Electronic | **Copies for the Disabled?** | No |
| **Who Will Republish the Content?** | Academic institution | **Minor Editing Privileges?** | Yes |
| **Duration of Use** | Life of current and all future editions | **Incidental Promotional Use?** | No |
| **Lifetime Unit Quantity** | Up to 499 | **Currency** | CAD |

## NEW WORK DETAILS

| | | | |
|---|---|---|---|
| **Title** | James Sturman PhD Thesis | **Institution Name** | University of Ottawa |
| **Instructor Name** | Elena Baranova | **Expected Presentation Date** | 2023-08-31 |

## ADDITIONAL DETAILS

| | | | |
|---|---|---|---|
| **Order Reference Number** | N/A | **The Requesting Person/Organization to Appear on the License** | James Sturman |

## REQUESTED CONTENT DETAILS

| | | | |
|---|---|---|---|
| **Title, Description or Numeric Reference of the Portion(s)** | all | **Title of the Article/Chapter the Portion Is From** | Communication—Design of LiNi0.2Mn0.2Co0.2Fe0.2Ti0.2O2 as a High-Entropy Cathode for Lithium-Ion Batteries Guided by Machine Learning |
| **Editor of Portion(s)** | na | | |

---

| | | | |
|---|---|---|---|
| **Volume of Serial or Monograph** | na | **Author of Portion(s)** | Electrochemical Society. |
| **Page or Page Range of Portion** | all | **Issue, if Republishing an Article From a Serial** | na |
| | | **Publication Date of Portion** | 1948-01-01 |

**Marketplace**

| | | | |
|---|---|---|---|
| **Order Date** | 16-May-2023 | **Type of Use** | Republish in a thesis/dissertation |
| **Order License ID** | 1355625-1 | **Publisher** | IOP Publishing |
| **ISSN** | 1945-7111 | **Portion** | Chapter/article |

## LICENSED CONTENT

| | | | |
|---|---|---|---|
| **Publication Title** | Journal of the Electrochemical Society | **Country** | United States of America |
| **Author/Editor** | Electrochemical Society. | **Rightsholder** | IOP Publishing, Ltd |
| **Date** | 01/01/1948 | **Publication Type** | e-Journal |
| **Language** | English | **URL** | http://www.scitation.org/JES |

## REQUEST DETAILS

| | | | |
|---|---|---|---|
| **Portion Type** | Chapter/article | **Rights Requested** | Main product and any product related to main product |
| **Page Range(s)** | all | **Distribution** | Canada |
| **Total Number of Pages** | 11 | **Translation** | Original language of publication |
| **Format (select all that apply)** | Print, Electronic | **Copies for the Disabled?** | No |
| **Who Will Republish the Content?** | Academic institution | **Minor Editing Privileges?** | Yes |
| **Duration of Use** | Life of current and all future editions | **Incidental Promotional Use?** | No |
| **Lifetime Unit Quantity** | Up to 499 | **Currency** | CAD |

## NEW WORK DETAILS

| | | | |
|---|---|---|---|
| **Title** | James Sturman PhD Thesis | **Institution Name** | University of Ottawa |
| **Instructor Name** | Elena Baranova | **Expected Presentation Date** | 2023-08-31 |

## ADDITIONAL DETAILS

| | | | |
|---|---|---|---|
| **Order Reference Number** | N/A | **The Requesting Person/Organization to Appear on the License** | James Sturman |

## REQUESTED CONTENT DETAILS

| | | | |
|---|---|---|---|
| **Title, Description or Numeric Reference of the Portion(s)** | all | **Title of the Article/Chapter the Portion Is From** | Investigation of Xanthan Gum and Carboxymethyl Cellulose Binders for the Silicon Anode of Lithium-Ion Batteries |
| **Editor of Portion(s)** | na | | |
| **Volume of Serial or Monograph** | na | **Author of Portion(s)** | Electrochemical Society. |
| **Page or Page Range of Portion** | all | **Issue, if Republishing an Article From a Serial** | na |
| | | **Publication Date of Portion** | 1948-01-01 |

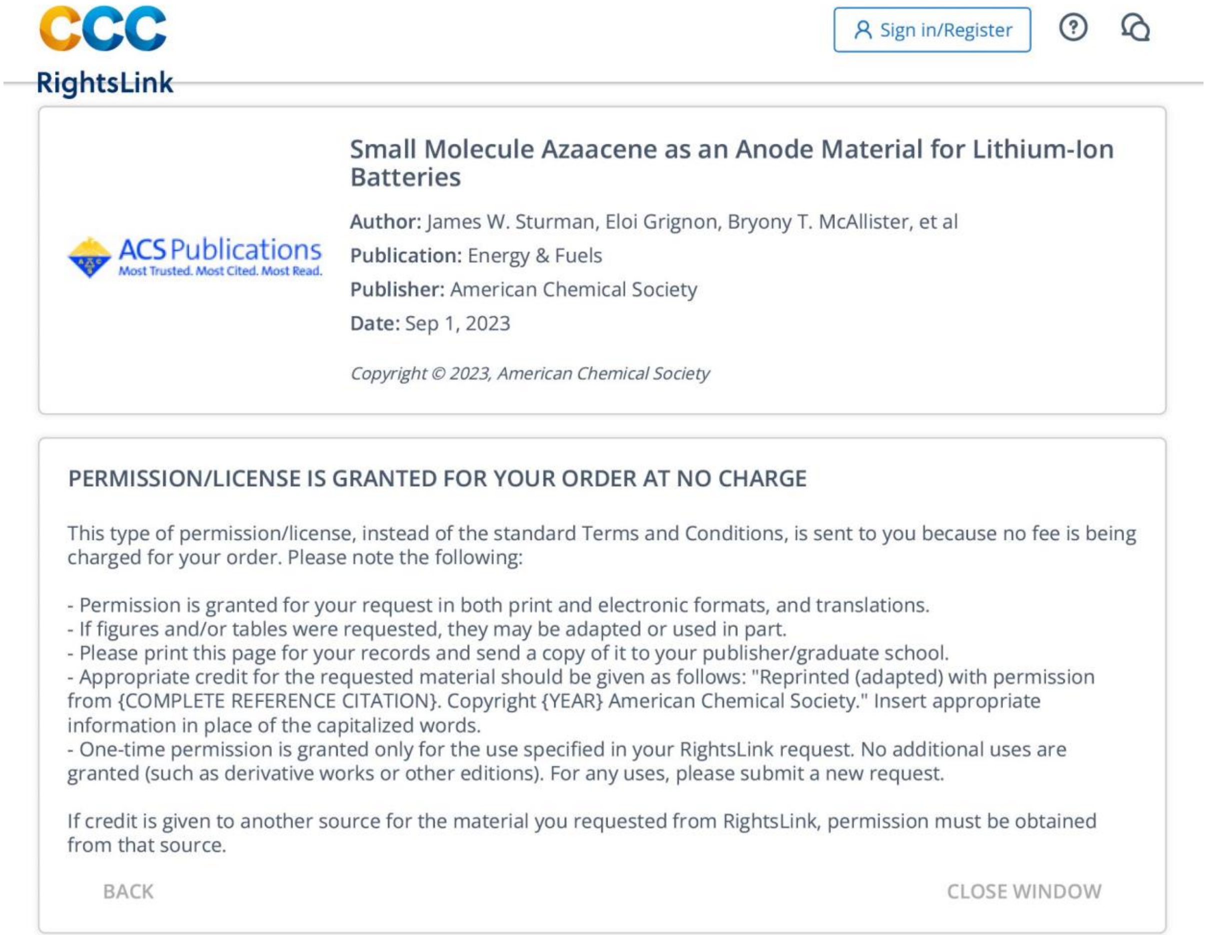

Small Molecule Azaacene as an Anode Material for Lithium-Ion Batteries

**Author:** James W. Sturman, Eloi Grignon, Bryony T. McAllister, et al
**Publication:** Energy & Fuels
**Publisher:** American Chemical Society
**Date:** Sep 1, 2023

PERMISSION/LICENSE IS GRANTED FOR YOUR ORDER AT NO CHARGE

This type of permission/license, instead of the standard Terms and Conditions, is sent to you because no fee is being charged for your order. Please note the following:

- Permission is granted for your request in both print and electronic formats, and translations.
- If figures and/or tables were requested, they may be adapted or used in part.
- Please print this page for your records and send a copy of it to your publisher/graduate school.
- Appropriate credit for the requested material should be given as follows: "Reprinted (adapted) with permission from {COMPLETE REFERENCE CITATION}. Copyright {YEAR} American Chemical Society." Insert appropriate information in place of the capitalized words.
- One-time permission is granted only for the use specified in your RightsLink request. No additional uses are granted (such as derivative works or other editions). For any uses, please submit a new request.

If credit is given to another source for the material you requested from RightsLink, permission must be obtained from that source.